A NOVEL FLYWHEEL AND OPERATION APPROACH FOR ENERGY RECOVERY AND STORAGE

A Dissertation

by

ZHIYANG WANG

Submitted to the Office of Graduate Studies of
Texas A&M University
in partial fulfillment of the requirements for the degree of

DOCTOR OF PHILOSOPHY

December 2011

Major Subject: Mechanical Engineering

A NOVEL FLYWHEEL AND OPERATION APPROACH FOR ENERGY RECOVERY AND STORAGE

A Dissertation

by

ZHIYANG WANG

Submitted to the Office of Graduate Studies of
Texas A&M University
in partial fulfillment of the requirements for the degree of

DOCTOR OF PHILOSOPHY

Approved by:

Chair of Committee,	Alan Palazzolo
Committee Members,	Gary Fry
	Reza Langari
	Steve Suh
Head of Department,	Jerald Caton

December 2011

Major Subject: Mechanical Engineering

ABSTRACT

A Novel Flywheel and Operation Approach for Energy Recovery and Storage.

(December 2011)

Zhiyang Wang,

B.S., Harbin Institute of Technology, China;

M.S., Harbin Institute of Technology, China

Chair of Advisory Committee: Dr. Alan B. Palazzolo

A flywheel has intrinsic advantages over other energy storage forms such as hydraulic storage, batteries and compressed air. These advantages include higher robustness, a longer life, greater energy density, higher efficiency, lower loss, better discharge depth and relatively easier recycling.

A novel shaftless flywheel was developed. By integrating the motor generator and the magnetic suspension into the flywheel disk, the novel design removes the need for a support shaft and enables its solid disk architecture, which was shown to have large advantages over traditional annular disc designs with shafts. This was illustrated by comparisons between annular and solid 4340 discs in stress levels, S-N life and fatigue life with cracks. The low speed nature of the system makes possible the usage of unlaminated structures, which reduces the system cost at partial expense of the performance.

A 4340 steel sample was tested to retrieve its magnetic property. The magnetic

levitation was then designed using magnetostatic analyses, which gave the position stiffness and current stiffness.

The eddy losses of the magnetic bearings were retrieved through FEM software CARMEN™. The total bearing loss was calculated based on the simulated eddy loss and measured hysteresis loss. The system equilibrium temperature was simulated with ANSYS™.

The frequency weakening effect of the magnetic bearing was analyzed with ANSYS™ harmonic analysis. The closed-loop control stability of the system was then investigated.

A motor concept was proposed with variable motor/generator gain capability, which was a key feature in optimizing the charge/discharge performances of the flywheel in both grid level and hybrid locomotive applications.

Based on EPA average data, the benefits of our hybrid locomotives on fuel and NOx savings were simulated on various train operations. The regenerative braking optimization was also discussed. The dissertation concludes with the discussion of the flywheel system isolation from train operation induced vibrations.

In conclusion, the novel shaftless flywheel developed has great advantages in both system life and cost over traditional designs. Analyses from magnetic, thermal and control stand of points verified the novel system's performance. The effectiveness and feasibility of implementing the developed flywheel systems on hybrid railway locomotives were also proved.

DEDICATION

To my family

ACKNOWLEDGMENTS

I would like to express my appreciation to Dr. Palazzolo for his immeasurable considerations and help on my research during my graduate study in the Vibration Control Electromachanical Lab at Texas A&M University. I also would like to thank Dr. Gary Fry, Dr. Reza Langari and Dr. Steve Suh for serving on my advisory committee.

I am grateful to my colleagues, Dr. Junyoung Park, Randall Tucker, Xiaohua Zhang, Zhengxin Zhang and Xu Han, for their priceless friendship and help. I also want to express my sincere appreciation to AAR (Association of American Railroads) and TRC (Turbomachinery Research Consortium) at Texas A&M University for their helpful advice and financial support.

I have to thank my parents, Yulu Wang and Xin Wei. I would not have finished this small achievement without their support and encouragement. I will love them forever.

I would also like to thank my wife, Ruiqi Long, for always standing beside me and supporting me. Her encouragement and help are sources of my inspiration and motivation during this whole process. Our love will live forever.

TABLE OF CONTENTS

Page

CHAPTER Page

CHAPTER Page

LIST OF FIGURES

FIGURE Page

FIGURE Page

FIGURE Page

FIGURE Page

FIGURE Page

FIGURE Page

FIGURE Page

FIGURE Page

FIGURE Page

FIGURE Page

LIST OF TABLES

NOMENCLATURE

A	=	Magnetic vector potential
B	=	Magnetic flux density
b	=	Regenerative braking optimization performance control parameter
$C_{H1/T}^{In}$	=	Damping of the inner isolators between 1st FW housing and train
$C_{H1/T}^{In\_Sh}$	=	Shear damping of the inner isolators between 1st housing and train
$C_{H1/T}^{Out}$	=	Damping of the outer isolators between 1st FW housing and train
$C_{H1/T}^{Out\_Sh}$	=	Shear damping of the outer isolators between 1st housing and train
C_{Hns}	=	Side supporting damping between nth flywheel housing and train
C_{PS}	=	Damping of bogie primary suspension
C_{SS}	=	Damping of bogie secondary suspension
D	=	Electric flux density
E	=	Electric field intensity or Young's modulus
F_{davis}	=	Drag forces calculated via modified Davis equation
F_{drive}	=	Total forward driving forces
$(F_{fn/Hn}^{AMB})_x$	=	Magnetic bearing forces in X on housing for nth flywheel assembly
$(F_{fn/Hn}^{AMB})_y$	=	Magnetic bearing forces in Y on housing for nth flywheel assembly
$(F_{fn/Hn}^{AMB})_z$	=	Magnetic bearing forces in Z on housing for nth flywheel assembly
$(F_{G/SF}^{x})_F$	=	X component of the force on front bogies imposed by track profile
$(F_{G/SF}^{x})_R$	=	X component of the force on rear bogies imposed by track profile

$(F^{y}_{G/SF})_F$ = Y component of the force on front bogies imposed by track profile

$(F^{y}_{G/SF})_R$ = Y component of the force on rear bogies imposed by track profile

$(F^{z}_{G/SF})_n$ = Z component of the force on the nth bogie generated by track profile

$(F^{AMB}_{Hn/fn})_x$ = Magnetic bearing forces in X on flywheel for nth flywheel assembly

$(F^{AMB}_{Hn/fn})_y$ = Magnetic bearing forces in Y on flywheel for nth flywheel assembly

$(F^{AMB}_{Hn/fn})_z$ = Magnetic bearing forces in Z on flywheel for nth flywheel assembly

$(F^{ISO}_{Hn/T})_x$ = Force on train in X direction by nth flywheel housing's isolators

$(F^{ISO}_{Hn/T})_y$ = Force on train in Y direction by nth flywheel housing's isolators

$(F^{ISO}_{Hn/T})_z$ = Force on train in Z direction by nth flywheel housing's isolators

$(F^{Side}_{Hn/T})_x$ = Force on train in X direction by nth flywheel housing side supports

$(F^{Side}_{Hn/T})_y$ = Force on train in Y direction by nth flywheel housing side supports

$(F^{x}_{SF/T})_F$ = X component of the force on train floor generated by front bogies

$(F^{x}_{SF/T})_R$ = X component of the force on train floor generated by rear bogies

$(F^{y}_{SF/T})_F$ = Y component of the force on train floor generated by front bogies

$(F^{y}_{SF/T})_R$ = Y component of the force on train floor generated by rear bogies

$(F^{z}_{SF/T})_n$ = Z component of the force on train floor generated by the nth bogie

F^{Cen}_{T} = Train centrifugal force

$(F^{ISO}_{T/Hn})_x$ = Isolators force on nth flywheel housing in X direction by train

$(F^{ISO}_{T/Hn})_y$ = Isolators force on nth flywheel housing in Y direction by train

$(F^{ISO}_{T/Hn})_z$ = Isolators force on nth flywheel housing in Z direction by train

$(F_{T/Hn}^{Side})_x$ = Force on nth flywheel housing in X direction by train side supports

$(F_{T/Hn}^{Side})_y$ = Force on nth flywheel housing in X direction by train side supports

F_{tm} = Traction motor forces generated via flywheel power

F_{train} = Total forward force on train

g_{air} = Air gaps

H = Magnetic field intensity

H_h = Flywheel housing height

$H_{H1/t}$ = Distance between 1st FW housing bottom and train floor

$H_{Hn/Hm}$ = Distance between nth FW housing bottom and mth FW housing *top*

I = Current within the coil

I_{pf} = Flywheel polar moment of inertia around X axis

I_{fnt} = nth flywheel transverse moment of inertia

I_{pt} = Slug car polar moment of inertia around X axis

I_{tt1} = Slug car transverse moment of inertia around X axis

I_{tt2} = Slug car transverse moment of inertia around Y axis

i_{fw} = Flywheel current

i_{tm} = Traction motor current

J = Electric current density

K_{fw} = Flywheel torque constant

$K_{H1/T}^{In}$ = Stiffness of the inner isolators between 1st FW housing and train floor

$K_{H1/T}^{In\_Sh}$ = Shear stiffness of the inner isolators between 1st housing and train floor

$K_{H1/T}^{Out}$ = Stiffness of the outer isolators between 1st FW housing and train floor

$K_{H1/T}^{Out\_Sh}$ = Shear stiffness of the outer isolators between 1st housing and train floor

K_{Hns} = Side supporting stiffness between nth flywheel housing and train

K_I = Stress intensity factor

K_{PS} = Stiffness of bogie primary suspension

K_{SS} = Stiffness of bogie secondary suspension

K_T = Transition stress intensity value

K_{th} = Threshold stress intensity value

K_{tm} = Traction motor torque constant

L_t = Slug car (train floor) length between front and rear bogies

m_{SF} = Bogie's side frame mass

$(M_{SF/T})_x$ = X component of the total moment on train floor imposed by bogies

$(M_{SF/T})_y$ = Y component of the total moment on train floor generated by bogies

$(M_{SF/T})_z$ = Z component of the total moment on train floor generated by bogies

m_{train} = Train total mass including the flywheel slug car.

$(M_{fn/Hn}^{AMB})_x$ = AMB moment around X axis on housing for nth flywheel assembly

$(M_{fn/Hn}^{AMB})_y$ = AMB moment around Y axis on housing for nth flywheel assembly

$(M_{Hn/fn}^{AMB})_x$ = AMB moment around X axis on flywheel for nth flywheel assembly

$(M_{Hn/fn}^{AMB})_y$ = AMB moment around Y axis on flywheel for nth flywheel assembly

$(M_{Hn/T}^{ISO})_x$ = Isolators' moments on train around X axis imposed by nth flywheel housing

$(M_{Hn/T}^{ISO})_y$ = Isolators' moments on train around Y axis imposed by nth flywheel housing

$(M_{Hn/T}^{ISO})_z$ = Isolators' moments on train around Z axis imposed by nth flywheel housing

$(M_{Hn/T}^{Side})_x$ = Side supporting mechanism moments on train around X axis imposed by nth flywheel housing

$(M_{Hn/T}^{Side})_y$ = Side supporting mechanism moments on train around Y axis imposed by nth flywheel housing

$(M_{T/Hn}^{ISO})_x$ = Isolators' moments on nth flywheel housing around X axis imposed by train

$(M_{T}^{Cen})_x$ = Train centrifugal force generated moments on train body

$(M_{T/Hn}^{ISO})_y$ = Isolators' moments on nth flywheel housing around Y axis imposed by train

$(M_{T/Hn}^{ISO})_z$ = Isolators' moments on nth flywheel housing around Z axis imposed by train

$(M_{T/Hn}^{Side})_x$ = Side supporting mechanism moments on the nth housing around X axis imposed by train

$(M_{T/Hn}^{Side})_y$ = Side supporting mechanism moments on the nth housing around Y axis imposed by train

N = Number of turns for the coil

N_f = Fatigue life in cycles

n_{tm} = Traction motor numbers

P_{diesel} = Diesel engine power

P_{fw} = Flywheel power

P_{tm} = Slug car traction motor power

r = Radial position on the disk

r_{gear} = Gear ratio between a traction motor and its wheels

R_i = Inner radius

R_o = Outer radius

R_{wheel} = Slug car wheel radius

S_{eq} = Equivalent stress variation

S_{max} = Maximum stress value

V_{fw} = Flywheel voltage

V_{tm} = Total voltage for traction motors connected in series

v_{train} = Train velocity

W_t = Slug car (train floor) width between left and right bogies

W_{train} = Train total weight including the flywheel slug car

x_{fn} = nth flywheel motion in X direction

$\dot{x}_{fn}$ = nth flywheel velocity in X direction

$\ddot{x}_{fn}$ = nth flywheel acceleration in X direction

x_{Hn} = nth flywheel housing motion in X direction

$\dot{x}_{Hn}$ = nth flywheel housing velocity in X direction

$\ddot{x}_{Hn}$ = nth flywheel housing acceleration in X direction

$(x_{SF})_F$ = Motion of the front bogie side frames in X direction

$(\dot{x}_{SF})_F$ = Velocity of the front bogie side frames in X direction

$(\ddot{x}_{SF})_F$ = Acceleration of the front bogie side frames in X direction

$(x_{SF})_R$ = Motion of the rear bogie side frames in X direction

$(\dot{x}_{SF})_R$ = Velocity of the rear bogie side frames in X direction

$(\ddot{x}_{SF})_R$ = Acceleration of the rear bogie side frames in X direction

x_t = Slug car (train floor) motion in X direction

$\dot{x}_t$ = Slug car (train floor) velocity in X direction

$\ddot{x}_t$ = Slug car (train floor) acceleration in X direction

y_{fn} = nth flywheel motion in Y direction

$\dot{y}_{fn}$ = nth flywheel velocity in Y direction

$\ddot{y}_{fn}$ = nth flywheel acceleration in Y direction

y_{Hn} = nth flywheel housing motion in Y direction

$\dot{y}_{Hn}$ = nth flywheel housing velocity in Y direction

$\ddot{y}_{Hn}$ = nth flywheel housing acceleration in Y direction

$(y_{SF})_F$ = Motion of the front bogie side frames in Y direction

$(\dot{y}_{SF})_F$ = Velocity of the front bogie side frames in Y direction

$(\ddot{y}_{SF})_F$ = Acceleration of the front bogie side frames in Y direction

$(y_{SF})_R$ = Motion of the rear bogie side frames in Y direction

$(\dot{y}_{SF})_R$ = Velocity of the rear bogie side frames in Y direction

$(\ddot{y}_{SF})_R$ = Acceleration of the rear bogie side frames in Y direction

y_t = Slug car (train floor) motion in Y direction

$\dot{y}_t$ = Slug car (train floor) velocity in Y direction

$\ddot{y}_t$ = Slug car (train floor) acceleration in Y direction

z_{fn} = nth flywheel motion in Z direction

$\dot{z}_{fn}$ = nth flywheel velocity in Z direction

$\ddot{z}_{fn}$ = nth flywheel acceleration in Z direction

z_{Hn} = nth flywheel housing motion in Z direction

$\dot{z}_{Hn}$ = nth flywheel housing velocity in Z direction

$\ddot{z}_{Hn}$ = nth flywheel housing acceleration in Z direction

$(z_{SF})_n$ = Motion of the nth bogie side frame in Z direction

$(\dot{z}_{SF})_n$ = Velocity of the nth bogie side frame in Z direction

$(\ddot{z}_{SF})_n$ = Acceleration of the nth bogie side frame in Z direction

z_t = Slug car (train floor) motion in Z direction

$\dot{z}_t$ = Slug car (train floor) velocity in Z direction

$\ddot{z}_t$ = Slug car (train floor) acceleration in Z direction

$(z_{Track})_n$ = Track profile under the nth bogie in Z direction

$(\dot{z}_{Track})_n$ = Track profile changing rate under the nth bogie in Z direction

Greek

Γ_{tm} = Slug car traction motor torque

γ = Poisson ratio

γ_p = Peclet number

Δ = Skin depth

σ_r = Radial stress

σ_θ = Circumferential (hoop) stress

θ_{fnx} = nth flywheel angular rotation around X axis

$\dot{\theta}_{fnx}$ = nth flywheel angular velocity around X axis

$\ddot{\theta}_{fnx}$ = nth flywheel angular acceleration around X axis

θ_{fny} = nth flywheel angular rotation around Y axis

$\dot{\theta}_{fny}$ = nth flywheel angular velocity around Y axis

$\ddot{\theta}_{fny}$ = nth flywheel angular acceleration around Y axis

θ_{fnz} = nth flywheel angular rotation around Z axis

$\dot{\theta}_{fnz}$ = nth flywheel angular velocity around Z axis

$\ddot{\theta}_{fnz}$ = nth flywheel angular acceleration around Z axis

θ_{Hnx} = nth flywheel housing angular rotation around X axis

$\dot{\theta}_{Hnx}$ = nth flywheel housing angular velocity around X axis

$\ddot{\theta}_{Hnx}$ = nth flywheel housing angular acceleration around X axis

θ_{Hny} = nth flywheel housing angular rotation around Y axis

$\dot{\theta}_{Hny}$ = nth flywheel housing angular velocity around Y axis

$\ddot{\theta}_{Hny}$ = nth flywheel housing angular acceleration around Y axis

θ_{Hnz} = nth flywheel housing angular rotation around Z axis

$\dot{\theta}_{Hnz}$ = nth flywheel housing angular velocity around Z axis

$\ddot{\theta}_{Hnz}$ = nth flywheel housing angular acceleration around Z axis

θ_{T1} = Slug car (train floor) angular rotation around X axis

$\dot{\theta}_{T1}$ = Slug car (train floor) angular velocity around X axis

$\ddot{\theta}_{T1}$ = Slug car (train floor) angular acceleration around X axis

θ_{T2} = Slug car (train floor) angular rotation around Y axis

$\dot{\theta}_{T2}$ = Slug car (train floor) angular velocity around Y axis

$\ddot{\theta}_{T2}$ = Slug car (train floor) angular acceleration around Y axis

θ_{T3} = Slug car (train floor) angular rotation around Z axis

$\dot{\theta}_{T3}$ = Slug car (train floor) angular velocity around Z axis

$\ddot{\theta}_{T3}$ = Slug car (train floor) angular acceleration around Z axis

μ_o = Vacuum permeability

μ_{4340} = Relative permeability for 4340

ρ = Density

Φ = Electric scalar potential

Ψ = Magnetic total scalar potential

ω = Rotational speed (rad/s)

ϖ_{fn} = nth flywheel rotating speed

ϖ_{fw} = Flywheel speed

ϖ_{tm} = Traction motor speed

CHAPTER I

INTRODUCTION

1.1 Overview

Research on renewable energy sources and their applications are more and more extensive these days because of their increasing demands and importance, which can be seen from numerous studies worldwide as in [1-8]. Among these research topics, energy storage system study is one of the key issues due to its important role in applications such as wind farms, solar farms, and hybrid vehicles.

The grid electricity annual NOx emission rate in U.S. is 0.8 kg/MWh in 2007 as released in EPA's eGRID2010 files [9]. According to U.S. Environmental Protection Agency (EPA)' line haul and switcher data [10], the NOx emissions for average diesel engine notches can vary at 8.93-16.58 kg/MWh, which is up to 20 times that of grid electricity. The grid electricity price for railroad is around 11.17 dollar/kWh by U.S. Energy Information Administration in [11]. At a diesel price of $3.5 dollar/gallon, the diesel unit energy price varies between 22.1 cents/kWh and 91.6 cents/kWh depending on the different power level efficiencies derived from EPA's report [10].The diesel fuel cost is approximately 2-8 times the cost of grid electricity, on an equivalent energy basis. In fairness to diesel power, its upper cost limit corresponds to very low power level which consumes a relatively small amount of fuel. For the purpose of both fuel and

---

This dissertation follows the style and format of the ASME Journal of Dynamic Systems, Measurement and Control.

NOx reduction, hybrid train locomotive utilizing different kinds of energy storage devices were developed or under developing these years. These energy storage devices include lithium-ion battery, accumulator batteries, super capacitors, fuel cells and flywheels, etc.

The first hybrid locomotive was introduced by JR East, Hitachi, and Tokyo Car Corporation [12]. Combining diesel engines, traction converter system and roof-mounted lithium-ion battery, the so-called New Energy train (Ne@train) was first tested in May 2003 and designed to have 20% fuel reduction and 50% NOx and particle reduction. The capacity of the battery array is 10kWh with an output of 250kW.

Canadian company RailPower built a hybrid switcher named Green Goat by assembling diesel engines and accumulator batteries (lead acid battery) [13, 14]. A fuel consumption reduction of 30-80% has been observed. The reductions in NOx and harmful PM-10 were reported to be between 80-90%. The lead-acid batteries will provide peak power of the operations while a high efficiency diesel engine provides lower powers and charges the battery. [15] noted that the GK10B model, a smaller version of ‘Green Goat’ called ‘Green Kid’, required a bank of lead-acid cells that can store 1200AH at 300VDC (360kWh) and can satisfy a peak power requirement of 650kW.The discharge depth of the battery bank is limited to 1/3 of total capacity to have a lifetime of 10 years.

French researchers are trying to build a demonstration hybrid locomotive called “Hybrid Locomotive for Demonstration and Investigations on Energetic” (LHyDIE). The sizing of the locomotive and its energy manage system was studied in [16]. A

conventional shunting and switcher diesel locomotive ‘BB63000’ was used as the basic platform of the project. As a result, a 215 kW diesel generator, 200 kWh of batteries (1200 cells of 135Ah batteries) and 1600 cells of 5000F/2.5V super capacitors were selected to replace the original diesel engine with 610kW rated power. The system volume was estimated to be 30 m^3. The cost for the energy sources only was estimated to be 60k€. [17] expanded the system and included flywheel as an additional power sources. The 5.33 kWh/325kW flywheel will supply high-frequency harmonics of the system. Three energy management strategies for the hybrid system were studied and compared.

Although lots of the current hybrid locomotives are using batteries, major efforts were also put into the research of flywheels as a power source. For example, UT Austin was trying to build a 130 kWh composite wheel with 2MW power that will be used on Advanced Locomotive Propulsion System (ALPS) [18-20]. There are several advantages of the flywheel energy storage systems. First, they can have higher energy storage per unit. This in turn means fewer units needed to be installed for a certain application and brings down both the installation and maintenance cost. Second, with proper design, the flywheels can bear much longer life span (charge-discharge cycles) than batteries will do. In addition to these, the flywheel systems will be much easier to be recycled. Due to these advantages, the flywheel energy storage systems are good not only for the hybrid locomotives but also for other areas such as grid level energy storage and regulation.

Korean Chungnam National University [21] built two flywheel energy storage

systems with 5kWh usable energy and maximum speed of 18k RPM. One flywheel is optimized to have bigger energy but strong gyroscopic coupling. Another is weaker on energy storage but have a much smaller gyroscopic term that make the control easier. The magnetic levitated system architecture used for their system is of the general practice nowadays, which consists of a composite flywheel with a shaft in the center and a set of PM biased homo-polar thrust and radial bearings. [22] proposed a small size flywheel storage system using magnetic bearing levitated by Lorentz force to reduce the loss.

Lots of efforts were put into improving the traditional architecture of homopolar magnetic bearings. Zhu [23] and Patrick [24] individually developed similar magnetic bearing structures that tries to combine radial and axial poles into the same structure. [23] is of the heteropolar type of magnetic bearing and [24] is a homopolar magnetic bearing. The aluminum ring in [23] replaces the permanent magnet ring used by [24]. However, their magnetic bearing design have to be bigger than the shaft/disk portion it supports and this limits its capability to support a disk without a shaft, which is crucial for our design as discussed later. Fang [25]proposed a ring shaped axial magnetic bearing with a ‘second air gap’ to bypass the PM path and reduce the AC axial flux path’s reluctance. The axial bearing designed was experimented and verified its low loss characteristics. However, since the ‘second air gap’ is sitting beside the permanent magnets, lots of PM flux will go directly through this air gap, as magnetic fringe fields, instead of supplying the bias flux for the axial bearing. This will weaken the load capabilities of the magnetic bearing given the same PM used. In addition to this, the

fringe may put the material at each end of the ‘second air gap’ nearer into saturation range and increase the path’s magnetic reluctant, which is a negative effect to the ‘second air gap’ benefits claimed. Fang [26] also tried to combine the axial control and moment control into a single combo bearing by discretizing the axial rings into several pieces. The functionality of the bearing was proved by the simulations and experiments. However, as admitted by the paper, the loss is high due to the variation of flux caused by non-continuous axial rings.

Disk strength setups a major barrier for how much energy the flywheel can store. This is why lots of these applications use composite materials since they are stronger than steels and theoretically have a better unit weight energy storage density. However, to improve mechanical strength, the shaft of the flywheel is generally press-fitted onto the disk to prevent radial separation of rotors. This method will leave the rotor vulnerable to fatigue crack propagation. Manufacturing effects on these were discussed in [27]. [28] proposed a semi-empirical approach to enhance the "crack growth" resistance of the rotor.

As will be discussed later, the center bore in traditional structures will increase the rotational hoop stress dramatically and reduce the maximum energy storage capability of the system. It will be a tough task for a composite wheel to be built shaftless since the material cannot construct a magnetic path and must rely on a shaft to levitate. The only finished shaftless flywheel design to the author’s knowledge is [29]. They used flux reluctance centering of the thrust bearings as the radial levitation of the flywheel. By doing this way, the need for the shaft as a carrier of radial bearings was eliminated and

the shaft was removed. However there are two major points that make this design totally different from our proposed shaftless design: the flux reluctance is generally weak and unsuitable for large scale energy storage used in locomotives or wind farms; the flywheel in [29] is actually with a short shaft buried in center and still in annular shape so the rotational hoop stress condition was not improved much, which still degrades the flywheel's energy storage capability. Beacon Power got $2.2M U.S. department of energy funding to develop a new low cost flywheel system [30]. Their proposed method is trying to cement magnets onto the inner surface of composite flywheels and support the flywheels with these magnets. However, the magnet will face both rotational stress and stress induced by supporting the flywheel itself. The different growth rate of the magnet and composite material will further deteriorate the stress problem. Thermal problem may also rise due to the low conductivity of composite materials. The design was also claimed to be shaftless. However, the flywheel still remains annular and the rotating stress condition will not improve much.

By using 4340 steel as the material, a true shaftless design can be realized. Even though the unit weight energy density is only close to the composite wheels, there are several advantages of the design. First, the volume energy density will be much higher since steel's density is more than 4 times that of composite materials. This leads to a much compact design and fits the applications that have strict space requirements, e.g. hybrid locomotives. Second, the material is readily available for mass production of the system. The cost of manufacture will be much lower. Third, material behavior was well studied and tested. The quality control during production is much easier than

composites. The last but not least, the recycle or repair of a steel wheel will be much easier and cheaper than a composite after their life cycles.

1.2 Contributions

The proposed research contains the following unique contributions:

(1) Designed a novel shaft-less steel flywheel that retains the advantages of the solid discs shown over annular structures in the aspect of stress level, S-N life and fatigue crack growth.

(2) Design of a combo, un-laminated, homo-polar magnetic bearings to support the proposed shaft-less flywheel. The structure of the magnetic bearing was optimized to have short AC flux paths to reduce eddy effect and increase closed loop stability for the designed low speed, low relative permeability structure .

(3) Determined eddy current induced frequency weakening effect on bearing current stiffness. Approximate transfer functions for the current stiffness were calculated and the closed loop stability of the flywheel system was proven.

(4) Study of the bearing loss on the novel un-laminated magnetic bearing. Eddy loss was simulated on approximate models. Hysteresis loss was calculated based on experiment results on 4340. The temperature of the vacuum enclosed rotor with bearing loss and motor loss was calculated with thermal FEM simulation.

(5) Developed a movable motor stator concept to have adjustable motor/generator constant

(6) Developed an optimized flywheel regenerative charging algorithm that balances both the energy recovery and braking distance.

(7) Verification of effectiveness of the fuel and NOx reductions by simulation of our flywheel energy storage system installed on a train.

(8) A novel vibration isolation system was developed to enable the train mounted flywheel system to traverse a bump at high speed without causing the flywheel to impact its catcher bearings.

CHAPTER II

DESIGN OF SHAFT-LESS FLYWEEL

2.1 Overview

Flywheel energy storage system is one that stores energy in the form of kinetic energy converted from other sources such as electricity. Generally, the system consists of a rotating disk, motor/generator, support bearing system and their housing. Magnetic bearings, especially those of the homo-polar types were widely used due to their low loss characteristics. Almost all past studied flywheel energy storage systems utilize an annular disk with a shaft press fitted onto it.

The chapter will start by comparing the stress level of annular and solid discs with same level of kinetic energy level induced by rotation. Based on the stress level, the corresponding S-N life and crack fracture cycle life will be calculated. Finally, a set of dimensions for the designed shaftless disk will be chosen for later studies in this dissertation.

2.2 Stress Comparison between Annular and Solid Discs

For a thin disk, the stress in the axial direction can be assumed to be zero. Assuming rotation is the only source of induced stresses, there will be tensile circumferential (hoop) and tensile radial stresses.

For solid discs, the radial stress will be:

$$\sigma_r(r) = \frac{\rho\omega^2}{8}(3+\gamma)(R_o^2 - r^2) \tag{2.1}$$

The hoop stress is:

$$\sigma_\theta(\mathrm{r}) = \frac{\rho\omega^2}{8}[(3+\gamma)R_o^2 - (1+3\gamma)\mathrm{r}^2] \tag{2.2}$$

The Maximum values appear at center of the disk for both radial and hoop stresses

$$(\sigma_r)_{max} = (\sigma_\theta)_{max} = (3+\gamma)(\frac{\rho\omega^2 R_o^2}{8}) \tag{2.3}$$

The maximum Von-Mises is:

$$\sigma_v = \sqrt{\frac{(\sigma_1-\sigma_2)^2 + (\sigma_2-\sigma_3)^2 + (\sigma_1-\sigma_3)^2}{2}} = \sqrt{\sigma_r^2 + \sigma_\theta^2 - \sigma_r\sigma_\theta} \tag{2.4}$$

The maximum value for rotational Von-Mises for solid discs will be:

$$(\sigma_v)_{max} = \sqrt{(\sigma_\mathrm{r})_{max}^2 + (\sigma_\theta)_{max}^2 - (\sigma_\mathrm{r})_{\max}(\sigma_\theta)_{\max}} = (3+\gamma)(\frac{\rho\omega^2 R_o^2}{8}) \tag{2.5}$$

For annular discs, the radial stress induced by rotating is:

$$\sigma_r(r) = \frac{\rho\omega^2}{8}(3+\gamma)\left(R_o^2 + R_i^2 - \frac{R_i^2 R_o^2}{r} - r^2\right) \tag{2.6}$$

The hoop stress for the annular disk will be:

$$\sigma_\theta(r) = \frac{\rho\omega^2}{8}[(3+\gamma)\left(R_o^2 + R_i^2 + \frac{R_i^2 R_o^2}{r}\right) - (1+3\gamma)r^2] \tag{2.7}$$

The maximum value for radial stress will be reached at $\sqrt{R_i R_o}$:

$$(\sigma_r)_{max} = (3+\gamma)(\frac{\rho\omega^2(R_o - R_i)^2}{8}) \tag{2.8}$$

The maximum value for hoop stress will be reached at R_i :

$$(\sigma_\theta)_{max} = [(1-\gamma)R_i^2 + (3+\gamma)R_o^2](\frac{\rho\omega^2}{4}) \tag{2.9}$$

The maximum of radial and hoop stress appears at different locations, so the position

where the maximum Von-Mises stress happens should be identified. For this purpose the radial stress and hoop stress difference was retrieved as:

$$\sigma_\theta(r) - \sigma_r(r) = \frac{\rho\omega^2}{8}\left[(3+\gamma)\frac{2R_o^2R_i^2}{r^2} + 2(1-\gamma)r^2\right] \geq 0 \tag{2.10}$$

Since both radial and hoop stresses caused by rotation will be tensional, we have:

$$\sigma_\theta(r) \geq \sigma_r(r) \geq 0 \tag{2.11}$$

According to Eq. 2.4,

$$\sigma_v = \sqrt{\sigma_r^2 + \sigma_\theta^2 - \sigma_r\sigma_\theta} \leq \sqrt{\sigma_r^2 + \sigma_\theta^2 - \sigma_r\sigma_r} = \sigma_\theta \tag{2.12}$$

Since at $r = R_i$, $\sigma_r = 0$ and $\sigma_\theta = (\sigma_\theta)_{max}$, σ_v for the annular disk also reach its maximum at this position:

$$(\sigma_v)_{max} = \sigma_v(R_i) = (\sigma_\theta)_{max} = [(1-\gamma)R_i^2 + (3+\gamma)R_o^2](\frac{\rho\omega^2}{4}) \tag{2.13}$$

It can be seen that when $R_i \to 0$, the maximum Von-Mises stresses for annular discs are twice as much as those for solid discs of the same outer radius.

4340 steel was selected as the material for the flywheel. 5in thickness was set due to the requirement of heat treatment depth. With proper heat treatment, 4340 steels' strength level can be well above 200ksi. So we will select a stress level between 150ksi and 200ksi for our design. By assuming a ratio of 0.1 for the inner diameter over outer diameter (ID/OD), the speed and energy levels vs. the disk outer diameter were presented as in the following plots. Fig. 2.1 and Fig. 2.2 gave speed and rotational dynamic energy comparison between annular and solid discs at a stress level of 150ksi. Fig. 2.3 and Fig. 2.4 presented the same information for a stress level of 200ksi. As can

be shown in these results, the maximum Von-Mises stress ratio between annular and solid structure is 2.0044. As can be expected, this ratio will change with different ID/OD ratio. For an ID/OD ratio equals to 0.02, the stress ratio will be 2.0002. If ID/OD=0.2, the stress ratio value will change to 2.0202. It was found that the volume and weight energy densities (Fig. 2.5 and Fig. 2.6) were independent of discs' OD and in linear relationship with maximum stresses.

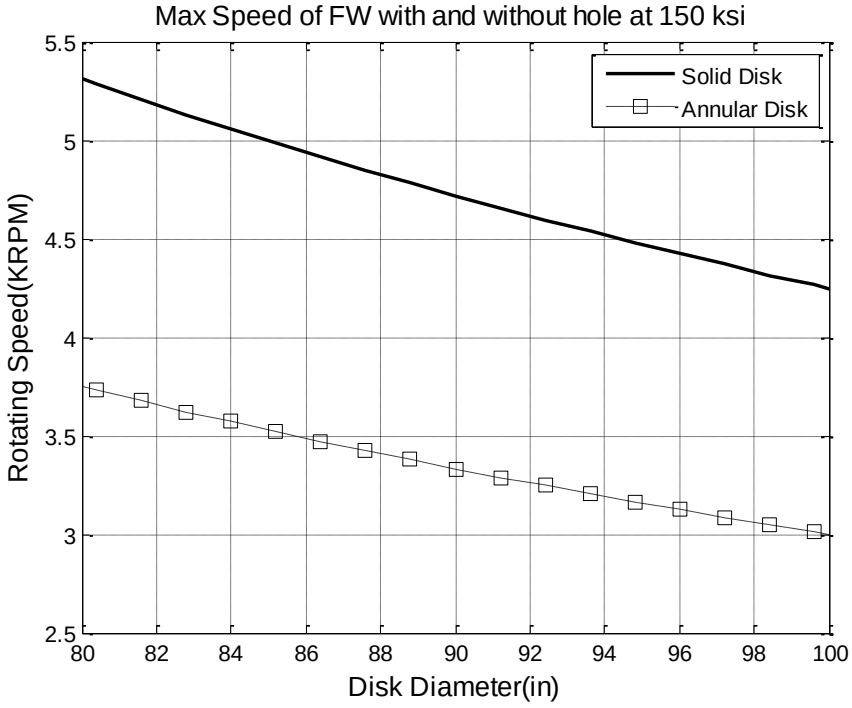

Fig. 2.1 Speed vs. OD Comparison between Annular and Solid Discs at 200ksi

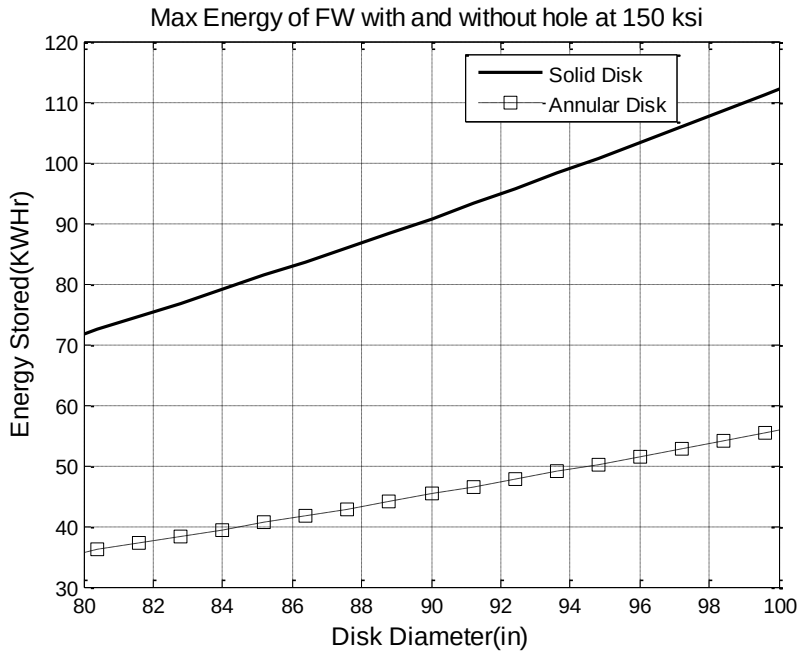

Fig. 2.2 Energy vs. OD Comparison between Annular and Solid Discs at 150ksi

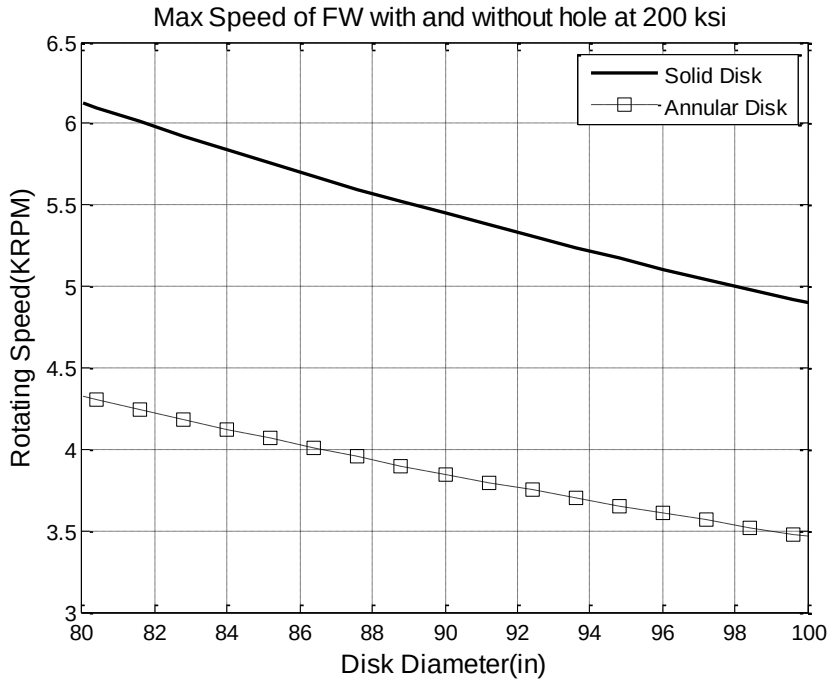

Fig. 2.3 Speed vs. OD Comparison between Annular and Solid Discs at 200ksi

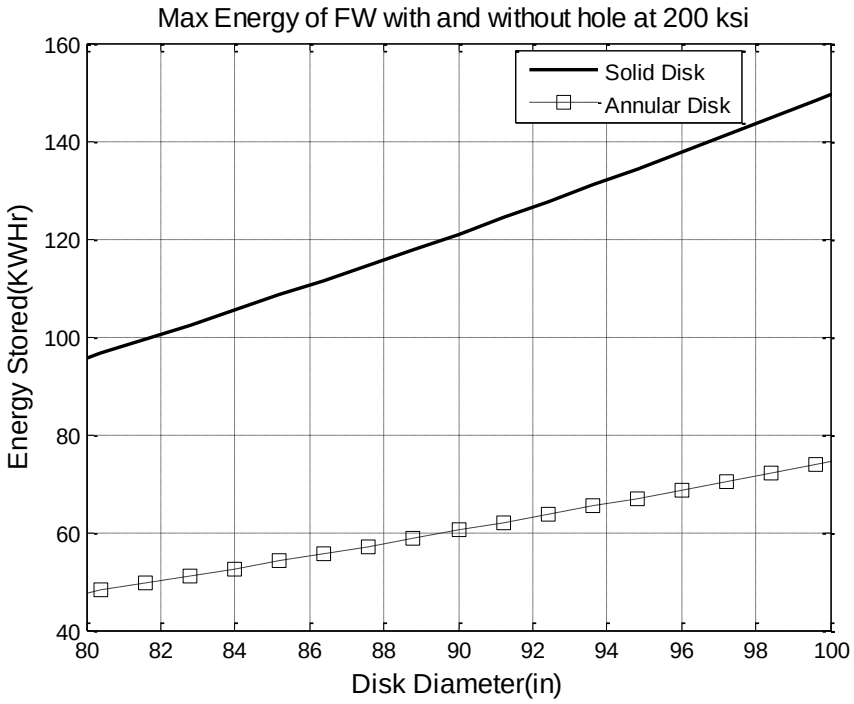

Fig. 2.4 Energy vs. OD Comparison between Annular and Solid Discs at 200ksi

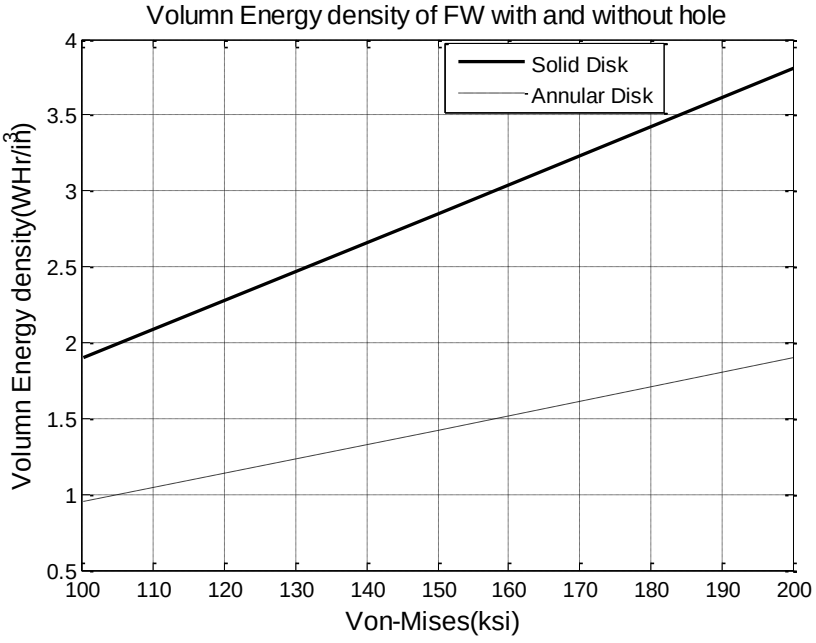

Fig. 2.5 Volume Energy Density for Solid and Annular Disk with ID/OD=0.1

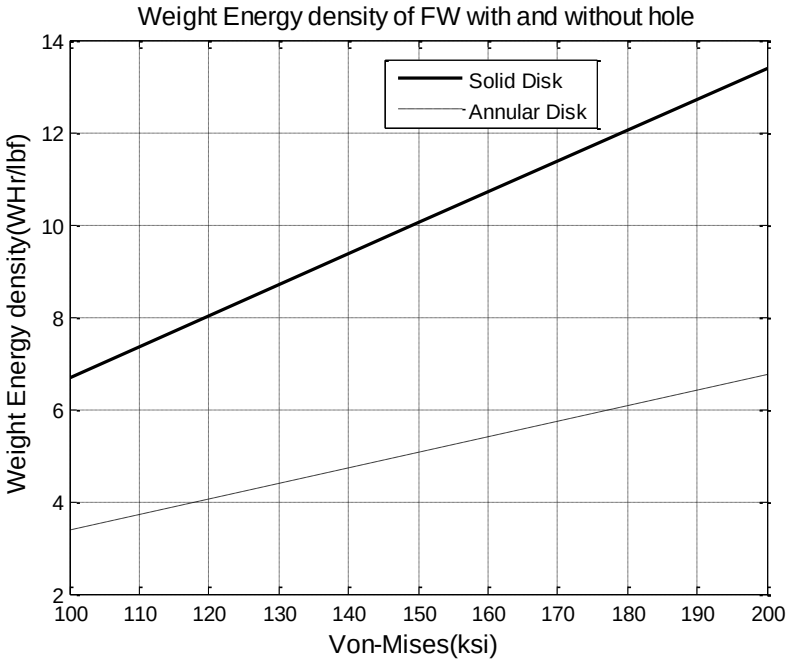

Fig. 2.6 Weight Energy Density for Solid and Annular Disk with ID/OD=0.1

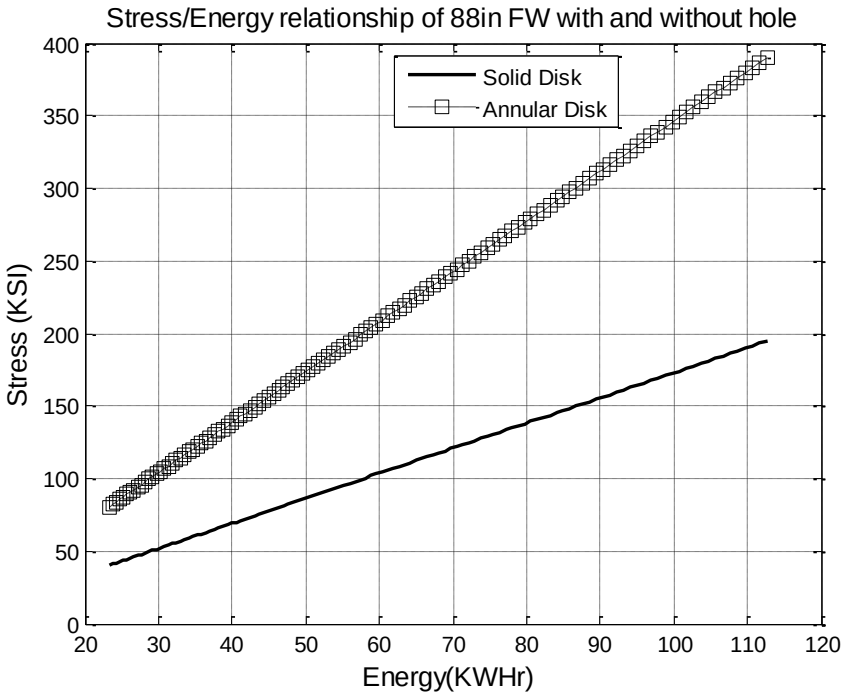

Fig. 2.7 Stress vs. Kinetic Energy for 88in Solid and Annular Discs with ID/OD=0.1

To better understand the energy density value calculated, several contemporary flywheel based energy storage system were studied. Optimal Energy Systems [31] had a 60MJ(16.7kWh) composite flywheel built with a rotor weight of 2744lbs. The weight based energy density (WBED) is 6Wh/lbs. NASA G3 flywheel was reported to have an WBED of 35Wh/kg (15.9Wh/lbs.) [32].UT-Austin CEM [18-20] built a flywheel for railway locomotives which had a rotor weight of 5100 lbs. and generator weight of 2160 lbs. Their system can store around 130 kWh of energy at a speed of 15,000rpm, so the WBED will be 17.9Wh/lbs. However the maximum speed reported in 2004 was 13,600 rpm, which gave an energy value of 106.9kWh and a WBED of 14.7Wh/lbs. It must be mentioned that all these flywheels are made from composite materials and the values plotted in Fig. 2.5 and Fig. 2.6 are for simple 4340 steel discs. So we will achieve a similar WBED with a much cheaper material. Also considering the steel density is about four times as the composite materials, our proposed design should have a much higher volume based energy density (VBED).

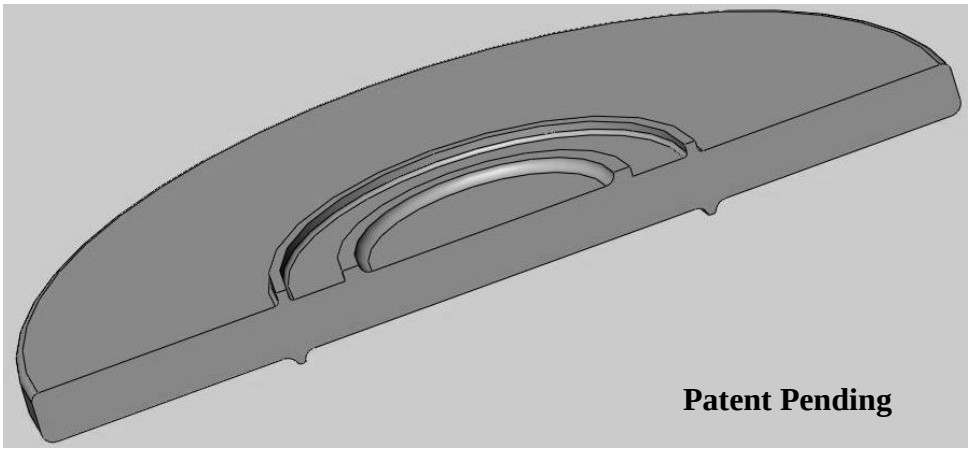

Fig. 2.8 3D Model of the 88in Solid Disk Designed

A disk with 88 inch outer diameter was tentatively selected as the study candidate in this dissertation. Fig. 2.7 shows the relationship between maximum stress level and corresponding kinetic energy of the disk. A 3D Solidworks^{TM} model was developed as in Fig. 2.8. The model was analyzed by ANSYS^{TM} and the maximum Von-Mises Stress caused by rotation was plotted against the theoretical values for the solid discs and annular discs (ID/OD=0.1). As can be seen in Fig. 2.9, the stress level for the designed model is close enough to be treated as a solid disk. It must be pointed out that the rim shapes and positions were not fully optimized in the 3D model analyzed. So it is reasonable to believe that, with appropriate optimization of the design, e.g. fillets position and radius, the stress difference between the real life flywheel and theoretical solid disk can be even smaller. So our design based on the theoretical solid disk stress formula should be acceptable.

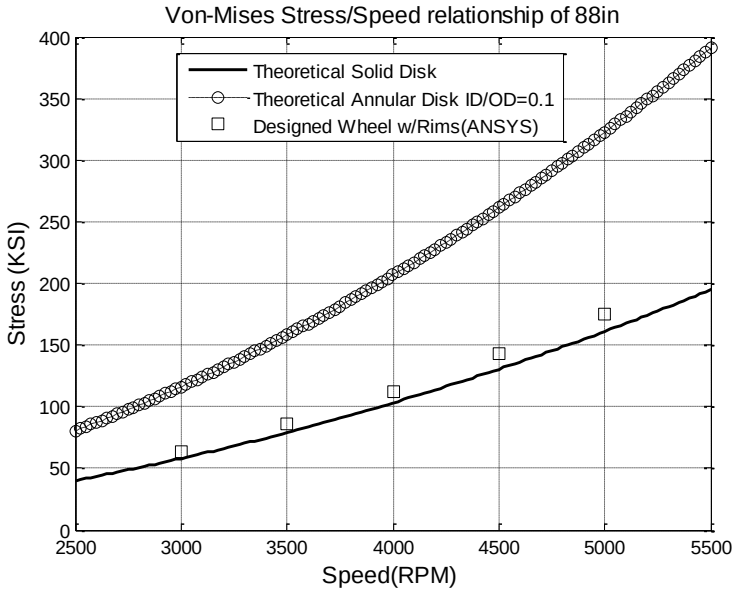

Fig. 2.9 Maximum Von-Mises Stress Comparison between 3D ANSYS Model and Theoretical Values

2.3 S-N Life Comparison between Annular and Solid Discs

S-N life depends on the maximum stress and minimum stress level experienced by structures. A stress ratio *R* was defined as:

$$R = \frac{\sigma_{min}}{\sigma_{max}} \tag{2.14}$$

In our case, the stress ratio *R* is in direct relationship with the maximum energy level stored in the rotor and the depth of discharge (DOD). Since the stress will never change signs in our cases, *R* value will always be positive. As also can be seen in Fig. 2.7, the energy stored and maximum stress are in linear relationship for a fixed design. So we can use *R* as a measurement of the DOD, their relationship is:

$$Depth\ of\ discharge(DOD) = (1 - R) * 100\% \tag{2.15}$$

[33] (MIL-HDBK-5H Figure 2.3.1.3.8(m)) gave out a S-N curve for un-notched AISI 4340 alloy steel bar and billet with *Ftu*=260ksi and provided an equivalent equations for the curve provided.

$$\log(N_f) = 11.62 - 3.75\log(S_{eq} - 80.0) \tag{2.16}$$

where

$$S_{eq} = S_{max}(1 - R)^{0.44} \tag{2.17}$$

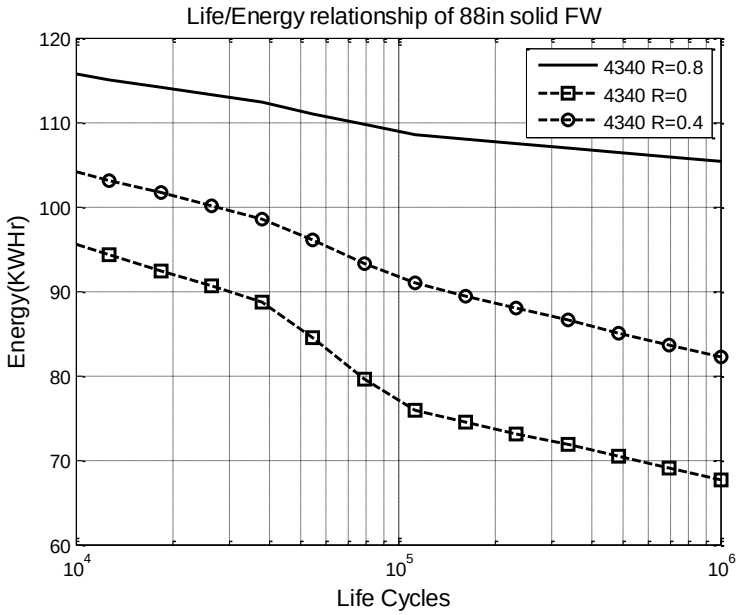

Fig. 2.10 Energy vs. S-N Life for Unnotched 4340 Solid Disk at Different DODs

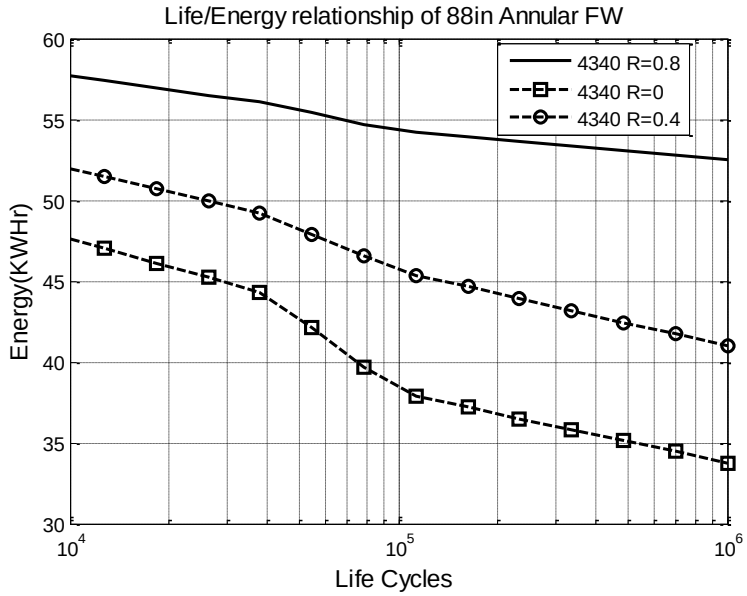

Fig. 2.11 Energy vs. S-N Life for Unnotched 4340 Annular Disk at Different DODs

[34] also presented S-N curves for non-notched 4340 specimen with multiple *R* values. The experimental results in the curve were used in this dissertation to predict the

S-N life for non-notched flywheels at different DOD. The stored energy vs. S-N cycle lives for solid discs and annular discs with ID/OD=0.1 were plotted as in Fig. 2.10 and Fig. 2.11, respectively. Three cases were plotted for these figures: R=0.8, R=0.4 and R=0. They correspond to different depth of discharge level at 20%, 60% and 100%. It is obvious that the solid disk is far superior to the annular one in the sense of S-N lives.

2.4 Fatigue Crack Growth Comparison between Annular and Solid Discs

To calculate fatigue crack growth rate, the stress intensity factor (SIF) must first be calculated. For both solid and annular cases, the radially oriented through-the-thickness cracks are the most critical situations. The circumferential stresses should be of the mode I type (opening mode) and vary along the crack. The Stress Intensity Factors (SIF) tends reach a constant maximum value as the position approaching the center part of the discs.

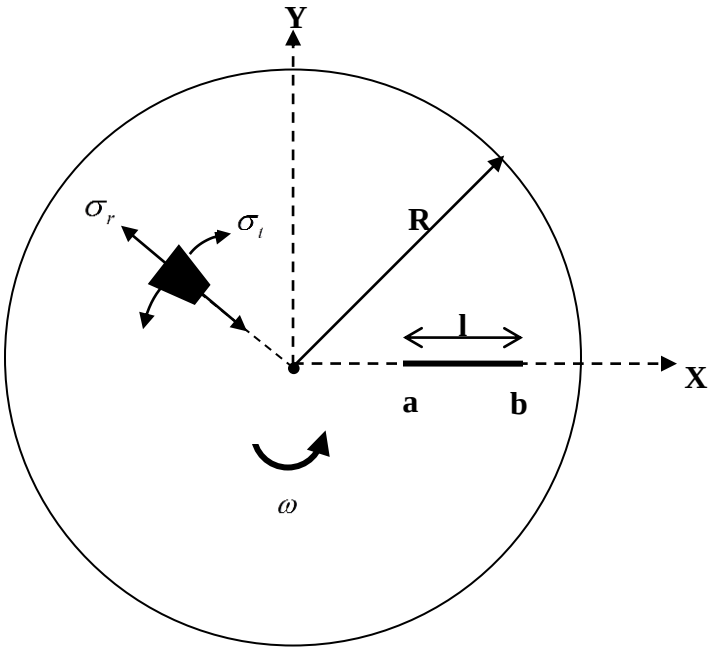

Fig. 2.12 Geometry and Coordinates of the Rotating Solid Disk

J.G.Blauel [35] gave out the SIF equations for solid discs as shown in Fig. 2.12. The SIF at the inner and outer crack tips can be defined as K_{Ia} and K_{Ib} and expressed as:

$$K_{Ia} = \frac{\sqrt{2}}{8\sqrt{\pi(b-a)}}\rho\omega^2 \int_a^b \left\{[(3+\nu)R^2 - (1+3\gamma)r^2]\sqrt{\frac{b-r}{r-a}}\right\} dr \qquad (2.18)$$

$$K_{Ib} = \frac{\sqrt{2}}{8\sqrt{\pi(b-a)}}\rho\omega^2 \int_a^b \left\{[(3+\nu)R^2 - (1+3\gamma)r^2]\sqrt{\frac{r-a}{b-r}}\right\} dr \qquad (2.19)$$

As is pointed out by J.G.Blauel [35], $K_{Ia} \approx K_{Ib}$ at $|r| \leq 0.2R$. The worst case will be that the crack rests right at the middle of the disk. Given the crack size is relatively small comparing to the disk radius, the SIF for this worst scenario of the solid disk with through-the-thickness crack is:

$$K_{Ia} \approx K_{Ib} = \frac{3+\gamma}{8}R^2\rho\omega^2\sqrt{\pi\frac{l}{2}} \qquad (2.20)$$

An annular disk with a radial crack located at inner wall was modeled as in Fig. 2.13. Bueckner et al. [36] gave out several formulas depending on the crack sizes for SIFs of this kind. Since the crack size of interest is very small compared to the radius of the disk, the formula can be given as:

$$K_I = 1.13\frac{3+\gamma}{4}\rho\omega^2 R_2^2\sqrt{h} \qquad (2.21)$$

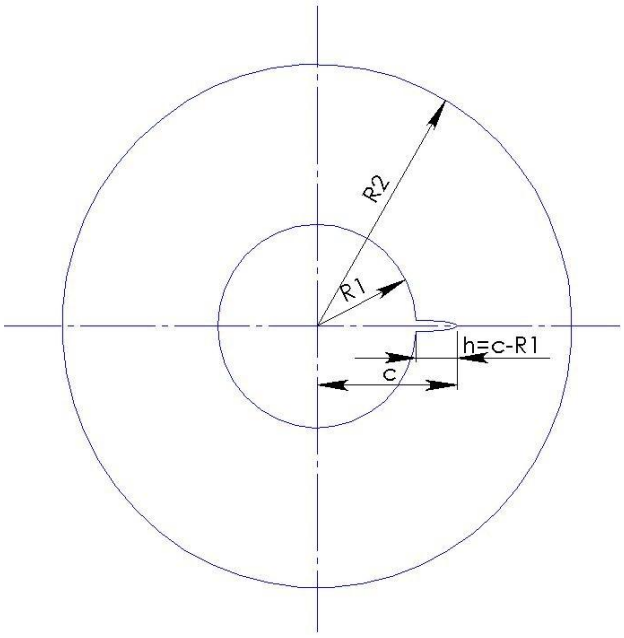

Fig. 2.13 Annular Disk with a Radial Oriented Crack at Inner Wall

Owen et al. [37] also gave a formula for stress intensity factor for spinning annular disk with a crack at the end of the bore diameter. The formula was applicable for one crack case as well as for case with two opposite cracks at opposite ends of the bore diameter. Their formulas were based on an approximate method suggested by Williams and Isherwood [38]. The effective stress acting on the crack can be defined as:

$$\sigma' = \frac{3\sigma_m + \sigma_n}{4} \tag{2.22}$$

where

$$\sigma_n = \frac{1}{R_2 - C}\int_{R_1}^{R_2} \sigma dr \tag{2.23}$$

$$\sigma_m = \frac{1}{C - R_1}\int_{R_1}^{C} \sigma dr \tag{2.24}$$

The stress intensity factor will be:

$$K_I = \sigma' \sqrt{\pi (c - R_1)} \tag{2.25}$$

Assuming

$$\sigma_o = (3 + \gamma) \frac{\rho \omega^2 R_2^2}{8} \tag{2.26}$$

Eq. 2.7 can be written as:

$$\sigma = \sigma_o \left(\frac{R_1^2}{R_2^2} + 1 + \frac{R_1^2}{r^2} - \frac{1 + 3\gamma}{3 + \gamma} \frac{r^2}{R_2^2} \right) \tag{2.27}$$

Then we have:

$$\begin{aligned} \sigma_n &= \frac{\sigma_o}{R_2 - C} \int_{R_1}^{R_2} \left(\frac{R_1^2}{R_2^2} + 1 + \frac{R_1^2}{r^2} - \frac{1 + 3\gamma}{3 + \gamma} \frac{r^2}{R_2^2} \right) dr \\ &= \frac{\sigma_o}{R_2 - C} \left[\left(\frac{R_1^2}{R_2^2} + 1 \right) r - \frac{R_1^2}{r} - \frac{1 + 3\gamma}{3 + \gamma} \frac{r^3}{3R_2^2} \right] \Bigg|_{R_1}^{R_2} \end{aligned} \tag{2.28}$$

$$\begin{aligned} \sigma_m &= \frac{\sigma_o}{C - R_1} \int_{R_1}^{C} \left(\frac{R_1^2}{R_2^2} + 1 + \frac{R_1^2}{r^2} - \frac{1 + 3\gamma}{3 + \gamma} \frac{r^2}{R_2^2} \right) dr \\ &= \frac{\sigma_o}{C - R_1} \left[\left(\frac{R_1^2}{R_2^2} + 1 \right) r - \frac{R_1^2}{r} - \frac{1 + 3\gamma}{3 + \gamma} \frac{r^3}{3R_2^2} \right] \Bigg|_{R_1}^{C} \end{aligned} \tag{2.29}$$

When R_1/R_2=0.01, R_2=80in, crack size h=0.1in, Owen's method will have a SIF of $K_I = 1.38(3 + \gamma)\rho\omega^2 R_2^2 \sqrt{h}/4$. This condition agrees with Bueckner's assumption that both R_1/R_2 and h/R_1 is small and the result is very close to the one presented in Eq. 2.21. Owen's method [37] was used to evaluate SIF in this dissertation for different crack sizes.

W.D.Pilkey [39] pointed out that there are three types of behavior for the fatigue crack propagation. These types are called region I, II and III. In region I, the stress

intensity factor fluctuation is less than a parameter called threshold stress intensity range (ΔK_{th}). Within this region, the flaw crack size won't grow. In region II, the crack growth rate will follow the Paris' law as listed in Eq. 2.30. In region III, the fluctuation of the SIF exceeds a transition value ΔK_T, and the crack size will grow at a much faster rate than predicted by Paris' law. For a loading with *R*=0, namely the stress fluctuates between zero and maximum value, the transition value of the SIF can be expressed as in Eq. 2.31, where *E* is Young's Modulus and σ_g is the mean value of tensile strength and yield strength.

$$\frac{dh}{dN} = C_I(\Delta K_I)^{m_I} \tag{2.30}$$

$$K_T = 0.04\sqrt{E\sigma_g} \tag{2.31}$$

W.D.Pilkey [39] also gives out some strength and fracture toughness data for 4340 steels which were converted as in Table 2.1. A K_{IC} value of 80ksi*in1/2 was selected and the critical size was plotted as in Fig. 2.14. With a Young's Modulus of 30700ksi, tensile strength of 231.3ksi and yield strength of 213.9ksi, a 100% discharge (*R*=0) process will have a $\boldsymbol{\Delta K_T}$ of 104.6 ksi*in1/2, which is much bigger than our K_{IC} value. This means the fracture crack size will stay in region II and never enter region III if a crack growth ever happens. So the cycle life to critical crack size can be accurately predicted with the crack growth equation provided by Paris's law as in Eq. 2.30 [39]. Liaw provided experimental results for $\boldsymbol{\Delta K_{th}}$ values at different *R* levels [40], some of which were selected and listed as in Table 2.2. These values will be used in our simulations to calculate the Region I crack size. For an *R* values of 0.5 (50% DOD), the threshold crack

size vs. energy level was presented in Fig. 2.15.

Propagation data for low-alloy steel in Table 7-20 of [39] was used and the cycle life to critical crack from 0.02in initial crack for *R*=0.5 (50% DOD) was shown in Fig. 2.16. The cycle life from threshold crack to critical crack vs. stored energy with 50% DOD was presented in Fig. 2.17. The initial crack sizes which have a cycle life of 10k with 50% energy discharge cycle were plotted in Fig. 2.18. It must be noted that crack size calculated are for through-the-thickness cracks located at the center of the solid disk and inner surfaces of the annular disk, which is the worst case scenario. All these results indicated much better characteristics of solid discs design over annular discs, which gave our flywheel storage system design great advantages over the others.

Table 2.1 Strength and Fracture Toughness Data for 4340

Alloy	Material Supply	Test Temp [^{o}C]	Yield Stress [ksi]	K_{IC} [ksi*in$^{1/2}$]
4340(205^{o}C temper)	Forging	21	229.2-240.8	40.04-60.06
4340(260^{o}C temper)	Plate	21	216.8-237.9	45.50-57.33
4340(425^{o}C temper)	Forging	21	197.3-211.0	71.89-82.81

Table 2.2 ΔK_{th} data for 4340 at Different R Values

R	0.1	0.5	0.8
ΔK_{th}[ksi*in$^{1/2}$]	7.43	4.3	2.95

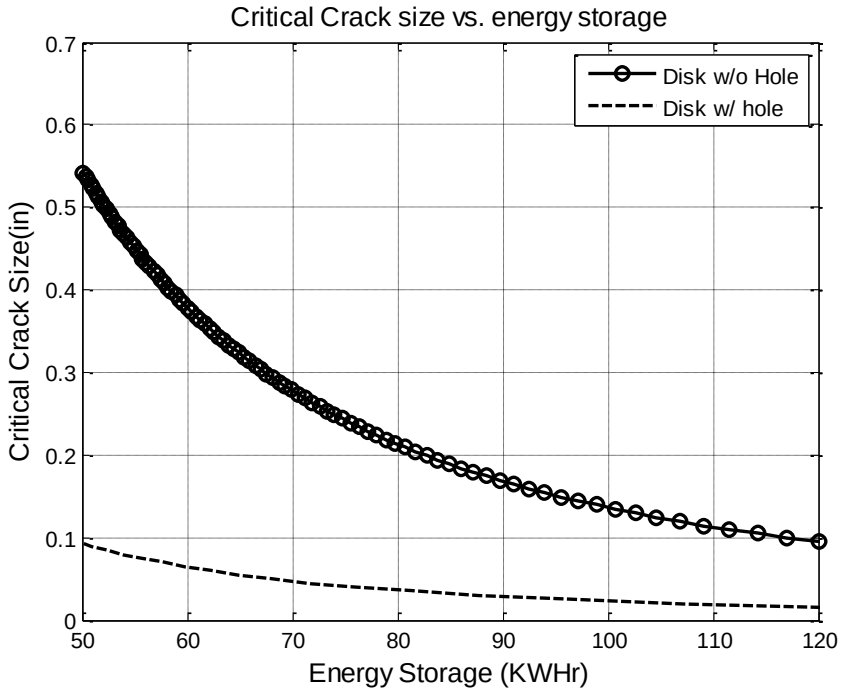

Fig. 2.14 Critical Crack Sizes vs. Energy Storage for 88in OD Discs

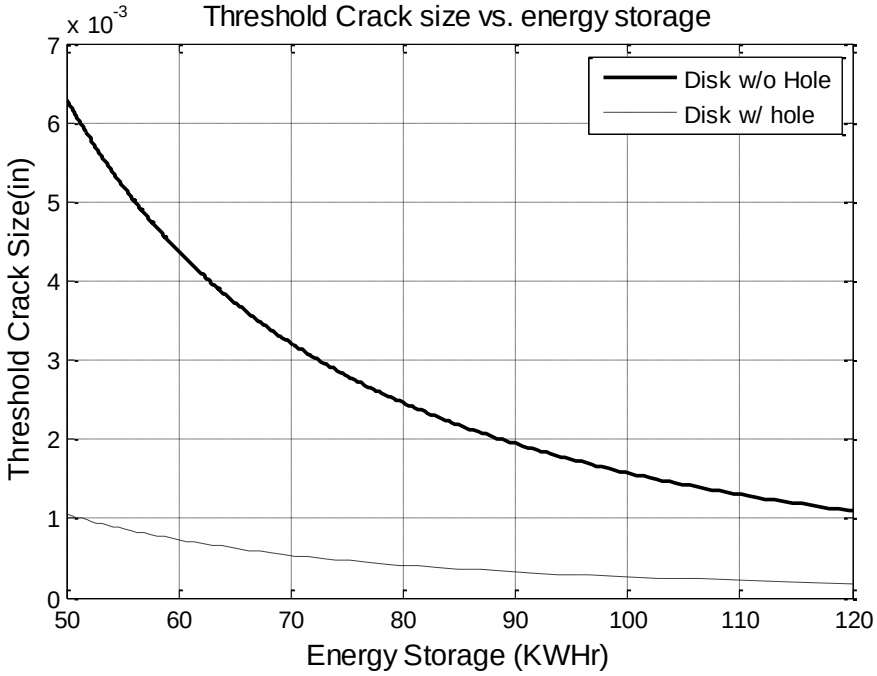

Fig. 2.15 Threshold Crack Sizes vs. Energy Storage for 50% DOD

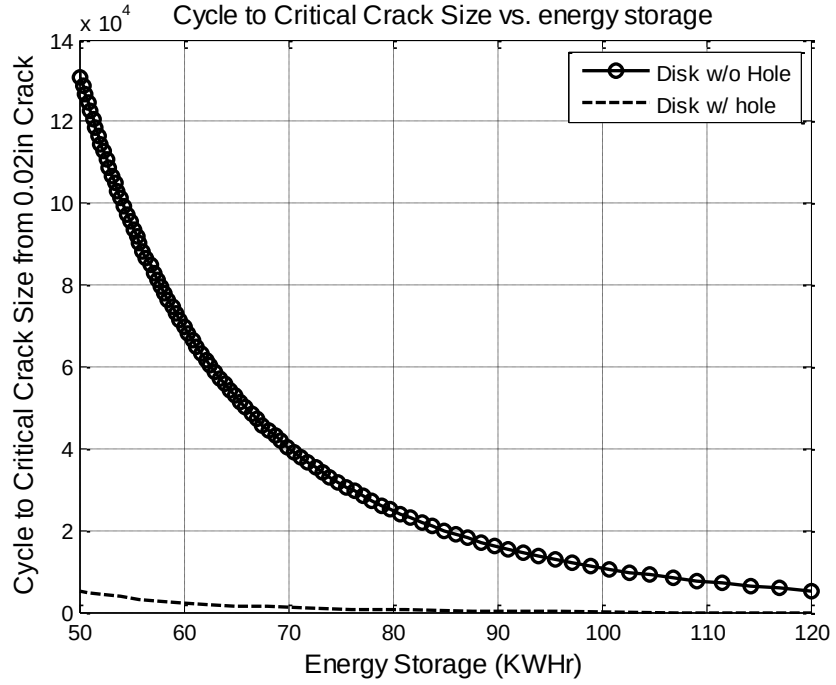

Fig. 2.16 Cycles to Critical Size from 0.02in Initial Crack

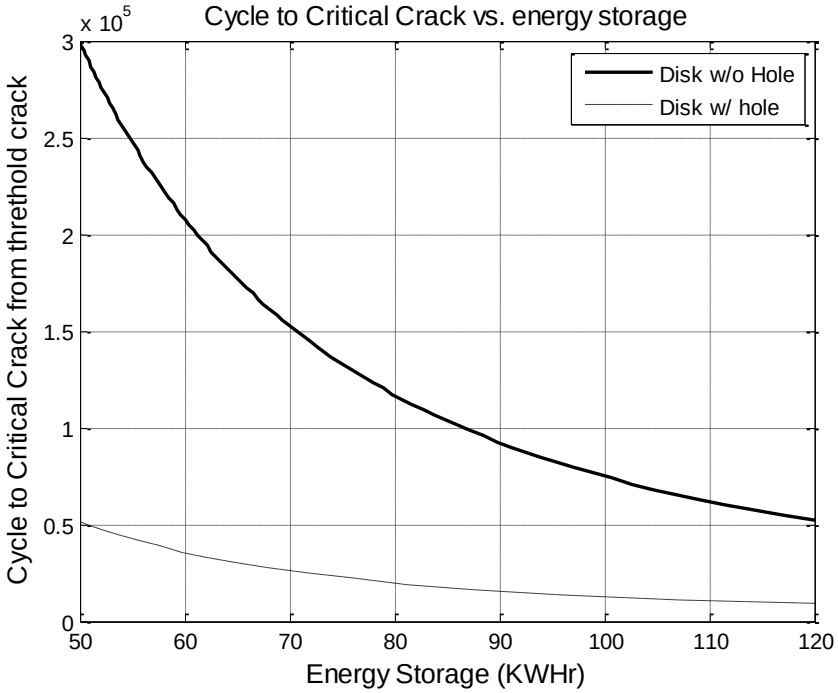

Fig. 2.17 Cycles to Critical Size from Threshold Crack Size

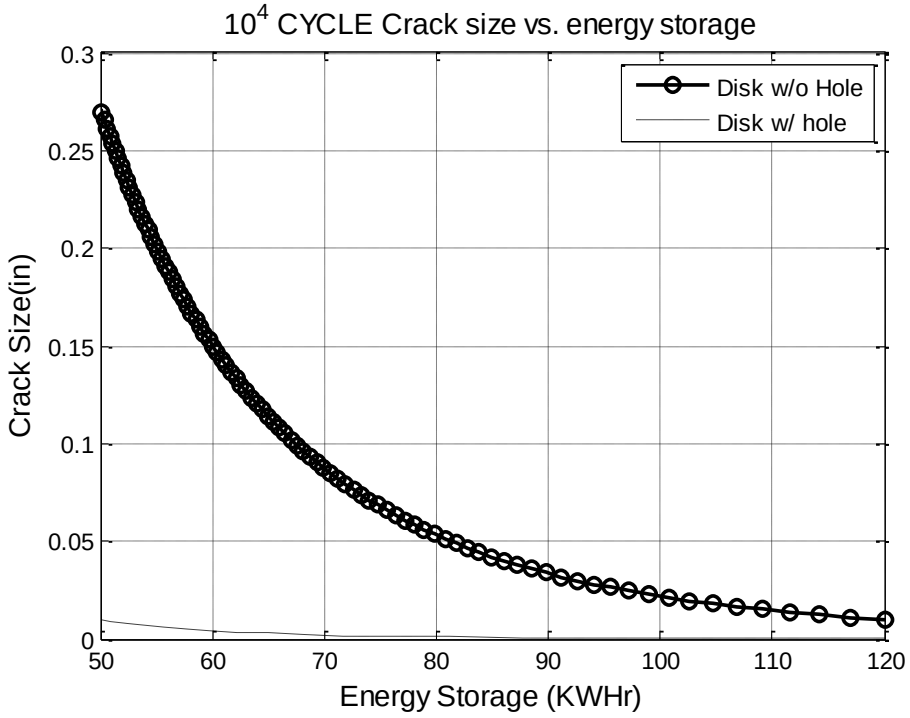

Fig. 2.18 Initial Crack Sizes with 10000 Cycle Life to Critical Crack

2.5 Conclusion

As discussed in this chapter, the solid disc design is much better than its annular counterparts and our design of flywheel is close enough to be treated as solid one. The major studying candidate in the following dissertation will be a solid disk flywheel with 88in diameter and 5in thickness. Rotating at 4906RPM, the 8600lbf flywheel will have a maximum Von-Mises stress of 155.6ksi, a total energy of 90kWh and a weight energy density of 10.38Wh/lbs. The S-N life will be 20k cycles for 100% energy discharge and more than 1000k cycles for 60% energy discharge. For an initial crack of 0.02in to reach critical size with 50% DOD, the cycle life will be 16.1k. The 90kWh wheel will not reach critical crack size within 10k cycles if the initial crack size is smaller than 0.0335in for 50% DOD.

CHAPTER III

DESIGN OF THE MAGNETIC BEARING

3.1 Overview

Magnetic bearings, especially the homo-polar ones, are well known for their low losses and relatively maintenance free characteristics. Due to the shaft-less design of the flywheel in this dissertation, traditional architectures of magnetic bearings cannot be used to support it. A novel design of permanent magnet biased, homo-polar magnetic bearing was built to serve this purpose. The axial bearing bias flux will provide an equilibrium point where the weight of the whole rotor will be supported solely by permanent magnet forces. The radial bearing bias flux will provide a point where the relationship between radial force and control current can be linearized. 3D static analysis using ANSYS^{TM} will be carried out in this chapter to calculate the static support of gravity loads and the bearings' current and position stiffness.

3.2 Novel Magnetic Bearing Design

Homo-polar bearings using permanent magnets as their sources of the bias flux. Even though this prevents actively varying the bias flux, the losses caused by bias currents on hetero-polar bearings can be avoided. The traditional homo-polar bearing structures were as shown in Fig. 3.1. Two sets of radial magnetic bearings, both biased by permanent magnets, were used to control radial/tilting motion of the flywheels. One set of thrust bearing is used to support the rotor weight and suppress axial disturbances.

However, for our design of shaftless flywheel, this traditional structure will not work

since there will be no shaft for thrust and radial bearings to work on. So we proposed a novel structure as illustrated in Fig. 3.2. The thrust, moment and radial control functionalities were embedded in one combo bearing structure. This design was built to both accommodate the shaftless characteristic of the flywheel and reduce the system's cost. Both the axial and radial section of the combo bearing was biased by the same sets of permanent magnets.

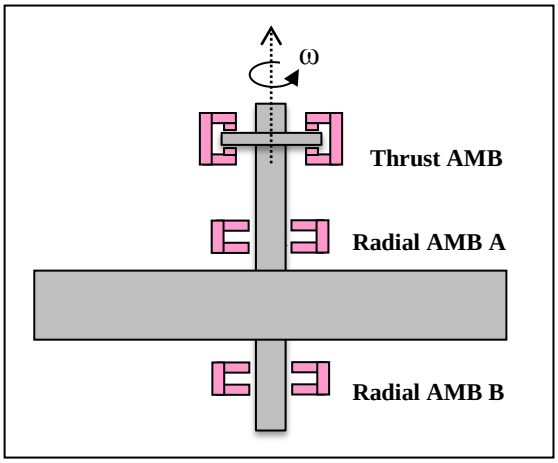

Fig. 3.1 Traditional Homo-polar Magnetic Bearing Supported Flywheel

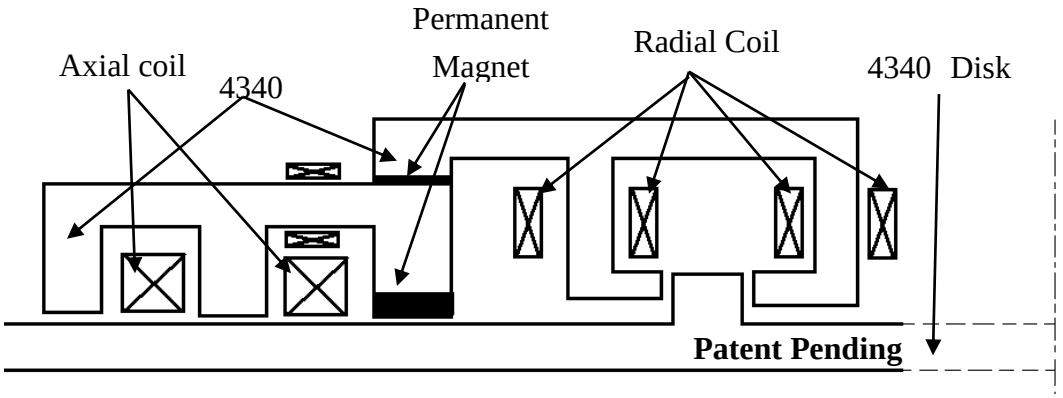

Fig. 3.2 2D Concept Draft of Magnetic Combo Bearing with Disk

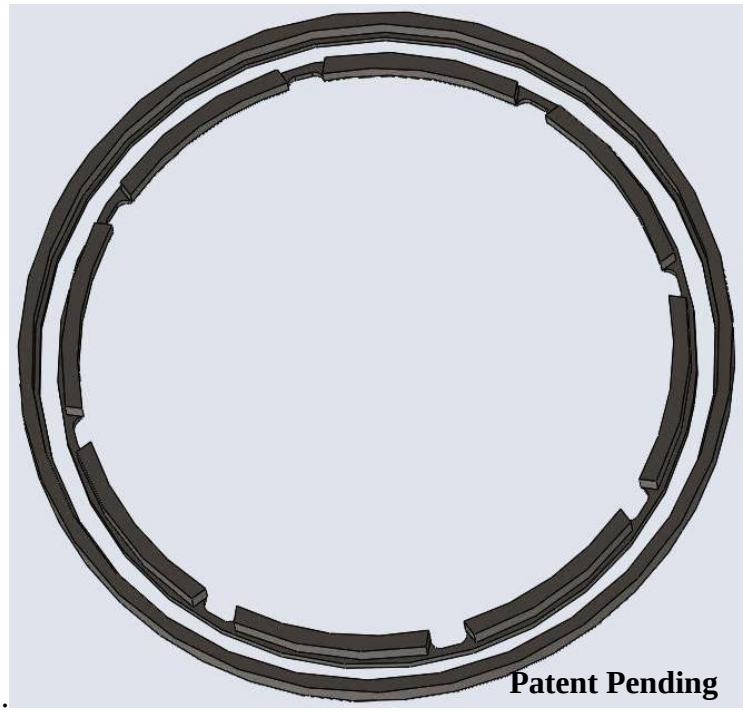

Fig. 3.3 3D Model of Radial Bearing Poles

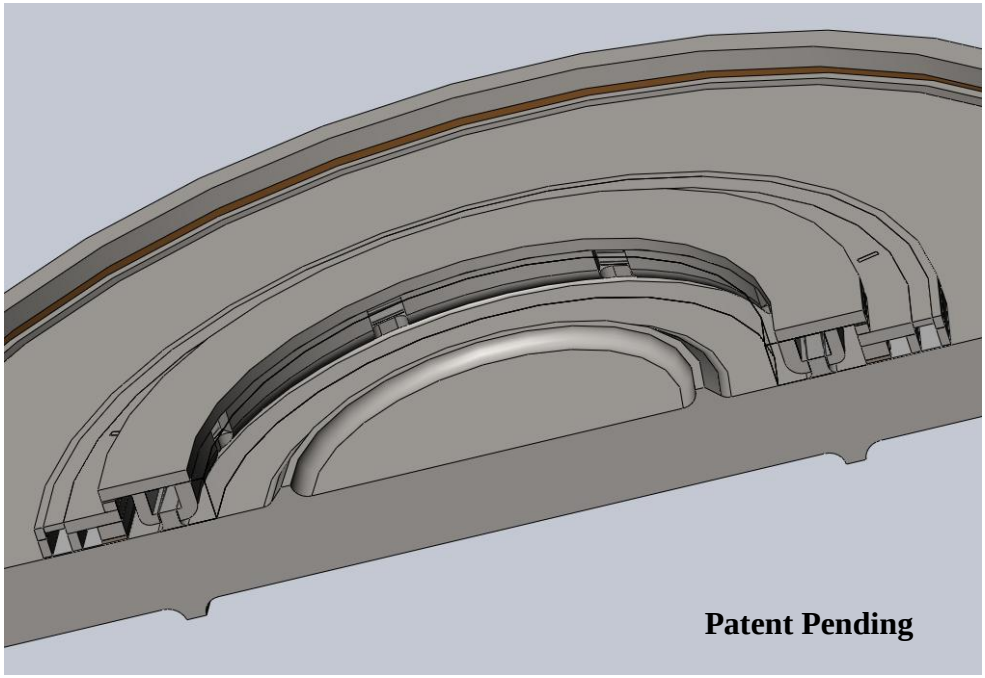

Fig. 3.4 3D Model of the Combo Magnetic Bearing with Disk

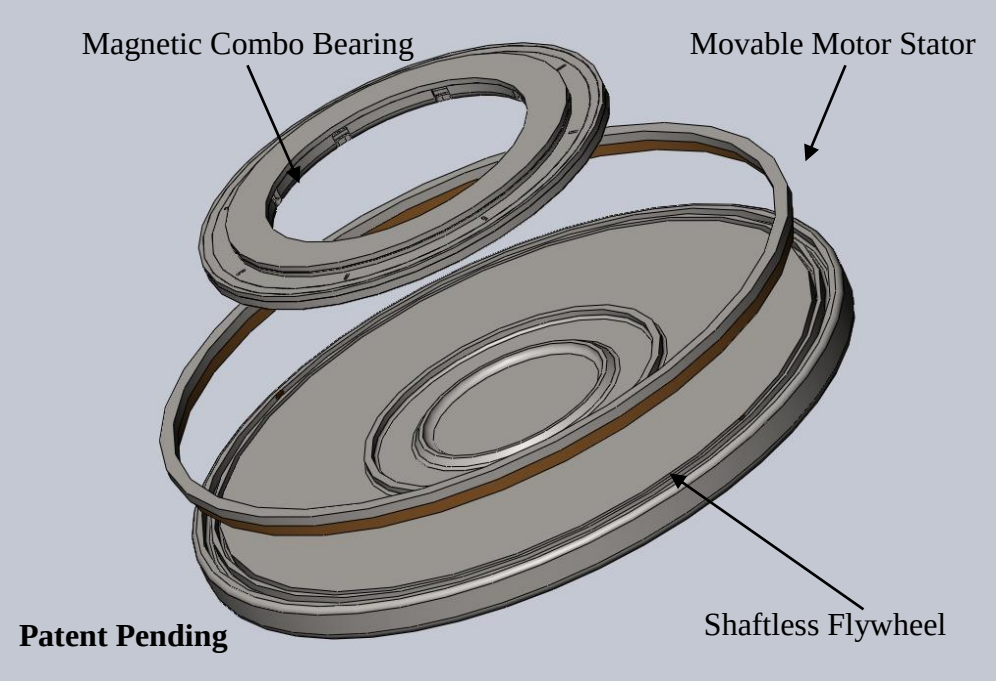

Fig. 3.5 Exploded View of the 3D Model for the Combo AMB

The outer portion of the bearing design realizes the axial and moment control functionality. Axial forces can be varied via the AC flux changes through the circular axial control poles. Moment control was realized by varying flux only in portions of the axial control poles. This variation will create unevenly distributed axial forces and generate moment around the targeted axis. By precisely controlling flux variation in portions opposite to each other with respect to the moment axis, the net axial forces can be zero while a big moment is generated by the bearing. The inner portion of the combo bearing was used to control the radial forces of the bearing. The flux variation in the radial poles was separated from the outer axial portion using the upper set of permanent magnets. In addition to providing some additional DC bias flux for the radial bearing, these magnets were there to provide a high reluctance and prevent the axial and radial

AC fluxes from entering each other's paths. The radial bearing consists of 8 poles pairs. The inner portions of these pairs are 8 dovetail structured discrete poles as show in Fig. 3.3. The outer portions are degraded into a circular ring. This architecture was used to reduce the DC bias flux fluctuation caused by the discrete nature of the radial poles. Since a high magnetic flux fluctuation will incur a high eddy loss, this measure was taken to reduce the overall steady state loss of the system. The 3D drawings model of the flywheel with the AMB is as shown in Fig. 3.4 and Fig. 3.5.

3.3 Experimental Measurement for 4340 Magnetic Property

The bearing was constructed with the same material as the flywheel, namely 4340 steel. To properly design the bearings, a 4340 sample ring was built and tested to retrieve the BH curve of the material. The experimental setup is as shown in Fig. 3.6. As is shown in the figure, an excitation voltage is sent to the input of the power amplifier. The amplifier then forces currents through the coils around the 4340 ring sample. The resulted magnetic field is then measured with tesla meter and the value was recorded as output. The input value is the current value going through the coil and is recorded as the output of the current probe.

Fig. 3.7 presents the sketch of the 4340 ring. The outer diameter of the ring is 52mm. The inner diameter is 43mm. The height of the ring is 11.5mm. A small cross section cut around 0.3mm was made to insert and measure the flux within the ring. The magnetic force when the ring coil was powered on will make the air thickness smaller. However, the later calculation results show that a gap value variation between 0.1 and 0.4mm will not make much difference on BH curve result. This is due to the fact that 4340 has a

relatively high relative permeability and the reluctance of the 4340 ring will dominate the magnetic circuit. The steel ring was stranded with 240 turns of wires in total. To increase the total inductance of the load for the power amplifier to work properly, an additional coil was connected in series with the ring coil. The coil is only for inductance purpose and will not have an effect on the magnet field within the 4340 ring.

By neglecting the flux fringing, we will have $B_{4340} = B_{air}$. So a magnetic circuit model equation can be written as:

$$NI = H_{4340}(l_{ring} - g_{air}) + H_{air}g_{air} \tag{3.1}$$

$$H_{4340} = (NI - \frac{B_{air}}{\mu_o}g_{air})/(l_{ring} - g_{air}) \tag{3.2}$$

$$\mu_{4340} = (l_{ring} - g_{air})/(\frac{NI\mu_o}{B_{air}} - g_{air}) \tag{3.3}$$

Fig. 3.6 Experimental Setup to Retrieve 4340 BH Curve

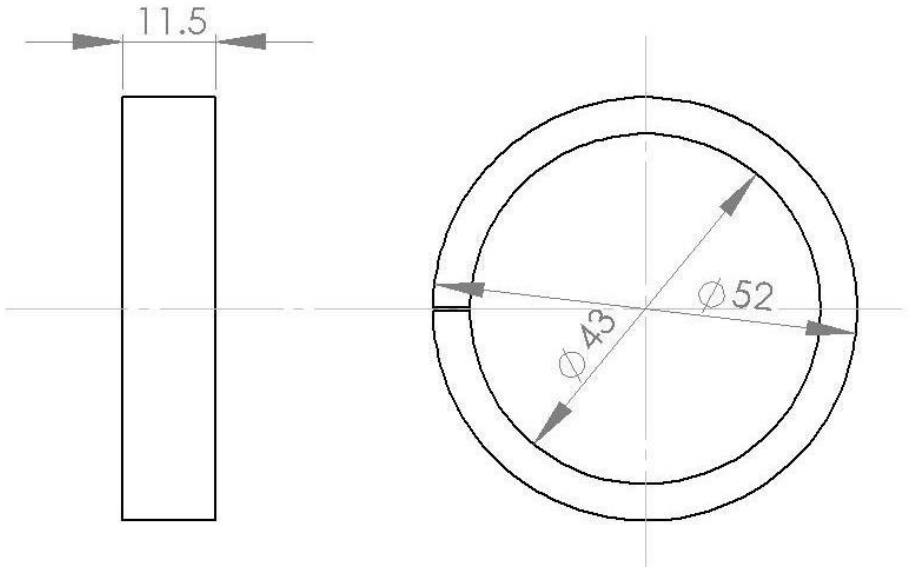

Fig. 3.7 Sketch of the 4340 Sample Ring

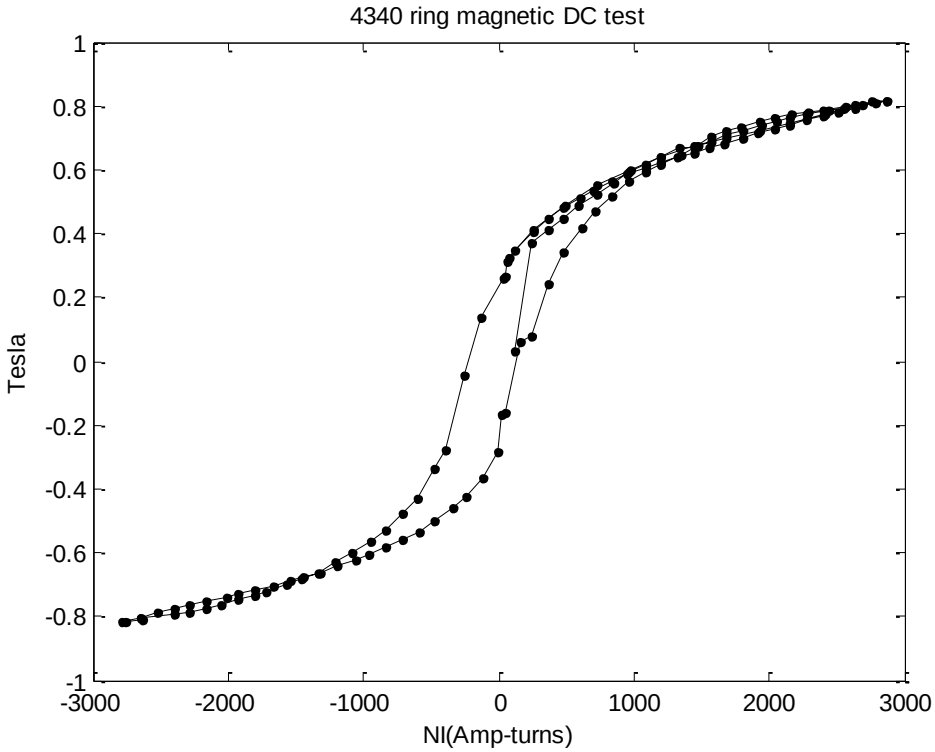

Fig. 3.8 4340 BH Curve Based on Ring Experiment

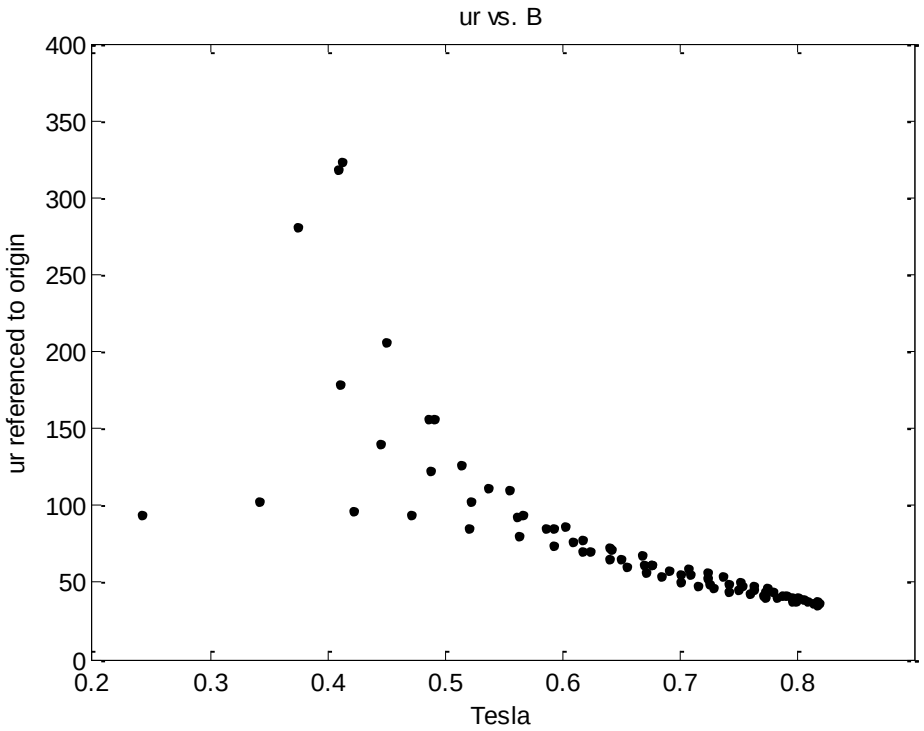

Fig. 3.9 4340 Relative Permeability

Using the DC current excitation value and corresponding magnetic flux density within the air gap, the DC BH curve can be calculated as in Fig. 3.8 using Eq. 3.2. When nonlinear analysis was carried out in this dissertation, the middle average line will be used as BH data in FEM inputs. The relative permeability with respect to the origin point can be calculated using Eq. 3.3 and presented as in Fig. 3.9. As can be seen, the average relative permeability will be around 40 to 150, depending on the flux density value. A relative permeability of 100 was used for FEM harmonic analysis of this dissertation since a flux density of 0.4-0.6 Tesla will be the most common range for the design discussed and a permeability of 100 is the most representative within this range.

3.4 Magnetic Bearing FEM Basics

FEM programs will be used to solve the combo magnetic bearing's characteristics using static, harmonic and transient solvers. All these FEM solvers start from the Maxwell's Equation:

$$\nabla \times H = J + \frac{\partial D}{\partial t} \tag{3.4}$$

$$\nabla \times E = -\frac{\partial B}{\partial t} \tag{3.5}$$

$$\nabla \cdot B = 0 \tag{3.6}$$

$$\nabla \cdot D = \rho \tag{3.7}$$

These field intensities and flux densities can also be related as:

$$B = \mu H \tag{3.8}$$

$$J = \sigma E \tag{3.9}$$

$$D = eE \tag{3.10}$$

3.4.1 Static Problem without Current Sources

For our magnetic bearing applications, we can assume that the electrical charge density is zero if there is no coil present. Then we will have:

$$\nabla \cdot D = \rho = 0 \tag{3.11}$$

For static problems, since we also have J=0, Eq. 3.4 becomes:

$$\nabla \times H = 0 \tag{3.12}$$

A parameter called total scalar potential Ψ can be introduced as in Eq. 3.13 which fulfills Eq. 3.12 automatically.

$$H = -\nabla\Psi \tag{3.13}$$

Plug it into Eq. 3.6 and Eq. 3.8, we have:

$$\nabla \cdot \mu(-\nabla\Psi) = 0 \tag{3.14}$$

This lead to Eq. 3.15, which will be the basic equations to solve by FEM programs for magneto-static problems in regions with no current sources.

$$-\nabla^2\Psi = 0 \tag{3.15}$$

3.4.2 Region with Eddy Currents Induced by Flux Variation or Motion but without Coils

Since there no coils within the region studied, Eq. 3.11 also holds for this case. From Eq. 3.4, we have:

$$\nabla \times H = J \tag{3.16}$$

Eq. 3.7, 3.9 and 3.10 turn into:

$$\nabla \cdot J = 0 \tag{3.17}$$

The magnetic vector potential A is defined as in Eq. 3.18, which fulfills Eq. 3.6 automatically:

$$B = \nabla \times A \tag{3.18}$$

Then the electric current density will be:

$$J = \nabla \times H = \nabla \times \frac{B}{\mu} = \nabla \times \frac{1}{\mu}(\nabla \times A) \tag{3.19}$$

By utilizing Ampere's Law, the current density can be separated into motion induced part and parts generated by other sources:

$$J = \sigma(E + v \times B) \tag{3.20}$$

Eq. 3.19 and Eq. 3.20 will convert to:

$$\nabla \times \frac{1}{\mu}(\nabla \times A) = \sigma(E + v \times B) \tag{3.21}$$

An electric scalar potential Φ was introduced as in Eq. 3.22. This equation will fulfill Eq. 3.5 automatically.

$$E = -\frac{\partial A}{\partial t} - \nabla\phi \tag{3.22}$$

In order to obtain a unique solution, divergence of A must also be specified as:

$$\nabla \cdot A = 0 \tag{3.23}$$

Then from Eq. 3.17 we have:

$$\nabla \cdot \varepsilon E = \nabla \cdot \varepsilon\left(-\frac{\partial A}{\partial t} - \nabla\phi\right) = -\varepsilon\frac{\partial}{\partial t}(\nabla \cdot A) - \varepsilon\nabla \cdot \nabla\phi = 0 \tag{3.24}$$

From Eq. 3.21 we have:

$$\nabla \times \frac{1}{\mu}(\nabla \times A) = \sigma\left(-\frac{\partial A}{\partial t} - \nabla\phi\ + v \times \nabla \times A\right) \tag{3.25}$$

William and Chan [41] pointed out that:

$$\nabla\phi = \nabla(A \cdot v) \tag{3.26}$$

So the final equation converts to:

$$\nabla \times \frac{1}{\mu}(\nabla \times A) - \sigma\left(-\frac{\partial A}{\partial t} - \nabla(A \cdot v) + v \times \nabla \times A\right) = 0 \tag{3.27}$$

We also have:

$$\nabla(A \cdot B) = (A \cdot \nabla)B + (B \cdot \nabla)A + A \times (\nabla \times B) + B \times (\nabla \times A) \tag{3.28}$$

This will change Eq. 3.27 into:

$$\nabla \times \frac{1}{\mu}(\nabla \times A) - \sigma\left(-\frac{\partial A}{\partial t} - A \times (\nabla \times v) - (A \cdot \nabla)v - (v \cdot \nabla)A\right) = 0 \qquad (3.29)$$

By assuming an element wise constant velocity *v*, the equation can be simplified into:

$$\nabla \times \frac{1}{\mu}(\nabla \times A) - \sigma\left(-\frac{\partial A}{\partial t} - (v \cdot \nabla)A\right) = 0 \qquad (3.30)$$

This equation will be used to solve harmonic or transient problems with eddy current effect caused either by motion or by flux fluctuation.

3.4.3 Source Coils and Boundary Conditions

The fields due to source coils were calculated using Biot-Savart Law as in Eq. 3.31.

$$H_s = \frac{1}{4\pi}\int_{\Omega} J_s \times \left(\frac{1}{R_{sc}}\right) d\Omega \qquad (3.31)$$

The boundary conditions can be specified by assigning values to components of the following quantities:

$$B \cdot n = \mu \nabla \Psi \cdot n = (\nabla \times A) \cdot n \qquad (3.32)$$

3.5 Magnetic Combo Bearing Static Parameter Analysis with ANSYS™

ANSYS™ 3D static magnetic analysis was used to design and decide the parameters of the combo magnetic bearing. Due to the node and element count limitations put by ANSYS license the author used, a half model was built with Solidworks™ and imported/meshed using ANSYS APDL. The half model use XZ as symmetry plane and Z axis as the axial direction. The nonlinearity of this problem mainly comes from BH characteristics of the 4340 steel. The BH curve used for this nonlinear static analysis is the one that retrieved by experiments as stated in earlier sections. The disk was

simplified into a smaller circular ring to reduce the node/element counts. It was made sure that enough volume of the disk was left so that the magnetic field simulation within the disk can be accurately modeled even with the simplification of the disk. This point was proven by the fact that the magnetic fields diminished far before they reached the boundary of the disk model. A thick layer of air was also built so that the thinnest air around the bearing assembly is 40mm. This was used to consider the fringing effect of the magnetic flux. The solid model is as presented in Fig. 3.10.

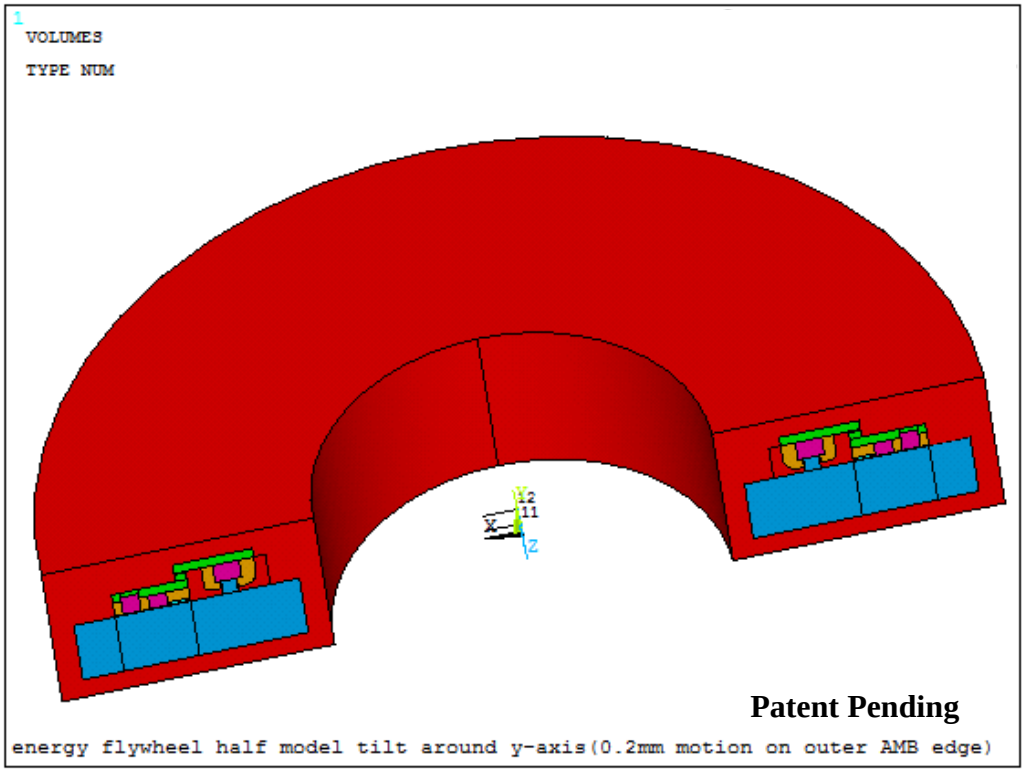

Fig. 3.10 Half Model of the ANSYS™ 3D Static Magnetic Analysis

SOLID96 was used to mesh the structure and SOURC36 was used to model coils. The structures were sliced into regular shapes and 'glued' together to mesh them with

hexahedral elements. Due to the irregular shape of the surrounding air, it was meshed with tetrahedral elements. The meshed structure is as shown in Fig. 3.11. Parallel flux boundary conditions were put around the surrounding air and on the symmetry plane.

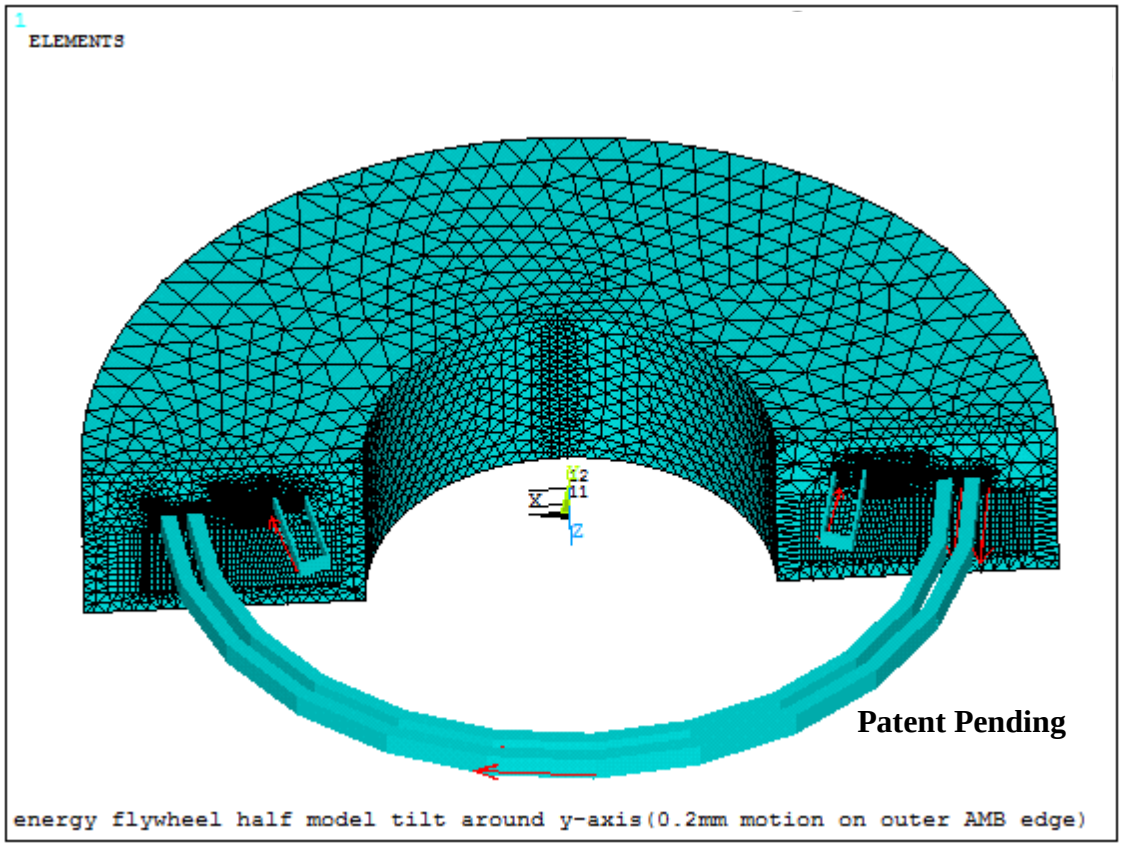

Fig. 3.11 Meshed ANSYS™ 3D Magnetic Bearing Half Model

The first static analysis carried out is the one which has a ‘zero’ position. This is the designed nominal position for the disk to stay during operations. At this position, the axial gap will be 1.5mm, the radial gap on outer radial pole is 2mm, and the radial gap on inner pole is 1mm. The flux density vector plot was shown as in Fig. 3.12. The half model axial force is between 18441.6N and 18662N, depending on if virtual work or

Maxwell method was used to calculate the force. This value equals to 4145.8lbf and 4195.4lbf, respectively. So the real bearing will have an axial force of 8292-8390lbf. The 88in solid disk discussed in Chapter II has a weight of 8600lbf. Considering the weight reduction by the motor grove cut at the outer diameter, the designed magnetic bearing's axial nominal lifting capacity should be very close to the flywheel weight.

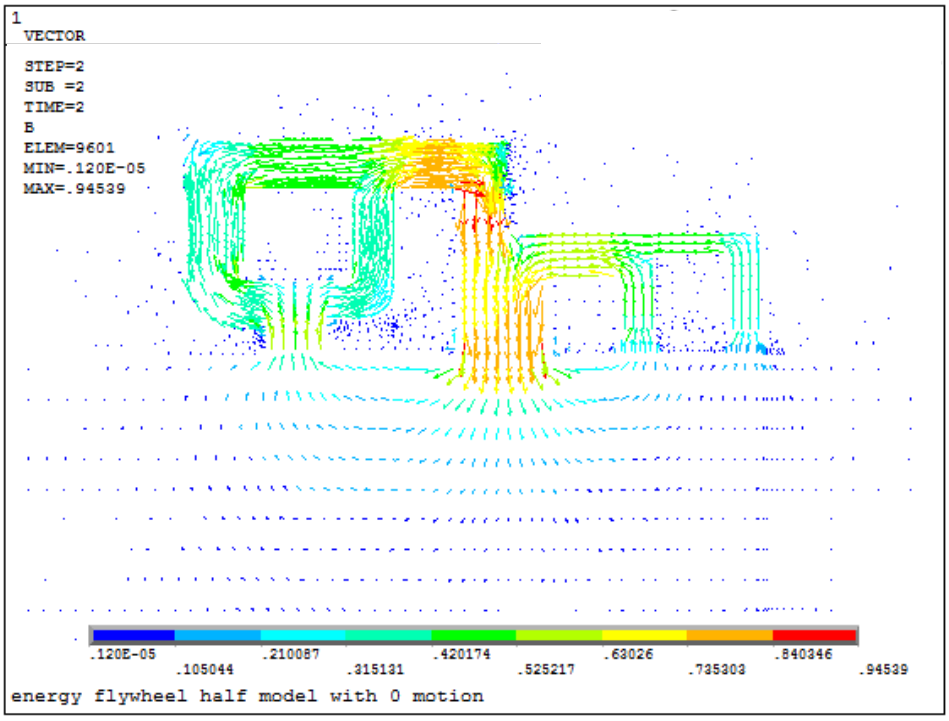

Fig. 3.12 Magnetic Flux Density at Zero Position

The magnetic flux density variations within the air around the disk step facing radial poles are as in Fig. 3.13 and Fig. 3.14. The flux variation is 0.2-0.37Tesla on inner surface of the disk step facing the radial and 0.27-0.3Tesla on outer surface. These relatively small variations were realized by dovetail inner radial poles and circular ring outer radial poles. With a smaller flux density variation, the eddy current loss during the

nominal operation of our system will also be much smaller. The magnetic flux density under the axial control poles is as plotted in Fig. 3.15.As can be seen, the flux density doesn't change in circumferential directions. This will also contribute to a low eddy loss during nominal operation.

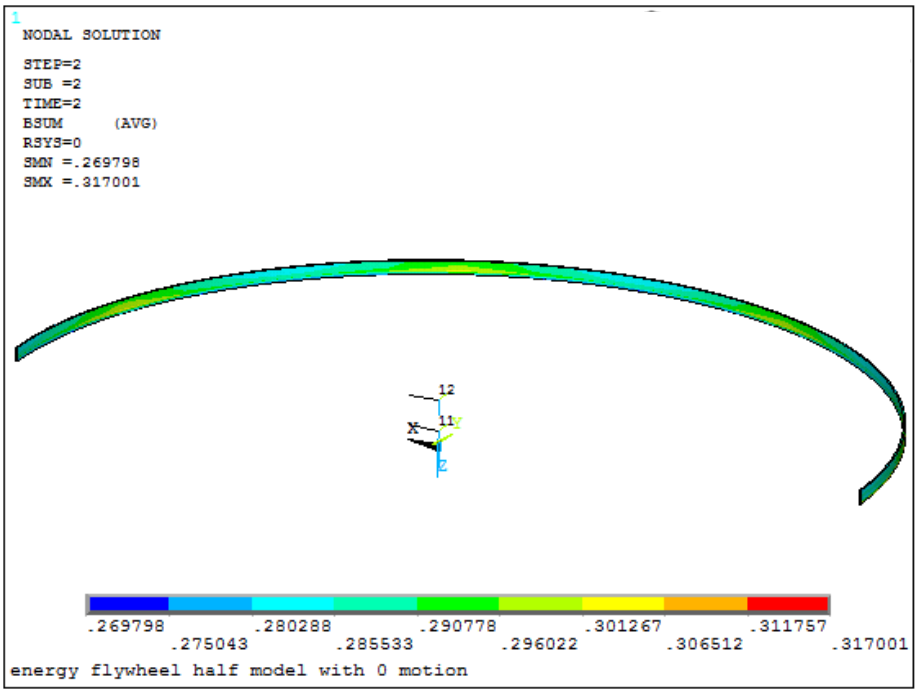

Fig. 3.13 Flux Density within Outer Surface Air of the Disk near Radial Poles at Zero Position

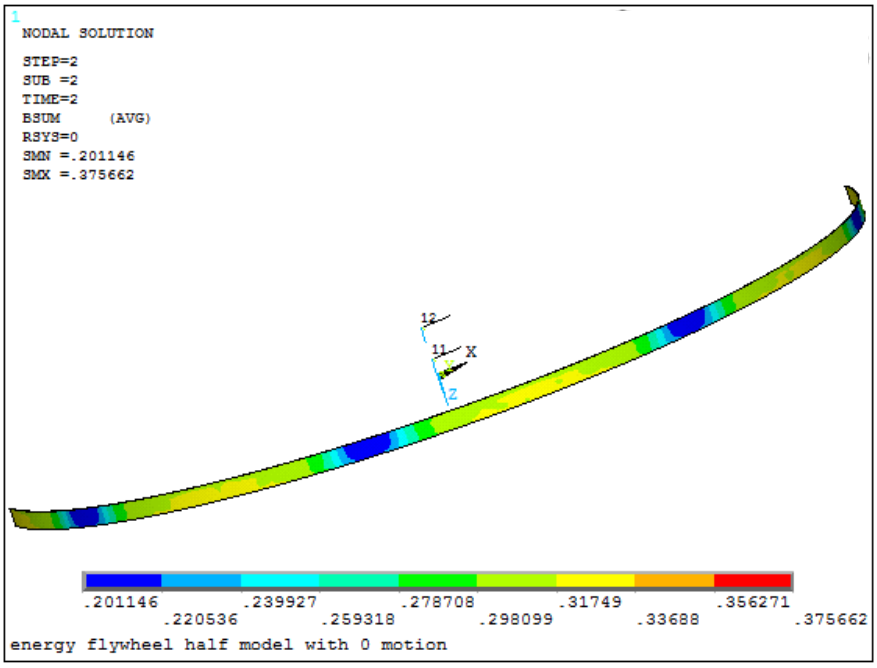

Fig. 3.14 Flux Density within Inner Surface Air of the Disk near Radial Poles at Zero Position

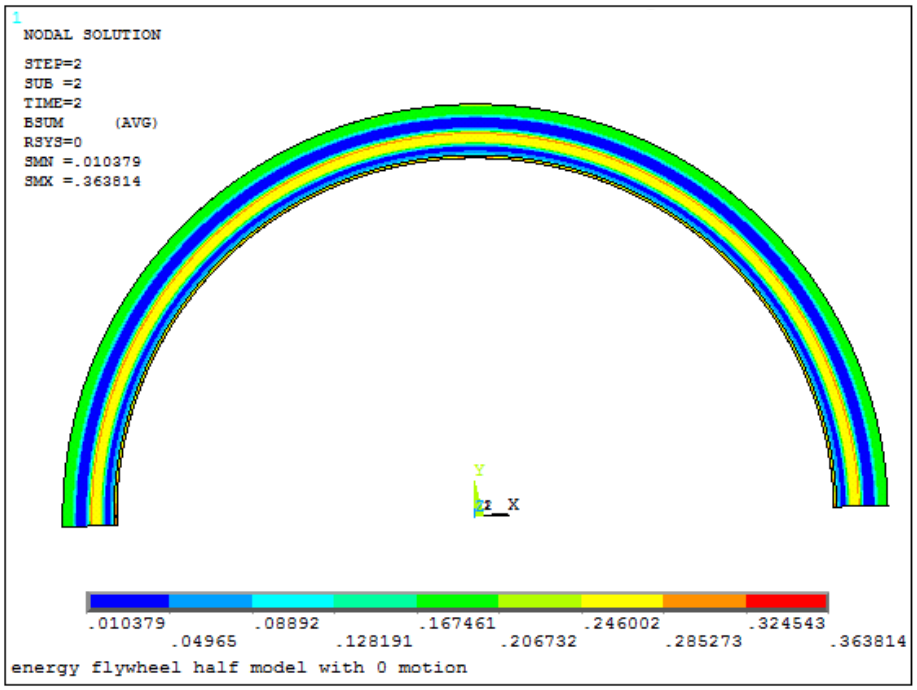

Fig. 3.15 Flux Density under Two Axial Poles at Zero Position

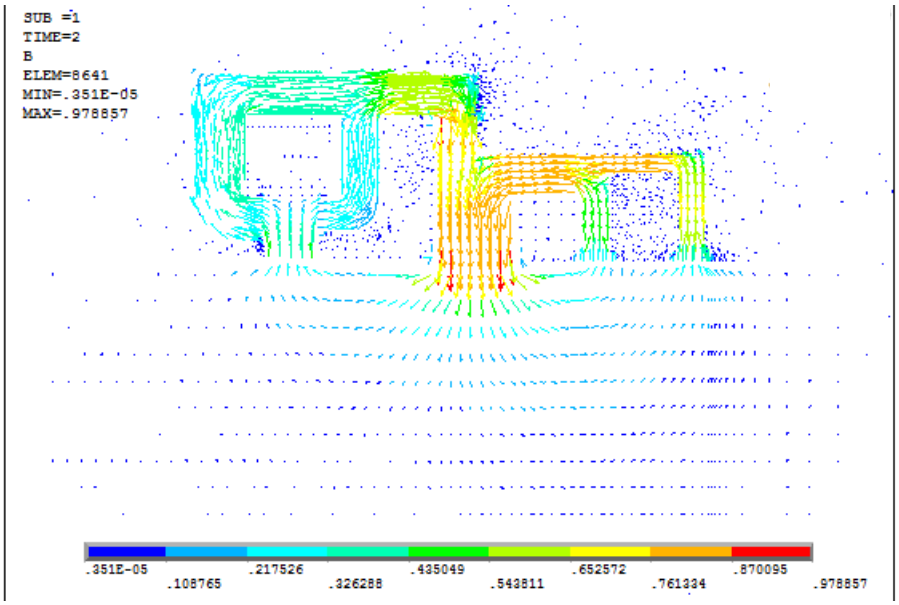

Fig. 3.16 Flux Density Plot with 1500 Amp-turns Axial Excitation at Zero Position

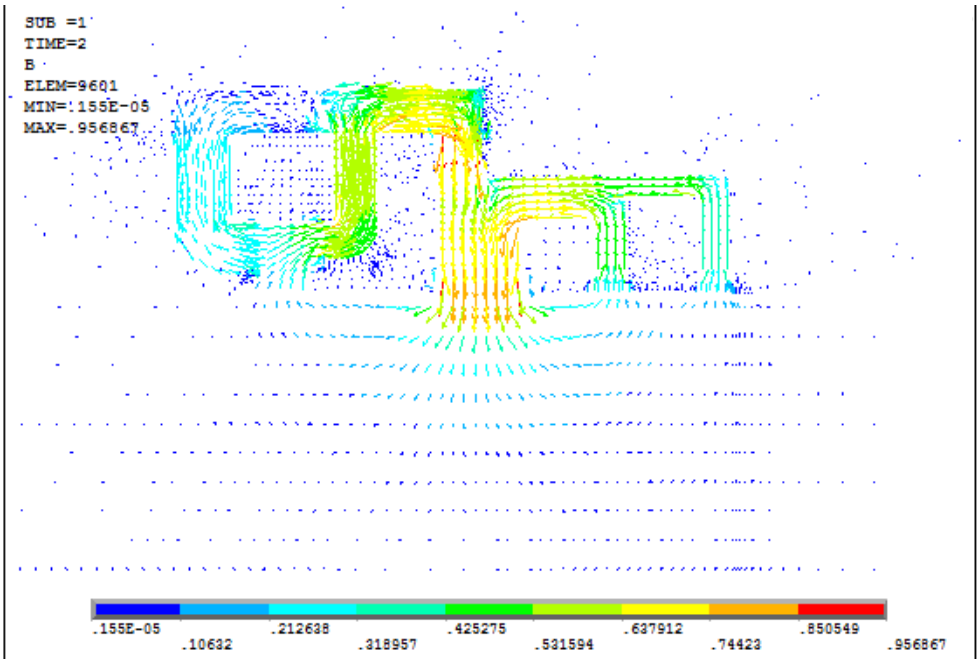

Fig. 3.17 Flux Density Plot with +/- 1500 Amp-turns on Opposite Radial Poles at Zero Position

1500 Amp-turns of current was put on axial coils and the flux density is as shown in Fig. 3.16. The flux density plot is plotted as in Fig. 3.17 if 1500 Amp-turns was put on one radial control pole and -1500 Amp-turns was put on the opposite pole. The excited radial pole pairs are in y direction. The only noticeable changes in forces and moments are also in y direction. This proves the radial bearing poles are decoupled automatically.

Several other simulations were also carried out by moving/tilting disk in different directions or imposing different current excitation on axial/radial/moment coils. These experiments were done to retrieve the current and position stiffness of the magnetic bearing design. After considering the symmetry conditions of different cases, the force/Moment results for the full model were calculated and listed in Table 3.1. F_r is the radial force, F_a is the axial force, and M_t is the moment generated by the moment coil. It was assumed that every bearing coil has 400 turns. The calculated position and current stiffness of the magnetic bearings is as shown in Table 3.2. The moment control has a coupled axial force with a stiffness of 138-142 N/A. This can be cancelled by axial coil control or unbalanced moment coil currents on opposite poles. Also due to the effect that this cross coupling force is pretty low compared to axial bearing forces (Axial Bearing current stiffness is about 2840 N/A), this effect will be neglected during our analysis but will be compensated during implementation of the physical system. The radial forces can actually be bigger since we are only simulating one pair of radial poles. Since we have 8 pole structures, the maximum force in single direction can reach 2.414 times of what a single radial pole pair can generate.

Table 3.1 Full Model Value Using ANSYS™

CASE	Maxwell Method				Virtual Work Method			
	F_r(N)	F_a(N)	ΔF_a(N)	M_t(Nm)	F_r(N)	F_a(N)	ΔF_a(N)	M_t(Nm)
0 motion	0	-37324	0	0	0	-36883	0	0
0.1mm –Z(axial)	0	-38394	-1070	0	0	-37942	-1059	0
0.0762mm –X(radial)	-122.9	-37324	0	0	-116.8	-36883	0	0
Tiltθy= -0.0164° (0.2mm at AMB edge)	0	-37360	-36	-543.8	0	-36913	-30	-535.8
1500 AmpTurns axial	0	-47970	-10646	0	0	-46721	-9838	0
-1500 AmpTurns axial	0	-26655	10669	0	0	-25919	10964	0
+/-1500 AmpTurns opposite radial pole pair on X axis	1266.4	-37291	33	0	1265.8	-36863	20	0
+/-3000 AmpTurns opposite moment pole pair around X axis	0	-36286	1038	2377.5	0	-35817	1066	2322.1

Table 3.2 Full Model Magnetic Bearing Stiffness Using ANSYS™

	Kpa(N/m)	Kpr(N/m)	Kpm(Nm/rad)	Kia(N/A)	Kir(N/A)	Kim(Nm/A)
Maxwell	-1.07e7	-1.61e6	1.90e6	2.84e3	8.16e2	317
Virtual Work	-1.06e7	-1.53e6	1.88e6	2.62e3-2.92e3	8.16e2	310

3.6 Conclusion

Novel combo magnetic bearing design architecture was first introduced and compared with traditional homo-polar magnetic bearing structures. The detailed design considerations were discussed. An experimental rig was setup to test the magnetic property of the heat treated 4340 steel. The experimental results were then transformed into nonlinear BH curves and relative permeability values. After this, basics of magnetic FEMs were introduced since FEM magnetic analysis software such ANSYS™ and OPERA-3D™ all use these principles as functions to be solved. Finally, ANSYS™ finite element model for the magnetic bearing/disk assembly was built and meshed to carry out the static analysis of the magnetic bearing's characteristics. The axial bearing's lifting capability was verified. Then several simulations were carried out where either the disk was moved/rotated in certain direction or current excitation was imposed on axial/radial/moment coils. These simulation results provide us the current and position stiffness values, which are key parameters of magnetic bearings and will be used in the later part of this dissertation.

CHAPTER IV

MAGNETIC BEARING FREQUENCY BEHAVIOR AND STABILITY ANALYSIS

4.1 Overview

Due to eddy current effects, magnetic bearing current stiffness will be weakened as the excitation frequency goes up. This effect will also cause a phase lag between input current and output control force of the magnetic bearing. This chapter will try to consider this effect by introducing a transfer function between input current and corresponding current stiffness. This was realized by utilizing ANSYS^{TM} harmonic analysis. PID control loops with compensators and filters were used to model the control of the magnetic bearing. The root locus for the whole closed loop system was plotted to verify the stability of the system.

4.2 Current Stiffness Transfer Functions of the Combo Magnetic Bearing

The magnetic field tends to converge to the surface of the metal structure as the excitation frequency rising up. This is called skin depth effect and will weaken the magnetic bearing capability as excitation frequency getting higher. The skin depth is defined as in Eq. 4.1, where f is the excitation frequency, μ is the permeability and σ is the conductivity.

$$\delta = \frac{1}{\sqrt{\pi f \mu \sigma}} \tag{4.1}$$

This equivalently generates a current stiffness that will diminish with input

frequencies. This phenomenon reduces the bandwidth that the magnet bearing will operate stable. This is why traditional magnetic bearings have laminated structures to reduce the eddy effects. Kenny [42] developed simulation models to investigate lamination thickness effects and plotted the mean flux and phase lag relationship for a lamination at a source frequency of 50 Hz. Kenny also plotted Total flux changes within a 12.7mm (0.5in) laminate. His results were based on laminates with a relative permeability of 1000 and conductivity of 2500/ohm-mm. As was seen in his results, a structure with thinner laminates will have better performance in both magnitude and phase lags.

However, even though laminates are quite effective for these applications and also readily compatible with our design, the cost of them plays a key factor in our decision to design a system without lamination. There are several factors contribute to this decision: First, both the disk and bearing are made with 4340, which has a relative low relative permeability (50-150 when flux density is bigger than 0.5Tesla (Fig. 3.9) vs. several thousand for traditional magnetic bearing material). This will make the frequency weakening curve less steep. This conclusion can be drawn by comparing Kenny's simulation results [42] with ours. The material Kenny used has a relative permeability about ten times of ours (1000 vs. 50-150) while the conductivity is higher than 50% of 4340 (2500/ohm-mm vs. 3356-4032/ohm-mm). So according to Eq. 4.1, at the same frequency, the skin depth for our material will be 2-3.9 times that of Kenny's material. So with the same performance, our laminates' thickness can be 2-3.9 times as big as Kenny's case. Second, our bearings were designed in a way that the AC path thickness is

smaller. This will make the eddy skin effect less affective. Last, the rotation speed is relatively low (4906RPM, 81.8Hz) so that the requirement for control bandwidth is also reduced.

All these factors contribute to the fact that, even though the AC performance of the unlaminated version will be worse than the laminated version of our design, it is still useable for the novel flywheel application. Given the fact that the gyroscopic term induced mode will require a higher bandwidth (up to twice of the rotating frequency), good isolations on angular rotations of the whole system will be needed to take care of the weakened performance at high frequency domain. If the angular isolation is not available, then a tape wound lamination structure should be used on the bearing to improve the performance on the moment control poles. It must be mentioned again that using laminated structures is 100% compatible with the current design of the combo bearing structure. The only difference is the improved performance at the expense of building cost.

Both harmonic and transient analysis can be used to simulate the eddy effects. The harmonic analysis is constrained to linear material properties with no bias flux (no permanent magnet or DC bias current allowed). However, the AC flux is generally a small perturbation with respect to bias flux and the transfer function of the current stiffness can be linearized with respect to the AC flux term. In addition to that, within the perturbation range, the materials properties can also be treated linear. The transient analysis can be carried out on PM biased, non-linear analysis and simulate actual forces/moments directly. However, the transient analysis will consume much more

computing resources as well as modeling efforts, and took much longer to run than the harmonic analysis. Based on these facts, harmonic analysis will be used and should be good enough for our purpose of concept design.

A relative permeability of 100 was selected during ANSYS™ harmonic analysis. The AC flux density changing with the excitation frequency was simulated and used to approximate the force behavior(For small AC flux density amplitude, the higher order terms in the magnetic force formula can be neglected).

Kim suggested that at least one layer of elements should be meshed within the skin depth to have accurate results in harmonic analysis [43]. His PhD dissertation also verified that a fine mesh outside the skin depth is not required given the existence of layers of elements in the skin depth [43]. To make the result more accurate, it was recommended by Vector Fields™ that 3 or more layers of elements to be meshed in skin depth [44]. In our 3D meshing, at least 4 layers or more of elements were meshed within the skin depth calculated with Eq. 4.1 using a frequency of 160 Hz, a relative permeability of 100 and 4340's conductivity of 3356/ohm-mm.

The averaged flux density values for various cases were as listed in Table 4.1. Since harmonic analysis is a linear analysis, the magnitude of the excitation and output can be scaled and normalized under our assumption without losing the accuracy of the analysis. The data was curved fitted to get numerical transfer functions with LABVIEW™ as shown in Fig. 4.1. The transfer functions were as listed in Eq. 4.2-4.4.

Table 4.1 Harmonic Response on Magnetic Bearing

Frequency(Hz)	Outer Control pole(axial bearing, Tesla)	Inner control pole (moment bearing, Tesla)	Inner control surface (radial bearing, Tesla)
1e-3	0.29@0^{o}	0.25T@0^{o}	0.5@0^{o}
18	0.1526@-34.32^{o}	0.168@-26.57^{o}	0.3276@-31.26^{o}
36	0.1124@-38.50^{o}	0.118@-36.38^{o}	0.2552@-34.62^{o}
54	0.0949@-41.58^{o}	0.1@-36.87^{o}	0.1985@-40.91^{o}
72	0.0828@-42.55^{o}	0.0922@-40.6^{o}	0.1769@-42.71^{o}
90	0.0746@-43.10^{o}	0.0851@-40.24^{o}	0.1628@-47.49^{o}
108	0.0679@-43.81^{o}	0.0786@-42.42^{o}	0.1421@-50.71^{o}
126	0.0629@-44.36^{o}	0.0736@-42.80^{o}	0.1204@-51.7^{o}
144	0.0585@-44.52^{o}	0.07@-44.42^{o}	0.1140@-52.13^{o}
162	0.0549@-44.78^{o}	0.0665@-45^{o}	0.1040@-54.78^{o}
180	0.0520@-44.84^{o}	0.0637@-46.27^{o}	0.0999@-55.20^{o}
300	0.0402@-44.90^{o}	0.0497@-49.90^{o}	0.0762@-66.80^{o}

$$\bar{T}_{axial}(s) = \frac{692.1\,s^2 + 9.87 * 10^5 s + 1.441 * 10^8}{s^3 + 5137s^2 + 2.451 * 10^6 s + 1.441 * 10^8} \tag{4.2}$$

$$\bar{T}_{radial}(s) = \frac{350s^3 + 1.935 * 10^5 s^2 + 3.211 * 10^8 s + 5.657 * 10^{10}}{s^4 + 1319s^3 + 1.294 * 10^6 s^2 + 7.877 * 10^8 s + 5.657 * 10^{10}} \tag{4.3}$$

$$\bar{T}_{moment}(s) = \frac{538s^2 + 4.651 * 10^5 s + 4.103 * 10^7}{s^3 + 2835s^2 + 9.403 * 10^5 s + 4.103 * 10^7} \qquad (4.4)$$

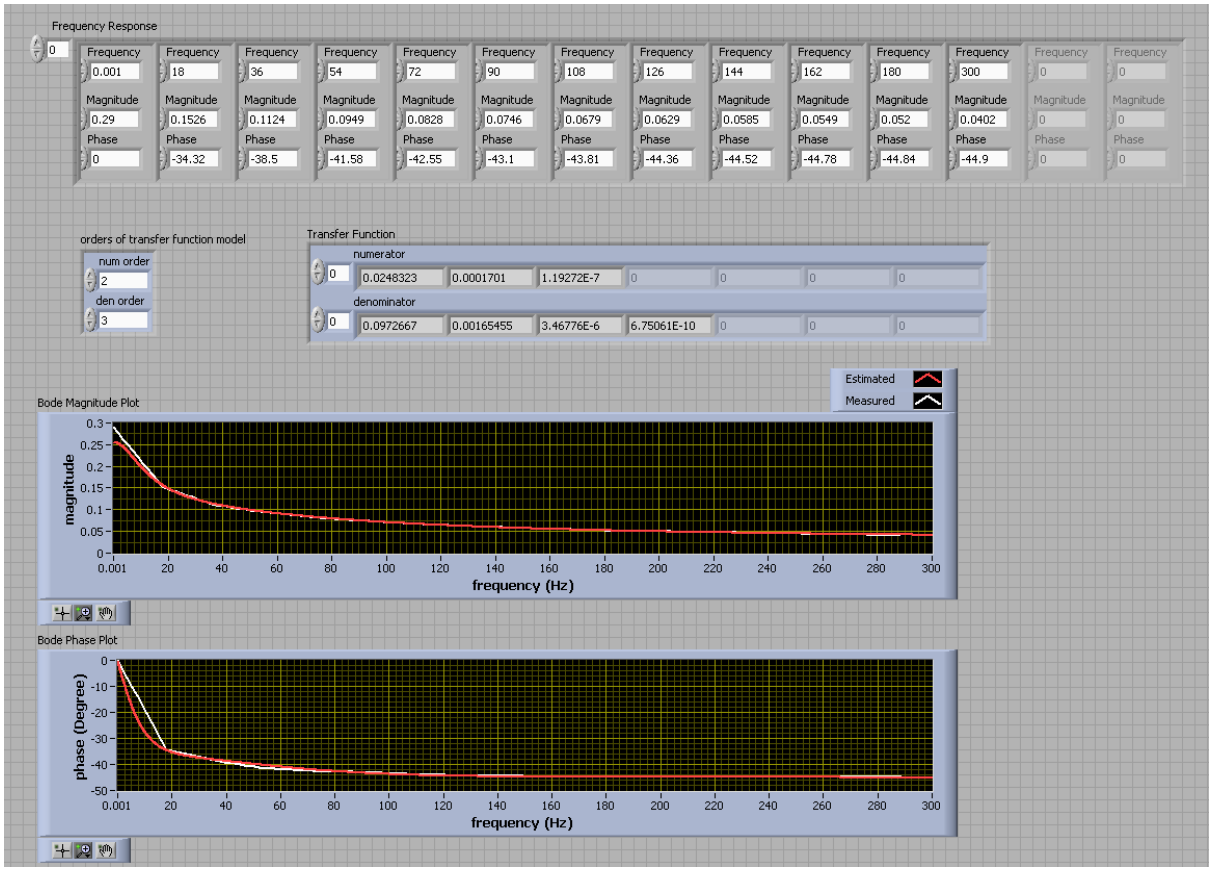

Fig. 4.1 Transfer Function Fit for Axial Bearing Outer Control Pole

4.3 Closed-loop Control Stability of the Combo Magnetic Bearing

The normalized transfer functions discussed above were used in modeling of our system control loops such as the axial one in Fig. 4.2. For moment control loops, the θ_x and θ_y channels will have cross coupled proportional and derivative terms to control the gyroscopic effect of the wheel.

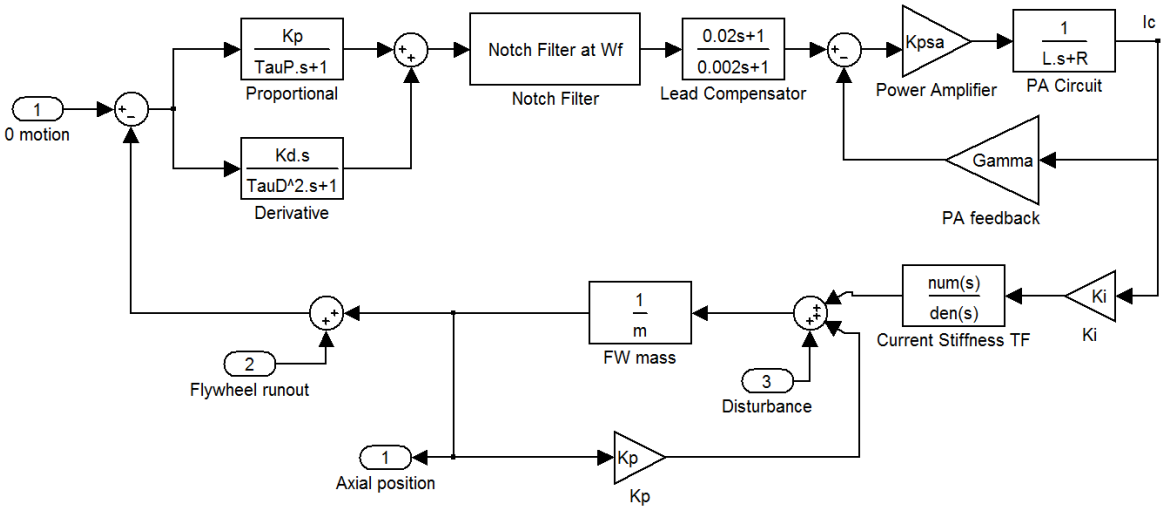

Fig. 4.2 Axial Bearing Control Loop Modelling

The low-pass character of the propotional and derivative channels can be modelled as(x and y is the radial direction and z is the axial direction)

$$\begin{cases} \dot{\psi}_{px} = -\dfrac{\psi_{px}}{\tau_p} + x + RO_x \\ x_s = \dfrac{\psi_{px}}{\tau_p} \end{cases} \tag{4.5}$$

$$\begin{cases} \dot{\psi}_{py} = -\dfrac{\psi_{py}}{\tau_p} + y + RO_y \\ y_s = \dfrac{\psi_{py}}{\tau_p} \end{cases} \tag{4.6}$$

$$\begin{cases} \dot{\psi}_{pz} = -\dfrac{\psi_{pz}}{\tau_p} + z + RO_z \\ z_s = \dfrac{\psi_{pz}}{\tau_p} \end{cases} \tag{4.7}$$

$$\begin{cases} \dot{\psi}_{p\theta x} = -\dfrac{\psi_{p\theta x}}{\tau_p} + \theta_x + RO_{\theta x} \\ \theta_{xs} = \dfrac{\psi_{p\theta x}}{\tau_p} \end{cases} \tag{4.8}$$

$$\begin{cases} \dot{\psi}_{p\theta y} = -\dfrac{\psi_{p\theta y}}{\tau_p} + \theta_y + RO_{\theta y} \\ \theta_{ys} = \dfrac{\psi_{p\theta y}}{\tau_p} \end{cases} \tag{4.9}$$

For derivative channels, the filter matrix can be defined as:

$$A_{DM} = \begin{bmatrix} -\dfrac{2}{\tau_D} & -\dfrac{1}{\tau_D^2} \\ 1 & 0 \end{bmatrix} \tag{4.10}$$

$$B_{DM} = \begin{bmatrix} 1 \\ 0 \end{bmatrix} \tag{4.11}$$

Then we can have the state space equation as:

$$\begin{cases} \dot{\psi}_{dx} = A_{DM}\psi_{dx} + B_{DM}\left(\dot{x} + \dot{RO}_x\right) \\ dx_s = \begin{bmatrix} 0 & \dfrac{1}{\tau_D^2} \end{bmatrix}\psi_{dx} \end{cases} \tag{4.12}$$

$$\begin{cases} \dot{\psi}_{dy} = A_{DM}\psi_{dy} + B_{DM}\left(\dot{y} + \dot{RO}_y\right) \\ dy_s = \begin{bmatrix} 0 & \dfrac{1}{\tau_D^2} \end{bmatrix}\psi_{dy} \end{cases} \tag{4.13}$$

$$\begin{cases} \dot{\psi}_{dz} = A_{DM}\psi_{dz} + B_{DM}\left(\dot{z} + \dot{RO}_z\right) \\ dz_s = \begin{bmatrix} 0 & \dfrac{1}{\tau_D^2} \end{bmatrix}\psi_{dz} \end{cases} \tag{4.14}$$

$$\begin{cases} \dot{\psi}_{d\theta x} = A_{DM}\psi_{d\theta x} + B_{DM}\left(\dot{\theta}_x + \dot{RO}_{\theta x}\right) \\ d\theta_{xs} = \begin{bmatrix} 0 & \dfrac{1}{\tau_D^2} \end{bmatrix}\psi_{d\theta x} \end{cases} \tag{4.15}$$

$$\begin{cases} \dot{\psi}_{d\theta y} = A_{DM}\psi_{d\theta y} + B_{DM}\left(\dot{\theta}_y + \dot{RO}_{\theta y}\right) \\ d\theta_{ys} = \begin{bmatrix} 0 & \dfrac{1}{\tau_D^2} \end{bmatrix}\psi_{d\theta y} \end{cases} \tag{4.16}$$

The PD controller gains can be assumed as:

$$\begin{cases} G_{PR} = \dfrac{K_{P\_r} - K_{pr}}{K_{ir}} \\ G_{DR} = \dfrac{C_{P\_r}}{K_{ir}} \\ G_{PA} = \dfrac{K_{P\_a} - K_{pa}}{K_{ia}} \\ G_{DA} = \dfrac{C_{P\_a}}{K_{ia}} \\ G_{P\theta} = \dfrac{K_{P\_\theta} - K_{p\theta}}{K_{i\theta}} \\ G_{D\theta} = \dfrac{C_{P\_\theta}}{K_{i\theta}} \\ G_{CP\theta} = \dfrac{\varsigma K_{P\_\theta}}{K_{i\theta}} \\ G_{CD\theta} = \dfrac{\gamma I_p \varpi_f}{K_{i\theta}} \end{cases} \tag{4.17}$$

The PD controller output (control current target) is:

$$\begin{cases} IC_x = -G_{PR}x_s - G_{DR}dx_s \\ IC_y = -G_{PR}y_s - G_{DR}dy_s \\ IC_z = -G_{PA}z_s - G_{DA}dz_s \\ IC_{\theta x} = -G_{P\theta}\theta_{xs} - G_{CP\theta}\theta_{ys} - G_{D\theta}d\theta_{xs} + G_{CD\theta}d\theta_{ys} \\ IC_{\theta y} = -G_{P\theta}\theta_{ys} + G_{CP\theta}\theta_{xs} - G_{D\theta}d\theta_{ys} - G_{CD\theta}d\theta_{xs} \end{cases} \tag{4.18}$$

The controller output will pass through a notch filter to get rid of the runout and imbalance impact on the magnetic bearing. The notch frequency will move together and equal to the 1X frequency. The notch filter matrix are:

$$\begin{cases} A_{notch} = \begin{bmatrix} -\dfrac{2}{c_{notch}\varpi_{notch}} & -\varpi_{notch}^2 \\ 1 & 0 \end{bmatrix} \\ B_{notch} = \begin{bmatrix} 1 \\ 0 \end{bmatrix} \\ C_{notch} = \begin{bmatrix} \dfrac{2(d_{notch} - 1)}{c_{notch}\varpi_{notch}} & 0 \end{bmatrix} \\ D_{notch} = 1 \end{cases} \tag{4.19}$$

$$\begin{cases}\dot{\psi}_{notch\_x} = A_{notch}\psi_{notch\_x} + B_{notch}IC_x \\ OUT_{notch\_x} = C_{notch}\psi_{notch\_x} + D_{notch}IC_x\end{cases} \tag{4.20}$$

$$\begin{cases}\dot{\psi}_{notch\_y} = A_{notch}\psi_{notch\_y} + B_{notch}IC_y \\ OUT_{notch\_y} = C_{notch}\psi_{notch\_y} + D_{notch}IC_y\end{cases} \tag{4.21}$$

$$\begin{cases}\dot{\psi}_{notch\_z} = A_{notch}\psi_{notch\_z} + B_{notch}IC_z \\ OUT_{notch\_z} = C_{notch}\psi_{notch\_z} + D_{notch}IC_z\end{cases} \tag{4.22}$$

$$\begin{cases}\dot{\psi}_{notch\_\theta x} = A_{notch}\psi_{notch\_\theta x} + B_{notch}IC_{\theta x} \\ OUT_{notch\_\theta x} = C_{notch}\psi_{notch\_\theta x} + D_{notch}IC_{\theta x}\end{cases} \tag{4.23}$$

$$\begin{cases}\dot{\psi}_{notch\_\theta y} = A_{notch}\psi_{notch\_\theta y} + B_{notch}IC_{\theta y} \\ OUT_{notch\_\theta y} = C_{notch}\psi_{notch\_\theta y} + D_{notch}IC_{\theta y}\end{cases} \tag{4.24}$$

The notch filter results were then sent to lead compensators to compensate phase lags caused by eddy currents to make the control loop stable. The lead compensators were defined by the following matrices.

$$\begin{cases}A_{LeadA} = -\dfrac{a0_{LeadA}}{a1_{LeadA}} \\ B_{LeadA} = 1 \\ C_{LeadA} = \dfrac{b0_{LeadA}}{a1_{LeadA}} - \dfrac{\mathrm{b}1_{LeadA}}{a1_{LeadA}} \cdot \dfrac{a0_{LeadA}}{a1_{LeadA}} \\ D_{LeadA} = \dfrac{b1_{LeadA}}{a1_{LeadA}} \\ a0_{LeadA} = 0.002; a1_{LeadA} = 1; b0_{LeadA} = 1; b1_{LeadA} = 0.01\end{cases} \tag{4.25}$$

$$\begin{cases} A_{LeadR} = -\dfrac{a0_{LeadR}}{a1_{LeadR}} \\ B_{LeadR} = 1 \\ C_{LeadR} = \dfrac{b0_{LeadR}}{a1_{LeadR}} - \dfrac{\mathrm{b1}_{LeadR}}{a1_{LeadR}} \cdot \dfrac{a0_{LeadR}}{a1_{LeadR}} \\ D_{LeadR} = \dfrac{b1_{LeadR}}{a1_{LeadR}} \\ a0_{LeadR} = 0.002; a1_{LeadR} = 1; b0_{LeadR} = 1; b1_{LeadR} = 0.02 \end{cases} \tag{4.26}$$

$$\begin{cases} A_{LeadMo} = -\dfrac{a0_{LeadMo}}{a1_{LeadMo}} \\ B_{LeadMo} = 1 \\ C_{LeadMo} = \dfrac{b0_{LeadMo}}{a1_{LeadMo}} - \dfrac{\mathrm{b1}_{LeadMo}}{a1_{LeadMo}} \cdot \dfrac{a0_{LeadMo}}{a1_{LeadMo}} \\ D_{LeadMo} = \dfrac{b1_{LeadMo}}{a1_{LeadMo}} \\ a0_{LeadMo} = 0.002; a1_{LeadMo} = 1; b0_{LeadMo} = 1; b1_{LeadMo} = 0.02 \end{cases} \tag{4.27}$$

$$\begin{cases} \dot{\psi}_{Lead\_x} = A_{LeadR}\psi_{Lead\_x} + B_{LeadR}OUT_{notch\_x} \\ OUT_{Lead\_x} = C_{LeadR}\psi_{Lead\_x} + D_{LeadR}OUT_{notch\_x} \end{cases} \tag{4.28}$$

$$\begin{cases} \dot{\psi}_{Lead\_y} = A_{LeadR}\psi_{Lead\_y} + B_{LeadR}OUT_{notch\_y} \\ OUT_{Lead\_y} = C_{LeadR}\psi_{Lead\_y} + D_{LeadR}OUT_{notch\_y} \end{cases} \tag{4.29}$$

$$\begin{aligned} \dot{\psi}_{Lead\_z} &= A_{LeadA}\psi_{Lead\_z} + B_{LeadA}OUT_{notch\_z} \\ OUT_{Lead\_z} &= C_{LeadA}\psi_{Lead\_z} + D_{LeadA}OUT_{notch\_z} \end{aligned} \tag{4.30}$$

$$\begin{cases} \dot{\psi}_{Lead\_\theta x} = A_{LeadMo}\psi_{Lead\_\theta x} + B_{LeadMo}OUT_{notch\_\theta x} \\ OUT_{Lead\_\theta x} = C_{LeadMo}\psi_{Lead\_\theta x} + D_{LeadMo}OUT_{notch\_\theta x} \end{cases} \tag{4.31}$$

$$\begin{cases} \dot{\psi}_{Lead\_\theta y} = A_{LeadMo}\psi_{Lead\_\theta y} + B_{LeadMo}OUT_{notch\_\theta y} \\ OUT_{Lead\_\theta y} = C_{LeadMo}\psi_{Lead\_\theta y} + D_{LeadMo}OUT_{notch\_\theta y} \end{cases} \tag{4.32}$$

The lead compensator's output was then used as the input of the power amplifier. The power amplifier was modelled as a closed feed back loop of LR circuit and the functions are:

$$\begin{cases} \dot{\psi}_{psa\_x} = -\dfrac{R_{psa\_r} + K_{psa\_r}\gamma_{psa\_r}}{L_{psa\_r}}\psi_{psa\_x} + OUT_{Lead\_x} \\ i_x = \dfrac{K_{psa\_r}}{L_{psa\_r}}\psi_{psa\_x} \end{cases} \tag{4.33}$$

$$\begin{cases} \dot{\psi}_{psa\_y} = -\dfrac{R_{psa\_r} + K_{psa\_r}\gamma_{psa\_r}}{L_{psa\_r}}\psi_{psa\_y} + OUT_{Lead\_y} \\ i_y = \dfrac{K_{psa\_r}}{L_{psa\_r}}\psi_{psa\_y} \end{cases} \tag{4.34}$$

$$\begin{cases} \dot{\psi}_{psa\_z} = -\dfrac{R_{psa\_a} + K_{psa\_a}\gamma_{psa\_a}}{L_{psa\_a}}\psi_{psa\_z} + OUT_{Lead\_z} \\ i_z = \dfrac{K_{psa\_r}}{L_{psa\_r}}\psi_{psa\_z} \end{cases} \tag{4.35}$$

$$\begin{cases} \dot{\psi}_{psa\_\theta x} = -\dfrac{R_{psa\_Mo} + K_{psa\_Mo}\gamma_{psa\_Mo}}{L_{psa\_Mo}}\psi_{psa\_\theta x} + OUT_{Lead\_\theta x} \\ i_{\theta x} = \dfrac{K_{psa\_Mo}}{L_{psa\_Mo}}\psi_{psa\_\theta x} \end{cases} \tag{4.36}$$

$$\begin{cases} \dot{\psi}_{psa\_\theta y} = -\dfrac{R_{psa\_Mo} + K_{psa\_Mo}\gamma_{psa\_Mo}}{L_{psa\_Mo}}\psi_{psa\_\theta y} + OUT_{Lead\_\theta y} \\ i_{\theta y} = \dfrac{K_{psa\_Mo}}{L_{psa\_Mo}}\psi_{psa\_\theta y} \end{cases} \tag{4.37}$$

The control current then will act on the magnetic bearings and generate forces as with the controllable canonical form of Eq. 4.2-4.4.

$$\begin{cases} \dot{\psi}_{AMB\_x} = \begin{bmatrix} -1319 & -1.294*10^6 & -7.877*10^8 & -5.657*10^{10} \\ 1 & 0 & 0 & 0 \\ 0 & 1 & 0 & 0 \\ 0 & 0 & 1 & 0 \end{bmatrix}\psi_{AMB\_x} + \begin{bmatrix} 1 \\ 0 \\ 0 \end{bmatrix} i_x \\ F_x = K_{ir}[350 \quad 1.935*10^5 \quad 3.211*10^8 \quad 5.657*10^{10}]\psi_{AMB\_x} \end{cases} \tag{4.38}$$

$$\begin{cases} \dot{\psi}_{AMB\_y} = \begin{bmatrix} -1319 & -1.294*10^6 & -7.877*10^8 & -5.657*10^{10} \\ 1 & 0 & 0 & 0 \\ 0 & 1 & 0 & 0 \\ 0 & 0 & 1 & 0 \end{bmatrix} \psi_{AMB\_y} + \begin{bmatrix} 1 \\ 0 \\ 0 \end{bmatrix} i_y \\ F_y = K_{ir}[350 \quad 1.935*10^5 \quad 3.211*10^8 \quad 5.657*10^{10}]\psi_{AMB\_y} \end{cases}$$

(4.39)

$$\begin{cases} \dot{\psi}_{AMB\_z} = \begin{bmatrix} -5137 & -2.451*10^6 & -1.441*10^8 \\ 1 & 0 & 0 \\ 0 & 1 & 0 \end{bmatrix} \psi_{AMB\_z} + \begin{bmatrix} 1 \\ 0 \\ 0 \end{bmatrix} i_z \\ F_z = K_{ia}[692.1 \quad 9.87*10^5 \quad 1.441*10^8]\psi_{AMB\_z} \end{cases}$$

(4.40)

$$\begin{cases} \dot{\psi}_{AMB\_\theta x} = \begin{bmatrix} -2835 & -9.403*10^5 & -4.103*10^7 \\ 1 & 0 & 0 \\ 0 & 1 & 0 \end{bmatrix} \psi_{AMB\_\theta x} + \begin{bmatrix} 1 \\ 0 \\ 0 \end{bmatrix} i_{\theta x} \\ M_x = K_{i\theta}[538 \quad 4.651*10^5 \quad 4.103*10^7]\psi_{AMB\_\theta x} \end{cases}$$

(4.41)

$$\begin{cases} \dot{\psi}_{AMB\_\theta y} = \begin{bmatrix} -2835 & -9.403*10^5 & -4.103*10^7 \\ 1 & 0 & 0 \\ 0 & 1 & 0 \end{bmatrix} \psi_{AMB\_\theta y} + \begin{bmatrix} 1 \\ 0 \\ 0 \end{bmatrix} i_{\theta y} \\ M_y = K_{i\theta}[538 \quad 4.651*10^5 \quad 4.103*10^7]\psi_{AMB\_\theta y} \end{cases}$$

(4.42)

Assuming small motions on angular dirrections, the closed loop dynamics of the system is :

$$\begin{cases} \ddot{x} = F_x/m_f \\ \ddot{y} = F_y/m_f \\ \ddot{z} = F_z/m_f \\ \ddot{\theta}_x = (M_x - I_p\varpi_f\dot{\theta}_y)/I_t \\ \ddot{\theta}_y = (M_y + I_p\varpi_f\dot{\theta}_z)/I_t \end{cases} \quad (4.43)$$

The above equations were assembled to form the dynamic matrices of the system and the

closed loop stabilities was studied by plotting the root locus of the system.When K_{P_r}=6.18e7N/m, C_{P_r}=4.92e5Ns/m, K_{P_a}=1.39e8N/m, C_{p_r}=4.42e5Ns/m, K_{p_θ}=1.94e7 Nm/rad, C_{p_θ}=1.85Nms/rad, ς=0.02, γ=0.02, the system modal frequencies were plotted as in Fig. 4.3. As is seen in the plot, the notch filters' frequencies follow the flywheel rotational speed. The corresponding root locus between 1RPM and 4910RPM was presented in Fig. 4.4. Fig. 4.5 shows the amplified root locus near the imaginary axis. It can be seen that the system has unstable poles. These poles are caused by the usage of notch filters at low frequecies. Since notch filters were used to isolate imbalance and runout errors at high speed, they can be cut off at low frequecies. Fig. 4.6 shows the zoomed in root locus for system with notch filter between 2900RPM and 4910RPM. This plot proves that the usage of notch filter when the rotor speed is high won't affect the closed system stability.

The notch filters were then totally removed for the system equation and the closed loop modal frequencies were plotted against the rotational speed as in Fig. 4.7. The dashed line in the plots identifies the flywheel rotating speed. As shown in this plot, the closed loop system modal frequencies do not coincide with the rotating speed between 266 rad/s and 514 rad/s. This means the system don't have resonance caused by syncronous frequecy between 2541RPM and 4910RPM. A speed variation between 2541RPM and 4910RPM is equavalent to a energy discharge depth of 73.2%. Fig. 4.8 presented the root locus of the system. Fig. 4.9 and Fig. 4.10 show the zoomed-in part of the root locus near the imaginery axix. The pole closest to the imaginery axis in Fig. 4.10 is -3.882 + 14.465i, which has a damping ratio of 0.26. This proves the closed

loop system stability.

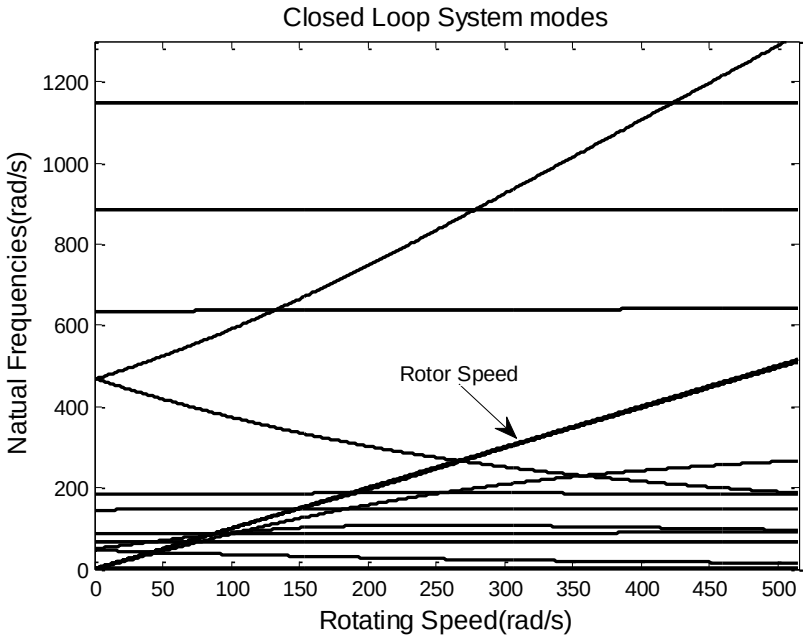

Fig. 4.3 Closed Loop System Modal Frequencies with Notch Filter

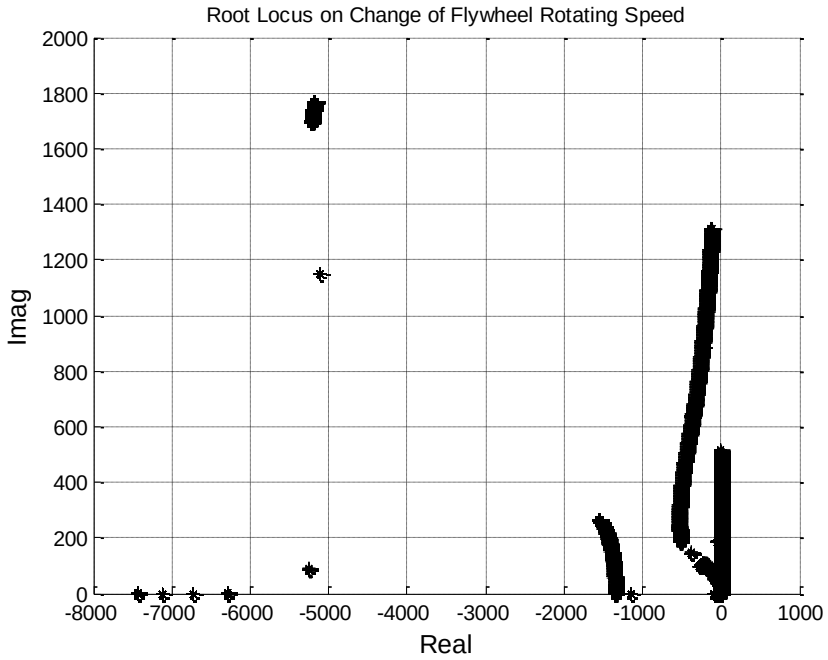

Fig. 4.4 Root Locus of Closed Loop System with Notch Filter

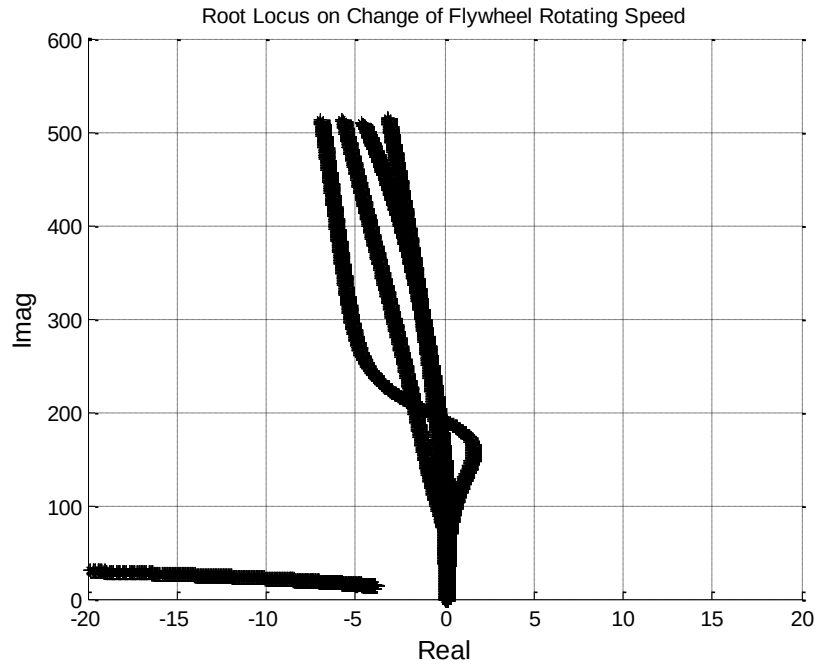

Fig. 4.5 Zoomed in Root Locus of Closed Loop System with Notch Filter

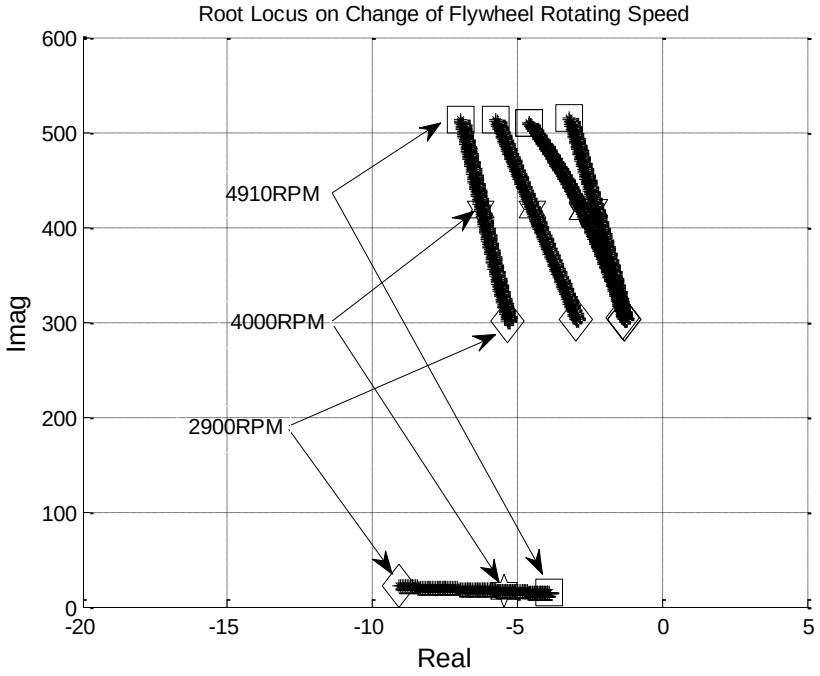

Fig. 4.6 Zoomed in Root Locus of Closed Loop System between 2900RPM and 4910RPM with Notch Filter

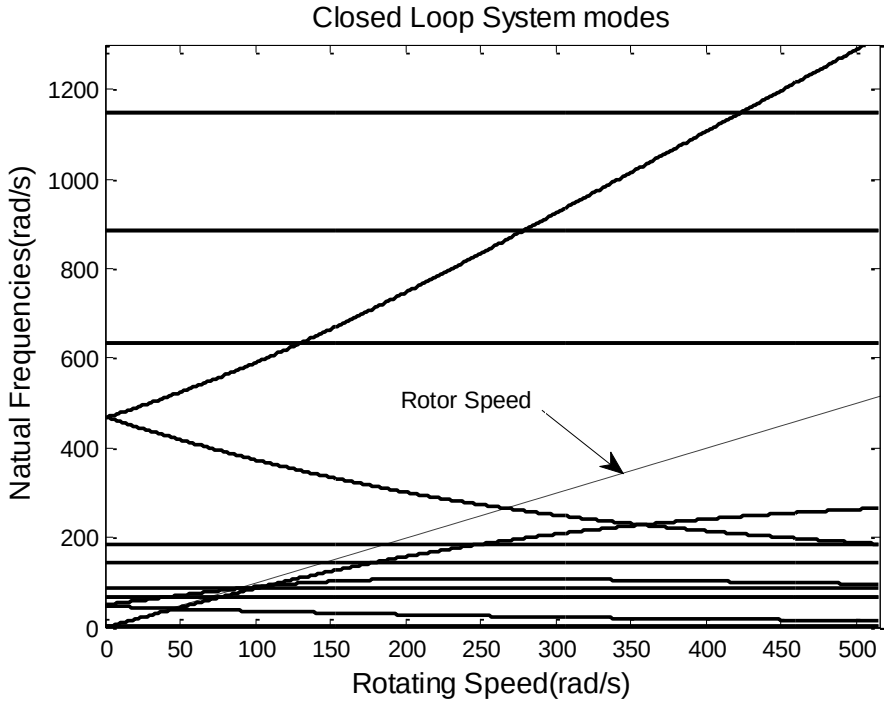

Fig. 4.7 Closed Loop System Modal Frequencies without Notch Filter

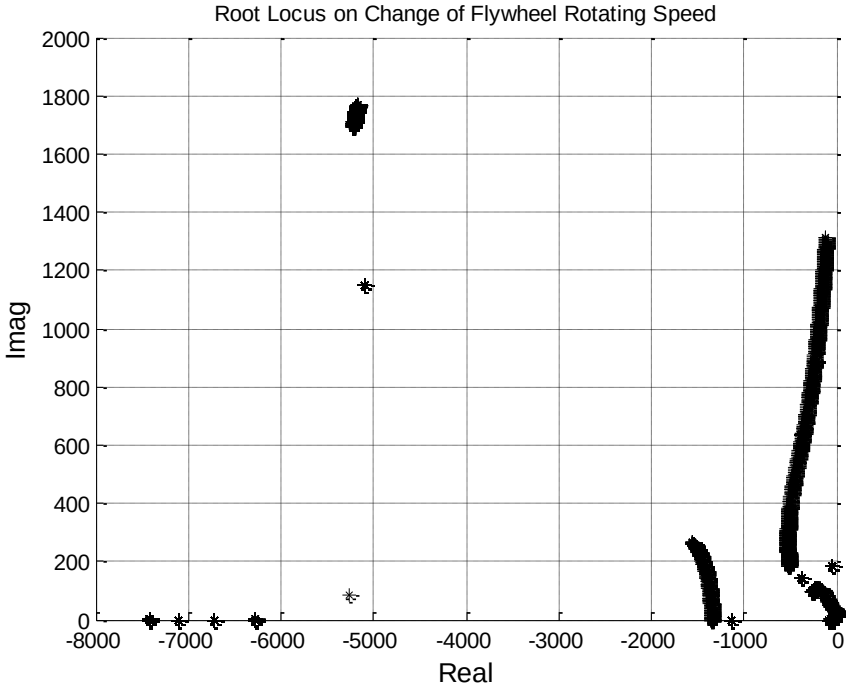

Fig. 4.8 Root Locus of Closed Loop System without Notch Filter

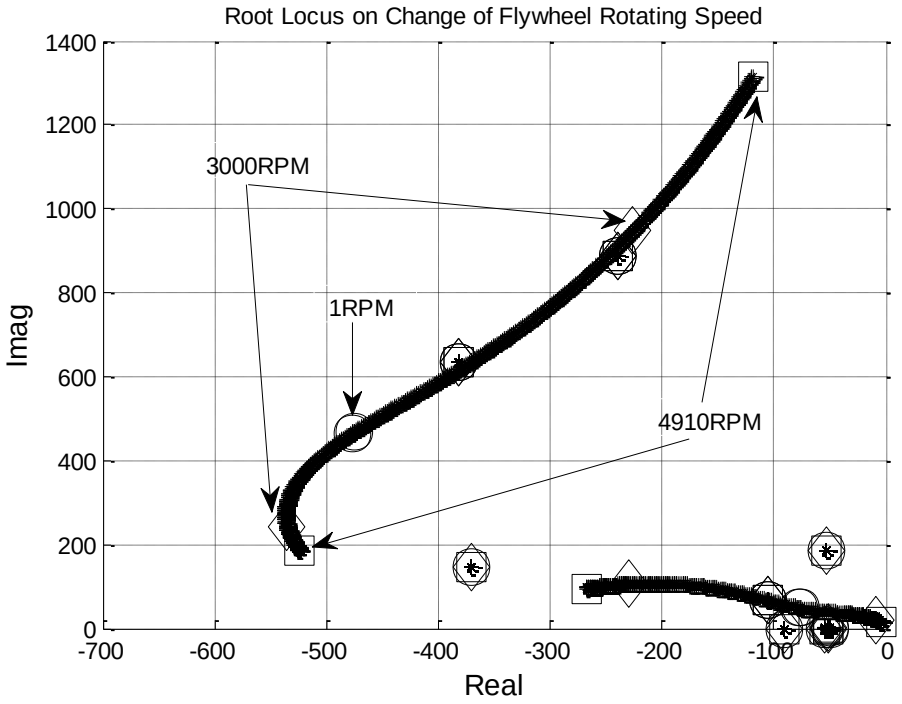

Fig. 4.9 Zoomed in Root Locus of Closed Loop System without Notch Filter

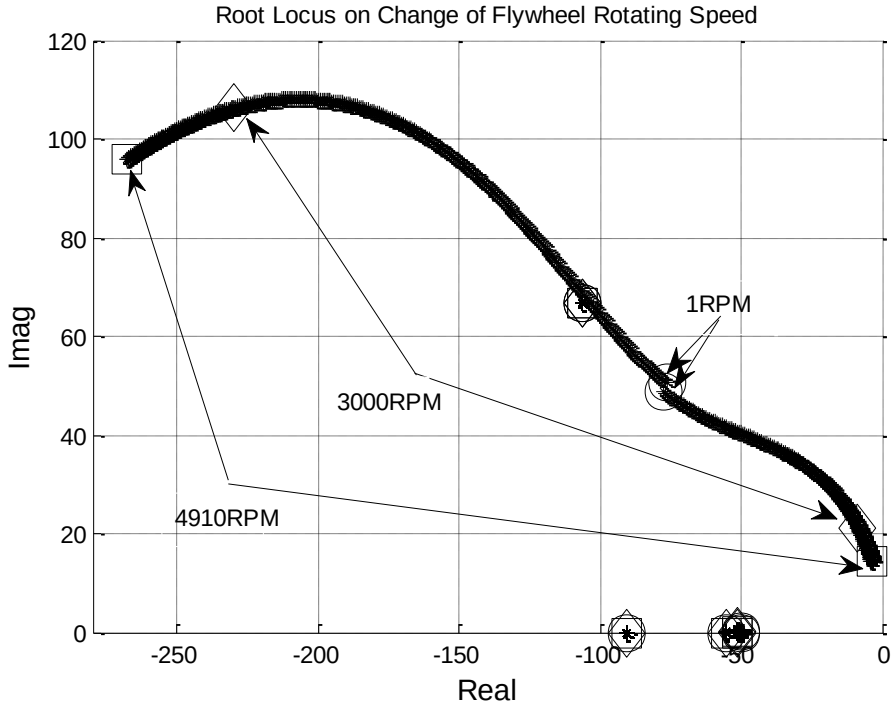

Fig. 4.10 2nd Zoomed in Root Locus of Closed Loop System without Notch Filter

4.4 Conclusion

The frequency weakening effects due to eddy currents on the magnetic bearing current stiffness were analyzed and simulated using ANSYS™ harmonic analysis. The resulted transfer functions were curved fitted and presented with LABVIEW™. After this, the closed loops control system equations were setup to study the stability of the system. The results proved that using notch filters when flywheel rotating speed is high will not affect stability of the whole system. It was also proved that the system is controllable and stable even with the introduction of the frequency weakening effects of the magnetic bearing stiffness. This eventually proves our novel magnetic bearing design is controllable and stable even with the unlaminated structure.

CHAPTER V

MAGNETIC BEARING LOSS, MOTOR CONCEPT AND EQUILIBRIUM TEMPERATURE WITHIN VACUUM

5.1 Overview

The bearing losses due to eddy effect and magnetic hysteresis property of the material used will be discussed in this chapter. This data marks the losses caused by magnetic bearings at their nominal positions.

To minimize the windage loss of the flywheel, the energy storage system will be vacuumed. This may sometimes lead to some thermal problems since radiation will be the only way of heat dispense. The bearing loss and assumed motor loss were used to simulate the energy storage equilibrium temperature with radiation as the only way of heat exchange.

The concept of a novel motor design will also be introduced in this chapter.

5.2 Magnetic Bearing Loss

5.2.1 Eddy Loss

Motion induced Eddy currents will generate heats on the rotor surface. This is the source of the eddy loss of magnetic bearings and is very important for high speed operations. To solve the FEM equations with velocity effects using Eq. 3.30, oscillations were commonly seen in the direction of motion. Peclet number was introduced to quantify how unstable a solution maybe. The Peclet number is changing with both physical parameters of the material and the element sizes. It can be defined as:

$$\gamma_p = \mu\sigma v h \tag{5.1}$$

where μ is the absolute permeability, σ is the absolute electric conductivity, v is the velocity and h is the element height in the velocity direction.

The problem tends to become unstable when the Peclet number γ_p exceeds two [45]. Methods to solve the oscillation of the solution include reducing the mesh size and using an upwinding method to solve the problem. They are discussed in details in [46]. However, due to the license limitation, computing power limitation and the scale of the flywheel, a Peclet number less than 2 is a target hard to fulfill. This is why a FEM motor code written by Vector Fields™ was used to calculate the eddy loss due to rotation. The software package name is CARMEN™, which can calculate the rotor eddy losses caused by rotational motions. This is a transient code which calculates the instantaneous distribution of the magnetic and electric field within the system at each rotational angle defined by the meshes. These values will be used to calculate the eddy loss power at each rotational angle. The rotor needs to be meshed so that it will be divided evenly in the circumferential direction. The rotational motion was defined by setup a slippage surface which resides between air layers of elements and separates the rotor and stator.

To fulfill the requirement of the CARMEN™ modeling, approximate models of axial and radial bearings were set up. For axial bearing, the CARMEN™ approximate model was constructed as an annular ring rotating below two poles. The rotor outer radius equals to the axial bearing position so that the circumferential velocity is same at 4910RPM. The total flux in axial direction retrieved by ANAYS™ static analysis was first calculated. Then flux density used in CARMEN™ analysis was set by achieving an

equal or higher total flux value than the value calculated from the real axial bearing poles. The approximate model of the axial bearing is as in Fig. 5.1.The dimensional figures are in millimeter. The relative permeability used is 100. The conductivity used is 4000/ohm-mm. The magnetic field was excited by a circular coil defined by current density. The resulted field was as shown in Fig. 5.2.To have a conservative value, 5000RPM of rotational speed was used instead of the projected running speed of 4910RPM.The power loss value plotted vs. rotational speed is as shown in Fig. 5.3. As can be seen, the eddy loss value tends to converge to a quasi-static value less than 90 Watts.

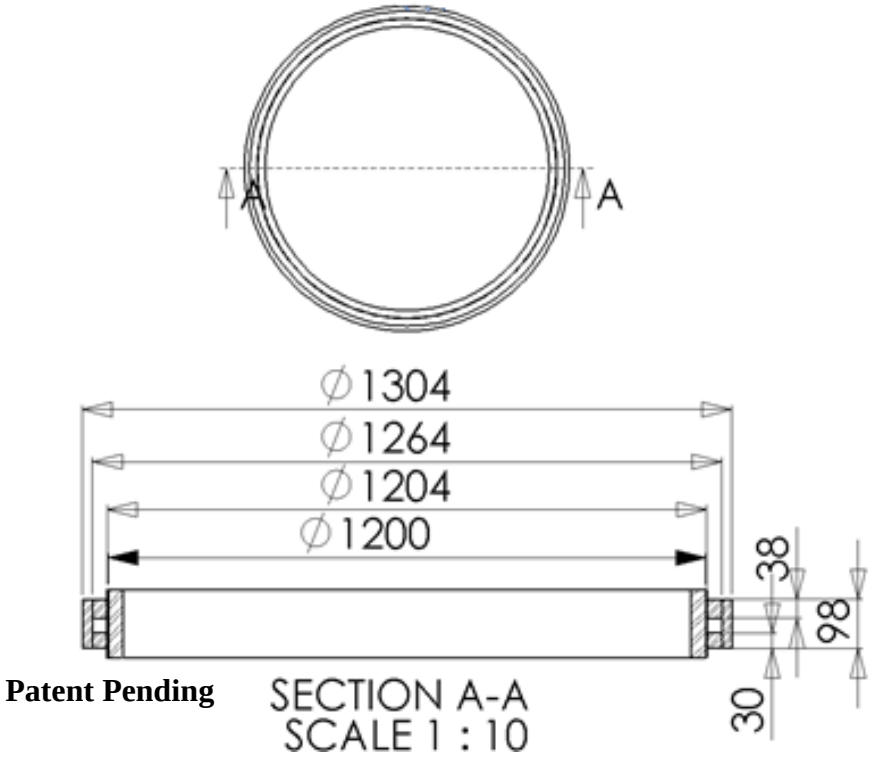

Fig. 5.1 Axial Bearing Approximate Model in CARMEN™

The radial bearing model for the CARMEN™ calculation used the same dimensional settings as the real radial bearing will be. It is as shown in Fig. 5.4.According to the static analysis using ANSYS™, the flux density variation in the air between dovetail poles and inner surface of disk step should be between 0.2 to 0.37 Tesla. The flux density variation between circular radial poles and outer surface of disk step will be 0.27-0.3 Tesla. Fields were generated so that the flux density values in the CARMEN™ model will have a similar/little bit bigger variation ranges but much higher DC offset values as shown in Fig. 5.5 and Fig. 5.6. This is done on purpose to have more conservative evaluation of losses data on the radial bearings.

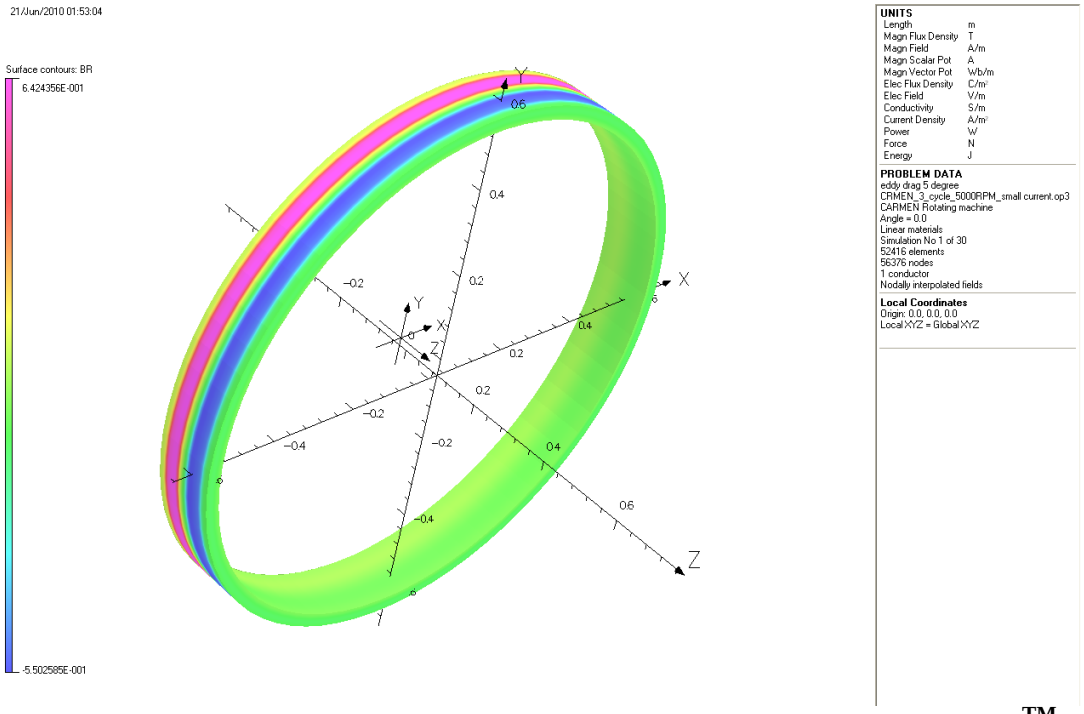

Fig. 5.2 Axial Bearing Approximate Model Flux Density in CARMEN™

Since CARMEN™ limits the slipping surface count to one, we separate the radial

bearing loss simulations into two parts. First the dovetail radial bearing poles will rotate with respect to the other parts of the bearing at 5000RPM. The eddy loss values vs. the rotational angles experienced by the rotors was as presented in Fig. 5.7 .After this, the circular radial bearing poles was programed to rotate at 5000RPM. The eddy loss value is as shown in Fig. 5.8. As are in the above results, the dovetail poles' rotation case will result an eddy current loss less than 170 Watts. The circular radial bearing poles' rotation will cause eddy current loss less than 6 Watts. Considering the 90Watts loss of axial bearing, a conservative eddy loss value for the whole magnetic bearing structure will be 90+170+6=266Watts. This is the loss data for a rotational speed of 5000RPM. The value should be even lower at our designed flywheel rotational speed of 4910RPM.

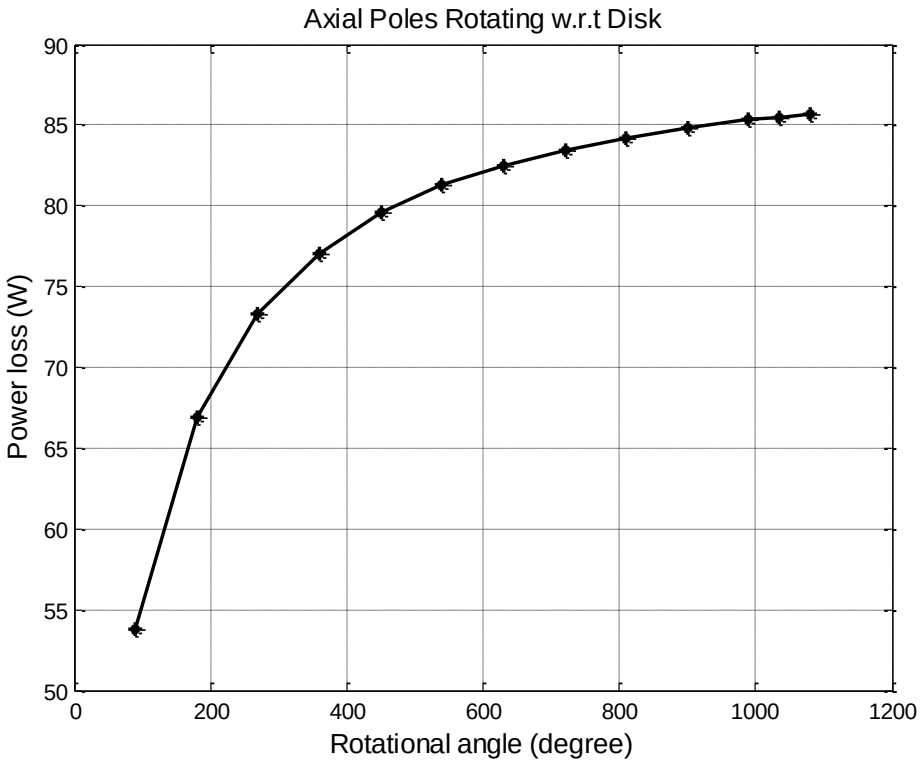

Fig. 5.3 Approximate Axial Bearing Loss at 5000RPM with CARMEN™

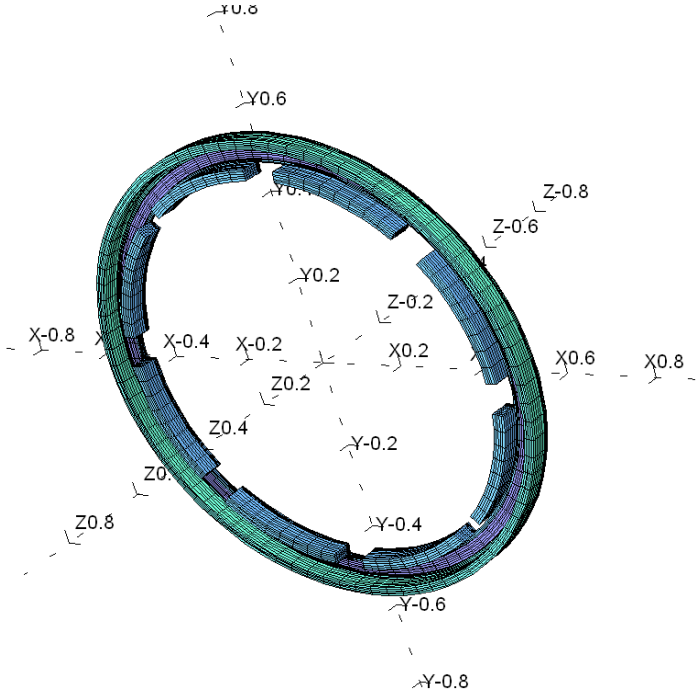

Fig. 5.4 Radial Bearing Model in CARMEN™

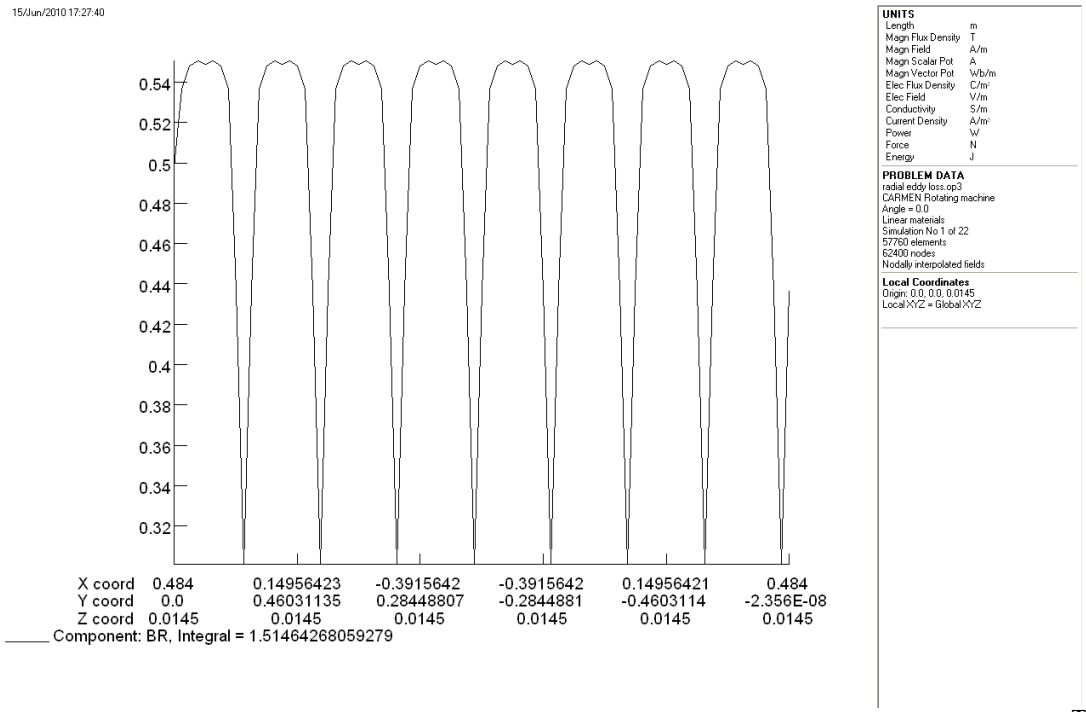

Fig. 5.5 Flux Density at Center of Air Facing Dovetail Radial Poles in CARMEN™

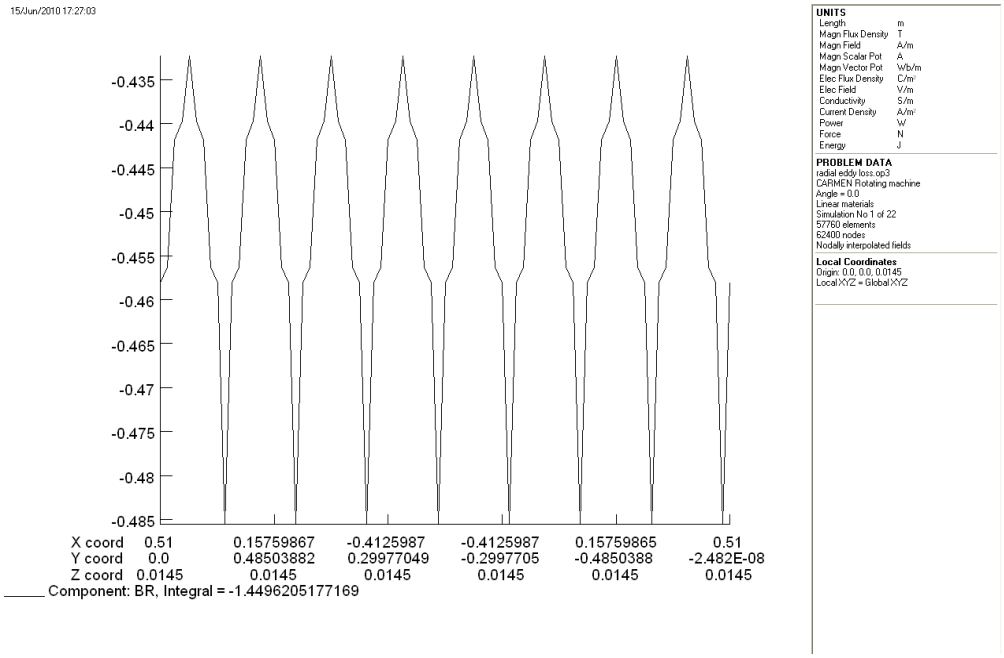

Fig. 5.6 Flux Density at Center of Air Facing Circular Radial Poles in CARMEN™

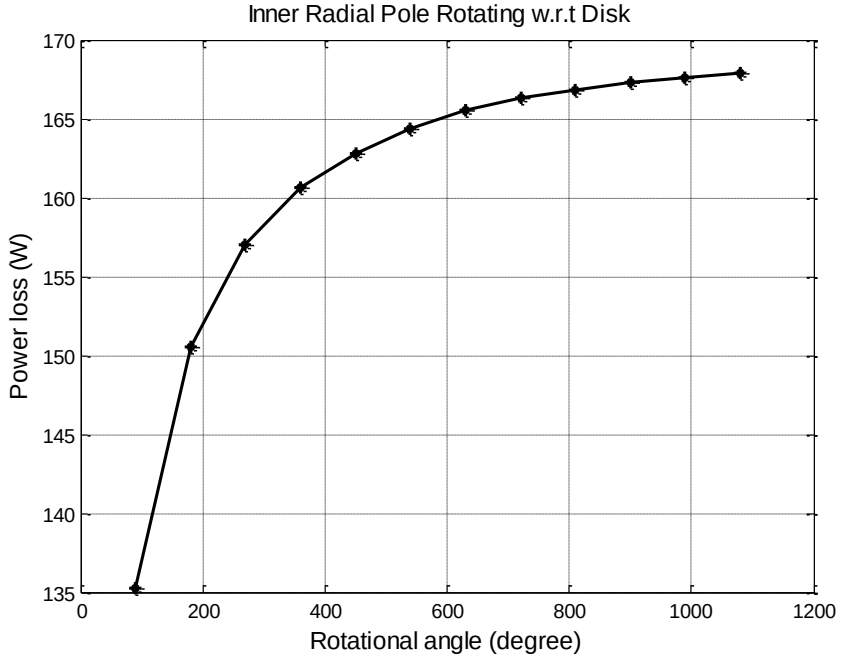

Fig. 5.7 CARMEN™ Losses Simulation with Dovetail Radial Pole Rotating

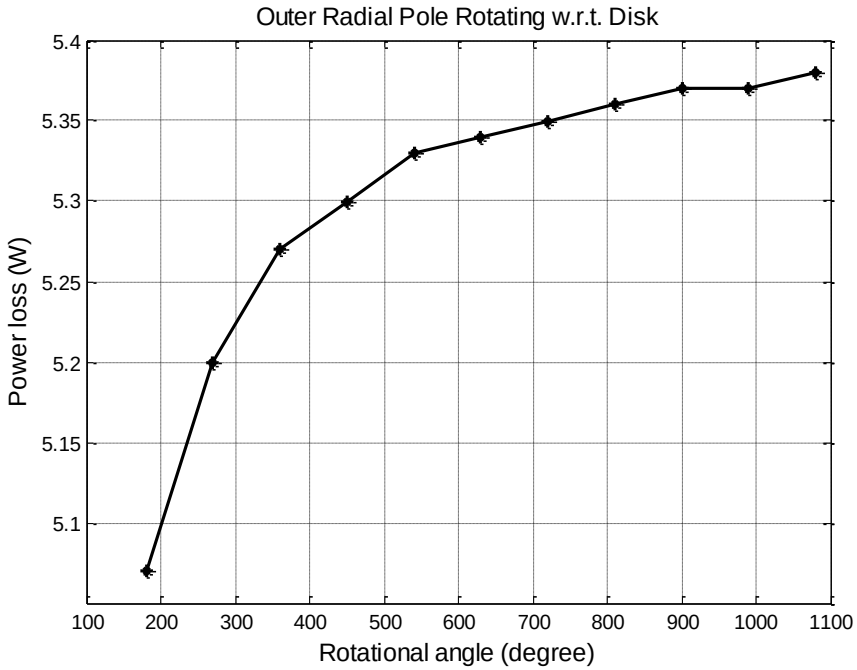

Fig. 5.8 CARMEN^{TM} Losses Simulation with Dovetail Circular Pole Rotating

5.2.2 Hysteresis Loss

Another source of loss for magnetic bearings comes from the hysteresis characteristics of magnetic materials. The value of the loss depends on the material property, the DC and AC variation of the flux density value, and the magnetize/demagnetize loop frequency (field changing frequency). To calculate the hysteresis loss of the magnetic bearings, only radial parts need to be considered since the axial bearing flux field variation is zero at the nominal position.

The test rig shown in Fig. 3.6 was used to retrieve the BH hysteresis loop under the operating conditions. As stated above, from the static analysis of the magnetic bearings, the disk rim surface on the inner radial bearing side (dovetail) will experience a flux density variation between 0.2-0.37Tesla. The disk rim surface on the outer radial bearing

side (circular) will experience flux density fluctuation of 0.27-0.3 Tesla. Using the test rig in Fig. 3.6, the AC hysteresis loop at 0.2Hz was retrieved using the flux density range values stated above. 0.2Hz excitation was selected so that the eddy current effect on measurement results can be neglected. LABVIEW^{TM} was used to serve the purpose of the data acquisition and save the data into EXCEL^{TM} format. MATLAB^{TM} program was then used to process the data using Eq. 3.1-Eq. 3.3, The results are presented in Fig. 5.9 and Fig. 5.10.

The area within the experimental hysteresis loop will be the loss for one flux cycle per volume of the magnetic material. The unit for this data is Joule/m^3. Since the radial bearing has 8 poles, the rim surface will experience 8*5000/60 flux variation cycles each second when the rotor is rotating at 5000RPM. The AC fluxes in our magnetic bearing design will mostly be contained within the disk step volume. Even though the AC flux variation changes along the radial position on the disk step rim, we can assume both the inner and outer radial bearing flux density occupies half of the rim in radial direction. This should give us a conservative estimate of the hysteresis loss the bearing will experience since the losses are in higher order relationship with flux density. Also considering the area under each side of the bearing, the volumes of the hysteresis loss regions were calculated. Using MATLAB^{TM} to retrieve the area of the hysteresis loop by integrating on Fig. 5.9 and Fig. 5.10, the hysteresis loss for inner and outer radial bearings at 5000RPM were 48.12 Watts and 0.464 Watts, respectively.

Considering both the eddy current losses and the hysteresis loss at 5000RPM, a conservative estimation for the total power loss of the magnetic bearings can be

calculated as 315 Watts. This loss value will be applicable when the 4340 rotor rests at the nominal position, which is the most common case when the system is in equilibrium state of its operation.

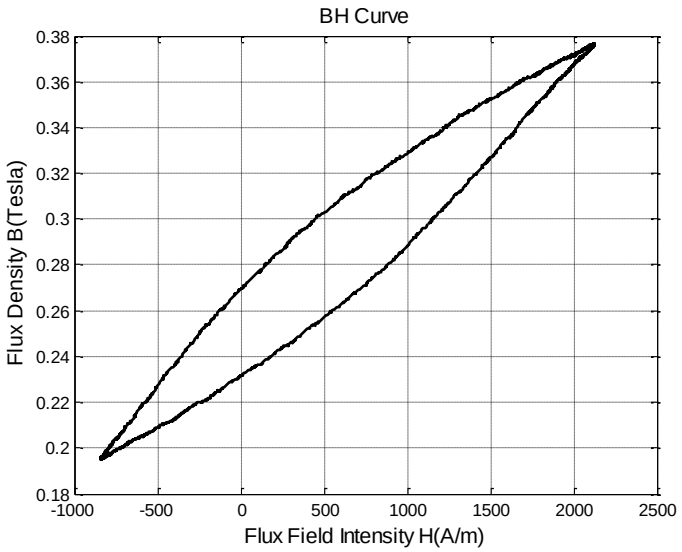

Fig. 5.9 Hysteresis Loop at 0.2Hz with B=0.195-0.376Tesla (Dovetail Radial Poles)

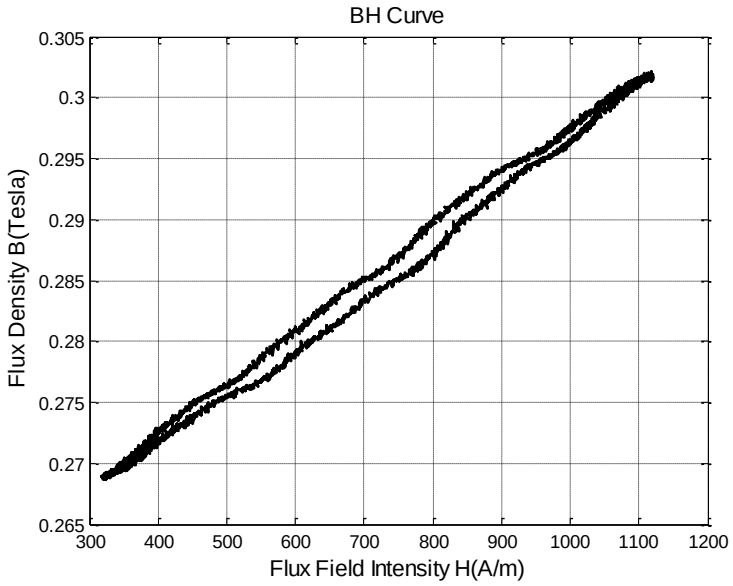

Fig. 5.10 Hysteresis Loop at 0.2Hz with B=0.269-0.302Tesla (Cicular Radial Poles)

5.3 Motor Concept Design for the Energy Storage System

A novel concept of motor was proposed to fit the need of the novel energy storage system. The rotor of the motor will be constructed with surface mounted magnets near the outer edge of the flywheel. The stator will be able to drop in/out from the motor magnetic field as shown in Fig. 3.5.

This design concept has multiple benefits over the traditional ones. Some of the most important ones are:

1. Traditional design requires a shaft to hold the motor's rotor assembly, which is not available in our solid design flywheel. The novel design of rotor utilizes surface mounted magnets, which fits perfectly with our shaft-less structure.
2. By moving the stator in and out, the Motor/Generator Constant can be changed by changing the stator coil length immerged in the magnetic field of the motor magnets. This control capability is essential for the optimization of the flywheel energy charging and delivery. One of the applications is the optimization of regenerative braking for trains as will be shown in the later chapters.
3. When the energy storage system is not in the charge/discharge phase, the stator coil can be totally lifted away from the motor magnetic field. This capability totally eliminates the motor loss when it is not in operation.

A simple model of the motor's rotor section with magnets was shown as in Fig. 5.11 and Fig. 5.12. The disk was made of 4340. The magnet used was N48 and magnetized in

radial direction. They were placed in such a way that the neighboring ones will have different polarization direction. The air slot for the stator coil is 30mm in the radial direction.

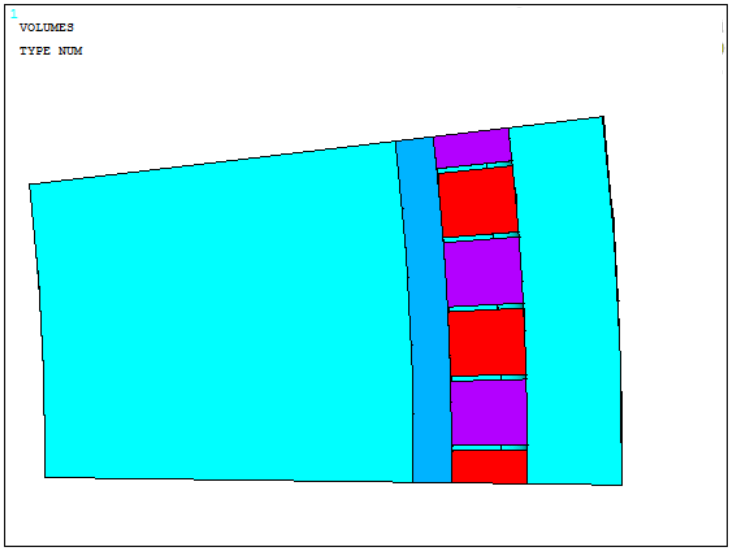

Fig. 5.11 Model of Rotor Section of the Novel Motor Concept (Top View)

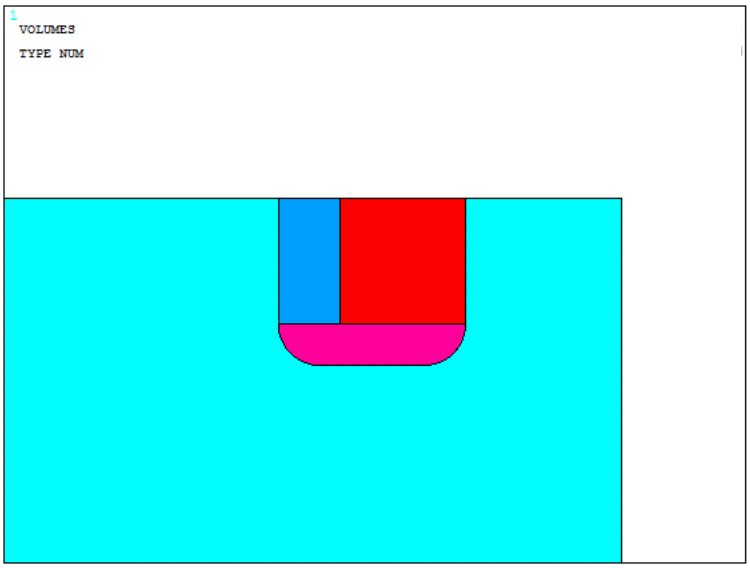

Fig. 5.12 Model of Rotor Section of the Novel Motor Concept (Side View)

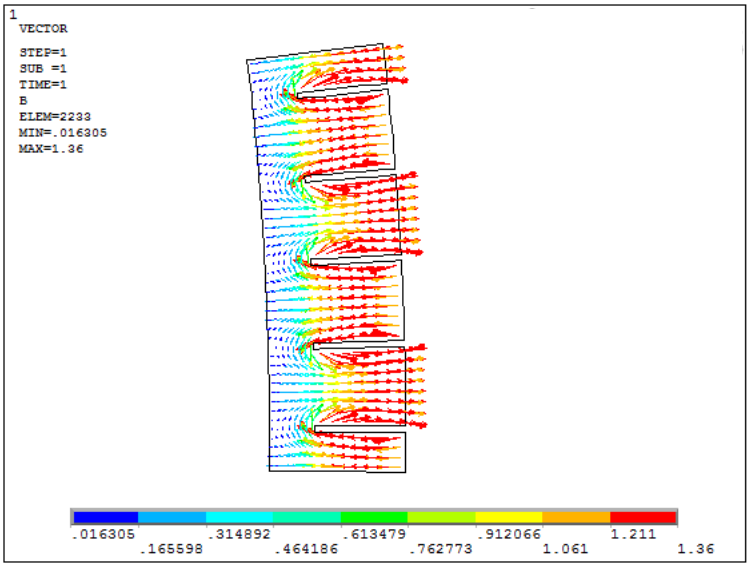

Fig. 5.13 Vector Plot of Magnet Flux Density within Motor Air and Magnets

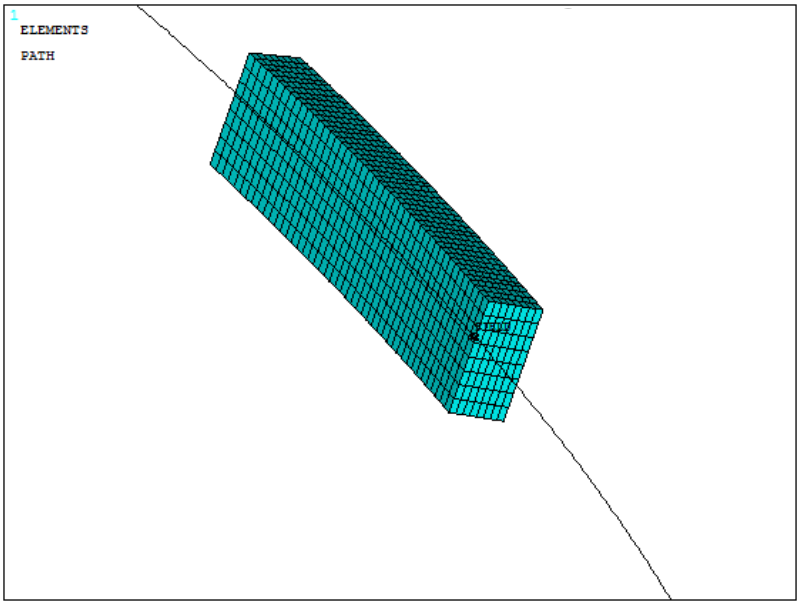

Fig. 5.14 Plot Path at the Center of Motor Air Slot

The flux density within the motor air and permanent magnets are as shown in Fig. 5.13. A path at the center of the motor air slot was created in ANSYS^{TM} as

Fig. 5.14. The flux densities along this patch were plotted as a reference to the flux density values that the motor stator coil will face during operation. The curves are as shown in Fig. 5.15. The result coordinates were changed to cylindrical one so that the Bx curve stands for the radial components of the flux densities. The radial component will be the one that will generate electricity within the stator coil. The amplitude for the radial flux density curve is 0.332Tesla.

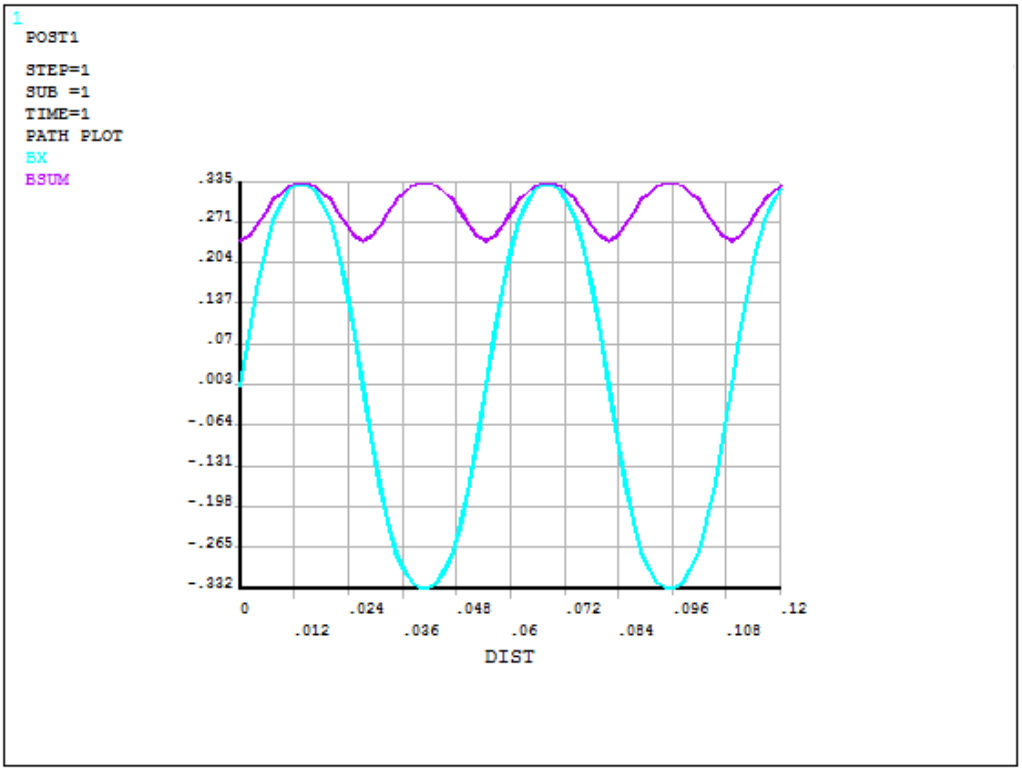

Fig. 5.15 Flux Densities at the Center of Motor Air Slot

Assuming there are totally 240 pieces of magnets (1.5 degrees for each), the stator coil radius is 1.0425m and the coil length in the field is 0.03m, the peak torque can be calculated using:

$$\tau_{M\_p} = N_{M\_coil} B_{M\_p} I_{M\_coil} L_{M\_coil} R_{M\_coil} \quad (5.2)$$

The calculated peak torque for the single coil is $\tau_{M\_p} = 249.20\text{Nm}$. The EMS value for the torque of the single phase coil will be $\tau_{M\_ems} = \tau_{M_p}/\sqrt{2} = 176.21\text{Nm}$. For a three phase motor, the total EMS torque will be $\tau_{M\_ems} = 528.63Nm$. The effective motor/generator constant for the each single phase will be $K_{M\_i} = 1.76Nm/A$. The maximum motor/generator constant can be increased in several ways:

1. Utilize multiple windings at each phase so that there will be multiple sections of stator coil for the same phase under each piece of magnet. This would effectively multiple the original N_{M_coil}.
2. Position the stator coil closer to the magnets assembly at the outer radius of the flywheel.
3. Increase the maximum stator coil immerging depth by increasing the motor slot depth.
4. Use Stronger magnets to generate greater motor field
5. Use a transformer at the outputs of the stator coils. This will effectively increase the motor/generator constant but decrease the effective maximum operational current limits.

To illustrate the effectiveness and importance of the variable motor/generator constant, a grid charging simulation on our designed flywheel was carried out to compare different cases. The maximum grid voltage was clamped at 500 Volts. There will be three phases in the motor. Each phase will have a maximum current capability of

200 Amps.

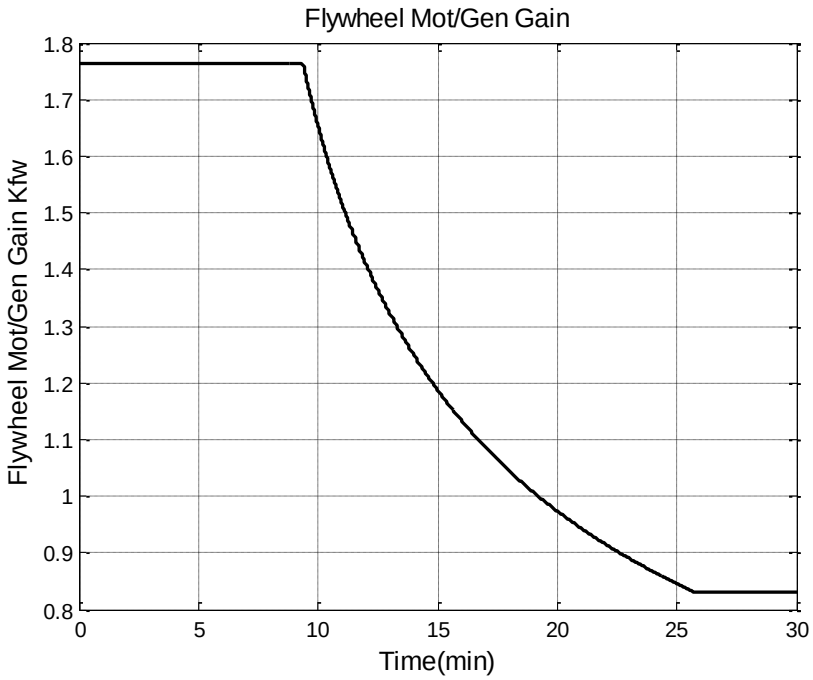

Fig. 5.16 Flywheel Mot/Gen Constant during Constant Current Grid Charging

First the grid charging using constant, maximum allowable current was simulated. This method cannot be realized without a variable Mot/Gen constant since the flywheel rotating speed will reach a threshold value that generate back EMF so high that the grid voltage cannot charge the flywheel anymore. This K_{fw} variation during the whole process can be seen as in Fig. 5.16. It took around 26 minutes for the flywheel to get fully charged. The flywheel speed and energy changes during the whole process were as in Fig. 5.17 and Fig. 5.18. The flywheel voltage was as in Fig. 5.19. As can be seen, the flywheel voltage stays at a constant value after the initial charging phase. This is realized by varying the Mot/Gen constant to keep the maximum charging current with a limited grid voltage value. Fig. 5.20 gave the corresponding torque value for the whole process.

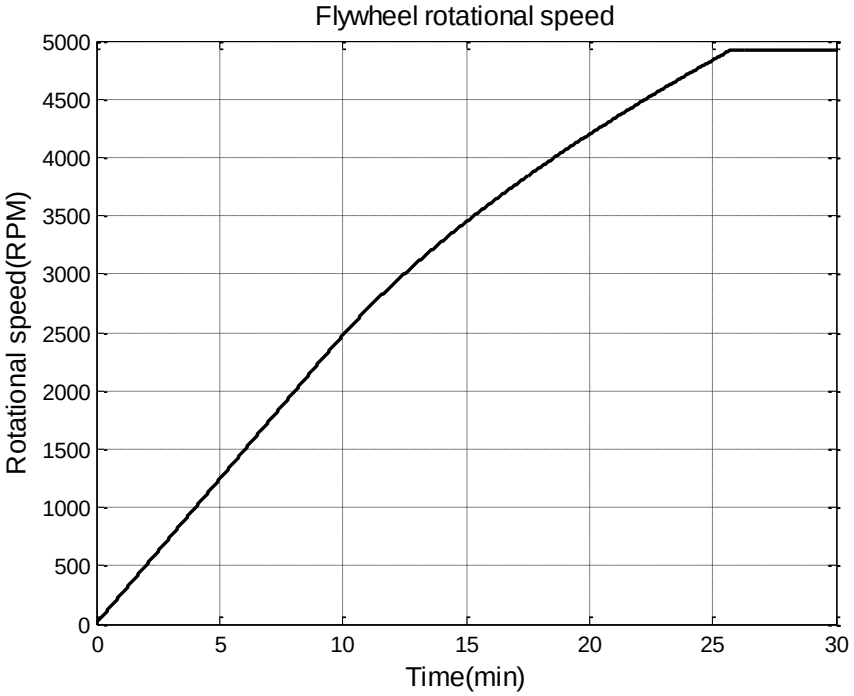

Fig. 5.17 Flywheel Speed during Constant Current Grid Charging

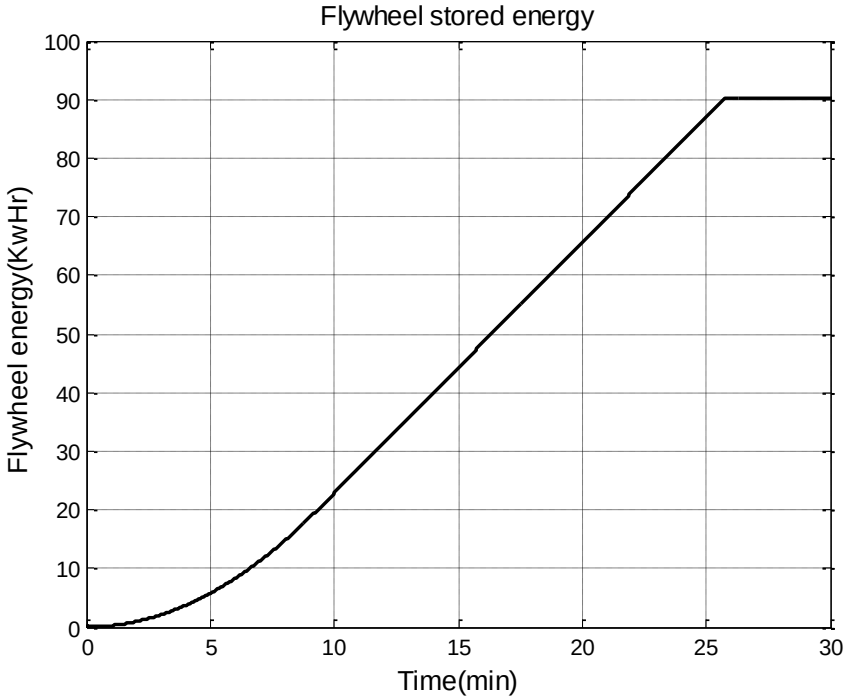

Fig. 5.18 Flywheel Energy during Constant Current Grid Charging

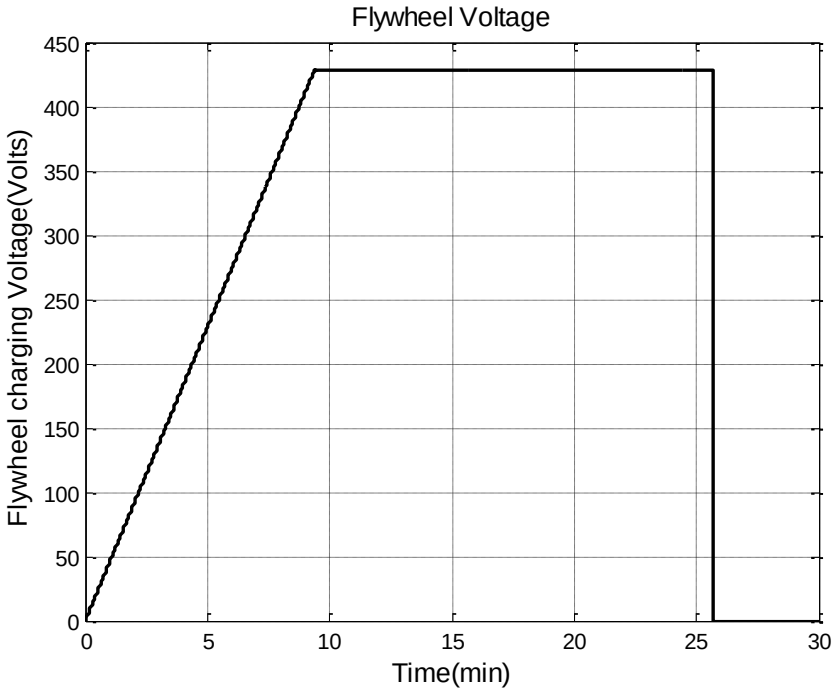

Fig. 5.19 Flywheel Voltage during Constant Current Grid Charging

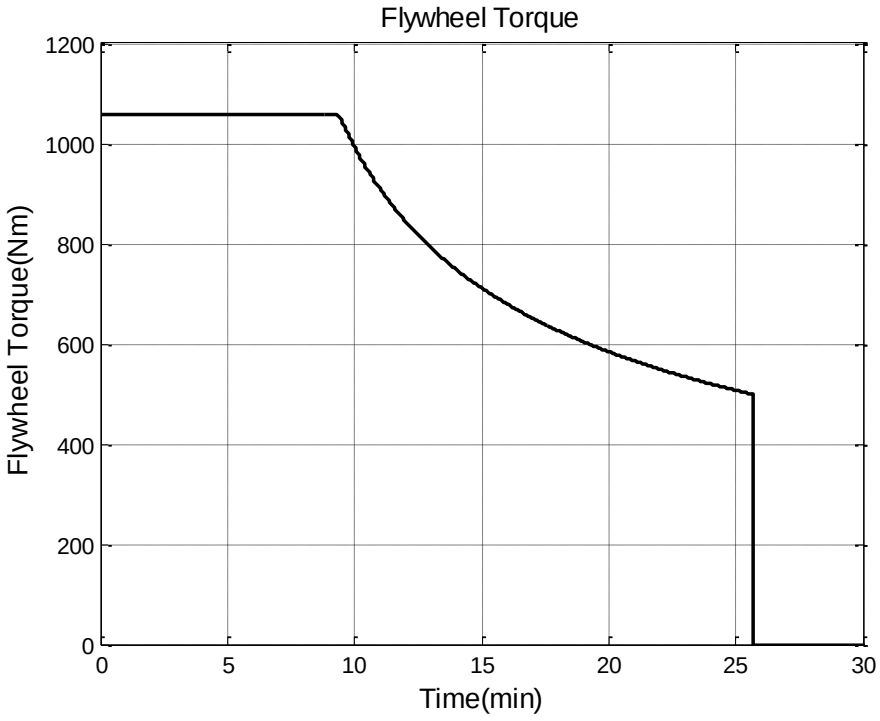

Fig. 5.20 Flywheel Torque during Constant Current Grid Charging

To show the advantage of the varying Mot/Gen constant design, grid charging cases for different, fixed constants were carried out. During the simulations, it was find that if some higher Mot/Gen constant will not allow the flywheel to be fully charged to 90kWh since the back EMF got higher than the grid voltage at an energy level much lower than the target. The Corresponding flywheel energy after the grid charging process can be seen as in Fig. 5.21. The time for the flywheel to be charged to the maximum value in the process was plotted as in Fig. 5.22. As can be seen in the plot, for the fixed Mot/Gen constant grid charging to achieve 90kWh flywheel energy, the minimum charge time given by the optimum constant value will be around 40 minutes. It is much longer than a constant current charging case as shown above.

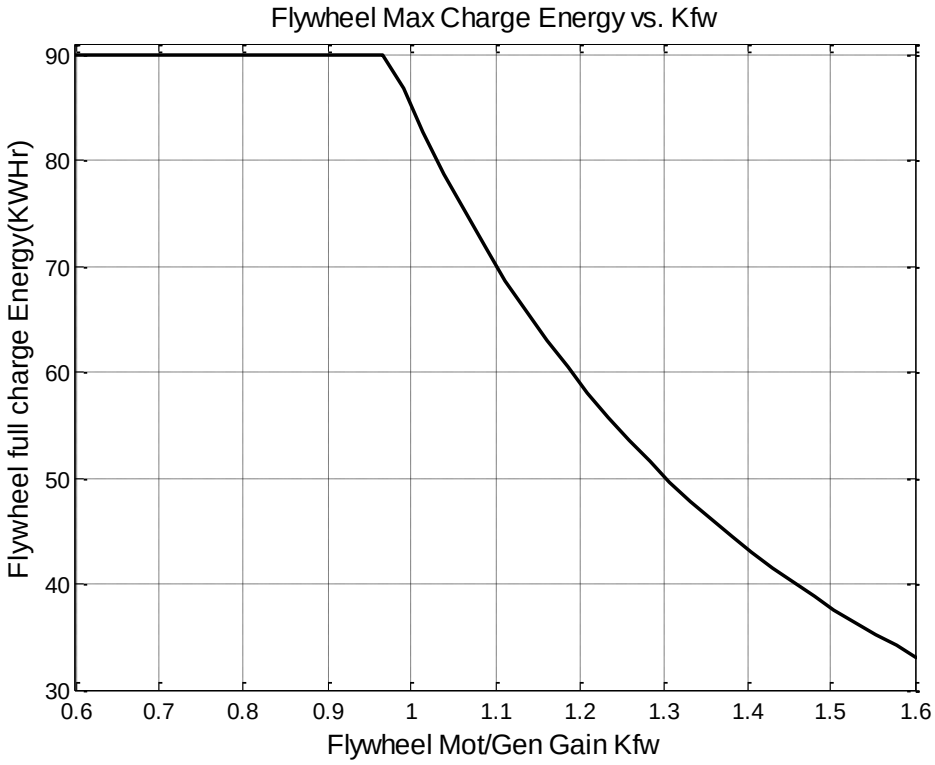

Fig. 5.21 Final Flywheel Energy for Grid Charging with Fixed Mot/Gen Constant

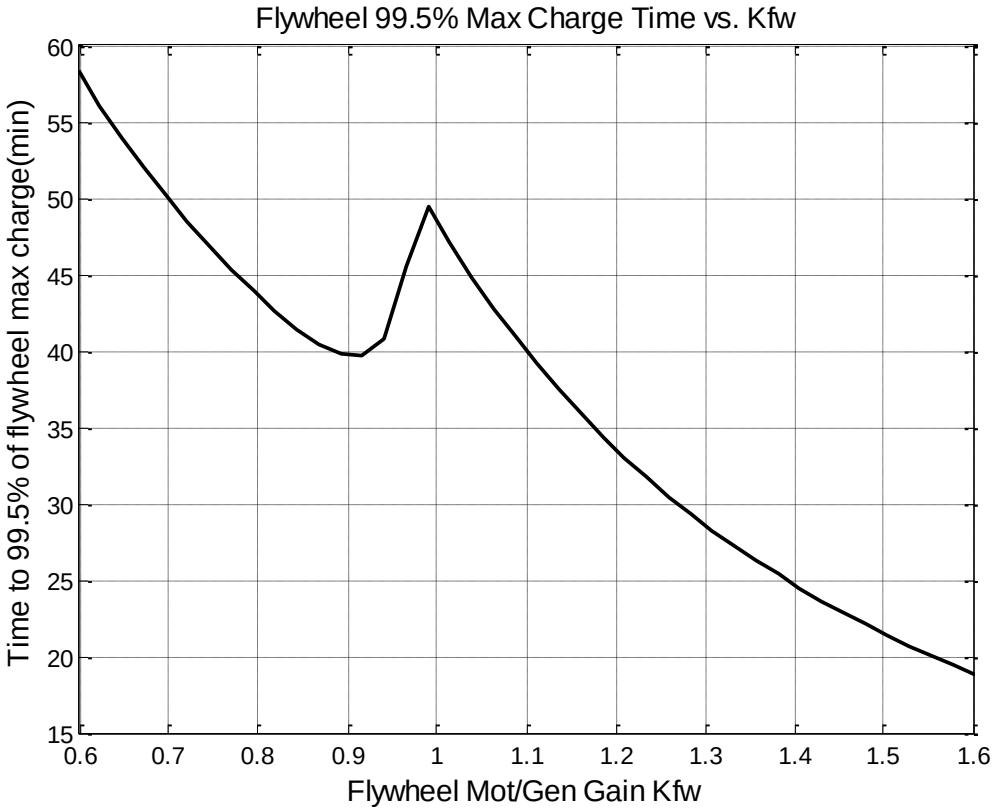

Fig. 5.22 Flywheel Charge Time for Grid Charging with Fixed Mot/Gen Constant

In conclusion, the variable Mot/Gen constant concept has much better performance than the traditional fixed constant design. First the variable design will always allow the flywheel to be fully charged to 90kWh while the fixed Mot/Gen constant cases can reach the target only for a limited range of constant values. Secondly, the charge time for the variable Mot/Gen constant case is much shorter even than the case where the most optimum fixed Mot/Gen constant was chosen.

5.4 Flywheel Equilibrium Temperature under Radiation

The flywheel will rotate in a vacuum condition to eliminate the windage loss for the system. This vacuum configuration might pose a problem for the cooling of the system

since radiation will primarily become the only way of heat exchange between the flywheel and the outer environment. Since both the eddy bearing loss and the eddy motor loss will generate heat on the flywheel, a study needs to be carried out the find out what the equilibrium temperature will be. To enhance the radiation heat exchange capability of the system, sprays will be put around both the flywheel and inner surfaces of the flywheels surrounding structures. The commercially available sprays can easily raise the emissivity of the surface to a value of 0.9. So we used an emissivity of 0.8 on both surfaces of our simplified 2D thermal radiation model to have a conservative evaluation of the problem.

A 2D axisymmetric model was setup in ANSYS^{TM}. The steady state temperature for the disk under radiation with only magnetic bearing losses (315 Watts) is as seen in Fig. 5.23. The y-axis is the rotating axis (symmetry axis) of the flywheel. The environmental temperature around the flywheel casing was set to be 22 Celsius (71.6 Fahrenheit). As can be seen, the highest temperature on flywheel is 32.5 Celsius when there is only magnetic bearing loss. This is a representative case when the motor is not in operation and the motor stator coil was lifted up (zero motor loss).

Fig. 5.24 presented a case when the motor is in operation and the heat caused by eddy current is 2kW (2% loss of a 200kW motor). As can be seen in the results, the final temperature of the flywheel will not exceed 72 Celsius, which is well below the specifications for the magnets that we used.

In conclusion, the thermal radiation analysis proves that our design will have an equilibrium temperature well within the operational specifications, with a 315 Watts

bearing loss and a 2kW motor loss.

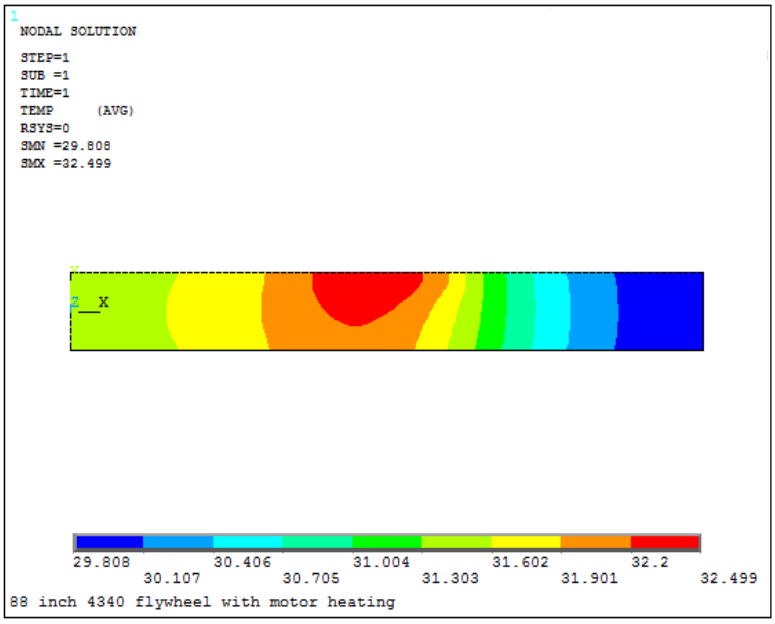

Fig. 5.23 Flywheel Temperature with Magnetic Bearing Loss

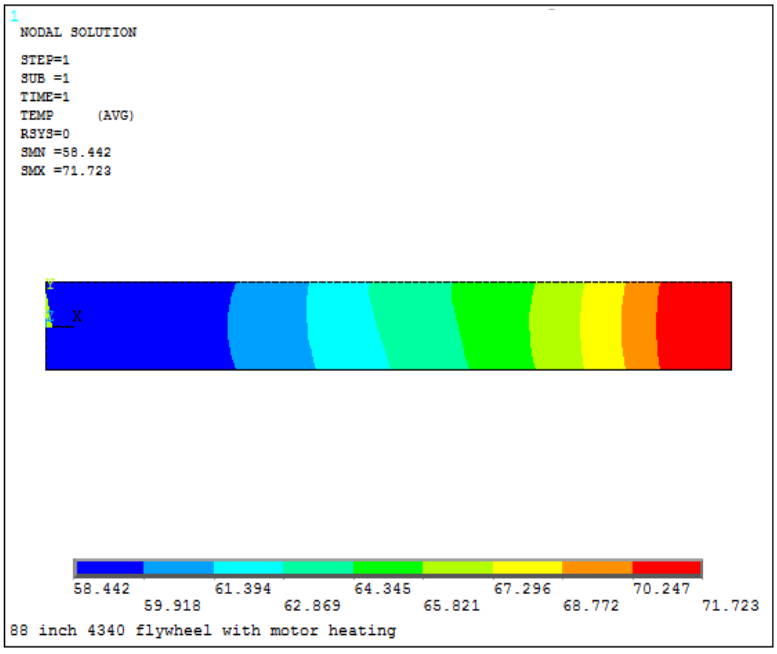

Fig. 5.24 Flywheel Temperature with Magnetic Bearing Loss + Motor Loss

5.5 Conclusion

The chapter begins with discussing the calculation of the losses for our magnetic bearing design. The eddy loss was retrieved via CARMEN^{TM} motor FEM simulation on approximate models of our bearing. The hysteresis loss was calculated based on experimental measurement on the 4340 sample ring available to the author. A conservative estimate of 315 Watts total loss was predicted for our magnetic bearing design. Given our designed energy storage capability of 90kWh, the storage system will have about 0.35% loss rate in one hour. The actual loss value will become smaller as the flywheel speed reduces due to the dependency of the eddy and hysteresis loss on spin speed.

After that, a novel concept design of motor/generator was proposed. The most significant feature of this design is the capability to vary the Mot/Gen constant in real time during the operation of the flywheel. This gives us the capability to control charge/discharge behavior of our energy storage system. A preliminary analysis was carried out on an example design. The maximum Mot/Gen constant was calculated based on ANSYS^{TM} static magnetic simulations. Based on the results, grid charging cases was studied. It was found the variable Mot/Gen constant motor have at least two big advantages over the invariable case. First, the flywheel can be guaranteed to be charged to our target value of 90kWh. Only a limited range of fixed Mot/Gen constant case can be charged to this target (flywheel back EMF went beyond the grid voltage). Second, the variable Mot/Gen constant case can realize the constant current charging algorithm, which will have a far shorter charging time than the best constant Mot/Gen coefficient

case under the same grid constrains.

Finally, the flywheel steady state temperature with radiation was simulated with ANSYS™ 2D thermal analysis. This was carried out to evaluate the operational conditions of the flywheel system when it was put into a vacuum. Both the motor idle and the motor active cases were simulated. The results verified that our flywheel will work in a reasonable and functional temperature range under the vacuum operational conditions.

CHAPTER VI

FLYWHEEL ENERGY STORAGE ON RAILWAY APPLICATIONS

6.1 Overview

Flywheel energy storage systems have a broad range of application areas such as wind farm storage and smart grid applications. Our novel design will be a perfect fit for these applications due to their needs for low cost, long life, high reliability energy storage systems. Another area of energy storage system will be for the locomotives. Even though our novel design of the flywheel system can easily be resized and put on everyday cars, this dissertation will mainly focus on its application on train locomotives.

This chapter will first focus on the development of optimization algorithms for the regenerative braking process. An algorithm that allows the user to balance between braking effort and energy recovery will be put forward. Effects on energy recovered by various parameters will be discussed.

After that, the dissertation will try to simulate the diesel fuel and NOx savings on Line Haul, Switcher and an assumed route for a High Speed Rail application. Since the real world engine data belongs to railroad companies, these simulations were based on the published average data retrieved by EPA's report.

Finally, the vibration isolation problem of the flywheel on the train locomotives will be addressed and the simulations will show that the flywheel assembly will pass the average bridge bumps and train turning simulations without a problem.

6.2 Architecture of Locomotives with Flywheel Energy Storage System

To implement the flywheel energy storage system, a carrier for these heavy masses must be selected. A slug car will serve this purpose perfectly since it is basically a train locomotive with traction motors but without engines. In real life railway applications, a slug car loaded with stones is generally added to increase the traction of the train. To substitute the stones with our flywheel energy storage system, we can get rid these not-so-useful loads. Another benefit of the structure comes from the fact that the diesel engine and the flywheel systems drive different sets of traction motors. This will make the circuit and control system much easier to implement. A concept picture of this architecture is as shown in Fig. 6.1. Considering the energy requirements for different applications discussed in this dissertation, 10 flywheels was used for Line Haul and Switcher service simulations, 8 flywheels was used for High Speed Rail application simulations. The number of flywheels used should be an even number since they will be separated into pairs of two that counter rotating with respect to each other. This is done to minimize the gyroscopic effects of the flywheels on the mounting environments.

A simplified flywheel power system flowchart is as shown in Fig. 6.2. The flywheel powers the traction motors during the driving phase, which will pass the driving torque to the locomotive's wheels via geared transmissions. During the braking phase, the traction motors will act as generators and charge the flywheels by supplying the EMF voltages. This replaces the current method of driving currents into resistance banks and converting the locomotive's kinetic energy into waste heat.

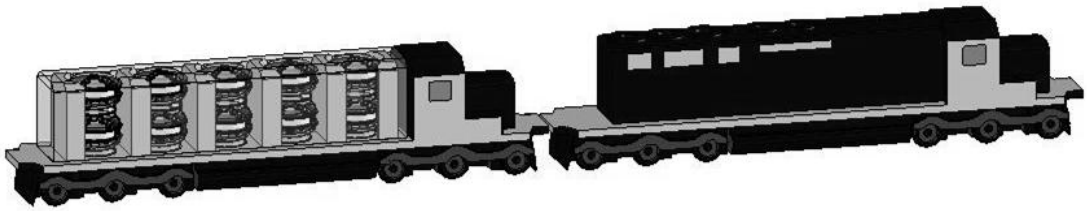

Fig. 6.1 Diesel Locomotive with a Slug Car

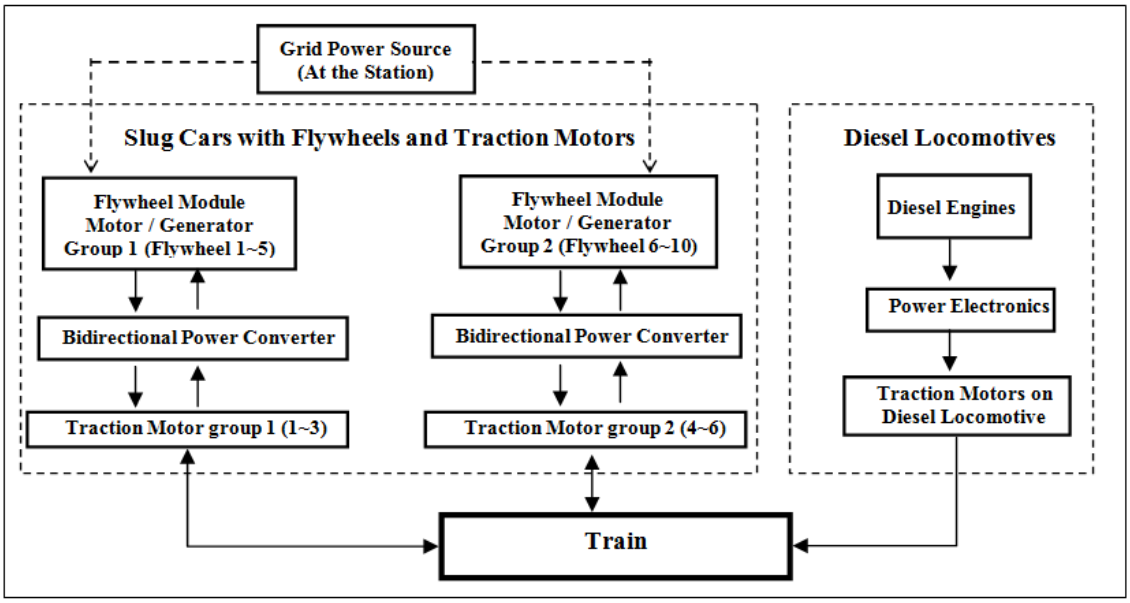

Fig. 6.2 Power Diagram for Diesel Locomotive with a Slug Car

6.3 Optimization of the Regenerative Braking

The dynamics of the train can be modeled as:

$$m_{train}\frac{dv_{train}}{dt} = F_{train} = F_{drive} - F_{davis} \tag{6.1}$$

The locomotive traction motor force generated by flywheel circuit will be:

$$F_{tm} = r_{gear}\Gamma_{tm}/R_{wheel} = r_{gear}(P_{tm}/\omega_{tm})/R_{weel} = P_{tm}\ /\ v_{train} \tag{6.2}$$

Since diesel engine and flywheel energy storage system drive different sets of

traction motors, the total drive forces when the locomotive is pulling the training are:

$$F_{drive} = F_{diesel} + n_{tm}F_{tm} = P_{diesel} / V_{train} + n_{tm}r_{gear}K_{tm}i_{tm} / R_{weel} \quad (6.3)$$

The total drive force when the train is braking is:

$$F_{drive} = n_{tm}F_{tm} = n_{tm}r_{gear}K_{tm}i_{tm} / R_{wheel} \quad (6.4)$$

An empirically based equation called Modified Davis Equation was used to account the drag forces caused by air resistance, track and rolling resistance, bearing resistance, windage and friction in the traction motors, lighting, etc. This drag force varies with train and car weight, velocity and other factors. In its standard form the Modified Davies Formula is given as [47]:

$$F_{davis} = W_{\text{train}} * R_u = A + Bv + Cv^2 \quad (6.5)$$

$$R_u = 0.6 + \frac{20}{w} + 0.01v + \frac{Kv^2}{wn} \quad (6.6)$$

where R_u is resistance in lb_f per ton, w is the weight per axle (in tons), n is number of axles per car, W is the total car weight on rails in tons (W=wn), v is speed in miles per hour and K is the air drag coefficient. We have:

$$\begin{cases} A = \left(0.6 + \frac{20}{w}\right) W_{train} \\ B = 0.01 W_{train} \\ C = K \end{cases} \quad (6.7)$$

The flywheel rotational (spin) motion is governed by:

$$I_{Pfw}\dot{\omega}_{fw} = \Gamma_{fw} = K_{fw}i_{fw} + C_{fw}\omega_{fw} \quad (6.8)$$

There are different types of flywheels in terms of volumes, weights, speeds and energy storage level. Also the slug car carrying flywheel assembly varies in different aspects such as traction motor counts and power, weights, electrical system

characteristics. For illustration it is assumed that the slug car has 6 traction motors and 10 flywheels, which could be operated in counter-rotating pairs to balance gyroscopic torques. The flywheels were divided into two groups. Each group will consist of 5 flywheels connected parallel and put in parallel with 3 traction motors connected in series. The system configuration for one such group is as shown in Fig. 6.3.

A large number of locomotives in the American fleet presently utilize DC diesel generator sets and DC traction motors, although induction motors with variable frequency drives VFD are gradually replacing the DC technology. Our current focus is to study and illustrate a novel hybrid power system consisting of flywheel and diesel generator, so a DC electrical system model is employed for illustration. For VFD cases, the power system can either by converted to DC using power electronics or a new specific case can be generated using similar procedure illustrated here. The traction control feedback system is omitted for the same reason.

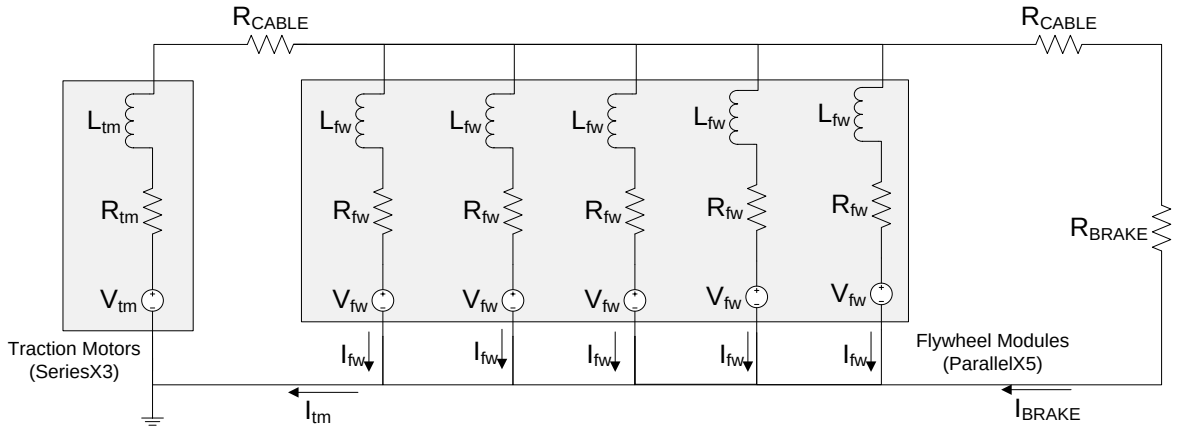

Fig. 6.3 Equivalent Circuit Model for One Group of 3 Traction Motors and 5 Flywheels

Kirchoff's laws yield:

$$i_{tm} = 5i_{fw} + i_{BRAKE} \tag{6.9}$$

$$\begin{bmatrix} (L_{tm} \times 5 + L_{fw}) & L_{tm} \\ L_{fw} & 0 \end{bmatrix} \begin{Bmatrix} \frac{d}{dt} i_{fw} \\ \frac{d}{dt} i_{BRAKE} \end{Bmatrix} = \begin{bmatrix} -(R_{fw} + R_{tm} \times 5 + R_{CABLE} \times 5) & -(R_{tm} + R_{CABLE}) \\ -R_{fw} & (R_{BRAKE} + R_{CABLE}) \end{bmatrix} \begin{Bmatrix} i_{fw} \\ i_{BRAKE} \end{Bmatrix} + \begin{bmatrix} V_{tm} - V_{fw} \\ -V_{fw} \end{bmatrix} \tag{6.10}$$

By maintaining a large R_{BRAKE}, i_{BRAKE} can be kept small and neglected. Since the flywheel will be operating in a vacuum, the wind drag terms in Eq. 6.8 can also be neglected. By rewriting the above functions, the electrical and electromechanical relations will be:

$$i_{tm} = 5i_{fw} \tag{6.11}$$

$$T_{f\omega} = K_{fw} i_{fw} \tag{6.12}$$

$$T_{tm} = K_{tm} \cdot 5i_{f\omega} \tag{6.13}$$

$$V_{tm} - V_{fw} = 5i_{fw}(R_{tm} + R_{CABLE}) + i_{fw}R_{fw} + [5L_{tm} + L_{fw}]\frac{di_{fw}}{dt} \tag{6.14}$$

$$V_{tm} = 3K_{tm}\omega_{tm} \tag{6.15}$$

$$V_{fw} = K_{fw}\omega_{fw} \tag{6.16}$$

$$P_{tm} = -6T_{tm}\omega_{tm} = -6K_{tm}5i_{fw}\omega_{tm} = -10V_{tm}i_{fw} \tag{6.17}$$

$$P_{fw} = 10T_{fw}\omega_{fW} = 10K_{fw}i_{fW}\omega_{fw} = 10V_{fw}i_{fw} \tag{6.18}$$

The symbols L_{fw}, R_{fw}, V_{fw} in Fig. 6.3 are the single flywheel module inductance, resistance and voltage, respectively, and L_{tm}, R_{tm}, V_{tm} are the total inductance, resistance and voltage of 3 traction motors connected in series. A diesel generator is not included in Fig. 6.3 since the flywheels are assumed to be positioned on a slug car, which has traction motors but not a diesel generator. The cable resistance between components is indicated as R_{CABLE} in Fig. 6.3.

A DC charging/discharging current was assumed in this model. The maximum current delivered to the flywheels by the traction motor-generators is typically less than 1000 amps and will diminish within a period of 2-20 minutes during braking. Since the current value has a very slow time variation (DC signal with amplitude changing very slowly), and the system inductance is low. The inductance voltage is far less than the resistive voltage drops and thus the inductance term in Eq. 6.14 can be neglected. The equation simplifies to:

$$V_{tm} - V_{fw} = \left(R_{fw} + 5R_{tm} + 5R_{CABLE}\right) i_{fw} \tag{6.19}$$

6.3.1 Maximum Flywheel Charging Algorithm

The flywheel charging algorithms were studied to have the maximum energy recovery during regenerative braking. After plugging in the modified-Davis force, the train acceleration becomes:

$$\begin{aligned} -m\frac{dV_{train}}{dt} = -m\frac{R_w}{r_g}\frac{d\omega_{tm}}{dt} = F_{train} \\ = \frac{r_{gear}}{R_{wheel}} K_{tm} 30 i_{fw} + A + B\frac{R_{\omega heel}\omega_{tm}}{r_{gear}} + C\frac{R_{wheel}^2}{r_{gear}^2}\omega_{tm}^2 \end{aligned} \tag{6.20}$$

which turns into:

$$-\frac{d\omega_{tm}}{dt}=\left(\frac{r_{gear}}{R_{wheel}}\right)^2\frac{30K_{tm}}{m}i_{fw}+\frac{r_{gear}}{mR_{wheel}}A+\frac{B}{m}\omega_{tm}+C\frac{R_{wheel}}{mr_{gear}}\omega_{tm}^2 \quad (6.21)$$

Since

$$\omega_{tm}=\frac{V_{tm}}{3K_{tm}} \quad (6.22)$$

we will have:

$$\begin{aligned}-\frac{dV_{tm}}{dt}=&\left(\frac{r_{gear}}{R_{wheel}}\right)^2\frac{90K_{tm}^2}{m}i_{fw}+\frac{3K_{tm}r_{gear}}{mR_{wheel}}A+\frac{B}{m}V_{tm}\\&+C\frac{R_{wheel}}{mr_{gear}}\frac{V_{tm}^2}{3K_{tm}}\end{aligned} \quad (6.23)$$

Integrate Eq. 6.23 till the hand braking is engaged:

$$\begin{aligned}\int_0^{t_f}-\frac{dV_{tm}}{dt}dt=\int_0^{t_f}&\left[\left(\frac{r_{gear}}{R_{wheel}}\right)^2\frac{90K_{tm}^2}{m}i_{fw}+\frac{3K_{tm}r_{gear}}{mR_{wheel}}A+\frac{B}{m}V_{tm}\right.\\&\left.+C\frac{R_{wheel}}{mr_{gear}}\frac{V_{tm}^2}{3K_{tm}}\right]dt=V_{tm0}-V_{tmf}\end{aligned} \quad (6.24)$$

Since V_{tm} is proportional to the train speed/traction motor speed, V_{tmo} and V_{tmf} is fixed given a fixed initial train speed and hand braking engaging speed. So the integration given by Eq. 6.24 will be a constant. With Eq. 6.19, we will have

$$\begin{aligned}\int_0^{t_f}&\left\{\left(\frac{r_{gear}}{R_{wheel}}\right)^2\frac{90K_{tm}^2}{m}i_{fw}+\frac{3K_{tm}r_{gear}}{mR_{wheel}}A\right.\\&+\frac{B}{m}\left[V_{fw}+\left(R_{fw}+5R_{tm}+5R_{CABLE}\right)i_{fw}\right.\\&\left.\left.+C\frac{R_{wheel}}{mr_{gear}}\frac{\left[V_{fw}+\left(R_{fw}+5R_{tm}+5R_{CABLE}\right)i_{fw}\right]^2}{3K_{tm}}\right\}dt=\text{const.}\end{aligned} \quad (6.25)$$

Expand the functions in Eq. 6.25 and multiple both sides with $15mr_{gear}K_{tm}/[C(5R_{tm}+5R_{CABLE}+R_{fw})R_{wheel}]$, we will have:

$$\begin{aligned}&\int_0^{t_f}\left\{\left(\frac{r_{gear}}{R_{wheel}}\right)^3\frac{1350K_{tm}^3}{C(5R_{tm}+5R_{CABLE}+R_{fw})}i_{fw}\right.\\&+\frac{45}{C(5R_{tm}+5R_{CABLE}+R_{fw})}\left(\frac{K_{tm}r_{gear}}{R_{wheel}}\right)^2A\\&+\frac{15Br_{gear}K_{tm}}{C(5R_{tm}+5R_{CABLE}+R_{fw})R_{wheel}}V_{fw}\\&+\frac{15Br_{gear}K_{tm}}{CR_{wheel}}i_{fw}+\frac{5}{(5R_{tm}+5R_{CABLE}+R_{fw})}V_{fw}^2\\&\left.+10V_{fw}i_{fw}+5(5R_{tm}+5R_{CABLE}+R_{fw})i_{fw}^2\right\}dt\\&=Const2\end{aligned}\tag{6.26}$$

Define several constants as:

$$\begin{cases}\widetilde{M}=\left(\frac{r_{gear}}{R_{wheel}}\right)^3\frac{1350K_{tm}^3}{C(5R_{tm}+5R_{CABLE}+R_{fw})}+\frac{15Br_{gear}K_{tm}}{CR_{wheel}}\\\widetilde{N}=5(5R_{tm}+5R_{CABLE}+R_{fw})\\\widetilde{H}=\frac{45}{C(5R_{tm}+5R_{CABLE}+R_{fw})}\left(\frac{K_{tm}r_{gear}}{R_{wheel}}\right)^2A\\\tilde{Q}=\frac{15Br_{gear}K_{tm}}{C(5R_{tm}+5R_{CABLE}+R_{fw})R_{wheel}}\\\tilde{R}=\frac{5}{(5R_{tm}+5R_{CABLE}+R_{fw})}\end{cases}\tag{6.27}$$

With the total flywheel power defined as in Eq. 6.18, Eq. 6.26 can be turned into:

$$\int_0^{t_f}\left\{\widetilde{M}i_{fw}+\widetilde{N}i_{fw}^2+\widetilde{\mathrm{H}}+\widetilde{\mathrm{Q}}V_{fw}+\widetilde{\mathrm{R}}V_{fw}^2+P_{fw}\right\}dt=Const2\tag{6.28}$$

The total flywheel energy recovered will be:

$$E_{fw} = \int_0^{t_f} \{P_{fw}\}\, dt$$
$$= Const2 - \int_0^{t_f} \left\{\widetilde{M} i_{fw} + \widetilde{N} i_{fw}^2 + \widetilde{\mathrm{H}} + \widetilde{\mathrm{Q}} V_{fw} + \widetilde{\mathrm{R}} V_{fw}^2\right\} dt \tag{6.29}$$

Assume the flywheel voltage can be controlled by K_{fw}, so that:

$$V_{fw} = \mathrm{K}_{bFB} V_{tm} \tag{6.30}$$

Since the flywheel will keep being charged, $1 \geq K_{B\_FB} \geq 0$. Eq. 6.19 will lead to:

$$i_{fw} = \frac{1 - K_{bFB}}{\left(5R_{tm} + 5R_{CABLE} + R_{fw}\right)} V_{tm} \tag{6.31}$$

Then we have:

$$\int_0^{t_f} \left(\widetilde{M} i_{fw} + \widetilde{N} i_{fw}^2 + \widetilde{\mathrm{H}} + \widetilde{\mathrm{Q}} V_{fw} + \widetilde{\mathrm{R}} V_{fw}^2\right) dt$$
$$= \int_{V_{tm0}}^{V_{tmf}} [\widetilde{M} \frac{1 - K_{bFB}}{5R_{tm} + 5R_{CABLE} + R_{fw}} V_{tm} + \widetilde{\mathrm{H}} + \widetilde{\mathrm{Q}} K_{bFB} V_{fw} \tag{6.32}$$
$$+ \widetilde{N} \left(\frac{1 - K_{bFB}}{5R_{tm} + 5R_{CABLE} + R_{fw}} V_{tm}\right)^2 + \widetilde{\mathrm{R}} \mathrm{K}_{bFB}^2 V_{fw}^2] \frac{1}{dV_{tm}/dt} dV_{tm}$$

V_{tmo} is the V_{tm} value when the regenerative braking starts. V_{tmf} is the V_{tm} value when the hand braking is engaged. Eq. 6.23 changes its form into:

$$\frac{dV_{tm}}{dt} = -\left(\frac{r_{gear}}{R_{wheel}}\right)^2 \frac{90 K_{tm}^2}{m} \frac{1 - K_{bFB}}{5R_{tm} + 5R_{CABLE} + R_{fw}} V_{tm} - \frac{3K_{tm} r_{gear}}{m R_{wheel}} A \tag{6.33}$$
$$- \frac{B}{m} V_{tm} - C \frac{R_{wheel}}{m r_{gear}} \frac{V_{tm}^2}{3K_{tm}}$$

Defining several constants as in Eq. 6.34, Eq. 6.33 turns into Eq. 6.35

$$\begin{cases} \widetilde{\mathrm{U}} = \left(\dfrac{r_{gear}}{R_{wheel}}\right)^2 \dfrac{90K_{tm}^2}{m(5R_{tm} + 5R_{CABLE} + R_{fw})} \\ \widetilde{W} = \dfrac{B}{m} \\ \tilde{X} = C\dfrac{R_{wheel}}{3K_{tm}mr_{gear}} \\ \tilde{Y} = \dfrac{3K_{tm}r_{gear}}{mR_{wheel}}A \end{cases} \tag{6.34}$$

$$\frac{dV_{tm}}{dt} = -UU(1 - K_{bFB})V_{tm} - \widetilde{W}V_{tm} - \tilde{X}V_{tm}^2 - \widetilde{\mathrm{Y}} \tag{6.35}$$

Assuming:

$$\begin{cases} \tilde{\mathrm{S}} = \dfrac{\widetilde{M}}{(5R_{tm} + 5R_{CABLE} + R_{fw})} \\ \widetilde{\mathrm{T}} = \dfrac{\widetilde{N}}{(5R_{tm} + 5R_{CABLE} + R_{fw})^2} \end{cases} \tag{6.36}$$

we will have:

$$\min\left(\int_0^{t_f} \left(\widetilde{M}i_{fw} + \widetilde{N}i_{fw}^2 + \widetilde{\mathrm{H}} + \widetilde{\mathrm{Q}}V_{fw} + \widetilde{\mathrm{R}}V_{fw}^2\right) dt\right)$$

$$= \min\left\{ \int_{V_{tmf}}^{V_{tm0}} \frac{1}{\widetilde{U}(1 - K_{bFB})V_{tm} + \widetilde{W}V_{tm} + \tilde{X}V_{tm}^2 + \widetilde{\mathrm{Y}}} \left[\tilde{S}(1 - K_{bFB})V_{tm} \right.\right. \tag{6.37}$$

$$\left.\left. + \tilde{T}\left((1 - K_{bFB})V_{tm}\right)^2 + \widetilde{\mathrm{H}} + \widetilde{\mathrm{Q}}K_{bFB}V_{fw} + \widetilde{\mathrm{R}}\mathrm{K}_{bFB}^2V_{fw}^2\right] dV_{tm} \right\}$$

Assume

$$f(V_{tm}, K_{bFB}) = \frac{1}{\widetilde{U}(1 - K_{bFB})V_{tm} + \widetilde{W}V_{tm} + \tilde{X}V_{tm}^2 + \widetilde{\mathrm{Y}}} \left[\tilde{S}(1 - K_{bFB})V_{tm} \right. \tag{6.38}$$

$$\left. + \tilde{T}\left((1 - K_{bFB})V_{tm}\right)^2 + \widetilde{\mathrm{H}} + \widetilde{\mathrm{Q}}K_{bFB}V_{fw} + \widetilde{\mathrm{R}}\mathrm{K}_{bFB}^2V_{fw}^2\right]$$

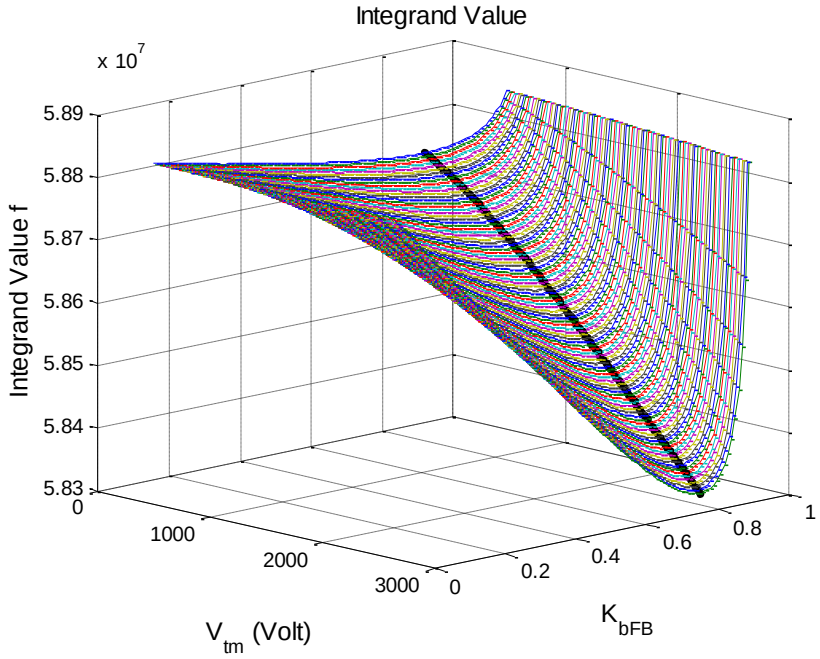

Fig. 6.4 f(V_{tm}, K_{bFB}) Plot for 3100ton Train Braking with 60MPH Initial Speed and K_{tm}=4

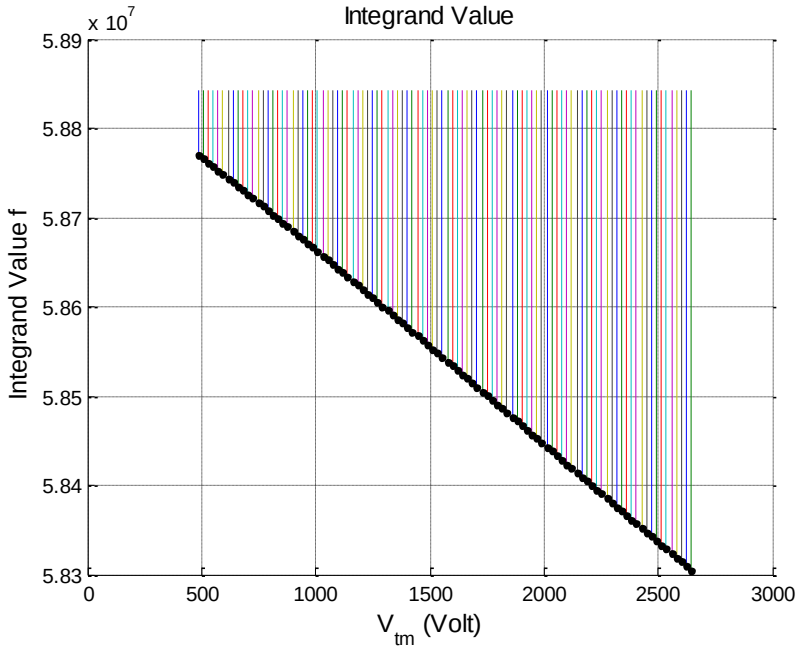

Fig. 6.5 f(V_{tm}, K_{bFB}) Value Projection at f-V_{tm} Plane

Since f(V_{tm}, K_{bFB})>=0 when $V_{tmo} \geq V_{tm} \geq V_{tmf}$, we can approximate the minimum of the

integration by minimizing its integrand f(V_{tm}, K_{bFB}) at each V_{tm} value. The integrand values vs. V_{tm} and K_{bFB} values are as plotted in Fig. 6.4 for a 3100 ton train braking from 60MPH with a K_{tm} value of 4Nm/A. The V_{tm} varies between V_{tmf} and V_{tmo}. The K_{bFB} varies between 0 and 1. The black dots mark the minimum position of f function for each V_{tm} input by varying the K_{bFB} value. Fig. 6.5 shows the projection of f function values on the f-V_{tm} plane. As can be seen in Fig. 6.5, by minimizing f value at each V_{tm} value, the area (integration) of the integrant f within our interested range was minimized for the case analyzed.

Using df/dK_{bFB}=0, the equation can be retrieved as:

$$\begin{gathered} -\left(\tilde{R}+\tilde{\mathrm{T}}\right)UU*V_{tm}^{3}K_{bFB}^{2} \\ +\left[2\tilde{Y}\tilde{R}V_{tm}^{2}+2\tilde{Y}\tilde{\mathrm{T}}V_{tm}^{2}+2\tilde{U}\tilde{R}V_{tm}^{3}+2\tilde{W}\tilde{R}V_{tm}^{3}+2\tilde{\mathrm{T}}\tilde{U}V_{tm}^{3}\right. \\ \left.+2\tilde{W}\tilde{T}V_{tm}^{3}+2\tilde{X}\tilde{R}V_{tm}^{4}+2\tilde{X}\tilde{T}V_{tm}^{4}\right]K_{\mathrm{bFB}} \\ +\left(-2\tilde{\mathrm{T}}V_{tm}^{2}+\tilde{Q}V_{tm}-\tilde{\mathrm{S}}V_{tm}\right)\left(\tilde{W}V_{tm}+\tilde{X}V_{tm}^{2}+\tilde{Y}\right) \\ -\tilde{\mathrm{T}}\tilde{U}V_{tm}^{3}+\tilde{H}\tilde{U}V_{tm}+\tilde{Q}\tilde{U}V_{tm}^{2}=0 \end{gathered} \tag{6.39}$$

Assuming

$$\begin{cases} \mathrm{CoefA}=-\left(\tilde{R}+\tilde{\mathrm{T}}\right)UU*V_{tm}^{3} \\ \mathrm{CoefB}=2\tilde{Y}\tilde{R}V_{tm}^{2}+2\tilde{Y}\tilde{\mathrm{T}}V_{tm}^{2}+2\tilde{U}\tilde{R}V_{tm}^{3}+2\tilde{W}\tilde{R}V_{tm}^{3}+2\tilde{\mathrm{T}}\tilde{U}V_{tm}^{3} \\ \qquad +2\tilde{W}\tilde{T}V_{tm}^{3}+2\tilde{X}\tilde{R}V_{tm}^{4}+2\tilde{X}\tilde{T}V_{tm}^{4} \\ CoefC=\left(-2\tilde{\mathrm{T}}V_{tm}^{2}+\tilde{Q}V_{tm}-\tilde{\mathrm{S}}V_{tm}\right)\left(\tilde{W}V_{tm}+\tilde{X}V_{tm}^{2}+\tilde{Y}\right) \\ \qquad -\tilde{\mathrm{T}}\tilde{U}V_{tm}^{3}+\tilde{H}\tilde{U}V_{tm}+\tilde{Q}\tilde{U}V_{tm}^{2} \end{cases} \tag{6.40}$$

Eq. 6.39 turns into:

$$\mathrm{CoefA}*K_{bFB}^{2}+\mathrm{CoefB}*K_{\mathrm{b}FB}+\mathrm{CoefC}=0 \tag{6.41}$$

Since –*CoefB*/2*CoefA*>=1, the only solution of Eq. 6.41 that may fulfill the condition 1≥K_{bFB}≥0 will be:

$$\mathrm{K}_{bFB} = \frac{-CoefB + \sqrt{CoefB^2 - 4CoefB \cdot CoefC}}{2CoefA} \tag{6.42}$$

The solution given by Eq. 6.42 is a necessary condition for the minimization of Eq. 3.38. Eq. 6.42 will be a sufficient condition if the second derivative of *f* (Eq. 6.43) is positive at K_{bFB} defined by Eq. 6.42.

$$\frac{1}{\mathrm{K}_{bFB}}\left(\frac{1}{\mathrm{K}_{bFB}} f\right) = \frac{\left(\tilde{R} + \tilde{T}\right)\left[2\tilde{Y}V_{tm}^2 + 2\tilde{W}V_{tm}^3 + 2\tilde{X}V_{tm}^4 + 2\tilde{U}V_{tm}^3(1 - \mathrm{K}_{bFB})\right]}{\left[\left(\tilde{U} + \tilde{W} - \tilde{U} * \mathrm{K}_{bFB}\right)V_{tm} + \tilde{X} * V_{tm}^2 + \tilde{Y}\right]^2} \tag{6.43}$$

Case 1: K_{bFB} from Eq. 6.42 satisfies $0 \leq K_{bFB} \leq 1$. In this case the right hand side of Eq. 6.43 is positive, so that Eq. 6.42 produces a minimum value of $f(V_{tm}, K_{bFB})$ (maximum value of harvested energy by the flywheel).

Case 2: K_{bFB} from Eq. 6.42 does not satisfy $0 \leq K_{bFB} \leq 1$. In this case $f(V_{tm}, K_{bFB})$ varies monotonically within [0, 1] and is minimum at one of the limits $K_{bFB}=0$, or $K_{bFB}=1$.

The K_{bFB} value as obtained from above yields the maximum harvested energy obtained from braking the train, and is utilized to obtain the required flywheel voltage, per Eq. 6.30: $V_{fw} = \mathrm{K}_{bFB} V_{tm}$.

6.3.2 Optimum Algorithm Balancing Flywheel Regenerative Energy Recovery and Braking Effort

The algorithm discussed above only gives the key that leads to the maximum energy harvesting during the regenerative braking. However, in the real life, there is always a requirement to maximum the energy recovery within a certain braking limits. So it is required that an algorithm to be developed to balance the braking and energy harvesting

effort and have the whole process controllable.

At any moment during the train braking, the ratio of the recovered energy over total train kinetic energy loss equals to their corresponding ratio of the power. Since this is a real time control algorithm and the future states are not retrievable, it is hard to cover the case where a previous smaller recovery ratio will lead to a higher recovery ratio later. So we assumed that an instantaneous maximum of the ratio of flywheel power over the train kinetic energy loss power will lead to the maximum regenerative energy recovery value.

The powers for flywheel and traction motors were as given in Eq. 6.17 and Eq. 6.18, respectively. The power induced by air and track drag force (Davis force) can be written as:

$$\begin{aligned} P_{davis} &= F_{davis} v_{train} \\ &= A\frac{R_{wheel}\omega_{tm}}{r_{gear}} + B\left(\frac{R_{wheel}\omega_{tm}}{r_{gear}}\right)^2 + C\left(\frac{R_{wheel}\omega_{tm}}{r_{gear}}\right)^2 \\ &= A\frac{R_{wheel}V_{tm}}{3r_{gear}K_{tm}} + B(\frac{R_{wheel}V_{tm}}{3r_{gear}K_{tm}})^2 + C(\frac{R_{wheel}\omega_{tm}}{3r_{gear}K_{tm}})^2 \end{aligned} \tag{6.44}$$

Assuming

$$\begin{cases} \hat{\mathrm{A}} = \dfrac{AR_{wheel}}{3r_{gear}K_{tm}} \\ \hat{B} = B(\dfrac{R_{wheel}}{3r_{gear}K_{tm}})^2 \\ \hat{C} = B(\dfrac{R_{wheel}}{3r_{gear}K_{tm}})^3 \end{cases} \tag{6.45}$$

the energy recovery power ratio is:

$$\frac{P_{fw}}{P_{kinetic}} = \frac{10V_{fw}i_{fw}}{P_{davis} - P_{tm}} = \frac{10[V_{tm} - (5R_{tm} + R_{CABLE} + R_{fw})i_{fw}]i_{fw}}{\hat{A}V_{tm} + \hat{B}V_{tm}^2 + \hat{C}V_{tm}^3 + 10V_{tm}i_{fw}} \quad (6.46)$$

The total braking force generated by 6 traction motors is given as

$$F_{BRAKE} = 6\frac{r_{gear}T_{tm}}{R_{wheel}} = 30\frac{r_{gear}K_{tm}}{R_{wheel}}i_{fw} \quad (6.47)$$

One objective is to increase the energy recovery efficiency expressed by Eq. 6.46. The second objective is to stop the train in an acceptable distance by increasing the braking force or from Newton's law by increasing the train's deceleration F_{BRAKE}/m_{train} (deceleration caused by slug car traction motor force). A single aggregate objective function (AOF) function is defined as:

$$\mathrm{T} = \frac{m_{train}^2}{F_{BRAKE}^2} + b^2\left(\frac{P_{kinetic}}{P_{fw}}\right)^2 \quad (6.48)$$

This consists of the weighted sum of the inverses of these 2 objectives, with the energy recovery component including the weighting factor *b*, where *b*>0. It should be noted that only the AOF is minimized, that is the braking forced and energy recovery are not independently maximized. This is a subjective approach since a decision manager must select *b*. Objective approaches as described in [48] and [49] may also be employed which utilize Pareto compliant ranking methods, favoring non-dominated solutions.

As proved below, the energy recovery efficiency is a monotonically increasing function of *b* and the braking effort is monotonically decreasing function of *b*.

The flywheel charging current i_{fw} can be controlled by changing the K_{fw} as discussed earlier. So i_{fw} value was selected to be the optimization variable of the algorithm.

Assume:

$$Q_1(i_{fw}) = \frac{m_{train}}{F_{BRAKE}} \tag{6.49}$$

$$Q_2(i_{fw}) = \frac{P_{kinetic}}{P_{fw}} \tag{6.50}$$

the minimization target function becomes

$$\mathrm{T}(\mathrm{i}_{fw}) = (Q_1(i_{fw}))^2 + b^2\big(Q_2(i_{fw})\big)^2 \tag{6.51}$$

Assume i_{fw1} and i_{fw2} are minimum solution within the range $[0, V_{tm}/(5\mathrm{R}_{tm} + 5\mathrm{R}_{CABLE} + \mathrm{R}_{fw}]$ for Eq. 6.51 at b_1 and b_2 (b_1>b_2). Since for a fixed i_{fw} value $Q_1(i_{fw})$ and $Q_2(i_{fw})$ are also fixed, we can assume:

$$Q_{11} = Q_1(i_{fw1}) \tag{6.52}$$

$$Q_{21} = Q_2(i_{fw1}) \tag{6.53}$$

$$Q_{12} = Q_1(i_{fw2}) \tag{6.54}$$

$$Q_{22} = Q_2(i_{fw2}) \tag{6.55}$$

Since i_{fw1} is the minimum solution at b_1 and i_{fw2} is the minimum solution at b_2, we have:

$$\mathrm{Q}_{11}^2 + b_1^2\mathrm{Q}_{21}^2 < \mathrm{Q}_{12}^2 + b_1^2\mathrm{Q}_{22}^2 \tag{6.56}$$

$$\mathrm{Q}_{12}^2 + b_2^2\mathrm{Q}_{22}^2 < \mathrm{Q}_{11}^2 + b_2^2\mathrm{Q}_{21}^2 \tag{6.57}$$

By adding Eq. 6.56 and Eq. 6.57, we have:

$$b_1^2\mathrm{Q}_{21}^2 + b_2^2\mathrm{Q}_{22}^2 < b_1^2\mathrm{Q}_{22}^2 + b_2^2\mathrm{Q}_{21}^2 \tag{6.58}$$

which converts to:

$$(b_1^2 - b_2^2)\mathrm{Q}_{21}^2 < (b_1^2 - b_2^2)\mathrm{Q}_{22}^2 \tag{6.59}$$

Since$(b_1^2 - b_2^2) > 0$,we have:

$$\mathrm{Q}_{21}^2 < \mathrm{Q}_{22}^2 \tag{6.60}$$

Since $Q_2(i_{fw})$>0

$$Q_{21} < Q_{22} \tag{6.61}$$

By definition of Eq. 6.50, this means, for a higher b value (b_1), the energy recovery efficiency is better.

By dividing Eq. 6.56 with b_1^2, dividing Eq. 6.57 with b_2^2 and adding the results together, we have:

$$\frac{\mathrm{Q}_{11}^2}{b_1^2} + \frac{\mathrm{Q}_{12}^2}{b_2^2} < \frac{\mathrm{Q}_{12}^2}{b_1^2} + \frac{\mathrm{Q}_{11}^2}{b_2^2} \tag{6.62}$$

which converts to:

$$(b_1^2 - b_2^2)\mathrm{Q}_{12}^2 < (b_1^2 - b_2^2)\mathrm{Q}_{11}^2 \tag{6.63}$$

Since $(b_1^2 - b_2^2) > 0$ and $\mathrm{Q}_1(\mathrm{i}_{\mathrm{fw}})$>0

$$Q_{12} < Q_{11} \tag{6.64}$$

By definition of Eq. 6.49, this means for a higher b value (b_1) the braking effort is smaller since it is the inverse of Q_1.

Eq. 6.48 can be expanded as:

$$\begin{aligned} T(i_{fw}) &= \frac{m_{train}^2}{F_{BRAKE}^2} + b^2\left(\frac{P_{kinetic}}{P_{fw}}\right)^2 = \frac{\widehat{H}}{i_{fw}^2} + \left(\frac{\hat{I} + \hat{J}i_{fw}}{\widehat{K}i_{fw} - \hat{L}i_{fw}^2}\right)^2 \\ &= \frac{1}{i_{fw}^2}\left[\left(\widehat{H} + \frac{\hat{J}^2}{\hat{L}^2}\right) - 2\frac{\hat{J}}{\hat{L}}\left(\hat{I} + \frac{\hat{J}\widehat{K}}{\hat{L}}\right)\frac{1}{\widehat{K} - \hat{L}i_{fw}} + \left(\hat{I} + \frac{\hat{J}\widehat{K}}{\hat{L}}\right)^2\left(\frac{1}{\widehat{K} - \hat{L}i_{fw}}\right)^2\right] \end{aligned} \tag{6.65}$$

where,

$$\begin{cases} \widehat{\mathrm{H}} = (\dfrac{m_{train}R_{wheel}}{30r_{gear}K_{tm}})^2 \\ \hat{I} = b\left(\hat{A}V_{tm} + \hat{B}V_{tm}^2 + \hat{C}V_{tm}^3\right) \\ \hat{J} = 10bV_{tm} \\ \widehat{K} = 10V_{tm} \\ \hat{L} = 10\left(5R_{tm} + 5R_c + R_{fw}\right) \end{cases} \tag{6.66}$$

The instantaneous flywheel current i_{fw} that minimizes the above AOF, and the instantaneous traction motor voltage V_{tm} and flywheel angular velocity ω_{fw} are substituted into Eq. 6.19 and Eq. 6.16 to obtain the required flywheel gain value:

$$K_{fw} = \frac{1}{\omega_{fw}}[V_{tm} - \left(R_{fw} + 5R_{tm} + 5R_{CABLE}\right)i_{fw}] \tag{6.67}$$

which is physically realized by the flux weakening approaches described earlier.

The function $T(i_{fw})$ in Eq. 6.65 is minimized with respect to i_{fw}, while treating V_{tm} as a constant at any given time and noting that $\widehat{H}, \hat{I}, \hat{J}, \widehat{K}$ and $\hat{L}$ are all positive constants. The function $T(i_{fw})$ equals $+\infty$ at $i_{fw} = 0$ and at $i_{fw} = V_{tm}/(R_{fw} + 5R_{tm} + 5R_{CABLE})$. By Eq. 6.19, the corresponding V_{fw} values are $V_{fw} = V_{tm}$ and $V_{fw} = 0$, respectively.

These points confirm that there must be a minimum value of T in the operational range of interest, i.e. $0 < V_{fw} < V_{tm}$ and $0 < i_{fw} < V_{tm}/(R_{fw} + 5R_{tm} + 5R_{CABLE})$, since T goes to $+\infty$ at both endpoints of interest.

Apply the stationary condition to Eq. 6.65 with respect to i_{fw}:

$$\frac{d}{di_{fw}}T(i_{fw}) = -\frac{2\widehat{H}}{i_{fw}^3} + 2\frac{\hat{I} + \hat{J}i_{fw}}{\widehat{K}i_{fw} - \hat{L}i_{fw}^2}\left[\frac{\hat{J}}{\widehat{K}i_{fw} - \hat{L}i_{fw}^2} - \frac{\hat{I} + \hat{J}i_{fw}}{\left(\widehat{K}i_{fw} - \hat{L}i_{fw}^2\right)^2}\left(\widehat{K} - 2\hat{L}i_{fw}\right)\right] = 0 \tag{6.68}$$

Setting the numerator of Eq. 6.68 equal to zero yields:

$$\begin{aligned}&\left(\hat{H}\hat{L}^3+\hat{J}^2\hat{L}\right)i_{fw}^3+\left(3\hat{I}\hat{J}\hat{L}-3\hat{H}\hat{K}\hat{L}^2\right)i_{fw}^2+\left(2\hat{I}^2\hat{L}-\hat{I}\hat{J}\hat{K}+3\hat{H}\hat{K}^2\hat{L}\right)i_{fw}\\&-\hat{I}^2\hat{K}-\hat{H}\hat{K}^3=0\end{aligned}\tag{6.69}$$

Define the coefficients as:

$$\begin{cases}C_a=\hat{H}\hat{L}^3+\hat{J}^2\hat{L}\\C_b=3\hat{I}\hat{J}\hat{L}-3\hat{H}\hat{K}\hat{L}^2\\C_c=2\hat{I}^2\hat{L}-\hat{I}\hat{J}\hat{K}+3\hat{H}\hat{K}^2\hat{L}\\C_d=-\hat{I}^2\hat{K}-\hat{H}\hat{K}^3\end{cases}\tag{6.70}$$

the discriminant of the cubic function in Eq. 6.69 is:

$$\Delta=18C_aC_bC_cC_d-4C_b^3C_d+C_b^2C_c^2-4C_aC_c^3-27C_a^2C_d^2\tag{6.71}$$

If $\Delta\le 0$, there will be only one real root as in Eq. 6.72

$$\begin{aligned}i_{fw}=&-\frac{C_b}{3C_a}\\&-\frac{1}{3C_a}\sqrt[3]{\frac{1}{2}\left(2C_b^3-9C_aC_bC_c+27C_a^2C_d+\sqrt{-27C_a^2\Delta}\right)}\\&-\frac{1}{3C_a}\sqrt[3]{\frac{1}{2}\left(2C_b^3-9C_aC_bC_c+27C_a^2C_d-\sqrt{-27C_a^2\Delta}\right)}\end{aligned}\tag{6.72}$$

As discussed above, there must be at least one minimum within the practical range of interest $i_{fw}\in[0,V_{tm}/(R_{fw}+5R_{tm}+5R_{CABLE})]$, and Eq. 6.72 is the only possible minimum position solution. So it can be concluded Eq. 6.72 is the optimum solution if $\Delta\le 0$, which is the case we see during later simulations.

If $\Delta>0$, there will be three real roots for Eq. 6.69. One of them is Eq. 6.72. The other two are as listed in Eq. 6.73 and Eq. 6.74:

$$i_{fw2} = -\frac{C_b}{3C_a} + \frac{1+i\sqrt{3}}{6C_a}\sqrt[3]{\frac{1}{2}\left(2C_b^3 - 9C_aC_bC_c + 27C_a^2C_d + \sqrt{-27C_a^2\Delta}\right)} - \frac{(1-i\sqrt{3})(C_b^2 - 3C_aC_c)}{6C_a\sqrt[3]{\frac{1}{2}\left(2C_b^3 - 9C_aC_bC_c + 27C_a^2C_d + \sqrt{-27C_a^2\Delta}\right)}} \tag{6.73}$$

$$i_{fw3} = -\frac{C_b}{3C_a} + \frac{1-i\sqrt{3}}{6C_a}\sqrt[3]{\frac{1}{2}\left(2C_b^3 - 9C_aC_bC_c + 27C_a^2C_d + \sqrt{-27C_a^2\Delta}\right)} - \frac{(1+i\sqrt{3})(C_b^2 - 3C_aC_c)}{6C_a\sqrt[3]{\frac{1}{2}\left(2C_b^3 - 9C_aC_bC_c + 27C_a^2C_d + \sqrt{-27C_a^2\Delta}\right)}} \tag{6.74}$$

As discussed above, for the $\Delta > 0$case, at least one of the three real roots must fall in the range $0 < V_{fw} < V_{tm}$ and $0 < i_{fw} < V_{tm}/(R_{fw} + 5R_{tm} + 5R_{CABLE})$. The procedure will be to evaluate T(i_{fw}) at each root , and then utilize the i_{fw} that produces the smallest T(i_{fw}), in the formula (Eq. 6.67) to change the K_{fw} value in real time.

6.3.3 Simulation Results for Regenerative Braking

Simulations were carried out to simulate and compare the two above mentioned algorithms for regenerative braking. Assume a 3100 ton train (including slug car weight of 100 ton) needs to be stopped from an initial speed of 60MPH. The regenerative braking will take place until the air brake kicks in at 11MPH.Each flywheel was original charged to 25kWh. The total flywheel energy before the regenerative braking is 250kWh. The flywheel charging current limit was set at 200 Amps. In the later sections of the dissertation, the method discussed in 6.3.1 will be referred as ‘maximum recovery

method'. The method discussed in 6.3.2 will be referred as 'balanced recovery method'. Since the balanced recovery method will be used in the real world applications due to its controllable characteristics, this dissertation will mainly focus on its discussion. The maximum recovery method will act as a benchmark for the balanced recovery method.

For a K_{tm} value of 4 (Nm/A) and b value equals to 25, an exemplary case of the balanced energy recovery method was first simulated. The train travel velocity and distance are as shown in Fig. 6.6. The train will be stopped at 5.77min with a distance of 3 miles. The flywheel speed changed from 2590RPM to 3321RPM as shown in Fig. 6.7. Around 160.0kWh of energy was recovered by flywheel as in Fig. 6.8. The maximum K_{fw} value is 7.94NM/A and appears at the initial phase of braking. The energy conversion chart is as in Fig. 6.9. After braking, around 58.4% of the total kinetic energy was recovered by the flywheel energy storage system. Around 19.3% energy was lost due to Davis forces. Resistance loss consumed 19.1% of total energy. During the final phase of braking, 3.2% went to air brake loss. The voltage and current information during braking can be seen in Fig. 6.10.

By varying the b value, system performance was evaluated for K_{tm}=4. The energy recovery value vs. b value is presented in Fig. 6.11. As can be seen, within the reasonable range (b=0-60), the energy recovered monotonically increases with the b value. The maximum energy recovery value is around 163.4kWh at b=52. With a bigger b value, the recovered energy curve runs flat and even starts to bend downward slowly. This is because the flywheel voltage is too close to the traction motor voltage at very high b value and the current goes through the R_{BRAKE} in Fig. 6.3 cannot be neglected.

This conclusion was verified by two cases. First, if the R_{BRAKE} is increased, the slope of the energy recovery curve will be flatter. Second, with a higher traction motor voltage (higher K_{tm}), the trailing curve bends quicker (Fig. 6.12). This is because a higher traction motor voltage will incur a bigger leakage current through R_{BRAKE}. The braking distance vs. *b* curve is as in Fig. 6.13. Fig. 6.14 shows the relationship between recovered energy and its corresponding braking distance.

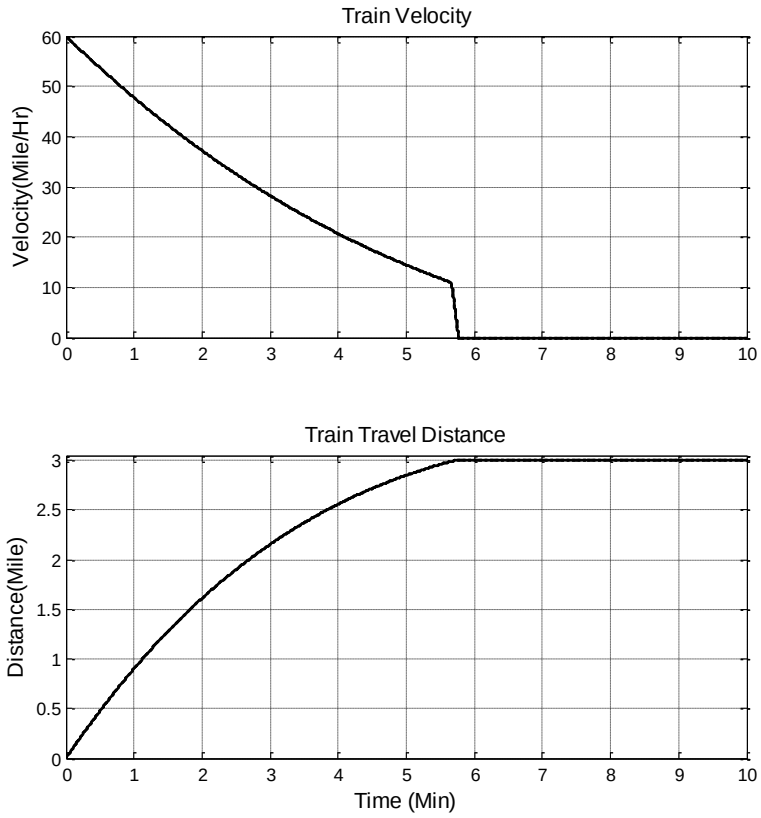

Fig. 6.6 Train Speed and Distance for Balanced Recovery Method (K_{tm}=4,*b*=25)

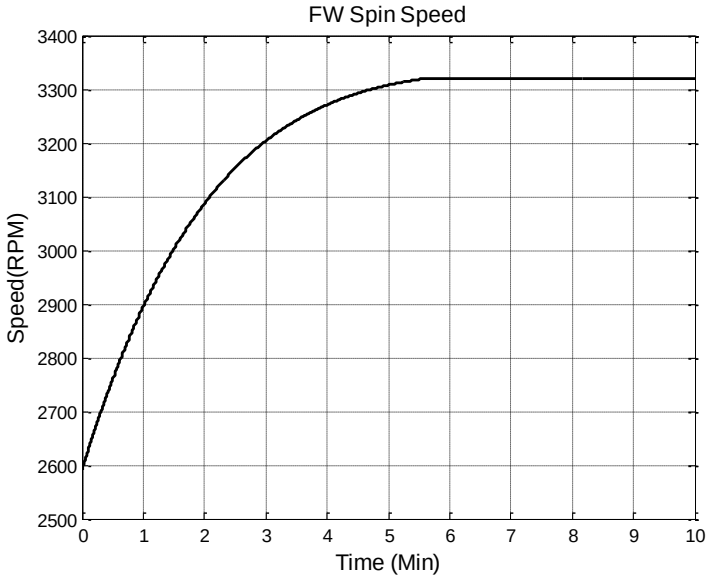

Fig. 6.7 Flywheel Speed and Distance for Balanced Recovery Method (K_{tm}=4,b=25)

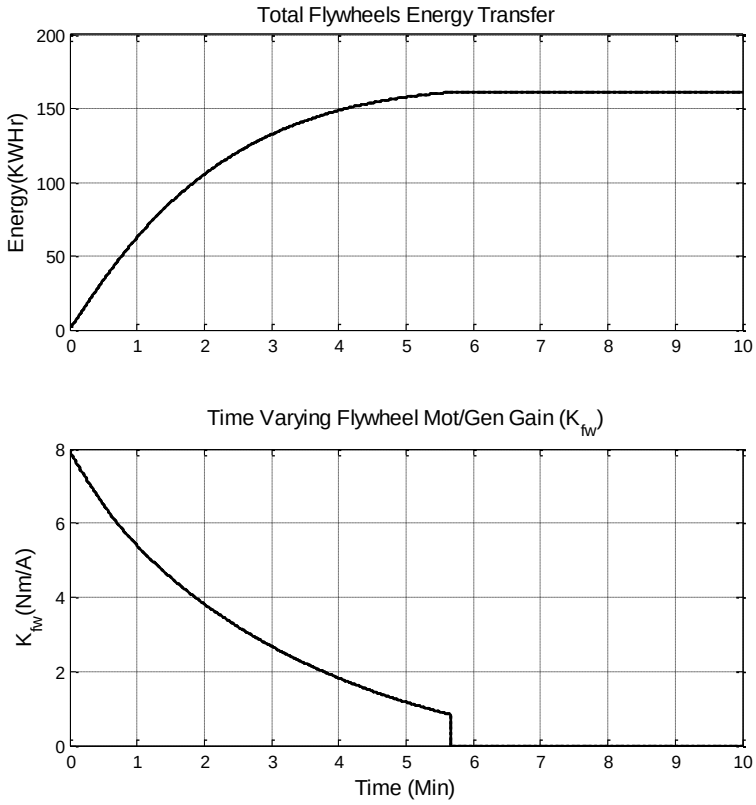

Fig. 6.8 Energy Recovery and K_{fw} for Balanced Recovery Method (K_{tm}=4,b=25)

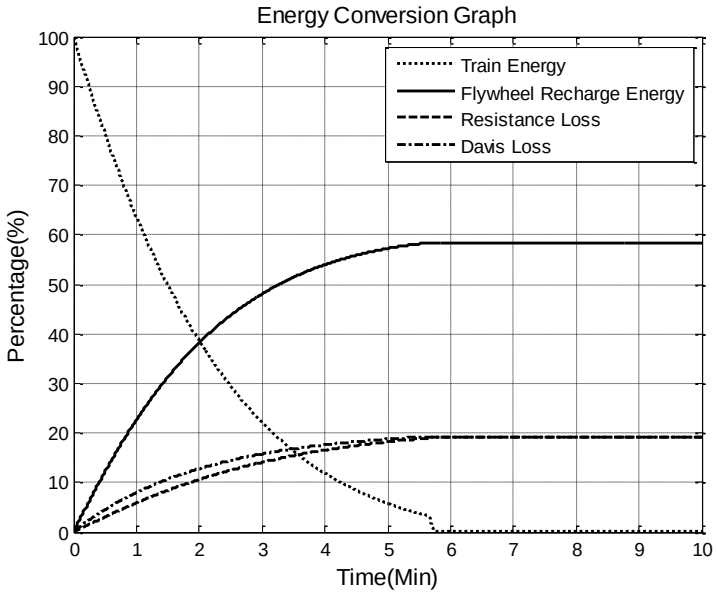

Fig. 6.9 Energy Distribution for Balanced Recovery Method (K_{tm}=4,b=25)

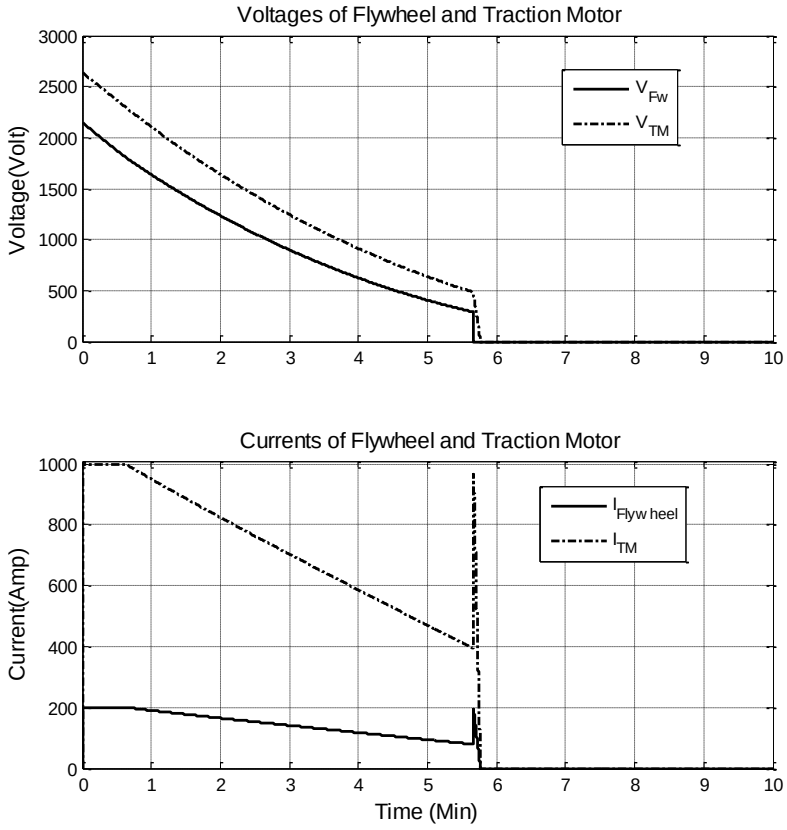

Fig. 6.10 Voltage and Current for Balanced Recovery Method (K_{tm}=4,b=25)

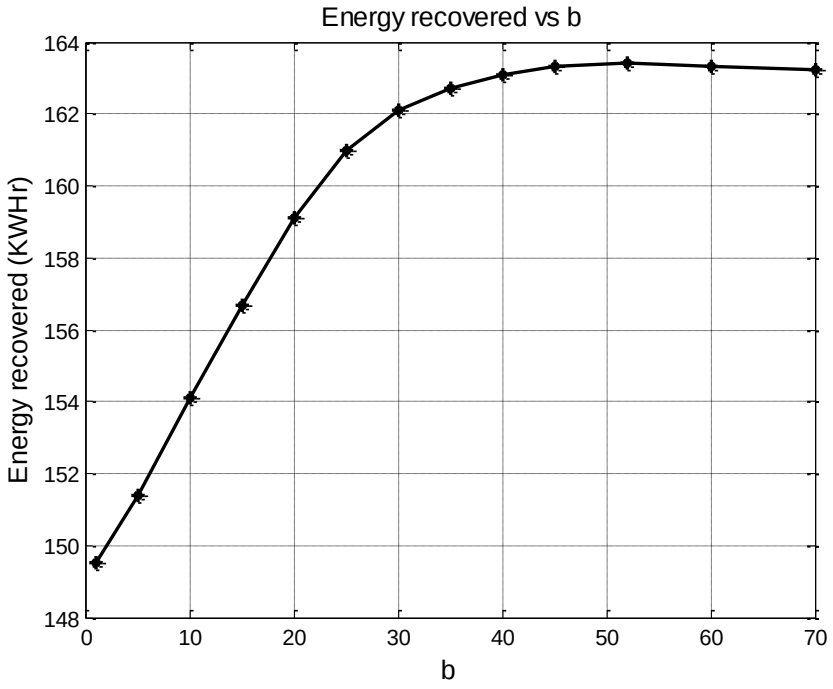

Fig. 6.11 Energy Recovery vs. b Value for Balanced Recovery Method (K_{tm}=4)

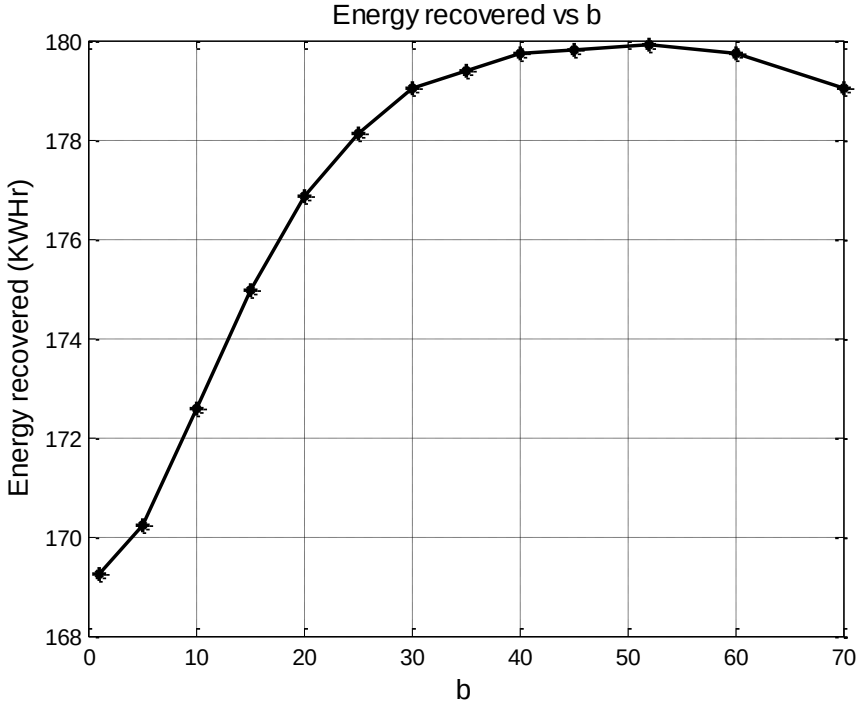

Fig. 6.12 Energy Recovery vs. b Value for Balanced Recovery Method (K_{tm}=5)

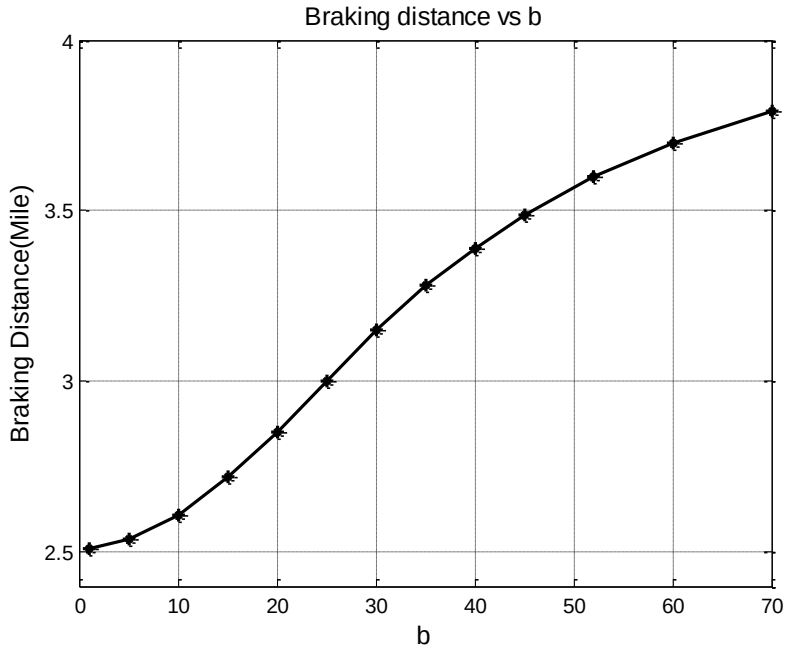

Fig. 6.13 Braking Distance vs. b Value for Balanced Recovery Method (K_{tm}=4)

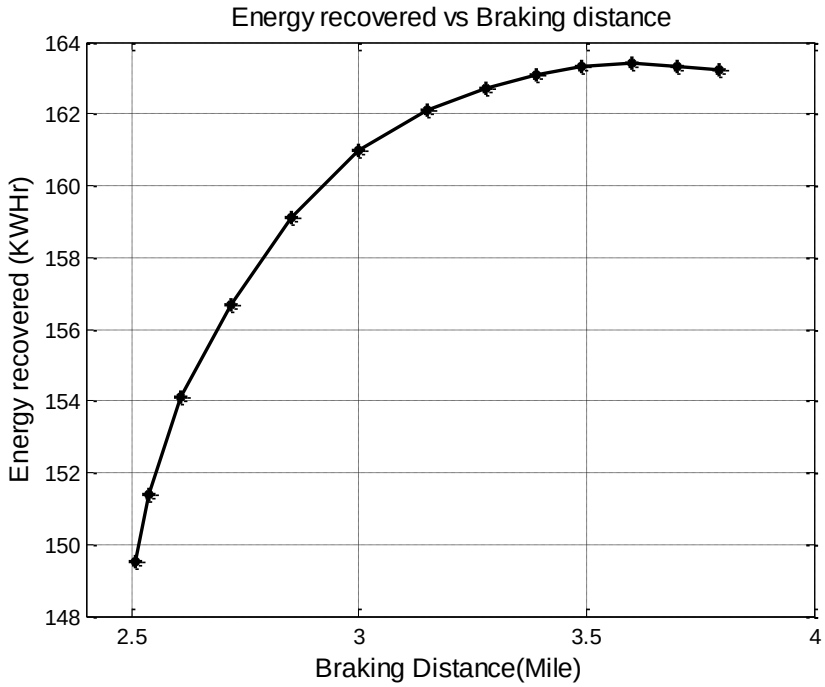

Fig. 6.14 Energy vs. Braking Distance Value for Balanced Recovery Method (K_{tm}=4)

As a benchmark to the balanced recovery method, a case was simulated using maximum recovery method with K_{tm}=4Nm/A. As shown in Fig. 6.15, the Energy recovered is around 162.3kWh, which is very close to the maximum energy can be recovered by the balanced recovery method. The maximum K_{fw} required during the whole process is biggest at the beginning and the value equals to 8.4 Nm/A. The energy distribution percentage during the braking is as in Fig. 6.16. Around 58.9% of the kinetic energy was recovered by the flywheels. Davis forces contribute around 26.6% of total kinetic energy loss. 11.3% of total energy was wasted on Resistance losses. 3.2% went to air brake loss during the final phase of train braking.

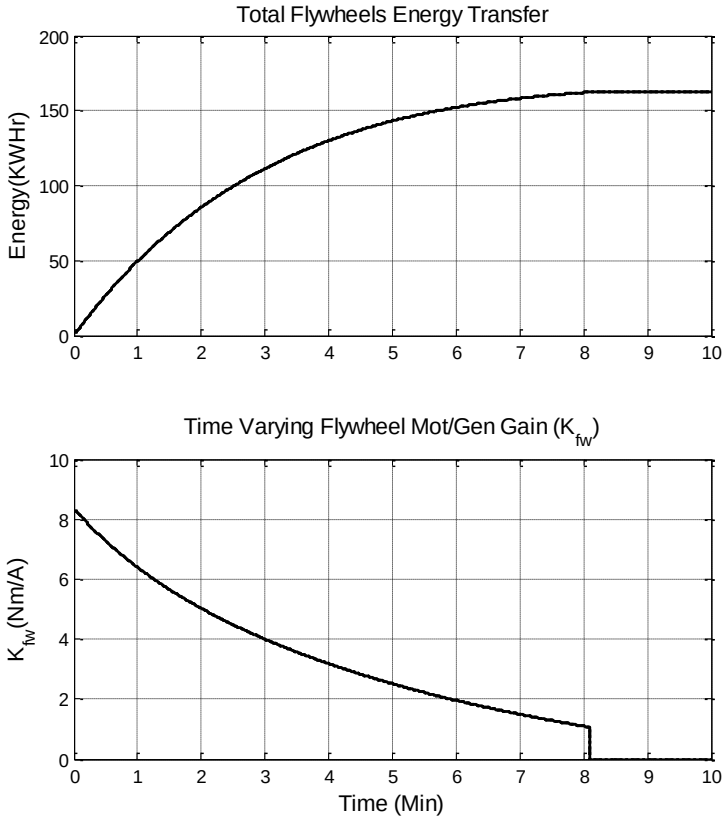

Fig. 6.15 Energy Recovery and K_{fw} for Maximum Recovery Method (K_{tm}=4)

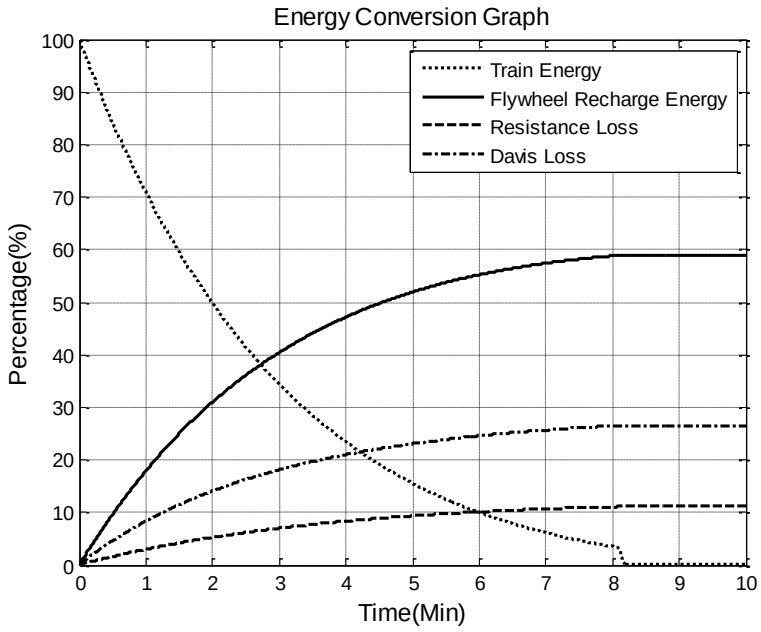

Fig. 6.16 Energy Distribution for Maximum Recovery Method (K_{tm}=4)

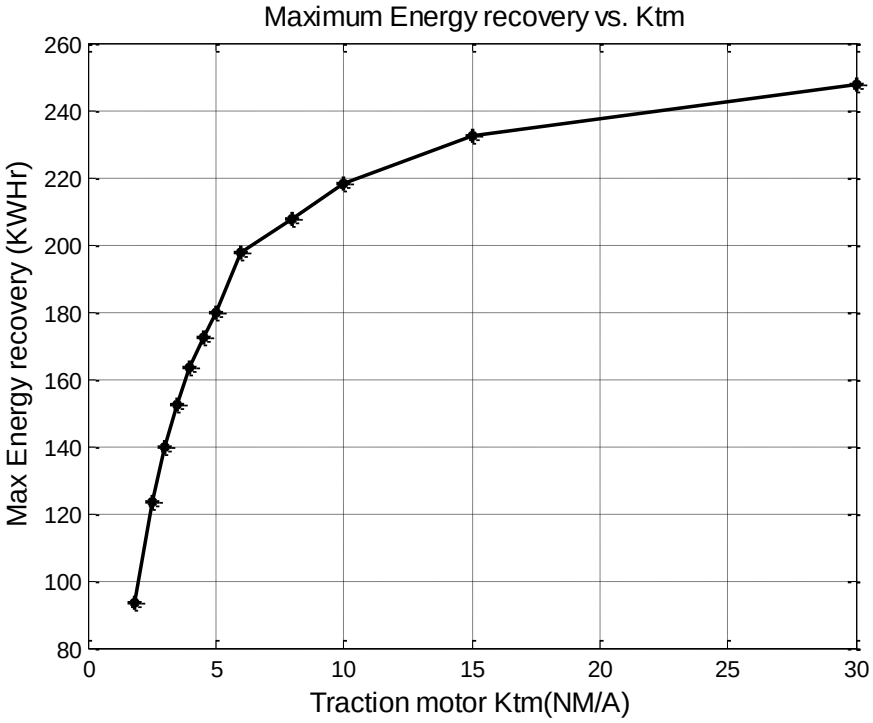

Fig. 6.17 Maximum Energy Recovery vs. K_{tm} for Balanced Recovery Method

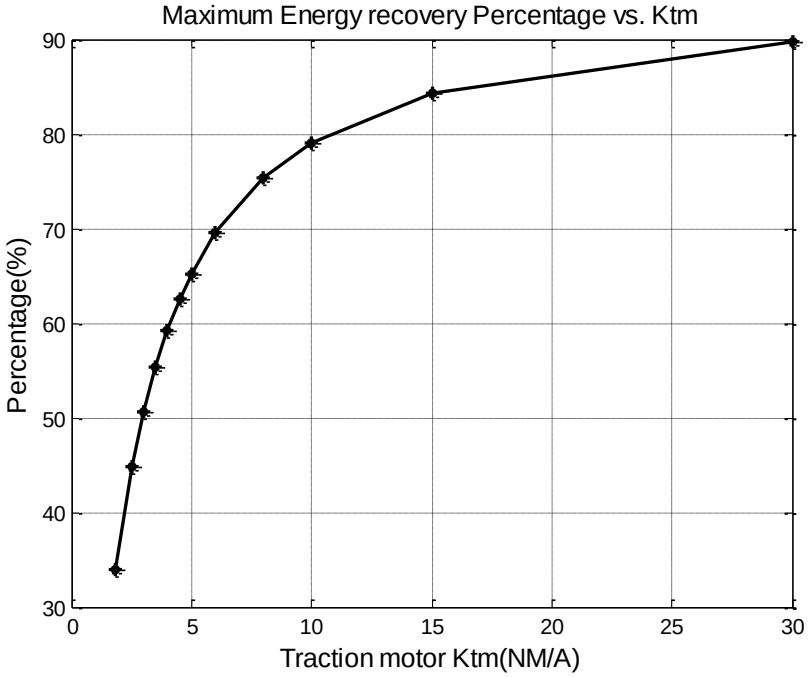

Fig. 6.18 Maximum Energy Recovery Percentage vs. K_{tm} for Balanced Method

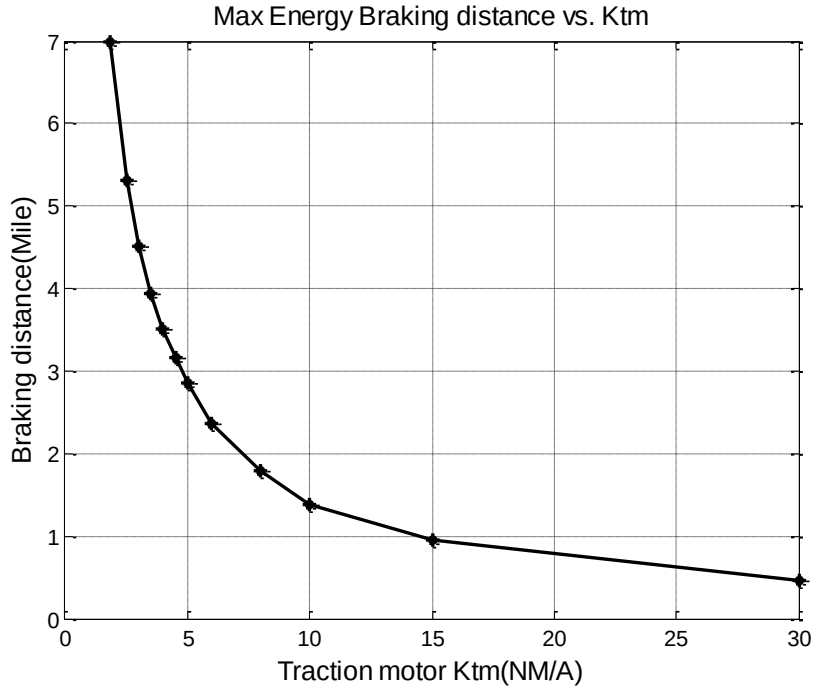

Fig. 6.19 Braking Distance for Maximum Energy vs. K_{tm} for Balanced Recovery Method

By comparing Fig. 6.11 and Fig. 6.12, it is easy to find out that the K_{tm} value has big effects on the energy can be recovered. This is easily understandable since a bigger K_{tm} means a bigger traction motor voltage at any given speed and hence a bigger charging capability for the traction motors. This in turn shortens the time needed to charge the flywheel and reduce the energy loss due to Davis forces and resistance loss. Fig. 6.17 shows the maximum energy that can be recovered corresponding to each given *b* value. Fig. 6.18 shows the maximum percentage of kinetic energy that can be recovered at different *b* values. As can be seen, the percentage can be low 30s at small K_{tm} value and nearly 90 with very high K_{tm}. The braking distances corresponding to maximum energy recovery were plotted as in Fig. 6.19. It is shown that a high K_{tm} value will not only lead to a bigger energy recovery percentage but also make the train stop at a shorter distance. These conclusions show that, to increase the regenerative braking efficiency, in addition to using the optimized charging algorithm discussed above, one should also try to maximize the K_{tm} value under the given physical system constraints.

6.4 Simulation of Energy Storage System Effect on Railway Locomotives

Before carrying out the simulations on the train operations, K_{tm} needs to be retrieved. [50] provided a plot on traction motor characteristics for the D77 traction motor used on a SD40 diesel locomotive. The K_{tm} values retrieved from voltage and speed relationships in [50] was plotted as Fig. 6.20. As shown in the previous section of the dissertation, a higher traction motor constant traction motor constant K_{tm} will lead to a better behavior during regenerative braking. So a constant K_{tm} of 5 Nm/A was used in the following simulations to have a conservative estimation of the performances that we

are interested in.

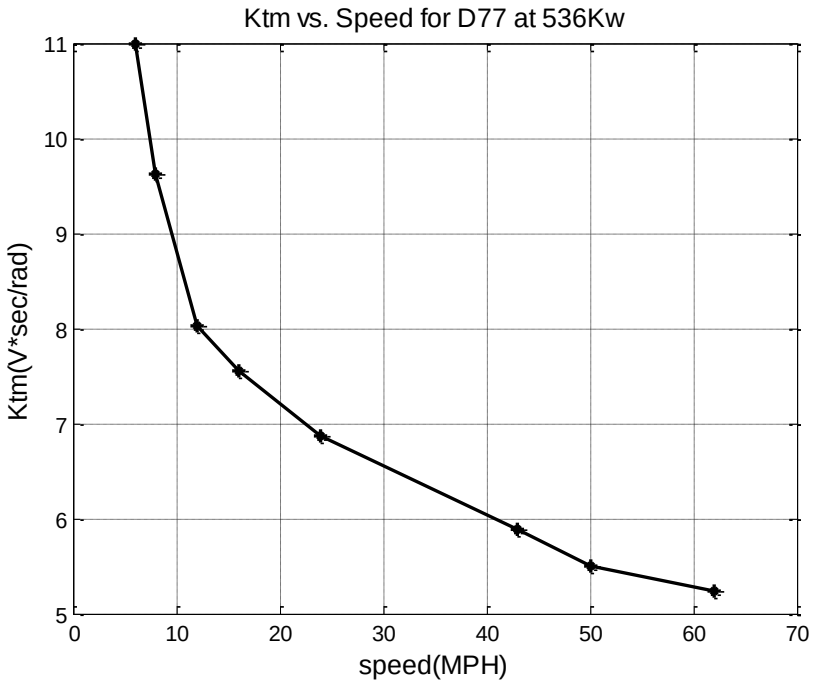

Fig. 6.20 D77 Traction Motor K_{tm} Calculated from [50]

6.4.1 Hybrid Line Haul Simulation

Since time logging data during railway operations is private for each railway companies, the best data the author can get is the EPA average schedule for the line haul operation as shown in the Table 6.1. A corresponding engine notch scheduling was calculated. Following this schedule, a 3000ton (no flywheel slug car) diesel train is simulated for a 3 hr. trip. As was shown in Fig. 6.21 and Fig. 6.22, the train traveled for about 51.7 Miles and reached a maximum velocity of about 61.5 Mile/Hr before the braking period during each cycle. The corresponding fuel consumption and NOx emissions are shown to be 171.0Gallon and 37.24Kg, respectively.

Table 6.1 EPA Average Line Haul Schedule Derived from [10]

Diesel Power Setting (DPS)	Gallon Per Hour + *dF/dt*	Power in [kW]	[kWh] per gallon	Engine Load Factor*	Line Haul Wgt. ** [%]	[Gallon] per Hour ++	[kWh] per Hour ++	[kg] of NO_X Per Hour+ dM_N/dt	[kg] of NO_X per Hour ++
Brake	23	88.4	3.84	0.028	12.5	2.9	11	1.34	0.17
Idle	4.4	18.7	4.3	0.0061	38.0	1.67	7.1	0.31	0.12
1	10.7	145.5	13.6	0.0475	6.5	0.69	9.5	1.30	0.08
2	23.6	298.4	12.7	0.0975	6.5	1.53	19.4	3.0	0.2
3	52.6	708.7	13.4	0.231	5.2	2.74	36.9	7.3	0.38
4	72.1	1044.4	14.5	0.341	4.4	3.2	46	14.0	0.62
5	103.6	1529.3	14.8	0.50	3.8	3.93	58.1	25.6	0.97
6	132.5	2066.4	15.6	0.675	3.9	5.2	80.6	33.6	1.31
7	161.6	2566	15.9	0.839	3.0	4.8	77	39.8	1.2
8	193.8	3058.6	15.8	1.000	16.2	31.4	495.5	47.0	7.6
						58.05	841.		12.67

* Fraction of Full Engine Power ** Percent of time at given diesel power setting
\+ For the given **Diesel Power Settings DPS** ++ For the given DPS and Line Haul Weight

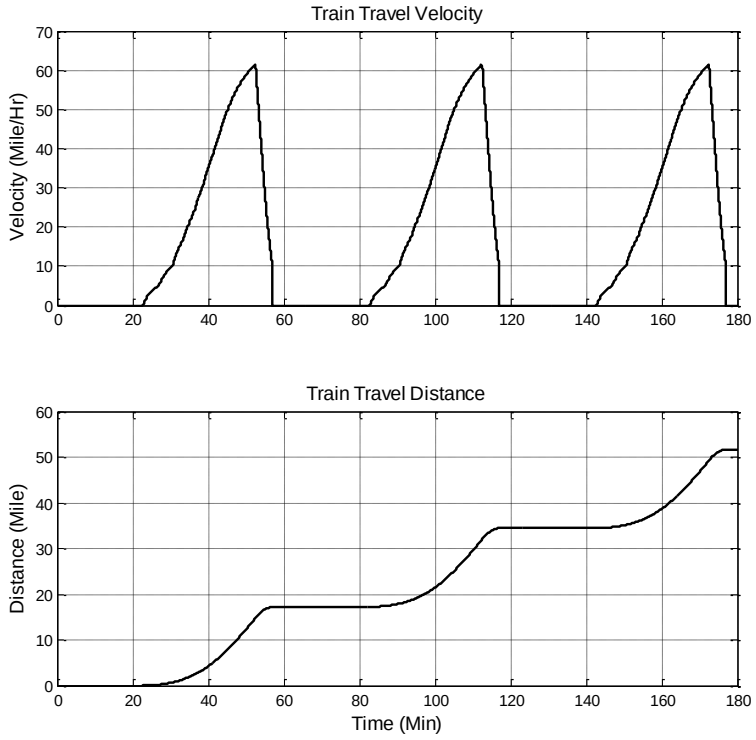

Fig. 6.21 Diesel Line Haul Travel Velocity and Distance

A hybrid line haul train was then simulated. The total weight of the train was increased by 100 ton to take into account the additional slug car. In real world applications, there will be slug car loaded with stones to increase the traction of the locomotive. Since these wasteful loads can be substituted by our flywheel assemblies, the actual additional weight by implementing the energy storage system can be way lower than the 100 ton used. This will lead to a better performance than what we predict here.

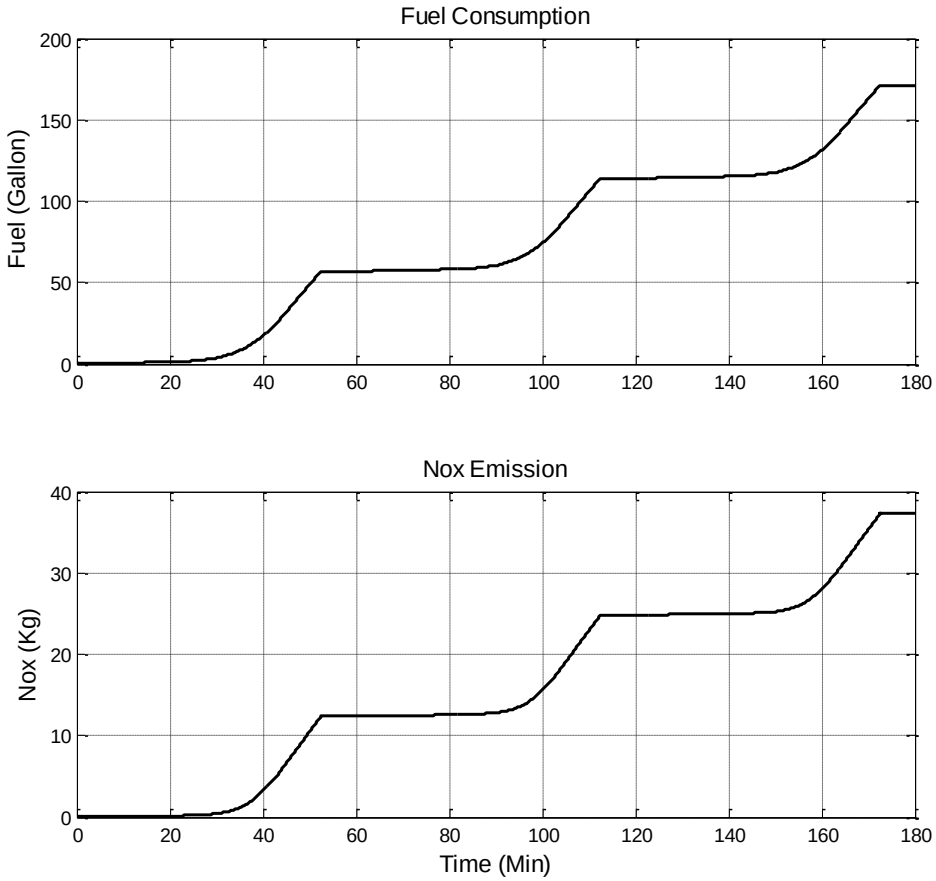

Fig. 6.22 Diesel Line Haul Fuel Consumption and NOx Emission

For the hybrid train, the idling power and notch 1-6 power will be supplied by the flywheel energy storage system. The power setting will be increased to count in the additional 100ton weight of the slug cars. Notch 7 and notch 8 will still be supplied by the diesel engine of the locomotives since they are the most efficient diesel notch settings. The power values during Notch 7 and 8 remain unchanged since they are fixed by diesel engines. Since the slug car and diesel engine have separate traction motors, the switching between flywheel power and diesel power pretty easy. Regenerative braking algorithm was used during braking phase with b=25.

A three hour operation of the hybrid line haul was simulated. The 10 flywheel energy storage system was initially charged to 900kWh (1205HPHr). The total distance traveled is 51.5Miles with a peak train velocity of 60.7MPH (Fig. 6.23). Flywheel spinning speed during the operation is as shown in Fig. 6.24. The flywheels were initially charged to 4915RPM, and then reached a minimum of 4303RPM during operations. The flywheels finally spin at a speed of 4864RPM after regenerative braking. Fig. 6.25 and Fig. 6.26 give out the voltage, current and power information about the flywheels and traction motors during the 3hr simulation. After the whole process, the flywheel energy storage system has a remaining energy of 882kWh, as can be seen in Fig. 6.27. This means that the regenerative braking recovered nearly 100% of the flywheel energy. It was made possible since the train was accelerated to a higher kinetic energy with energy of notch 7 and 8. The adhesion value was also plotted as Fig. 6.28. The adhesion value stays in a relatively safe range except during the phase of air braking. This proves that our simulation does not have a traction problem.

As is shown in Fig. 6.29, during the 3 hour process, the total fuel consumption is 113.1 gallon, with a total NOx emission of 26.10kg. Compared with the diesel case, this is a 33.9% fuel reduction with 29.9% NOx reduction. Using the rain flow counting algorithm [51], the stress cycles within the three hour operation of the hybrid line haul is as shown in Fig. 6.30(the final point is the recharging of the flywheel back to 900kWh). Using the S-N curve and method used in Chapter II of this dissertation, the S-N life for non-notched discs are 3e6 cycles (infinite). With the fatigue calculation method used in Chapter II, it takes 80k simulated cycles for a 0.02in crack at the weakest location to grow to a critical size. This converts to a 240k hours of operation, or more than 27 years for a 3 shift operation of the locomotive.).

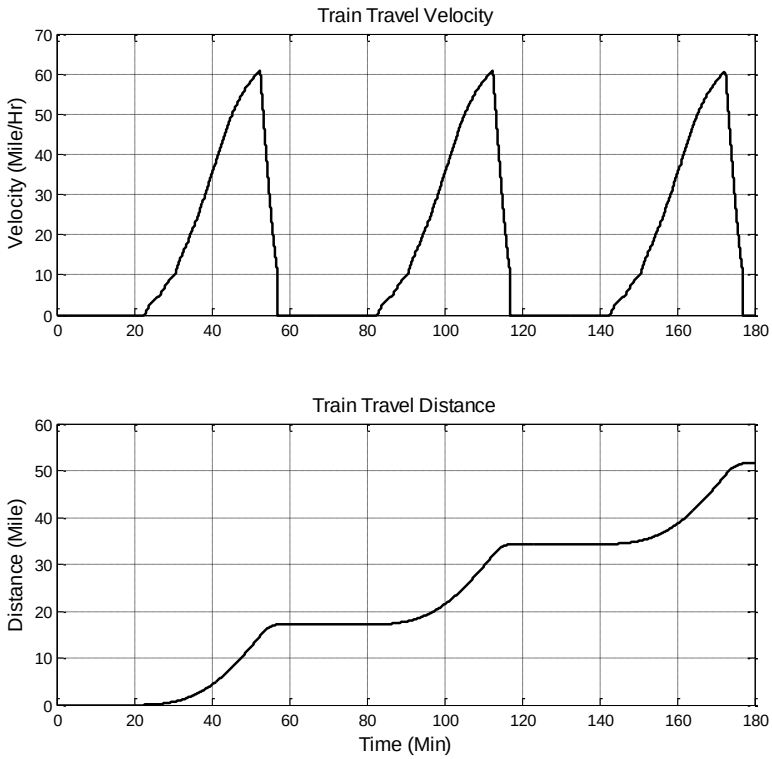

Fig. 6.23 Hybrid Line Haul Travel Velocity and Distance

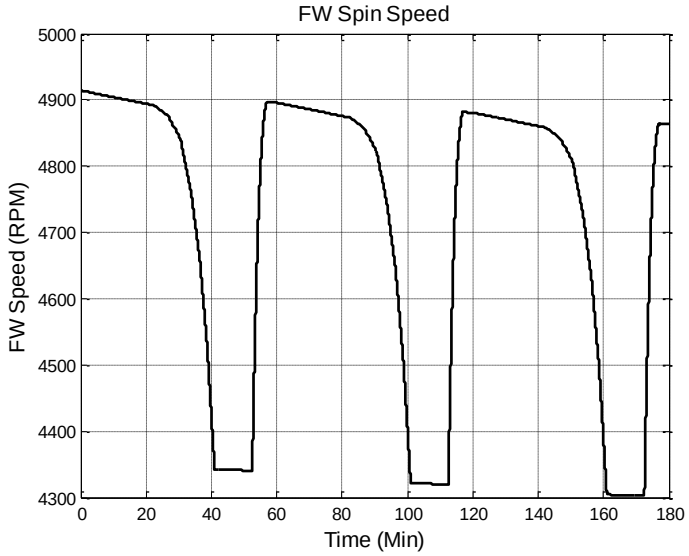

Fig. 6.24 Hybrid Line Haul Flywheel Spin Speed

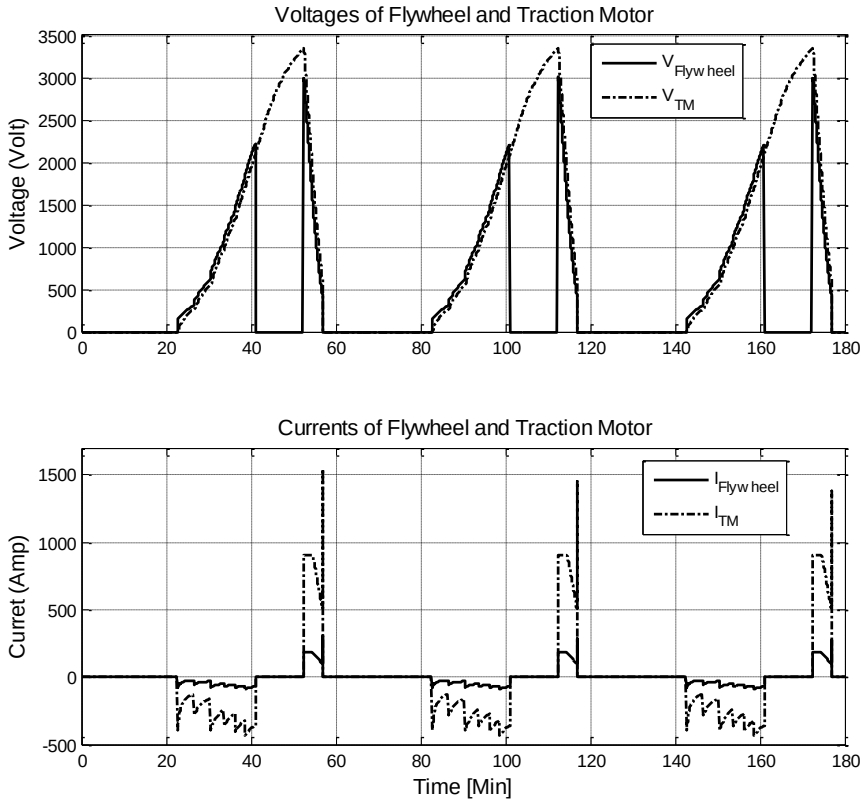

Fig. 6.25 Hybrid Line Haul Voltage and Currents for Flywheels and Traction Motors

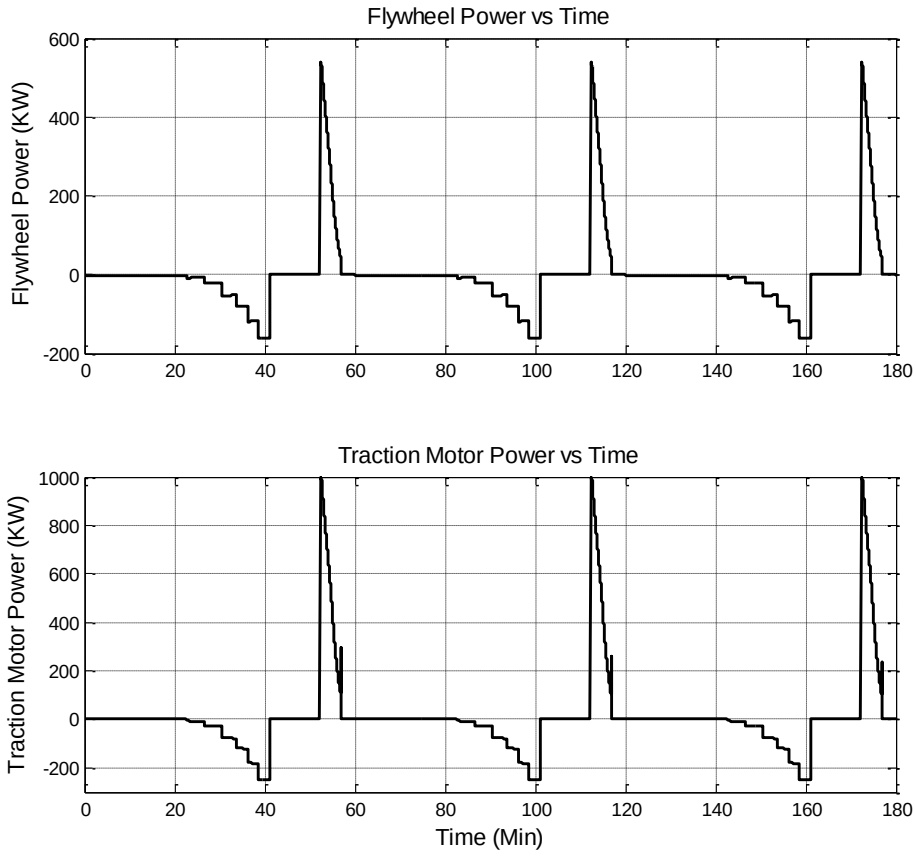

Fig. 6.26 Hybrid Line Haul Flywheel and Traction Motor Power

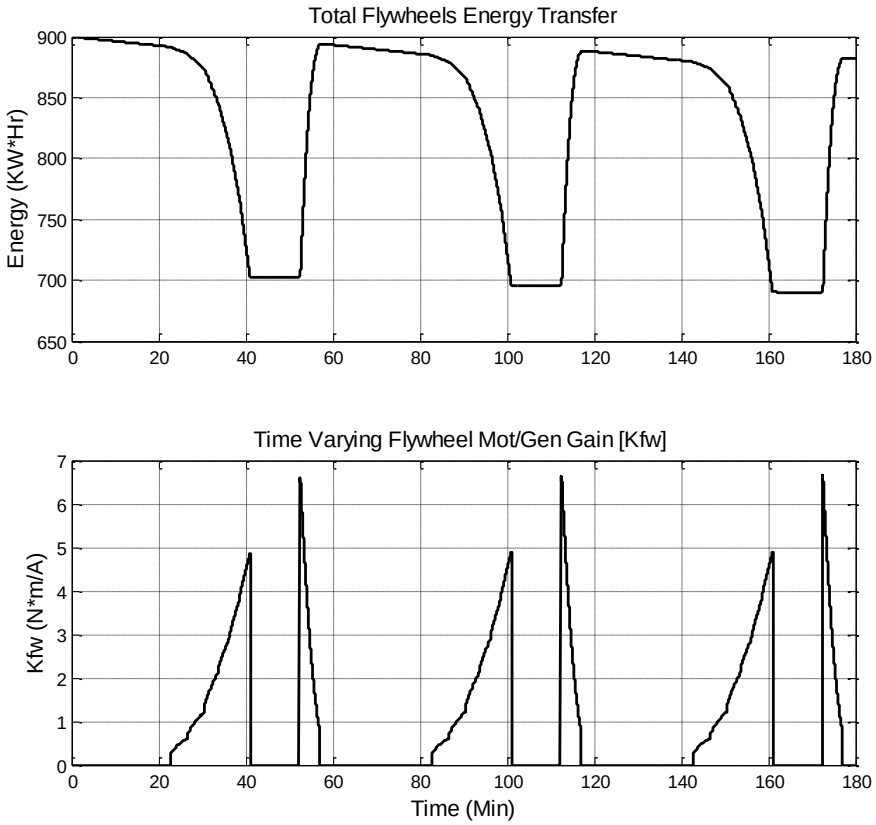

Fig. 6.27 Hybrid Line Haul Flywheel Energy and K_{fw} Values

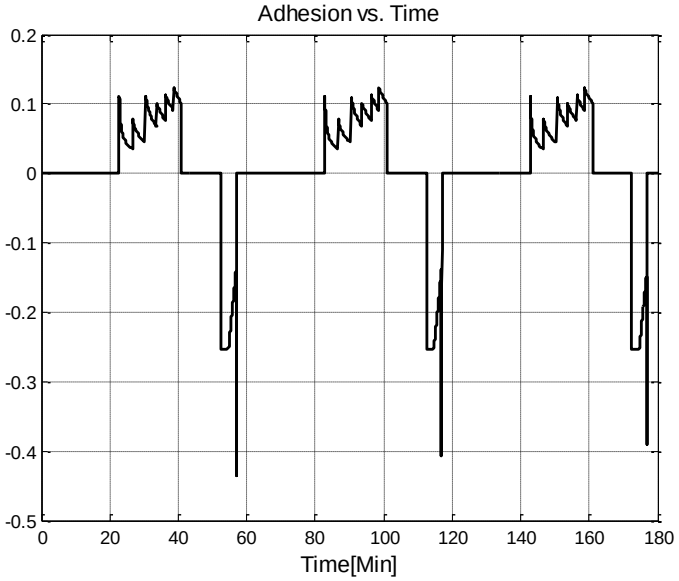

Fig. 6.28 Hybrid Line Haul Adhesion Values

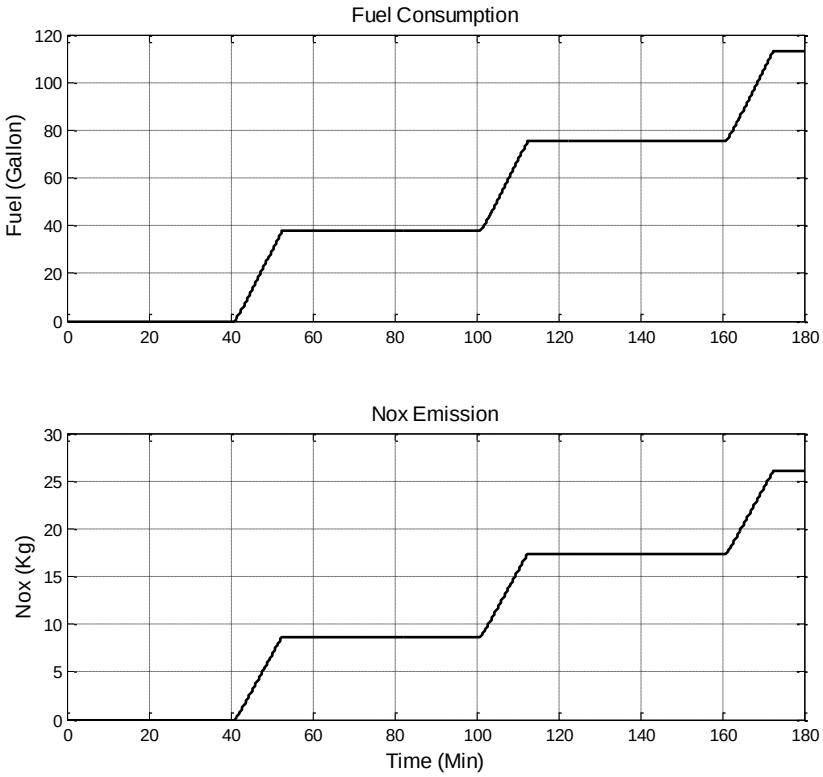

Fig. 6.29 Hybrid Line Haul Fuel Consumption and NOx Emission

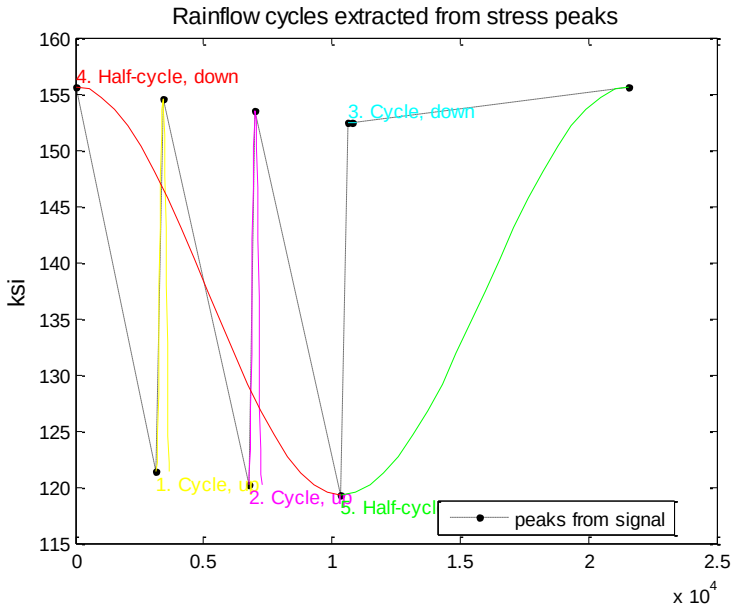

Fig. 6.30 Hybrid Line Haul Flywheel Peak Stress Rain Flow Counting

6.4.2 All Flywheel Powered Switcher Simulation

The EPA average schedule for the Switcher Service and the corresponding engine notch scheduling are as shown in the Table 6.2. Following this schedule, a 3000ton (no flywheel slug car) diesel switcher (together with its loads) is simulated for a 1 hr. trip. As was shown in Fig. 6.31 and Fig. 6.32, the switcher traveled for about 19.0 Miles with a maximum velocity of about 36.5 Mile/Hr before braking during each cycle. The corresponding diesel consumption is 60.2gallon. The total NOx emissions are 10.57kg.

The switcher will stay in the train stations, where the electric outlet is readily available and easily accessible. In addition to this, the duration of notch 7 and 8 in switcher services is relatively short comparing to the Line Haul service. So it was decided that the flywheel energy storage system can supply the power needs for all notch settings and an all flywheel powered switcher was simulated.

An additional weight of 100ton was added to the switcher system to take into account the additional slug car. The notch 1-8 power values will be increased proportionally to count in the additional weight increase. Totally three hours' operation of the all flywheel powered switcher was simulated. The 10 flywheel energy storage system was also initially charged to 900kWh. The total distance traveled is 19.0 Miles with a peak train velocity of 36.5MPH (Fig. 6.33). Fig. 6.34 plotted the flywheel spinning speed during the operation. The flywheels were initially charged to 4915RPM, and then reached a minimum of 3442RPM during the last hour of operation. After the regenerative braking phase of the last cycle, the flywheels finally spin at a speed of 3678RPM. Fig. 6.35 and Fig. 6.36 provided the voltage, current and power information

about the flywheels and traction motors during the whole process.

Table 6.2 EPA Average Switcher Schedule Derived from [10]

Diesel Power Setting (DPS)	Gallon Per Hour + dF/dt	Power in [kW]	[kWh] per gallon	Engine Load Factor*	Switch Wgt. ** [%]	[Gallon] per Hour ++	[kWh] per Hour ++	[kg] of NOx Per Hour+ dMN/dt	[kg] of NOx per Hour ++
Brake	23	88.4	3.84	0.028	0	0	0	1.34	0
Idle	4.4	18.7	4.3	0.0061	59.8	2.63	11.18	0.31	0.19
1	10.7	145.5	13.6	0.0475	12.4	1.33	18.04	1.30	0.16
2	23.6	298.4	12.7	0.0975	12.3	2.91	36.70	3.0	0.37
3	52.6	708.7	13.4	0.231	5.8	3.05	41.10	7.3	0.42
4	72.1	1044.4	14.5	0.341	3.6	2.60	37.60	14.0	0.50
5	103.6	1529.3	14.8	0.50	3.6	3.73	55.05	25.6	0.92
6	132.5	2066.4	15.6	0.675	1.5	1.99	31.00	33.6	0.50
7	161.6	2566	15.9	0.839	0.2	0.032	5.13	39.8	0.08
8	193.8	3058.6	15.8	1.000	0.8	0.155	24.47	47.0	0.38
						18.43	260.27		3.52

* Fraction of Full Engine Power ** Percent of time at given Diesel Power Setting
\+ For the given Diesel Power Setting DPS ++ For the given DPS and Line Haul Weight

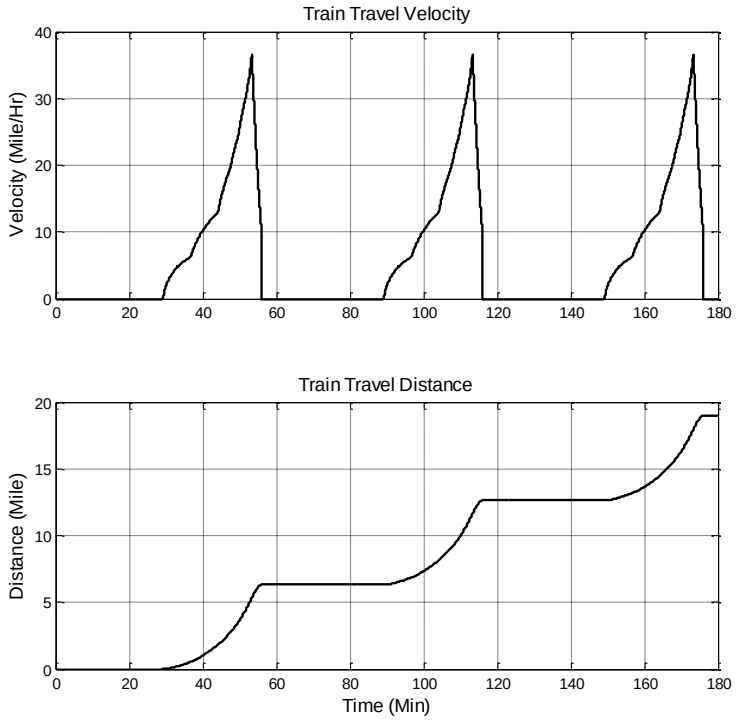

Fig. 6.31 Diesel Switcher Travel Velocity and Distance

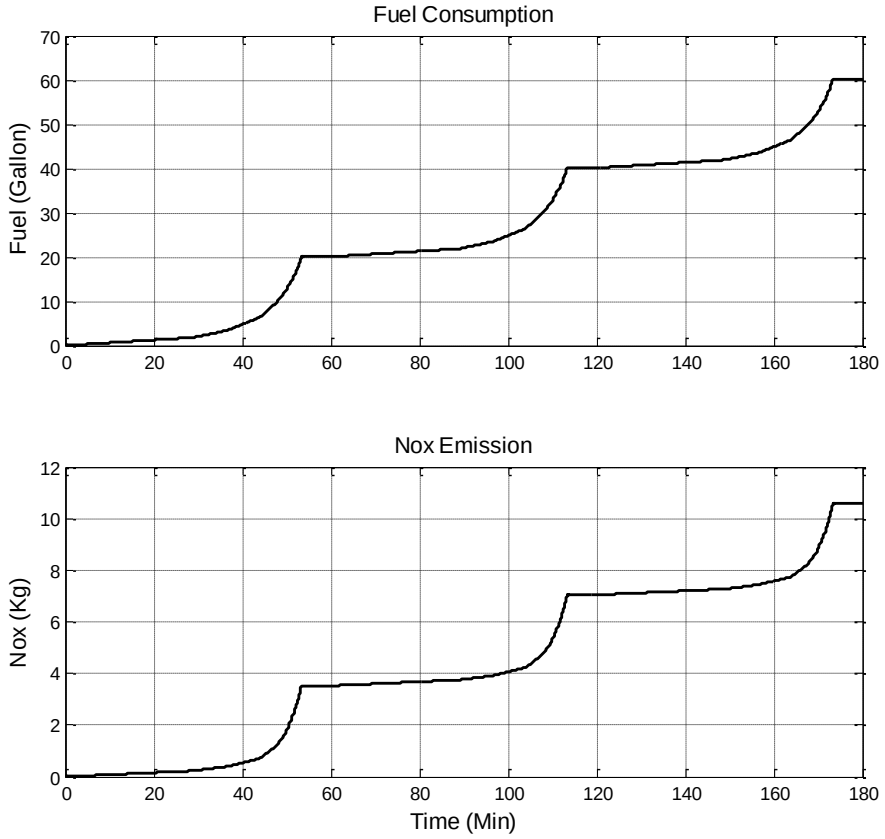

Fig. 6.32 Diesel Switcher Fuel Consumption and NOx Emission

After the whole 3 hour operation, the flywheel system has a remaining energy of 504kWh, which can be seen in Fig. 6.37. The maximum K_{fw} needed is 6.25Nm/A, which appeared during the last cycle since the same power needs to be delivered at a lower flywheel speed. The regenerative breaking only recovered around 32% of the energy used in each cycle. This is because all kinetic energy of the switcher was generated via flywheel power and there is no extra energy to cover the losses of the operations and efficiency of the regenerative braking. The adhesion values were plotted as Fig. 6.38. Similar to the hybrid line haul case, this plot proves the flywheel powered switcher will not have a traction problem.

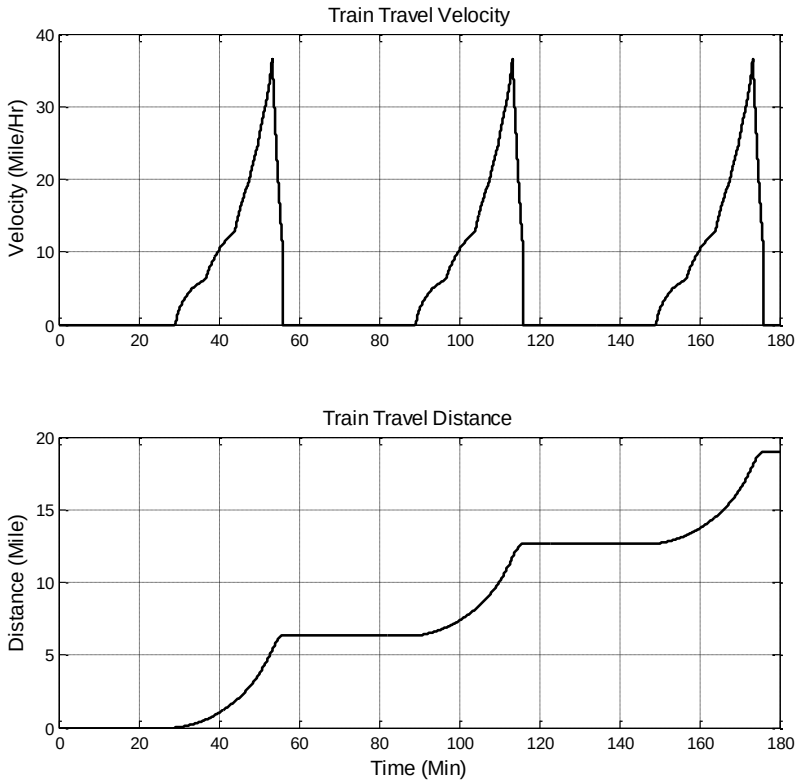

Fig. 6.33 Flywheel Powered Switcher Travel Velocity and Distance

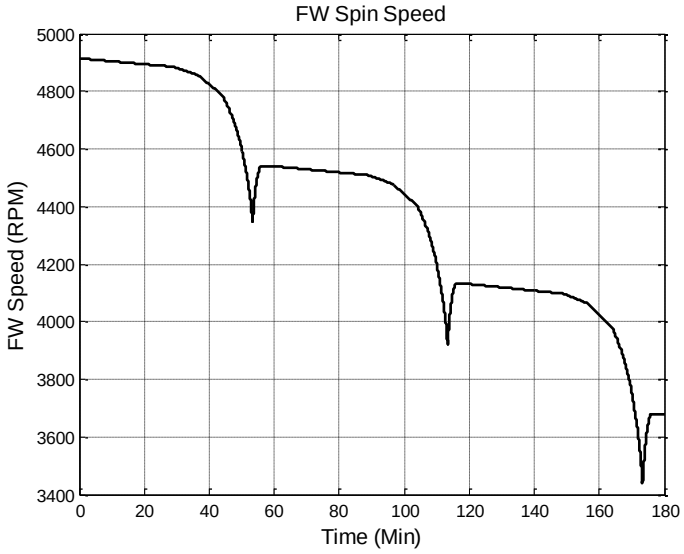

Fig. 6.34 Flywheel Powered Switcher Flywheel Spin Speed

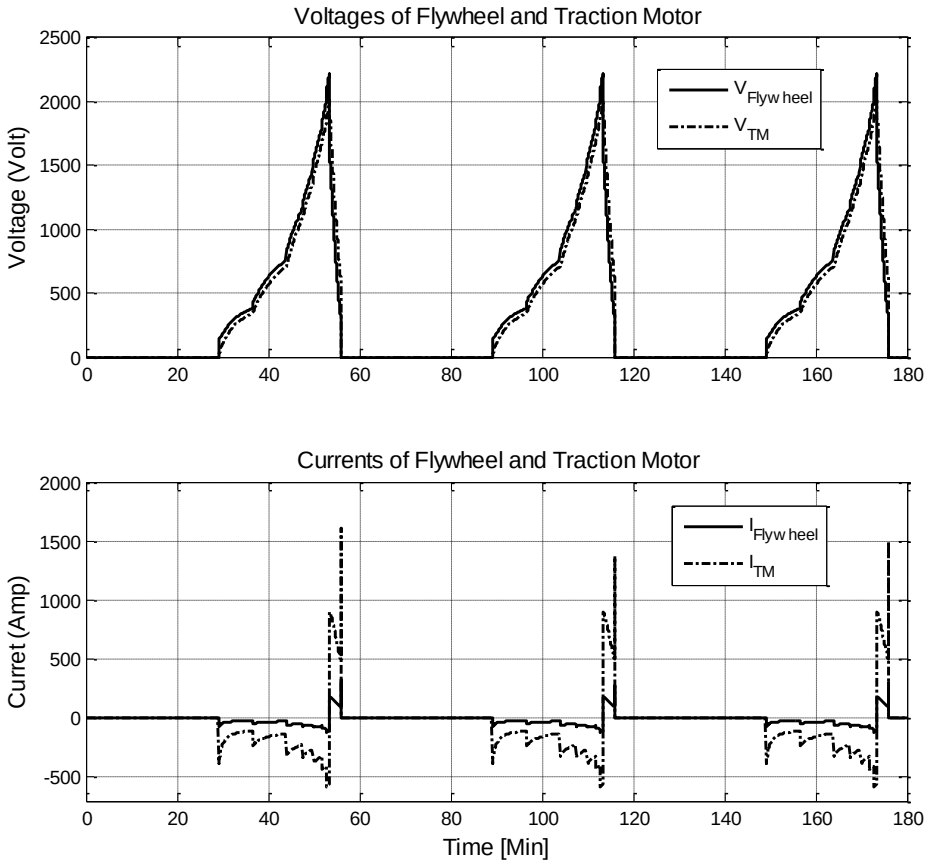

Fig. 6.35 Flywheel Powered Switcher Voltages and Currents

As is shown in Fig. 6.39, since only electric energy is used, there is zero diesel consumption and zero NOx emission for the flywheel powered switcher. This is a 100% fuel reduction with 100% NOx reduction. The stress cycles, considering the recharging of the flywheel system, were counted using rain flow counting algorithm [51] as in Fig. 6.40. Using method provided in Chapter II, the S-N lives for non-notched flywheels are 72992 cycles. This equals 218976 hours (25 years) of continuous operation. It will take 15k simulated cycles for a 0.02in through-the-thickness crack at the weakest location to grow to a critical size. This converts to a 45k hours of operation, or more than

5 years for a continuous 24hr operation of the switcher and 15 years for a single shift operation of the switcher. The lives of the flywheels will be greatly improved if they get recharged every one or two hours since this will reduce the depth of discharge and stress variation within the flywheels.

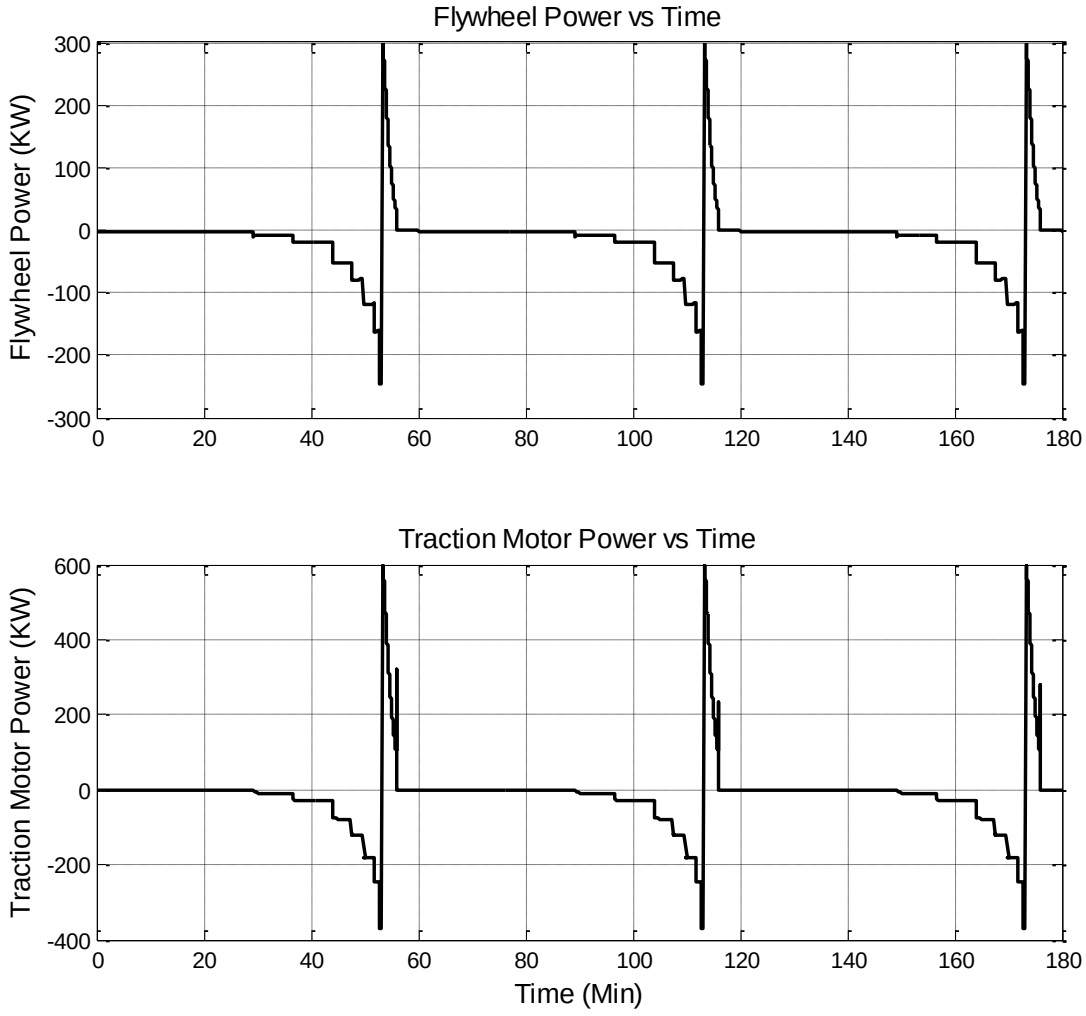

Fig. 6.36 Flywheel Powered Switcher Flywheel and Traction Motor Power

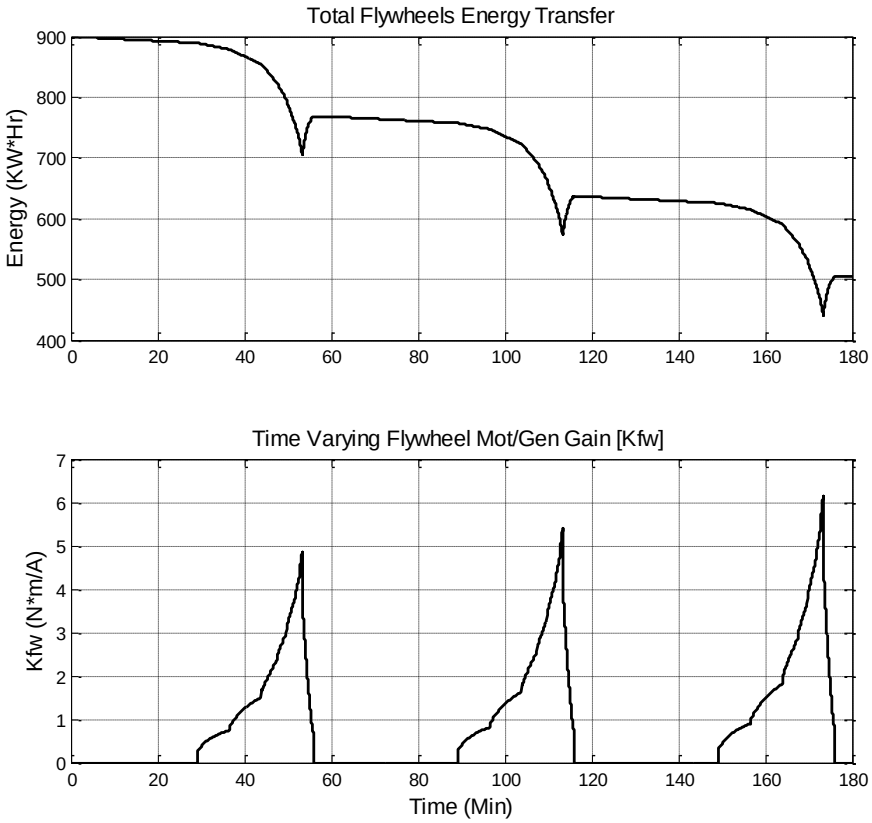

Fig. 6.37 Flywheel Powered Switcher Flywheel Energy and K_{fw} Values

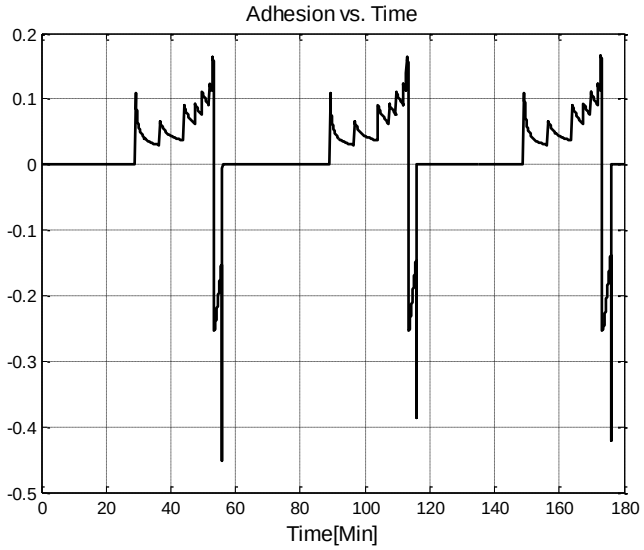

Fig. 6.38 Flywheel Powered Switcher Adhesion Values

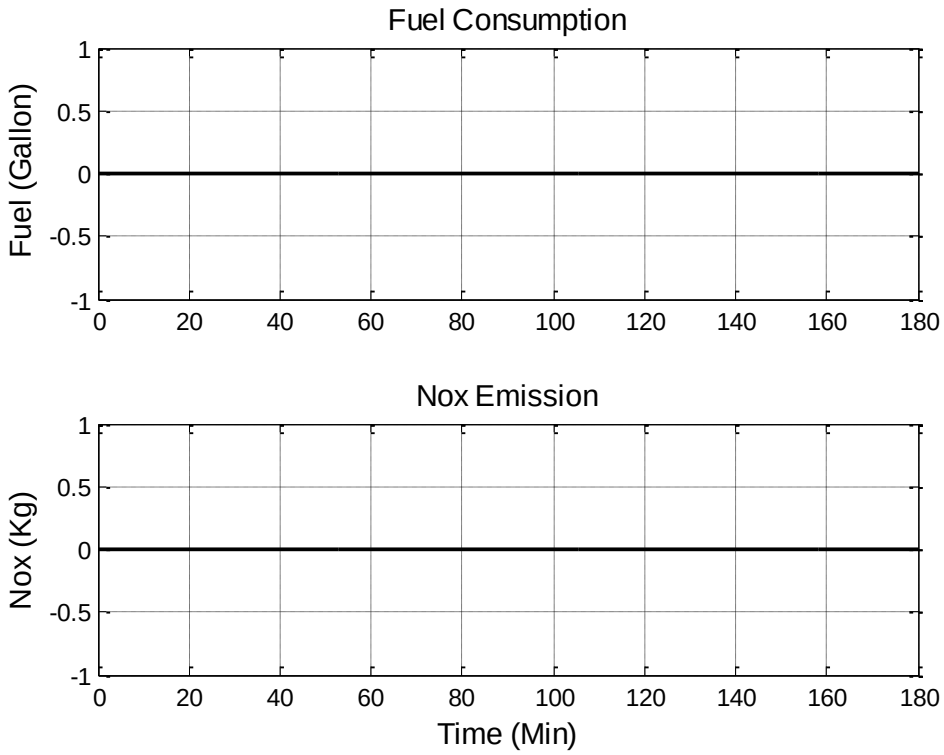

Fig. 6.39 Flywheel Powered Switcher Fuel Consumption and NOx Emission

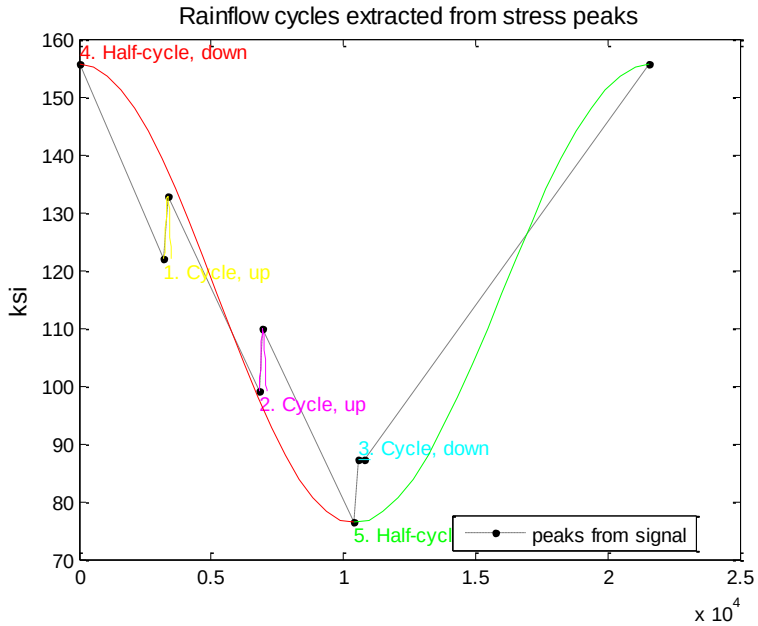

Fig. 6.40 Flywheel Powered Switcher Flywheel Peak Stress Rain Flow Counting

6.4.3 High Speed Rail Simulation

In this section, the high speed passenger train in the United States was simulated. The proposed high speed rail (HSR) in US will have a maximum speed of more than 120MPH and act as a commuter train between cities. This simulation was done to serve the purpose to modify the diesel engines so that the HSR service can be done on non-electrified tracks. Data for the high speed rail power schedules is very limited for the author. So the EPA average schedule for notch 1-7 of the line haul operation (Table 6.1) was used. Then the notch 8's duration was fine-tuned so that the train travels the required distance. It is a reasonable procedure if we assume that the diesel engines' starting phases remain the same and notch 8, the most efficient notch, is the one that will carry the train through most of its traveling distance.

Following this method, an 1100 ton (no flywheel slug car) diesel train is simulated for an assumed route as in Table 6.3 . The Davis force was assumed to be 40% less than predicted by Eq. 6.5 since the passenger trains have smoother shapes and the track resistance will also be smaller. As was shown in Fig. 6.41, the HSR traveled for about 480.2 Miles within 435.2 minutes. The maximum velocity of the HSR is about 124.4 MPH. Fig. 6.42 shows that the HSR consumed 771 gallons of diesel and released 173kg of NOx.

Totally 8 flywheels, each initially charged to 90kWh, will be equipped on the HSR. The totally weight simulated is 1200ton for the hybrid HSR. Since the kinetic energy is higher than line hauls before braking and that means more energy can be recovered, it was decided that part of notch 7 and 8 will be supplied with flywheel power. The diesel

power will be switched in during notch 7 or 8 depending on a threshold set on flywheel speeds. The threshold was decided so that the flywheel can get fully recharged after regenerative braking.

Table 6.3 Assumed Route for High Speed Rail

Destinations	Distances(miles)
Boston - Hartford	100
Hartford - New Haven	50
New Haven - New York	85
New York - Trenton	60
Trenton - Philadelphia	40
Philadelphia - Wilmington	30
Wilmington - Baltimore	70
Baltimore - Washington DC	45
(Total)	480

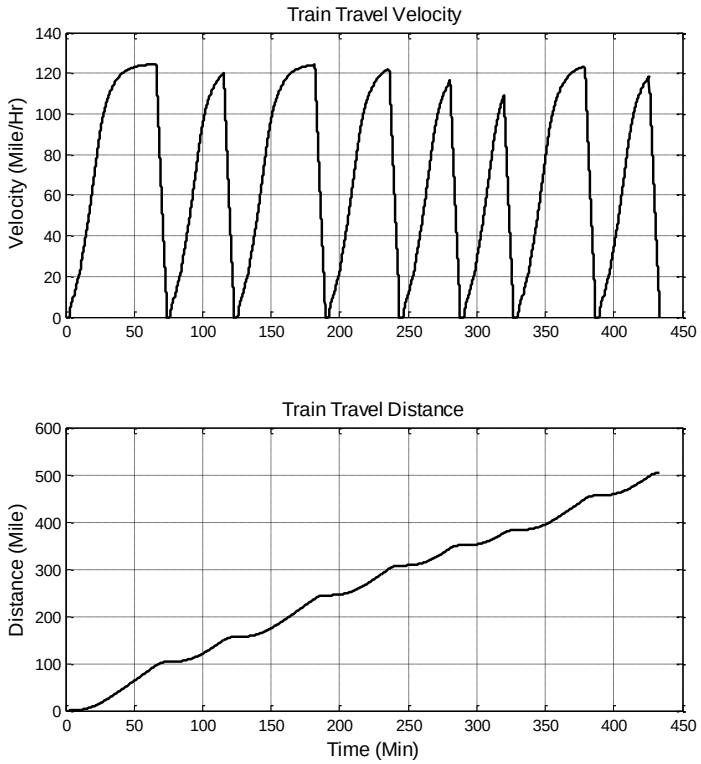

Fig. 6.41 HSR Travel Velocity and Distance

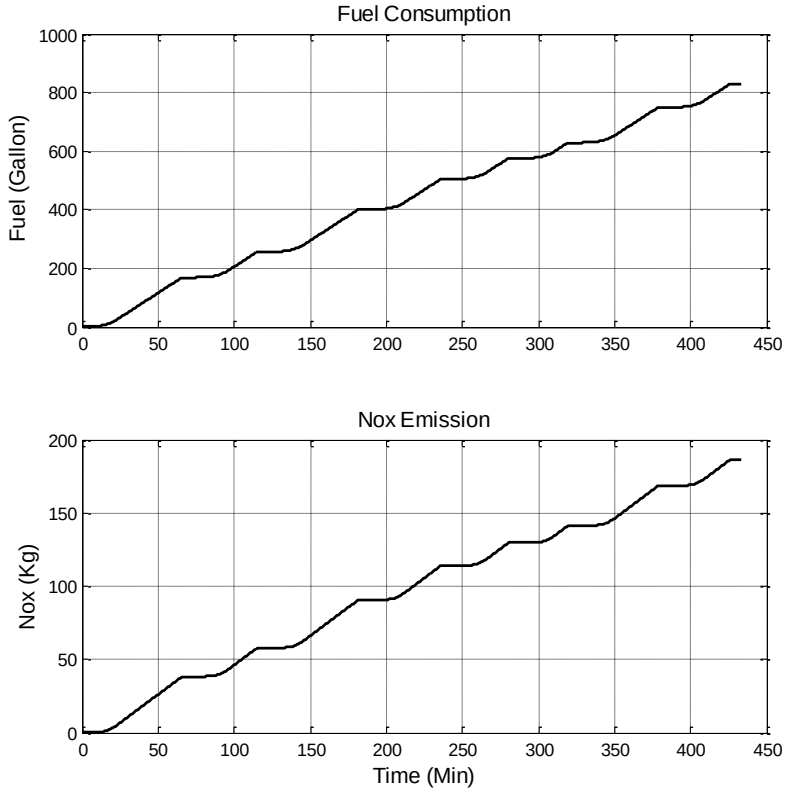

Fig. 6.42 HSR Fuel Consumption and NOx Emission

Since the HSR will have a deeper discharge depth for the flywheel, a high limit of K_{fw}=10 Nm/A was set in the simulation to keep the K_{fw} value within a reasonable range. The flywheel charging current limit was changed to 80 Amps. This is done to keep the acceleration/deceleration limit value similar to the line hauls due to the weight reduction. The flywheel will stop recharge at 90kWh for safety reasons and the braking energy will be dumped via backup resistance bank.

As shown in Fig. 6.43, the total travelling distance of 480.0 miles was finished within 440.6 minutes. The highest speed reached in this process is 120.5MPH. Fig. 6.44 plotted the flywheel spinning speed during the trip. The flywheels were initially charged

to 4915RPM, and the lowest speed is 4026RPM during population phase. The initial speed of 4915 RPM was then restored after regenerative braking. Fig. 6.45 and Fig. 6.46 plotted the voltage, current and power information about the flywheels and traction motors during the simulated trip.

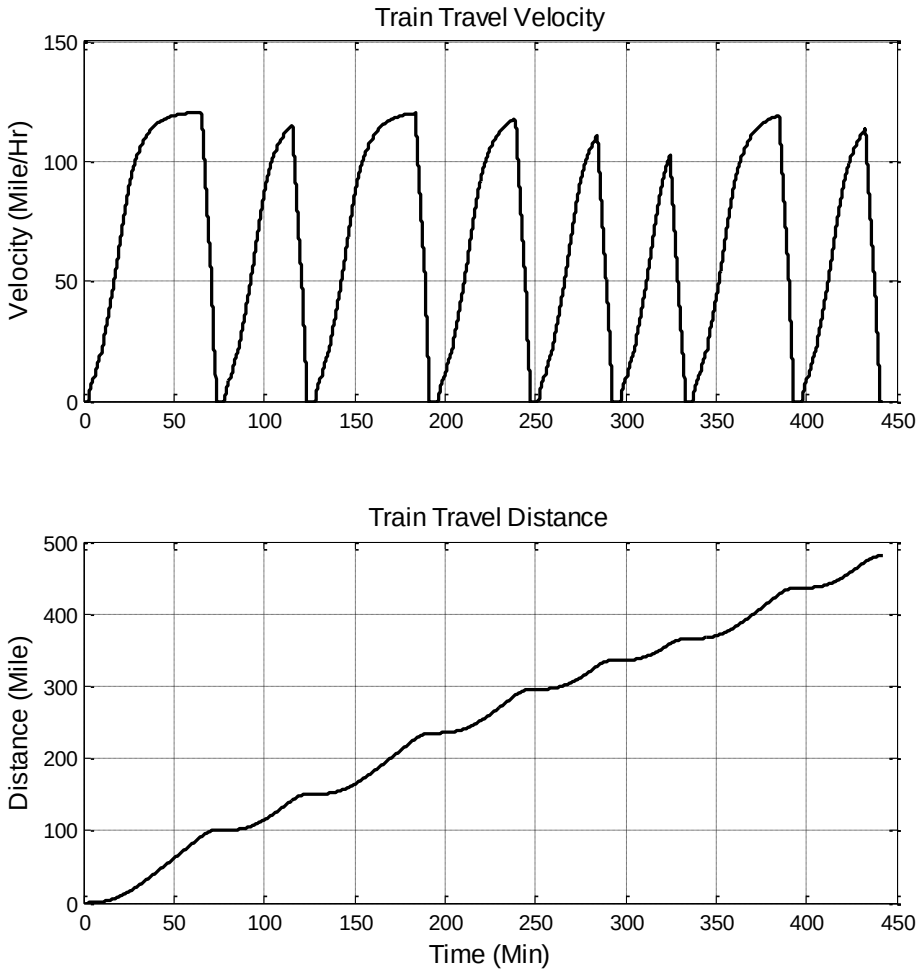

Fig. 6.43 Hybrid HSR Travel Velocity and Distance

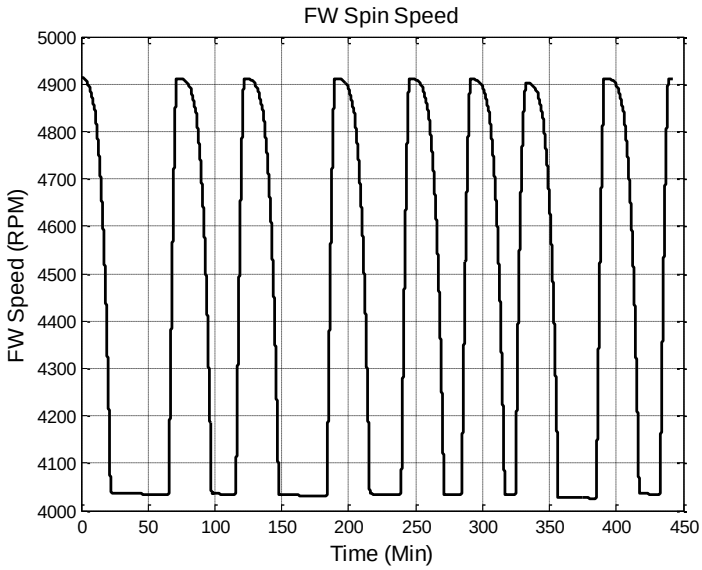

Fig. 6.44 Hybrid HSR Flywheel Spin Speed

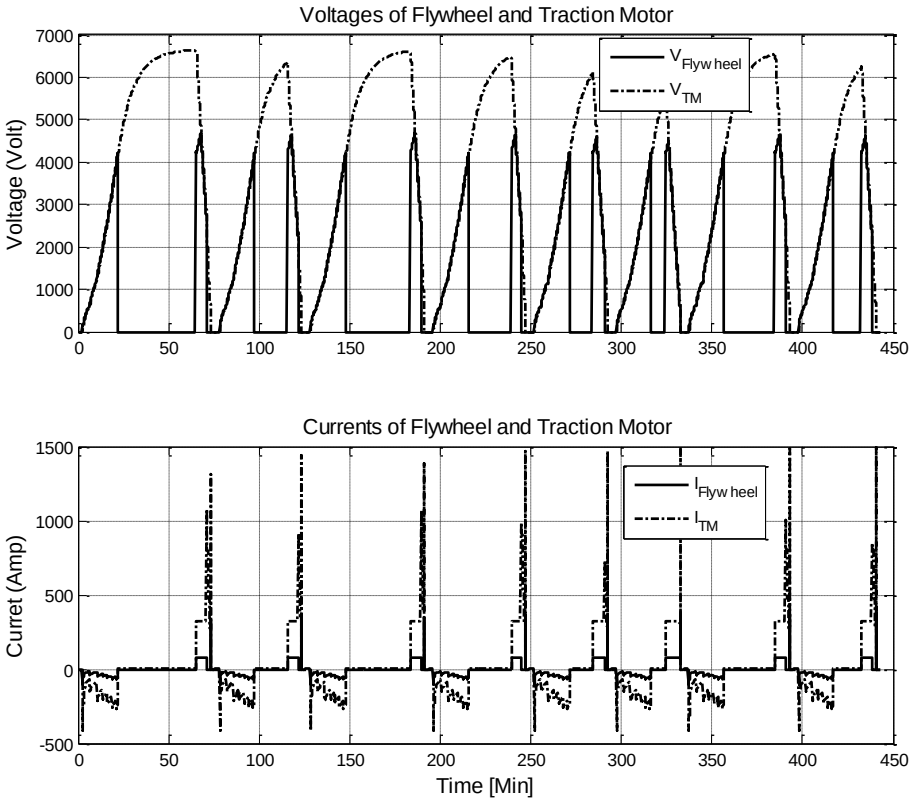

Fig. 6.45 Hybrid HSR Voltages and Currents

After the whole trip, the flywheel system has a remaining energy of 720kWh since the regenerative braking recovered 100% of the flywheel energy, which can be seen in Fig. 6.47. The maximum K_{fw} needed is 10Nm/A since it is limited during simulation. The adhesion values were plotted as Fig. 6.48. The adhesion results are very similar to the previous cases. They proved the HSR powered by flywheels will not have a traction problem.

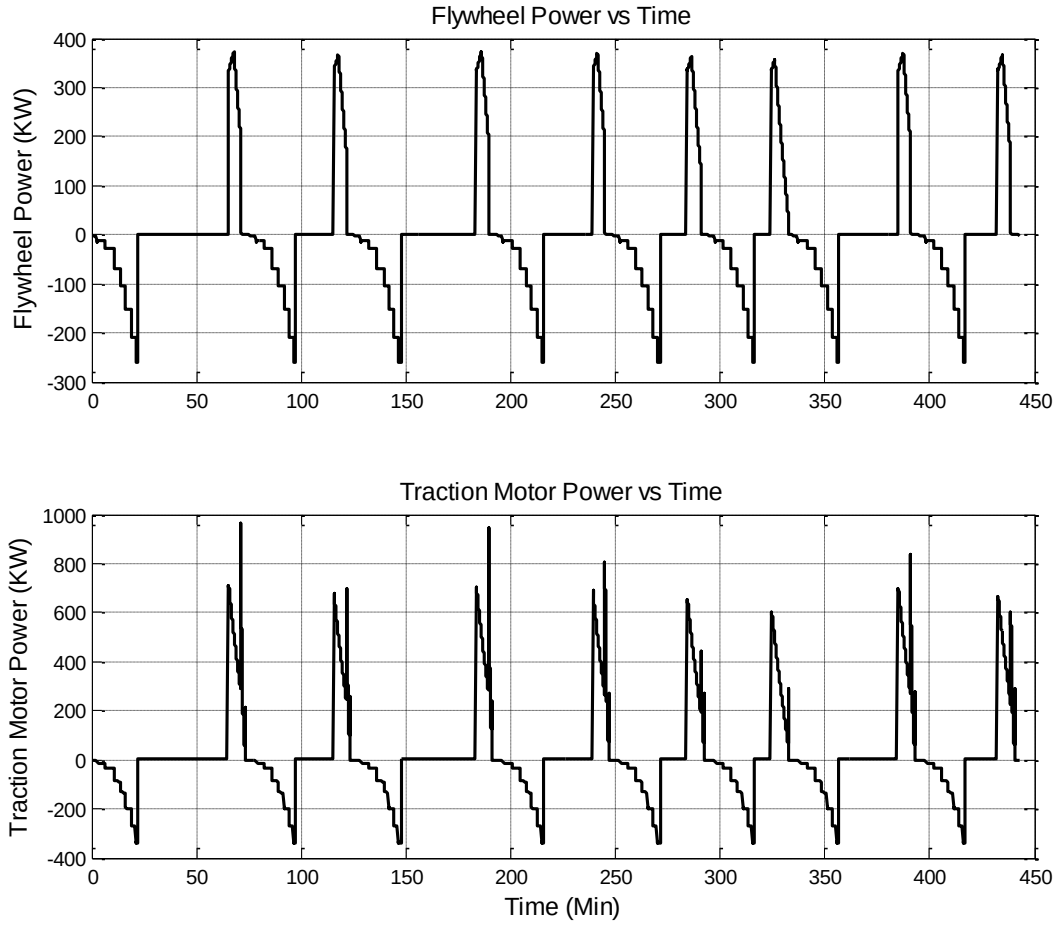

Fig. 6.46 Hybrid HSR Flywheel and Traction Motor Power

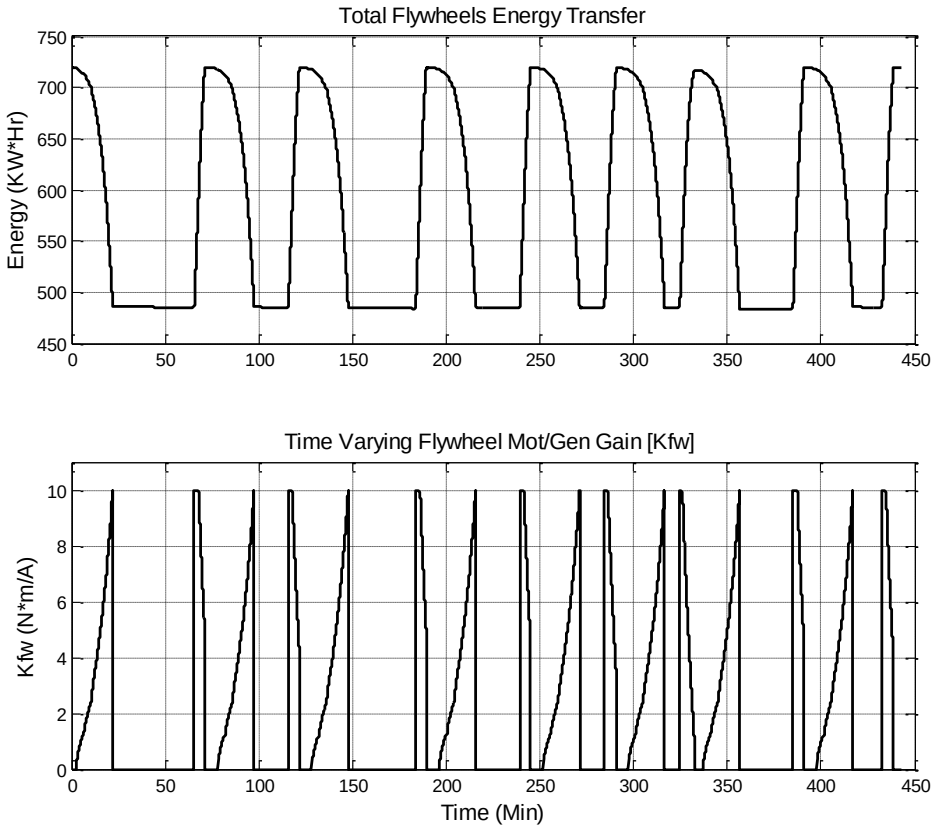

Fig. 6.47 Hybrid HSR Flywheel Energy and K_{fw} Values

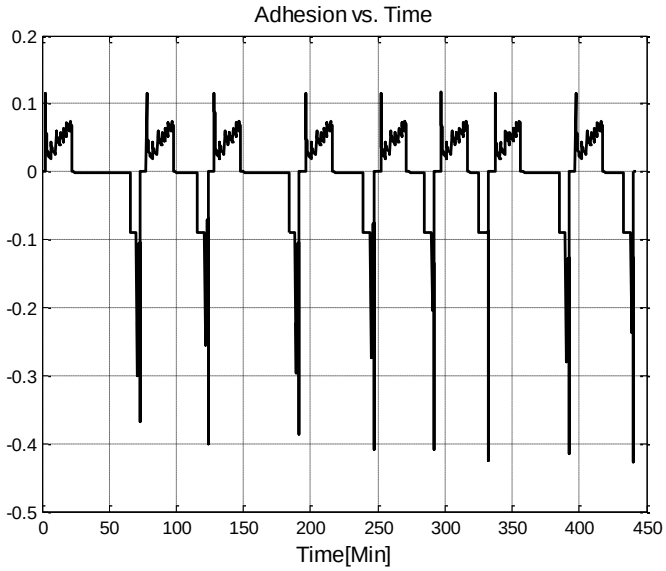

Fig. 6.48 Hybrid HSR Adhesion Values

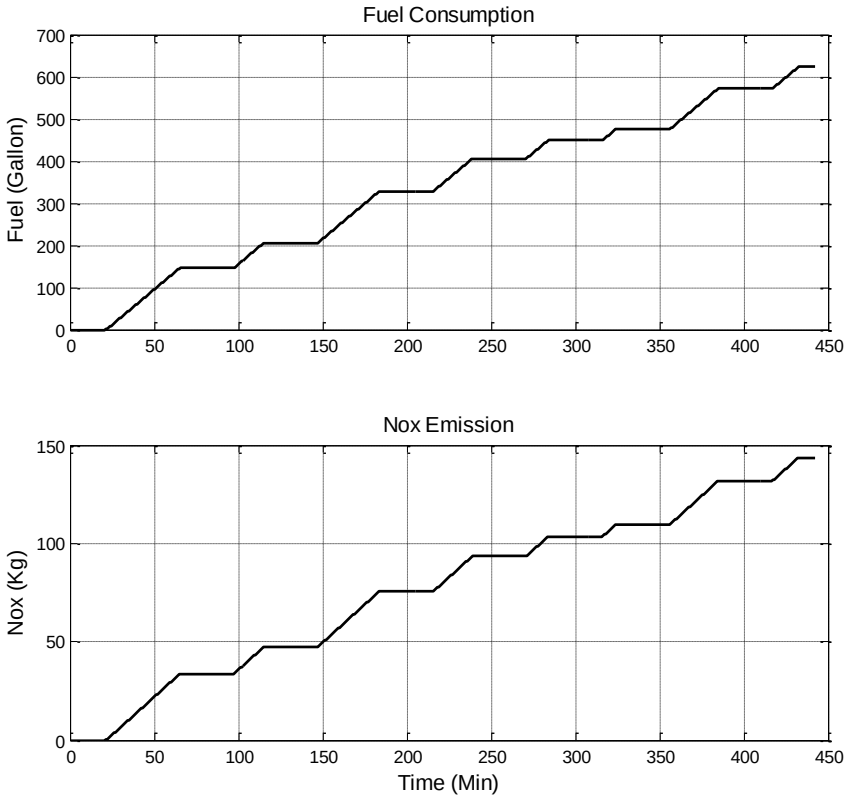

Fig. 6.49 Hybrid HSR Fuel Consumption and NOx Emission

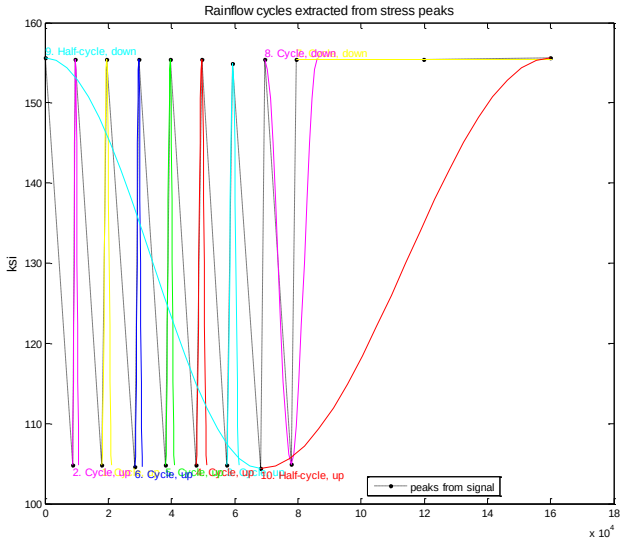

Fig. 6.50 Hybrid HSR Flywheel Peak Stress Rain Flow Counting

Fig. 6.49 shows that the total diesel consumption is 623gallon, with a NOx emission of 144kg. This data marks a 19.2% reduction in diesel and 16.8% reduction in NOx. The stress cycles for HSR route simulation were also counted using the rain flow counting algorithm [51] mentioned above. The result is listed as in Fig. 6.50. The predicted S-N lives for non-notched flywheels are 1.25e6 cycles (infinite). It will take 8.3k simulated cycles for a 0.02in through-the-thickness crack at the weakest location to grow to a critical size. This converts to a 4.15k round trips and 11.4 years of operation if one round trip was made each day (14 hours/ 960 miles per day). The lives of the flywheels will be greatly improved if 10 flywheels were used instead of 8 since this will reduce the depth of discharge and the stress alternation of the flywheel system.

6.5 Simulation of Flywheel Vibration Isolations

Vibration isolation is a key problem for train mounted flywheel energy storage systems due to the harsh environments that the systems will encounter during operation. The isolation of the rotational degree of freedoms is generally the hardest and most important aspect to be solved in all of these isolation systems. This is due to several reasons: First, the rotational disturbance will incur gyroscopic effects that causing forward whirl with much higher frequency (nearly twice of the rotational speed), this put a pressure on the bandwidth behavior of the magnetic bearings. Second, to control the gyroscopic effects, a large moment needs to be generated by the magnetic bearing. Finally, the large moment will create an uneven distribution of the magnetic field and may increase the eddy loss on the rotor. This is why lots of proposed flywheel systems on train use gimbal mounts.

Zhang,X.H. first started the work trying to isolate our flywheel system on groups of vibration isolators instead of gimbal mounts [52]. He built up models considering floor vibration input through bogies and car bodies. In his models, the magnetic bearing systems on flywheels were treated as constant stiffness/damping. With his simulation, he found that the flywheel system can successfully survive the sinusoidal floor vibrations generated from AAR's data. However, the flywheel will hit the catcher bearings if the train is passing a bump with 1:150 slope (33mm rise within 5.1m track length) at a speed of 50 MPH. This data is an average retrieved from [53]. It was found out that to pass the bump, the flywheel first need to be temporarily de-levitated to sit on catcher bearing to reduce the gyroscopic effects. In his thesis, Zhang also confirmed the effectiveness of using gimbal mounts [52].

In this dissertation, the author will try to expand the isolation design on the basis of Zhang's work [52]. First, the feedback loop magnetic bearing levitation model was used to substitute the constant spring/damping model for magnetic bearing used in Zhang's work. Then the isolator position/arrangements were modified so that the energy storage system can pass the ramp without the need of de-levitation. After this, the turning of a train was simulated to verify the isolation will also pass the test of the curvature.

The major change from Zhang's isolation method is to move the isolators with big stiffness from the outer diameter of the flywheel housing to the center areas. These springs were used to support the weight of the flywheel assemblies and hence have very big stiffness value. By moving them from the outer diameter to the center areas, the isolation properties for rotational motions from train floor can be improved by a large

margin without compromising the load capability of the isolation system. The final isolator arrangements are as shown in Fig. 6.51.

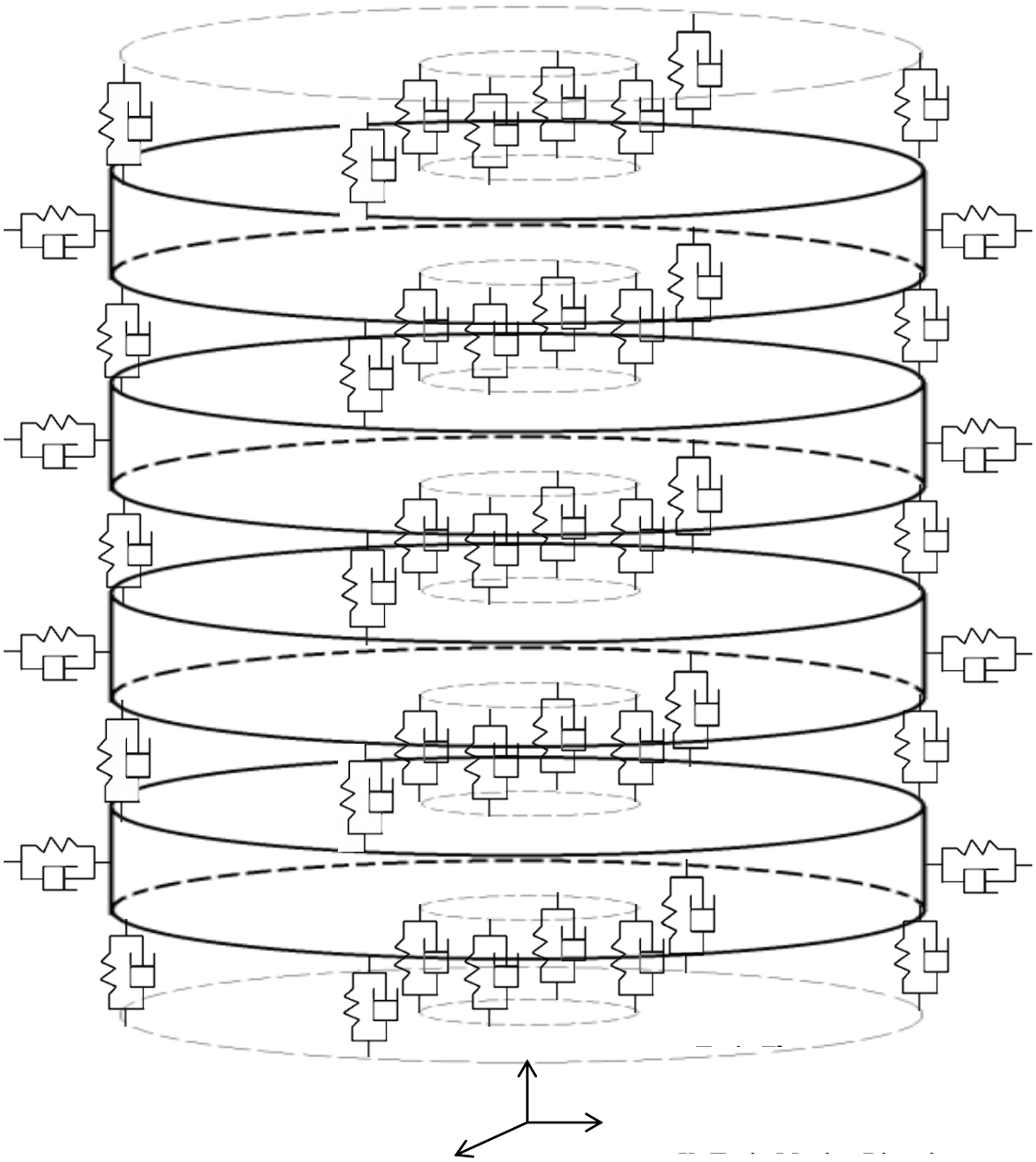

Fig. 6.51 Flywheel Isolation Scheme on Slug Cars

As shown in Fig. 6.51, the center groups of spring/damper between flywheels and train floor provide weight support of the flywheels. The outer groups of spring/damper provide supports/damping for the flywheel control moment transferred via the housing. The sides of the flywheel housings were also connected to the slug car body via springs/damper with ball-joints. This mechanism will provide forces to counteract the assembly's centrifugal forces without generating moments on flywheel housings.

To simplify the problem, the rotational motions of the bogies were neglected. The bogies were modeled as side frame masses with primary and secondary suspensions. Using this bogie model, the interaction between track and train floor was modeled as in Fig. 6.52. To simplify the problem, the axial and shear stiffness and damping for the suspensions were assumed to be the same.

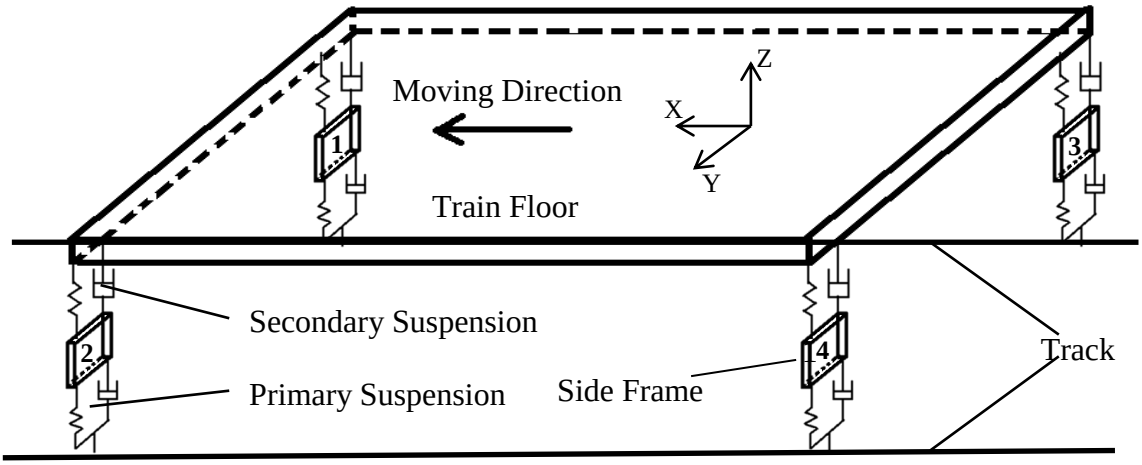

Fig. 6.52 Interaction between Track and Train Floor

The vertical forces between track profile (G) input and side frames (SF) are

generated by primary suspension (PS) and can be written as:

$$(F^z_{G/SF})_1 = -K_{PS}((z_{SF})_1 - (z_{Track})_1) - C_{PS}((\dot{z}_{SF})_1 - (\dot{z}_{Track})_1) \quad (6.75)$$

$$(F^z_{G/SF})_2 = -K_{PS}((z_{SF})_2 - (z_{Track})_2) - C_{PS}((\dot{z}_{SF})_2 - (\dot{z}_{Track})_2) \quad (6.76)$$

$$(F^z_{G/SF})_3 = -K_{PS}((z_{SF})_3 - (z_{Track})_3) - C_{PS}((\dot{z}_{SF})_3 - (\dot{z}_{Track})_3) \quad (6.77)$$

$$(F^z_{G/SF})_4 = -K_{PS}((z_{SF})_4 - (z_{Track})_4) - C_{PS}((\dot{z}_{SF})_4 - (\dot{z}_{Track})_4) \quad (6.78)$$

Assume the profile change of both tracks in horizontal(y) and longitude(x) directions as same, then the motions of the two front side frames in x and y directions should be same, respectively. Also considering the two front side frames were connected in horizontal plane, it was decided that the front side frames were modeled as a single mass in motion equations of x and y direction. The rear side frames were treated the same way. The force equations are:

$$(F^x_{G/SF})_F = -2K_{PS}(x_{SF})_F - 2C_{PS}(\dot{x}_{SF})_F \quad (6.79)$$

$$(F^x_{G/SF})_R = -2K_{PS}(x_{SF})_R - 2C_{PS}(\dot{x}_{SF})_R \quad (6.80)$$

$$(F^y_{G/SF})_F = -2K_{PS}(y_{SF})_F - 2C_{PS}(\dot{y}_{SF})_F \quad (6.81)$$

$$(F^y_{G/SF})_R = -2K_{PS}(y_{SF})_R - 2C_{PS}(\dot{y}_{SF})_R \quad (6.82)$$

The side frame motion will in turn generate forces on the train floor through the secondary suspension (SS) as:

$$(F^z_{SF/T})_1 = -K_{ss}\left(z_t - \frac{L_t\theta_{T2}}{2} - \frac{W_t\theta_{T1}}{2} - (z_{SF})_1\right) - C_{ss}\left(\dot{z}_t - \frac{L_t\dot{\theta}_{T2}}{2} - \frac{W_t\dot{\theta}_{T1}}{2} - (\dot{z}_{SF})_1\right) \quad (6.83)$$

$$(F^z_{SF/T})_2 = -K_{ss}\left(z_t - \frac{L_t\theta_{T2}}{2} + \frac{W_t\theta_{T1}}{2} - (z_{SF})_2\right) - C_{ss}\left(\dot{z}_t - \frac{L_t\dot{\theta}_{T2}}{2} + \frac{W_t\dot{\theta}_{T1}}{2} - (\dot{z}_{SF})_2\right) \quad (6.84)$$

$$(F^z_{SF/T})_3 = -K_{ss}\left(z_t + \frac{L_t\theta_{T2}}{2} - \frac{W_t\theta_{T1}}{2} - (z_{SF})_3\right) - C_{ss}\left(\dot{z}_t + \frac{L_t\dot{\theta}_{T2}}{2} - \frac{W_t\dot{\theta}_{T1}}{2} - (\dot{z}_{SF})_3\right) \quad (6.85)$$

$$(F^z_{SF/T})_4 = -K_{ss}\left(z_t + \frac{L_t\theta_{T2}}{2} + \frac{W_t\theta_{T1}}{2} - (z_{SF})_4\right) - C_{ss}\left(\dot{z}_t + \frac{L_t\dot{\theta}_{T2}}{2} + \frac{W_t\dot{\theta}_{T1}}{2} - (\dot{z}_{SF})_4\right) \quad (6.86)$$

$$(F^x_{SF/T})_F = -2K_{ss}(x_t - (x_{SF})_F) - 2C_{ss}(\dot{x}_t - (\dot{x}_{SF})_F) \quad (6.87)$$

$$(F^x_{SF/T})_R = -2K_{ss}(x_t - (x_{SF})_R) - 2C_{ss}(\dot{x}_t - (\dot{x}_{SF})_R) \quad (6.88)$$

$$(F^y_{SF/T})_F = -2K_{ss}\left(y_t + \frac{L_t\theta_{T3}}{2} - (y_{SF})_F\right) - 2C_{ss}\left(\dot{y}_t + \frac{L_t\dot{\theta}_{T3}}{2} - (\dot{y}_{SF})_F\right) \quad (6.89)$$

$$(F^y_{SF/T})_F = -2K_{ss}\left(y_t - \frac{L_t\theta_{T3}}{2} - (y_{SF})_F\right) - 2C_{ss}\left(\dot{y}_t - \frac{L_t\dot{\theta}_{T3}}{2} - (\dot{y}_{SF})_F\right) \quad (6.90)$$

The slug car length between front and rear bogies is Lt. The width between left and right bogies are Wt. These forces will generate moments on the train floor as:

$$(M_{SF/T})_x = [-(F^z_{SF/T})_1 + (F^z_{SF/T})_2 - (F^z_{SF/T})_3 + (F^z_{SF/T})_4]W_t/2 \tag{6.91}$$

$$(M_{SF/T})_y = [-(F^z_{SF/T})_1 - (F^z_{SF/T})_2 + (F^z_{SF/T})_3 + (F^z_{SF/T})_4]L_t/2 \tag{6.92}$$

$$\begin{aligned}(M_{SF/T})_z = {} & [(F^y_{SF/T})_1 + (F^y_{SF/T})_2 - (F^y_{SF/T})_3 - (F^y_{SF/T})_4]L_t/2 \\ & + [(F^x_{SF/T})_1 - (F^x_{SF/T})_2 + (F^x_{SF/T})_3 - (F^x_{SF/T})_4]W_t/2\end{aligned} \tag{6.93}$$

The motion of the side frames can be written as:

$$(\ddot{Z}_{SF})_1 = [(F^z_{G/SF})_1 - (F^z_{SF/T})_1]/m_{SF} \tag{6.94}$$

$$\left(\ddot{Z}_{SF}\right)_2 = [(F^z_{G/SF})_2 - (F^z_{SF/T})_2]/m_{SF} \tag{6.95}$$

$$(\ddot{Z}_{SF})_3 = [(F^z_{G/SF})_3 - (F^z_{SF/T})_3]/m_{SF} \tag{6.96}$$

$$(\ddot{Z}_{SF})_4 = [(F^z_{G/SF})_5 - (F^z_{SF/T})_5]/m_{SF} \tag{6.97}$$

$$(\ddot{x}_{SF})_F = [(F^x_{G/SF})_F - (F^x_{SF/T})_F]/2m_{SF} \tag{6.98}$$

$$(\ddot{x}_{SF})_R = [(F^x_{G/SF})_R - (F^x_{SF/T})_R]/2m_{SF} \tag{6.99}$$

$$(\ddot{y}_{SF})_F = [(F^y_{G/SF})_F - (F^y_{SF/T})_F + F^{Cen}_{SF}]/2m_{SF} \tag{6.100}$$

$$(\ddot{y}_{SF})_R = [(F^y_{G/SF})_R - (F^y_{SF/T})_R + F^{Cen}_{SF}]/2m_{SF} \tag{6.101}$$

Zhang [52] used Sun [54]'s parameters in his modeling of the boggies system. These values in [54] are: K_{SS}=2.555MN/m, C_{SS}=30kNs/m, K_{PS}=6.5MN/m, C_{PS}=10kNs/m and M_{bogie}=3600kg.

In this dissertation, since the bogie was divided in two parts, M_{SF}= M_{bogie}/2=1800kg.

As in [54], the primary suspension has two sets of spring/dampers, so K_{PS}=13MN/m was used since we only have one primary suspension spring modeled in our bogie model. Also since we neglected tracks' damping as in [54], where the C_{PS} is an assumed value,the C_{PS} value used in this dissertation was assumed to be C_{PS}=40kNs/m. The bogie separation width *Wt* will be 1.6m. The bogie separation distance will be 15m.

The forces generated by the side supporting spring/dampers (K_{ns}/C_{ns}) of housing are:

$$(F_{H1/T}^{Side})_x = -2K_{H1s}(x_t - x_{H1}) - 2C_{H1s}(\dot{x}_t - \dot{x}_{H1}) \quad (6.102)$$

$$(F_{H2/T}^{Side})_x = -2K_{H2s}(x_t - x_{H2}) - 2C_{H2s}(\dot{x}_t - \dot{x}_{H2}) \quad (6.103)$$

$$(F_{H3/T}^{Side})_x = -2K_{H3s}(x_t - x_{H3}) - 2C_{H3s}(\dot{x}_t - \dot{x}_{H3}) \quad (6.104)$$

$$(F_{H4/T}^{Side})_x = -2K_{H4s}(x_t - x_{H4}) - 2C_{H4s}(\dot{x}_t - \dot{x}_{H4}) \quad (6.105)$$

$$(F_{H1/T}^{Side})_y = -2K_{H1s}(y_t - y_{H1}) - 2C_{H1s}(\dot{y}_t - \dot{y}_{H1}) \quad (6.106)$$

$$(F_{H2/T}^{Side})_y = -2K_{H2s}(y_t - y_{H2}) - 2C_{H1s}(\dot{y}_t - \dot{y}_{H2}) \quad (6.107)$$

$$(F_{H3/T}^{Side})_y = -2K_{H3s}(y_t - y_{H3}) - 2C_{H1s}(\dot{y}_t - \dot{y}_{H3}) \quad 6.108)$$

$$(F_{H4/T}^{Side})_y = -2K_{H4s}(y_t - y_{H4}) - 2C_{H1s}(\dot{y}_t - \dot{y}_{H4}) \quad (6.109)$$

The rotational axis of the slug car was setup to be on the train floor. The I_{pt} and I_{tt} values are calculated with respect to this axis. The moments on the slug car generated by the side supporting mechanisms of the flywheel assembly can be written as:

$$(M_{H/T}^{Side})_x = -(F_{H1/T}^{Side})_y(H_{H1/t} + H_h/2) - (F_{H2/T}^{Side})_y(H_{H2/H1} + H_{H1/t} + H_h/2) - (F_{H3/T}^{Side})_y(H_{H3/H2} + H_{H2/H1} + H_{H1/t} + H_h/2) - (F_{H4/T}^{Side})_y(H_{H4/H3} + H_{H3/H2} + H_{H2/H1} + H_{H4/t} + H_h/2 \quad (6.110)$$

$$(M_{H/T}^{Side})_y = (F_{H1/T}^{Side})_x(H_{H1/t} + H_h/2) + (F_{H2/T}^{Side})_x(H_{H2/H1} + H_{H1/t} + H_h/2) + (F_{H3/T}^{Side})_x(H_{H3/H2} + H_{H2/H1} + H_{H1/t} + H_h/2) + (F_{H4/T}^{Side})_x(H_{H4/H3} + H_{H3/H2} + H_{H2/H1} + H_{H4/t} + H_h/2) \quad (6.111)$$

The rotational axis of the flywheel houses were also set at the bottom of the housing, with I_{pHn} and I_{tHn} calculated with respect to this axis. The moments of the side supporting mechanisms on the flywheel housings are:

$$(M_{T/H1}^{Side})_x = (F_{H1/T}^{Side})_y H_h/2 \quad (6.112)$$

$$(M_{T/H2}^{Side})_x = (F_{H2/T}^{Side})_y H_h/2 \quad (6.113)$$

$$(M_{T/H3}^{Side})_x = (F_{H3/T}^{Side})_y H_h/2 \quad (6.114)$$

$$(M_{T/H4}^{Side})_x = (F_{H4/T}^{Side})_y H_h/2 \quad (6.115)$$

$$(M_{T/H1}^{Side})_y = -(F_{H1/T}^{Side})_x H_h/2 \quad (6.116)$$

$$(M_{T/H2}^{Side})_y = -(F_{H2/T}^{Side})_x H_h/2 \quad (6.117)$$

$$(M_{T/H3}^{Side})_y = -(F_{H3/T}^{Side})_x H_h/2 \quad (6.118)$$

$$(M_{T/H4}^{Side})_y = -(F_{H4/T}^{Side})_x H_h/2 \quad (6.119)$$

Assuming the flywheel assembly has an offset D_{Hx} from center of the train floor in x (train motion) direction, the vibration isolator forces/moments on train floor (Fig. 6.51)

can be written as:

$$(F_{H1/T}^{Iso})_x = 4(K_{H1/T}^{In\_Sh} + K_{H1/T}^{Out\_Sh})(x_{H1} - x_t) + 4(C_{H1/T}^{In\_Sh} + C_{H1/T}^{Out\_Sh})(\dot{x}_{H1} - \dot{x}_t) \quad (6.120)$$

$$(F_{H1/T}^{Iso})_y = 4(K_{H1/T}^{In\_Sh} + K_{H1/T}^{Out\_Sh})(y_{H1} - y_t) + 4(C_{H1/T}^{In\_Sh} + C_{H1/T}^{Out\_Sh})(\dot{y}_{H1} - \dot{y}_t) \quad (6.121)$$

$$(F_{H1/T}^{Iso})_z = 4(K_{H1/T}^{In} + K_{H1/T}^{Out})(z_{H1} - z_t + D_{Hx}\theta_{T2}) + 4(C_{H1/T}^{In} + C_{H1/T}^{Out})(\dot{z}_{H1} - \dot{z}_t + D_{Hx}\dot{\theta}_{T2}) \quad (6.122)$$

$$(M_{H1/T}^{Iso})_x = \left(K_{H1/T}^{In} D_{H1}^{In} + K_{H1/T}^{Out} D_{H1}^{Out}\right)(\theta_{H1x} - \theta_{T1}) + (C_{H1/T}^{In} D_{H1}^{In} + C_{H1/T}^{Out} D_{H1}^{Out})(\dot{\theta}_{H1x} - \dot{\theta}_{T1}) \quad (6.123)$$

$$(M_{H1/T}^{Iso})_y = -(f_{H1/T}^{Iso})_z D_{Hx} + (K_{H1/T}^{In} D_{H1}^{In} + K_{H1/T}^{Out} D_{H1}^{Out})(\theta_{H1y} - \theta_{T2}) + (C_{H1/T}^{In} D_{H1}^{In} + C_{H1/T}^{Out} D_{H1}^{Out})(\dot{\theta}_{H1y} - \dot{\theta}_{T2}) \quad (6.124)$$

$$(M_{H1/T}^{Iso})_z = 4\left(K_{H1/T}^{In\_Sh} D_{H1}^{In} + K_{H1/T}^{Out\_Sh} D_{H1}^{Out}\right)(\theta_{H1z} - \theta_{T3}) + 4(C_{H1/T}^{In\_Sh} D_{H1}^{In} + C_{H1/T}^{Out\_Sh} D_{H1}^{Out})\left(\dot{\theta}_{H1z} - \dot{\theta}_{T3}\right) \quad (6.125)$$

$$(M_T^{Cen})_x = -F_T^{Cen} H_{car}/2 \quad (6.126)$$

The forces and moments exerted on the first flywheel housing by train floor via vibration isolators are:

$$(F_{T/H1}^{Iso})_x = -(F_{H1/T}^{Iso})_x \quad (6.127)$$

$$(F_{T/H1}^{Iso})_y = -(F_{H1/T}^{Iso})_y \quad (6.128)$$

$$(F_{H1/T}^{Iso})_z = -(F_{H1/T}^{Iso})_z \quad (6.129)$$

$$(M_{T/H1}^{Iso})_x = -(M_{H1/T}^{Iso})_x \tag{6.130}$$

$$(M_{T/H1}^{Iso})_y = -(K_{H1/T}^{In} D_{H1}^{In} + K_{H1/T}^{Out} D_{H1}^{Out})(\theta_{H1y} - \theta_{T2}) - (C_{H1/T}^{In} D_{H1}^{In} + C_{H1/T}^{Out} D_{H1}^{Out})(\dot{\theta}_{H1y} - \dot{\theta}_{T2}) \tag{6.131}$$

$$(M_{T/H1}^{Iso})_z = -(M_{H1/T}^{Iso})_z \tag{6.132}$$

Since the isolator interactions for the H1&H2 pair, H2&H3 pair, H3&H4 pair and H4&T pair are similar to those between H1 and train floor, their force/moment equations will be almost identical to Eq. 6.120-Eq. 6.132. By substituting is the stiffness and damping values of the inner/outer isolators between these pairs, their corresponding forces/moments equations can be easily reproduced. This is why these equations are not listed in this dissertation.

The motions of the train floor can be written as:

$$\ddot{x}_T = [(F_{SF/T})_x + (F_{H1/T}^{Iso})_x + (F_{H4/T}^{Iso})_x + (F_{H/T}^{Side})_x]/m_t \tag{6.133}$$

$$\ddot{y}_T = [(F_{SF/T})_y + (F_{H1/T}^{Iso})_y + (F_{H4/T}^{Iso})_y + (F_{H/T}^{Side})_y + (F_T^{Cen})_y]/m_t \tag{6.134}$$

$$\ddot{z}_T = [(F_{SF/T})_z + (F_{H1/T}^{Iso})_z + (F_{H4/T}^{Iso})_y]/m_t \tag{6.135}$$

$$\ddot{\theta}_{T1} = [(M_{SF/T})_x + (M_{H1/T}^{Iso})_x + (M_{H4/T}^{Iso})_x + (M_{H/T}^{Side})_x + (M_T^{Cen})_x]/I_{tt1} \tag{6.136}$$

$$\ddot{\theta}_{T2} = [(M_{SF/T})_y + (M_{H1/T}^{Iso})_y + (M_{H4/T}^{Iso})_y + (M_{H/T}^{Side})_y]/I_{tt2} \tag{6.137}$$

$$\ddot{\theta}_{T3} = [(M_{SF/T})_z + (M_{H1/T}^{Iso})_z + (M_{H4/T}^{Iso})_y]/I_{pt} \tag{6.138}$$

The magnetic bearings will generate forces/moments on the flywheel based on relative motions between flywheel and its housing. The forces/moments values at

any given will also depend on the previous controller/filters states. These forces/moments will be generated using Eq. 4.5-Eq. 4.43 as discussed in section 4.3 of chapter IV. The flywheel1's motions are:

$$\ddot{x}_{f1} = (F_{H1/f1}^{AMB})_x / m_{f1} \tag{6.139}$$

$$\ddot{y}_{f1} = [(F_{H1/f1}^{AMB})_y + (F_{f1}^{Cen})_x] / m_{f1} \tag{6.140}$$

$$\ddot{z}_{f1} = (F_{H1/f1}^{AMB})_z / m_{f1} \tag{6.141}$$

$$\ddot{\theta}_{f1x} = ((M_{H1/f1}^{AMB})_x - I_{pf}\varpi_{f1}\dot{\theta}_{f1y}) / I_{f1t} \tag{6.142}$$

$$\ddot{\theta}_{f1y} = ((M_{H1/f1}^{AMB})_y + I_{pf}\varpi_{f1}\dot{\theta}_{f1x}) / I_{f1t} \tag{6.143}$$

The forces/moments on the 1st flywheel housing by magnetic bearings of the 1st flywheel are:

$$(F_{f1/H1}^{AMB})_x = -(F_{H1/f1}^{AMB})_x \tag{6.144}$$

$$(F_{f1/H1}^{AMB})_y = -(F_{H1/f1}^{AMB})_y \tag{6.145}$$

$$(F_{f1/H1}^{AMB})_z = -(F_{H1/f1}^{AMB})_z \tag{6.146}$$

$$(M_{f1/H1}^{AMB})_x = -(M_{H1/f1}^{AMB})_x - (F_{f1/H1}^{AMB})_y H_h/2 \tag{6.147}$$

$$(M_{f1/H1}^{AMB})_y = -(M_{H1/f1}^{AMB})_y + (F_{f1/H1}^{AMB})_x H_h/2 \tag{6.148}$$

The equations of motions for flywheel housing 1 are:

$$\ddot{x}_{H1} = [(F_{f1/H1}^{AMB})_x + (F_{T/H1}^{Iso})_x + (F_{H2/H1}^{Iso})_x - (F_{H1/T}^{Side})_x] / m_{H1} \tag{6.149}$$

$$\ddot{y}_{H1} = [(F_{f1/H1}^{AMB})_y + (F_{T/H1}^{Iso})_y + (F_{H2/H1}^{Iso})_y - (F_{H1/T}^{Side})_y + (F_{H1}^{Cen})_x] / m_{H1} \tag{6.150}$$

$$\ddot{z}_{H1} = [(F_{f1/H1}^{AMB})_z + (F_{T/H1}^{Iso})_z + (F_{H2/H1}^{Iso})_z]/m_{H1} \quad (6.151)$$

$$\ddot{\theta}_{H1x} = [(M_{f1/H1}^{AMB})_x + (M_{T/H1}^{Iso})_x + (M_{H2/H1}^{Iso})_x + (M_{H1}^{Cen})_x + (M_{T/H1}^{Side})_x]/I_{H1t} \quad (6.152)$$

$$\ddot{\theta}_{H1y} = [(M_{f1/H1}^{AMB})_y + (M_{T/H1}^{Iso})_y + (M_{H2/H1}^{Iso})_y + (M_{T/H1}^{Side})_y]/I_{H1t} \quad (6.153)$$

$$\ddot{\theta}_{H1z} = [(M_{T/H1}^{Iso})_z + (M_{H2/H1}^{Iso})_z]/I_{H1t} \quad (6.154)$$

As discussed above, the equations of motions for the other flywheel-housing pairs, namely f2-H2, f3-H3 and f4-H4, can be retrieved in a similar form as Eq. 6.120-Eq. 6.132 and Eq. 6.139-Eq. 6.154 by substituting the corresponding isolator stiffness/damping. All these equations were used to retrieve the bump passing and curve turning simulation results as shown below.

6.5.1 Bump Passing Simulation

The same bump model as in Zhang's work was modeled in the simulation [52]. This is an average bump size near railway bridges proposed by Nicks [53].The dimensions used by Zhang [52] is as in Fig. 6.53.

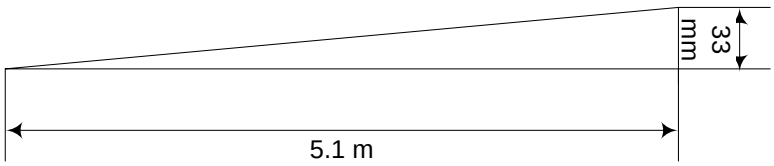

Fig. 6.53 Average Bridge Bump Size

It was found by the author that the counter rotating pairs need to stay together to avoid the gyroscopic effects on train floors. To realize this, the stiffness between

flywheel housings were set to be a very high value to simulate bolting the housings together.

It was also found that, even though the outer circle isolators' stiffness needs to be low to avoid the transmission of train floor rotational vibration, a certain amount of damping was required at the outer circle to counteract the control moment of the flywheels and keep the system stable. The basic parameters used in the simulations were as in Table 6.4.

The outer diameter of the combo magnetic bearing will be less than 1.4m and the axial air gap is 2mm.The radial air gap is 2mm at the outer surface and 1mm at the inner surface. As in Table 6.4, the axial catcher bearing is positioned at a diameter of 0.7m with a gap of 0.7mm.The radial catcher bearing has a gap of 0.5mm. So the catcher bearing dimension can ensure that the disk will not hit the bearing structure.

Table 6.4 Isolator Parameters

Isolator Parameters	Values
g_{CatchA} (Axial Cather bearing gap)	0.7mm
D_{CatchA} (Axial Cather bearing diameter position)	0.7m
g_{CatchR} (Radial Cather bearing gap)	0.5mm
D_{Hx} (Distance from the housing center to floor center in x dir.)	0mm
$H_{H1/t}$ (Housing1 to train floor distance)	63.5mm
H_h (Flywheel housing height)	740mm
M_h(Flywheel housing weight)	4347kg
I_{Hnp}(Polar moment of inertia for housing)	60 kgm^2
I_{Hnt}(Transvers moment of inertia for housing)	3230kgm^2
K_{Hns}(Housing side support stiffness)	10MN/m
C_{Hns}(Housing side support damping)	100kNs/m
D_{H1}^{In} (inner circle isolators' positions in diameter)	400mm
D_{H1}^{OUT}(outer circle isolators' positions in diameter)	2280mm
$K_{H1/T}^{In}$(Inner circle isolator stiffness between H1 and train)	7.372MN/m
$C_{H1/T}^{In}$(Inner circle isolator damping between H1 and train)	400kNs/m
$K_{H1/T}^{OUT}$(Outer circle isolator stiffness between H1 and train)	73.72kN/m

Table 6.4 Continued

Isolator Parameters	Values
$K_{H1/T}^{OUT}$(Outer circle isolator stiffness between H1 and train)	73.72kN/m
$C_{H1/T}^{OUT}$(Outer circle isolator damping between H1 and train)	400kNs/m
$K_{H1/T}^{In\_sh}$(Inner isolator shear stiffness between H1 and train)	735kN/m
$C_{H1/T}^{In\_sh}$(Inner isolator shear damping between H1 and train)	50kNs/m
$K_{H1/T}^{OUT\_sh}$(Outer isolator shear stiffness between H1 and train)	735N/m
$C_{H1/T}^{OUT\_sh}$(Outer isolator shear damping between H1 and train)	50kNs/m
$K_{H2/H1}^{In}$(Inner circle isolator stiffness between H2 and H1)	5.529MN/m
$C_{H2/H1}^{In}$(Inner circle isolator damping between H2 and H1)	300kNs/m
$K_{H2/H1}^{OUT}$(Outer circle isolator stiffness between H2 and H1)	7372MN/m
$C_{H2/H1}^{OUT}$(Outer circle isolator damping between H2 and H1)	40kNs/m
$K_{H2/H1}^{In\_sh}$(Inner isolator shear stiffness between H2 and H1)	551kN/m
$C_{H2/H1}^{In\_sh}$(Inner isolator shear damping between H2 and H1)	37.5kNs/m
$K_{H2/H1}^{OUT\_sh}$(Outer isolator shear stiffness between H2 and H1)	735kN/m
$C_{H2/H1}^{OUT\_sh}$(Outer isolator shear damping between H2 and H1)	50kNs/m
$K_{H3/H2}^{In}$(Inner circle isolator stiffness between H3 and H2)	3.686MN/m
$C_{H3/H2}^{In}$(Inner circle isolator damping between H3 and H2)	200kNs/m
$K_{H3/H2}^{OUT}$(Outer circle isolator stiffness between H3 and H2)	7372MN/m
$C_{H3/H2}^{OUT}$(Outer circle isolator damping between H3 and H2)	40kNs/m
$K_{H3/H2}^{In\_sh}$(Inner isolator shear stiffness between H3 and H2)	367.5kN/m
$C_{H3/H2}^{In\_sh}$(Inner isolator shear damping between H3 and H2)	25kNs/m
$K_{H3/H2}^{OUT\_sh}$(Outer isolator shear stiffness between H3 and H2)	735N/m
$C_{H3/H2}^{OUT\_sh}$(Outer isolator shear damping between H3 and H2)	50kNs/m
$K_{H4/H3}^{In}$(Inner circle isolator stiffness between H4 and H3)	1.843MN/m
$C_{H4/H3}^{In}$(Inner circle isolator damping between H4 and H3)	100kNs/m
$K_{H4/H3}^{OUT}$(Outer circle isolator stiffness between H4 and H3)	7372MN/m
$C_{H4/H3}^{OUT}$(Outer circle isolator damping between H4 and H3)	40kNs/m
$K_{H4/H3}^{In\_sh}$(Inner isolator shear stiffness between H4 and H3)	183.75kN/m
$C_{H4/H3}^{In\_sh}$(Inner isolator shear damping between H4 and H3)	12.5kNs/m
$K_{H4/H3}^{OUT\_sh}$(Outer isolator shear stiffness between H4 and H3)	735kN/m
$C_{H4/H3}^{OUT\_sh}$(Outer isolator shear damping between H4 and H3)	50kNs/m
$K_{T/H4}^{In}$(Inner circle isolator stiffness between train and H4)	1.843MN/m
$C_{T/H4}^{In}$(Inner circle isolator damping between train and H4))	100kNs/m
$K_{T/H4}^{OUT}$(Outer circle isolator stiffness between train and H4))	73.72kN/m
$C_{T/H4}^{OUT}$(Outer circle isolator damping between train and H4))	400kNs/m
$K_{T/H4}^{In\_sh}$(Inner isolator shear stiffness between train and H4))	183.75kN/m
$C_{T/H4}^{In\_sh}$(Inner isolator shear damping between train and H4))	12.5kNs/m
$K_{T/H4}^{OUT\_sh}$(Outer isolator shear stiffness between train and H4))	735N/m
$C_{T/H4}^{OUT\_sh}$(Outer isolator shear damping between train and H4))	50kNs/m

The simulation results are presented in the following graphs for the train passing the average bridge bump as defined above. Fig. 6.54 and Fig. 6.55 show the train floor's vibration responses to the bump. There is virtually no longitudinal and lateral motion during the whole simulation. The maximum vertical motion is 44.5mm. The final steady state motion for the train floor is 33mm, which is exactly the bump height. The rotational vibration around the longitudinal axis (Theta1) is between -1.25e-6 rad and 1.80e-6 rad. The rotational vibration along the lateral axis (Theta 2) stays between -2.47e-3 rad and 2.84e-4 rad. The steady state angle is -2.2e-3rad when the front bogies are on top of the bump and the rears ones are at the bottom.

Fig. 6.56 and Fig. 6.57 plot the response of housing for flywheel 1(the most bottom one). Similar to the train floor, the longitudinal and lateral motion relative to the train floor is zero. The relative motion between the housing and train floor is between -0.83mm and 1.01mm. The relative rotation around train traveling direction axis (theta1) stays between -1.66e-6 and 1.25e-6 rad. The relative rotational vibration around lateral axis (theta2) has amplitude between -1.23e-3 rad and 1.42e-3 rad.

The relative motion between center of flywheel 1 and its housing are shown Fig. 6.58 and Fig. 6.59. As can be seen in the figures, the axial vibration amplitude at center of the flywheel 1 is between -0.037mm and 0.047mm. The relative rotation around Theta1 is between -1.87e-4 rad and 1.92e-4 rad. Rotation around Theta 2 axis is between -4.89e-5 and 4.71e-5 rad.

Due to small amplitude of the relative rotation between flywheels and housings, it can be assumed that the maximum motion under axial catcher bearings appears on two

horizontal axes, which is a combination of axial and angular relative motion between flywheels and their housings. The relative angular motions were converted to linear motions at axial catcher bearing radius and combined with the axial relative vibrations between center of flywheel and its housing. The resulted amplitudes at the 4 point (positive and negative point at each of the 2 horizontal axes) were evaluated and the maximum value was taken as the maximum motion under axial catcher bearings. The maximum relative radial motion between flywheel and its housing is actually the relative motion to radial catcher bearings. The relative motions between flywheel 1 and its catcher bearings are plotted in Fig. 6.60.The maximum relative motion appears under axial catcher bearing with a value of 0.083mm, which is 11.8% of catcher bearing gap.

Fig. 6.61-Fig. 6.64 presents the vibrations for flywheel 2 and its housing. The vertical vibration of the housing stays within the range of -0.83mm to 1.02mm. The housing 2 rotational vibration amplitude is less than 1.27e-6 rad for Theta1 and 1.42e-3 rad for Theta2. The relative transitional motions between centers of flywheel 2 and housing 2 are identical to those between flywheel 1 and its housing. The relative rotational motion of flywheel 2 around lateral axis (Theta2) is similar to the flywheel 1 assembly (between -4.94e-5 rad and 4.71e-5 rad). However, the rotational vibration for Theta1 of flywheel 2 has similar amplitude but opposite direction to that of flywheel 1, namely between -1.93e-4 rad and 1.88e-4 rad. The reason for this behavior is that the Theta1 motion during bump passing is caused by gyroscopic effect and flywheel 1 and flywheel 2 counter-rotate with each other. The biggest motion under axial catcher bearing is 0.102mm (14.5% of axial catcher bearing gap) as shown in Fig. 6.65.

Fig. 6.66-Fig. 6.69 shows the motion of the flywheel 3 and its housing. For the housing 3, the positive & negative peak relative rotation is 1.25e-6 rad & -1.28e-6 rad for Theta1 and 1.42e-3 rad & -1.24e-3 rad for Theta 2. The housing vibrates relative to the train floor between -0.83mm and 1.02mm. The biggest relative motion between center of flywheel 3 and it housing are 0.047mm in the positive direction and 0.037mm in the negative direction. The relative rotation between the flywheel and housing is -1.87e-4rad to 1.92e-4rad for Theta1 and -4.88e-5rad to 4.70e-5rad for Theta2. Fig. 6.70 shows that the maximum possible motion under axial catcher bearing for flywheel 3 is same as flywheel 1, with a value of 0.083mm (11.8% of axial catcher bearing gap).

The vibrations for flywheel 4 and its housing are almost identical to those of flywheel 2 assembly (Fig. 6.71-Fig. 6.74). The vertical vibration between housing and floor is -0.83mm to 1.01mm. The Theta1 motion between housing and floor is -1.33e-6rad to 1.26e-6rad. The values for the Theta2 motion between housing and train floor stays in the range of -1.24e-3rad and 1.42e-3rad. The vertical vibration for the center of flywheel relative to the housing is -0.037mm to 0.047mm. The rotational vibration between flywheel and its housing is -1.93e-4rad to 1.88e-4rad for Theta1 and -4.95e-5rad to 4.73e-5rad for Theta2. The maximum motion under axial catcher bearing for flywheel 4 is same as flywheel 2 with a value of 0.102mm and 14.5% of axial catcher bearing gap (Fig. 6.75).

As shown above, the relative motions for all flywheels and their housings are almost identical due to the high stiffness between flywheel housings. The only difference is the relative rotation around Theta1 between flywheels and their housing. This is due to the

gyroscopic effect caused by counter rotating flywheels. Coupled with the relative axial vibrations, this will also cause some small difference on maximum motions under axial catcher bearings between group FW1&FW3 and group FW2&FW4. For these reasons, the power amplifiers of the flywheels also behave very similarly. So only the amplifiers information of flywheel 1's magnetic bearings is presented here as in Fig. 6.76-Fig. 6.80.

The results confirm that the flywheel system can safely pass the average ramp without hitting the catcher bearing or power amplifier saturation.

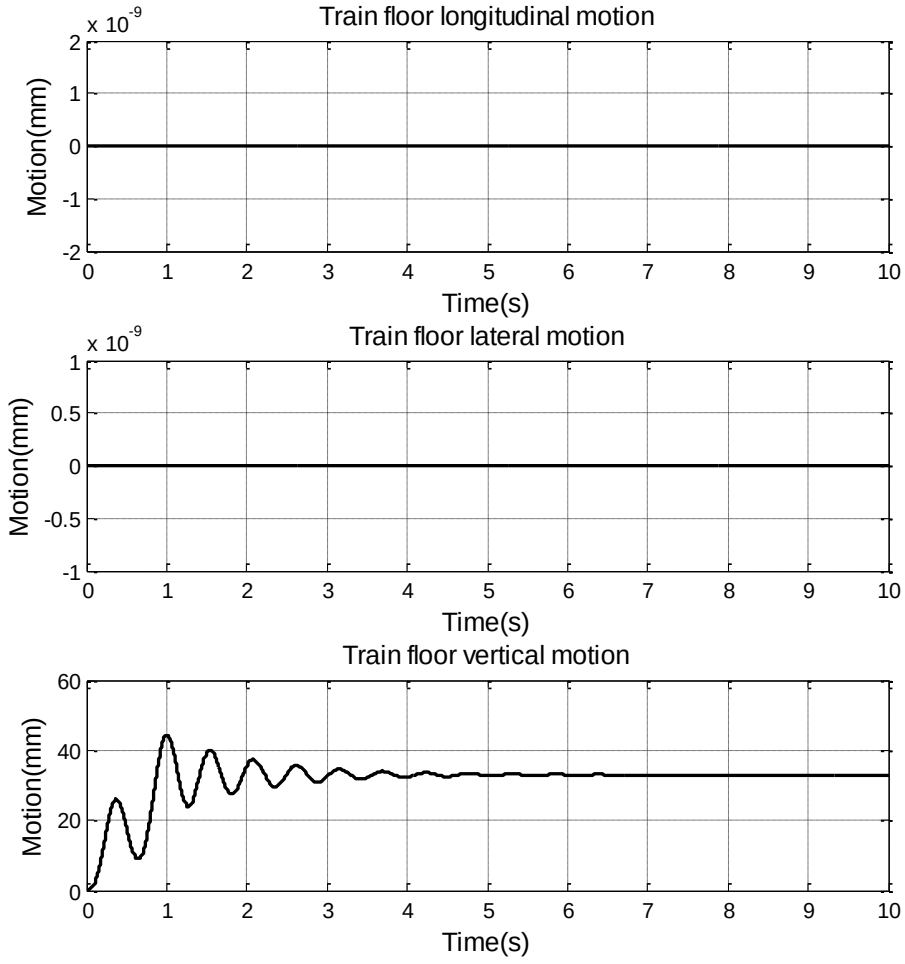

Fig. 6.54 Train Floor Transitional Vibration Responses due to Average Bridge Bump

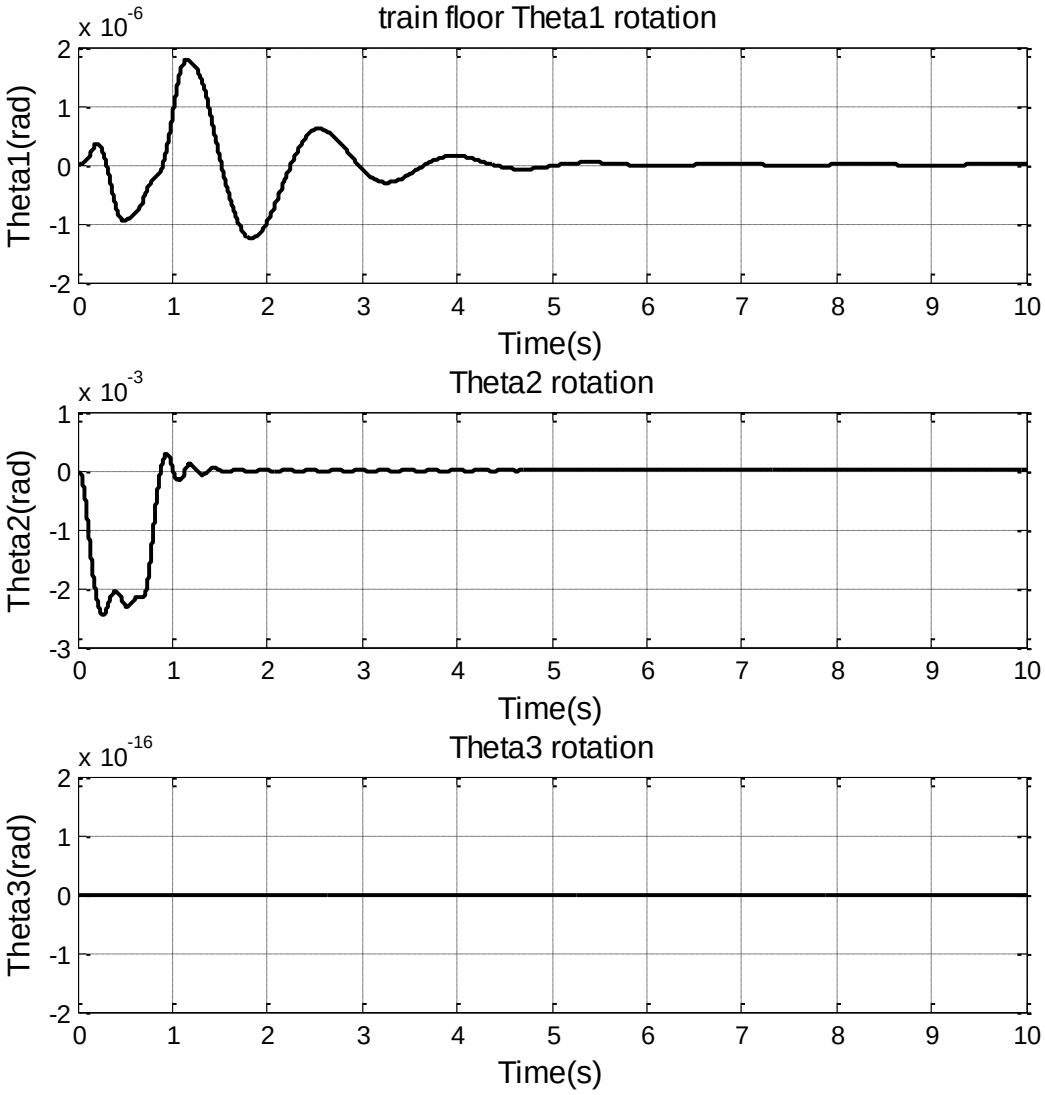

Fig. 6.55 Train Floor Rotational Vibration Responses due to Average Bridge Bump

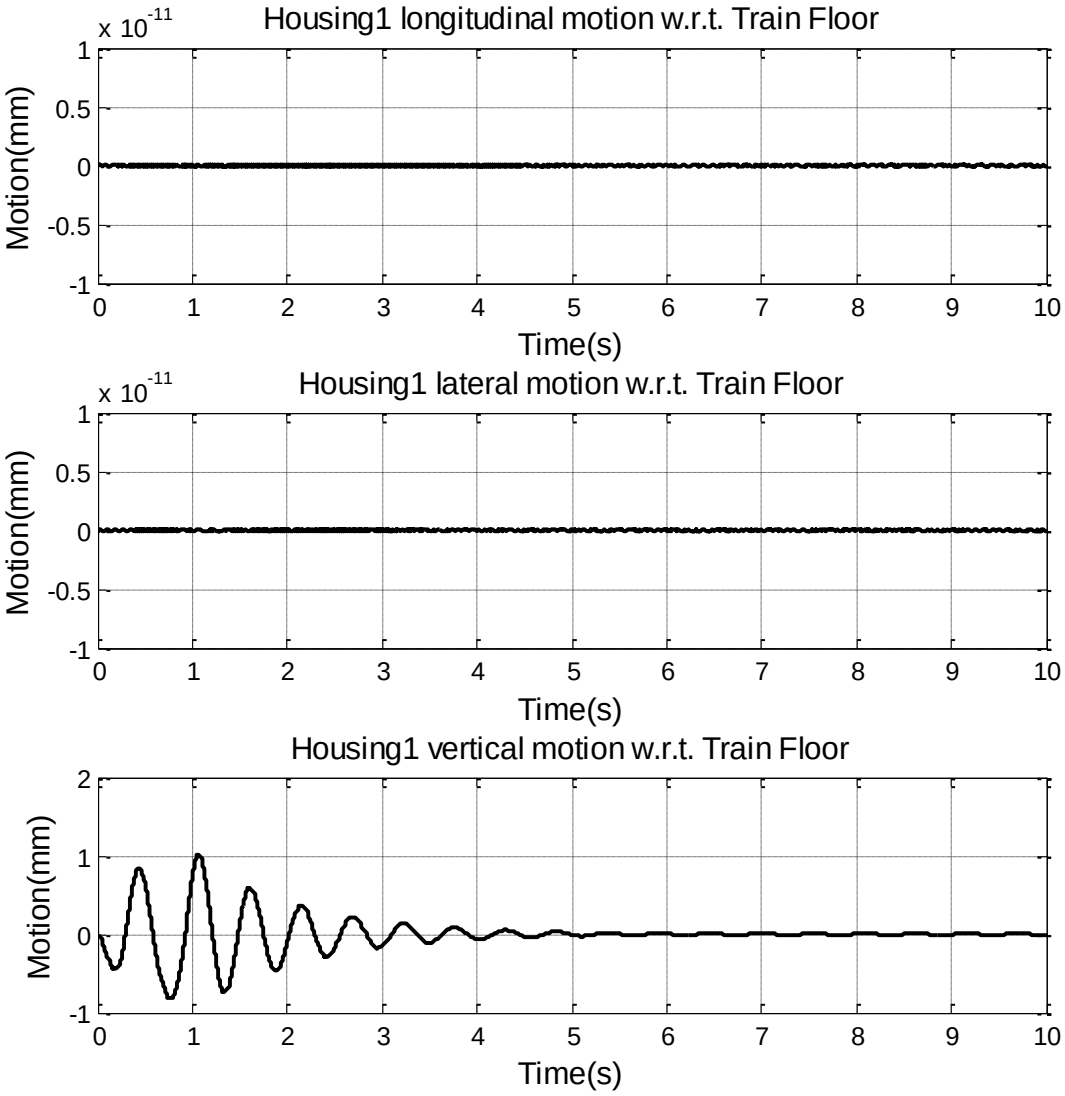

Fig. 6.56 FW1 Housing Transitional Vibration Responses due to Average Bridge Bump

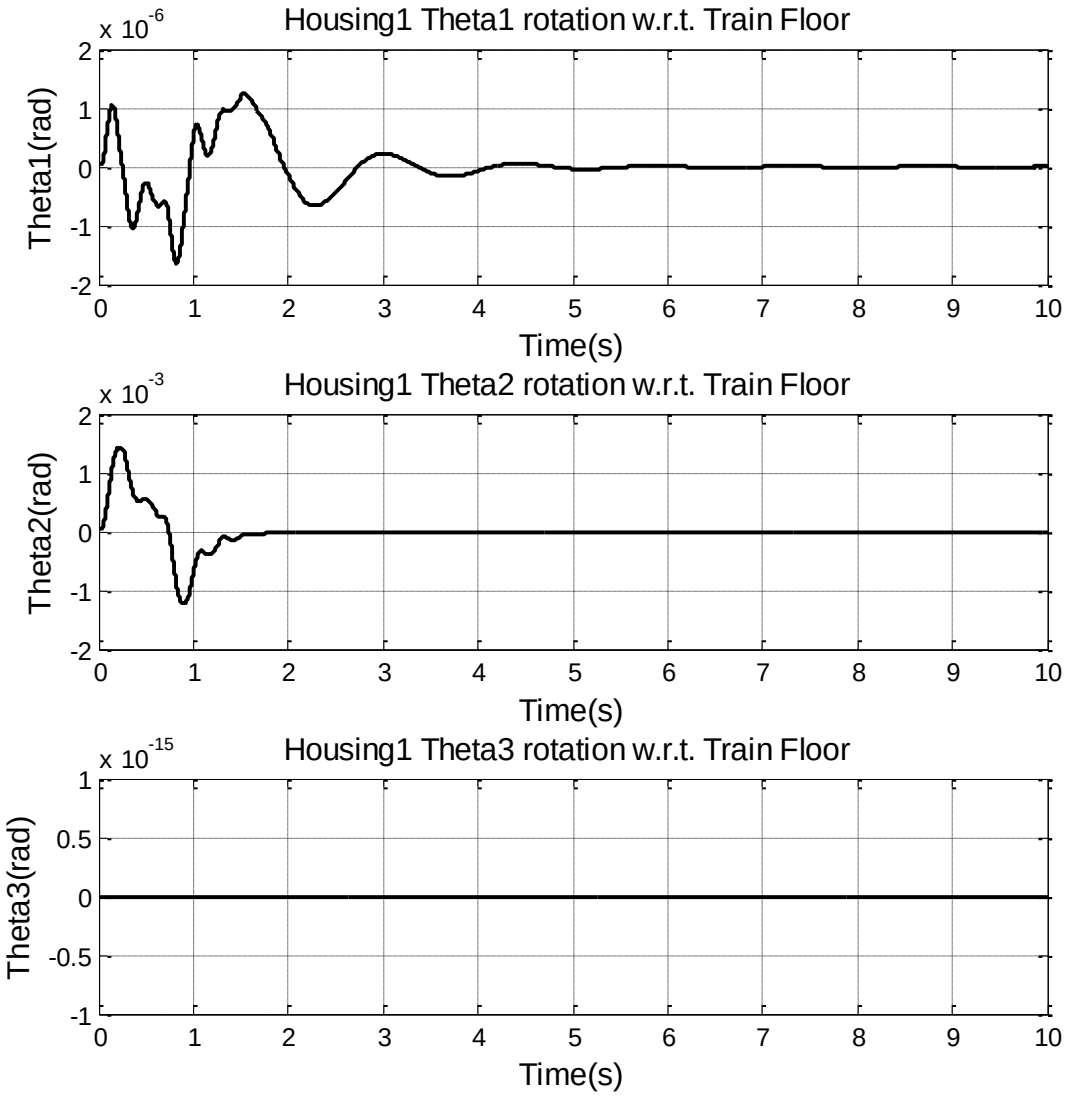

Fig. 6.57 FW1 Housing Rotational Vibration Responses due to Average Bridge Bump

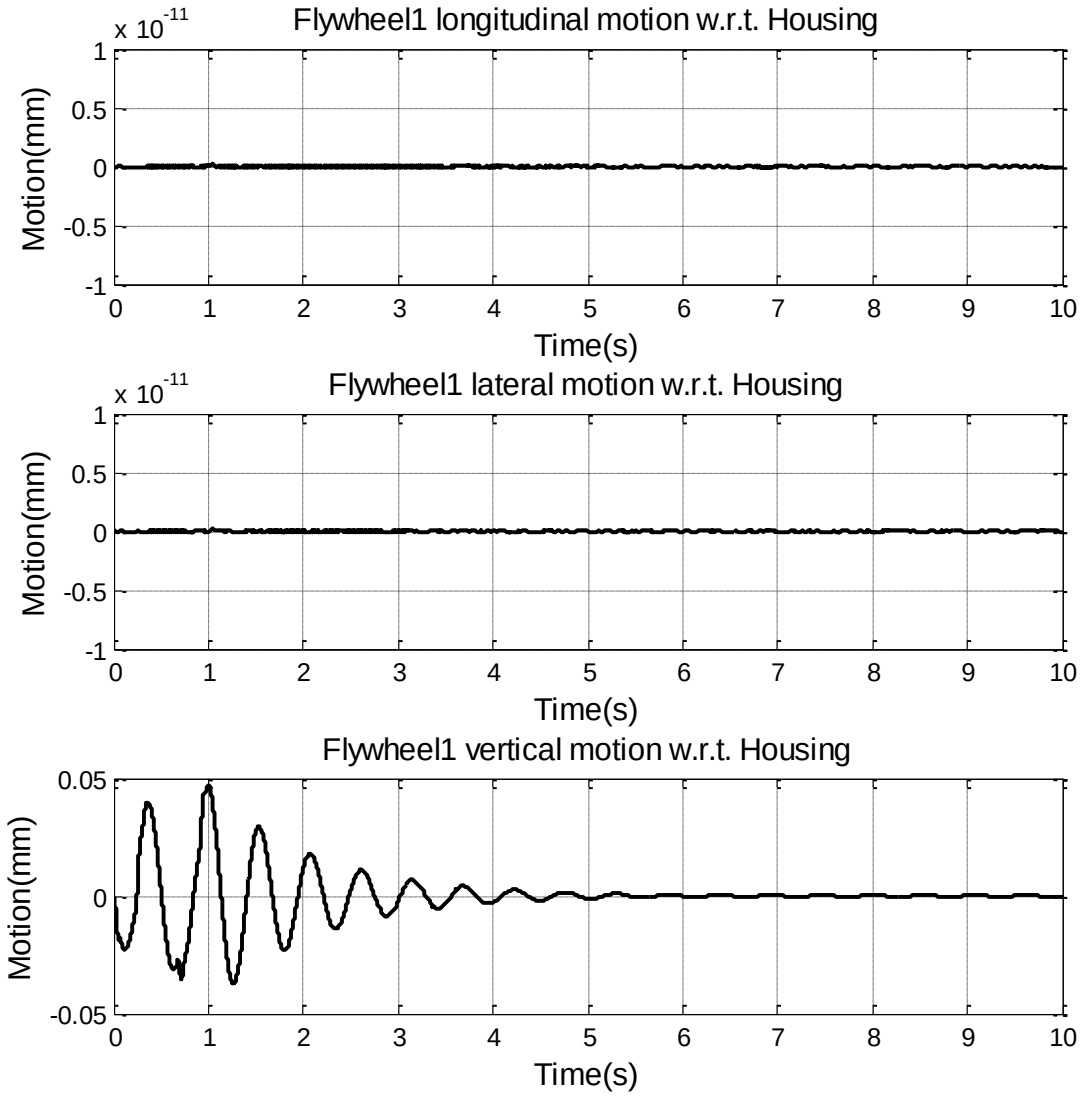

Fig. 6.58 Flywheel 1 Transitional Vibration Responses due to Average Bridge Bump

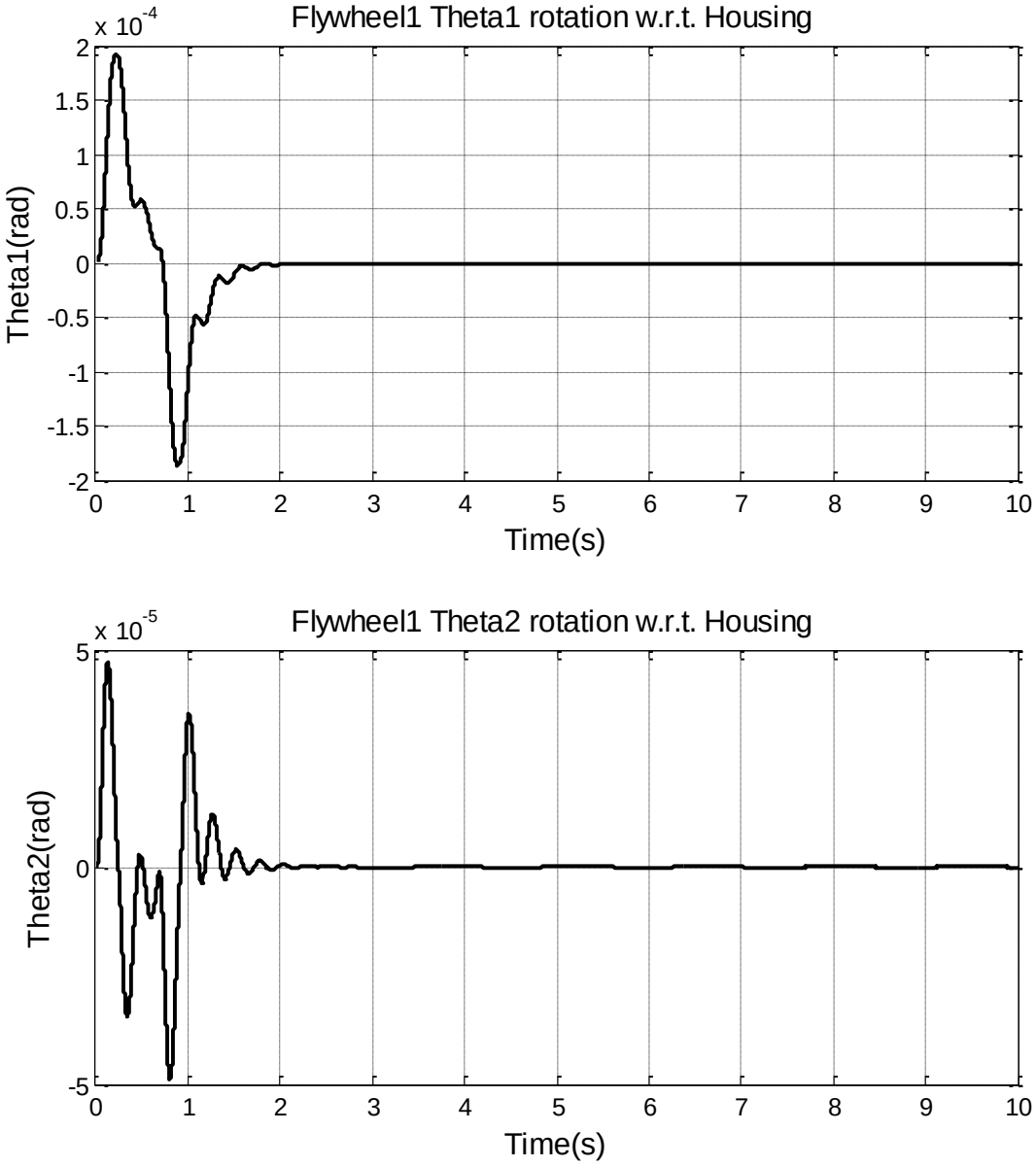

Fig. 6.59 Flywheel 1 Rotational Vibration Responses due to Average Bridge Bump

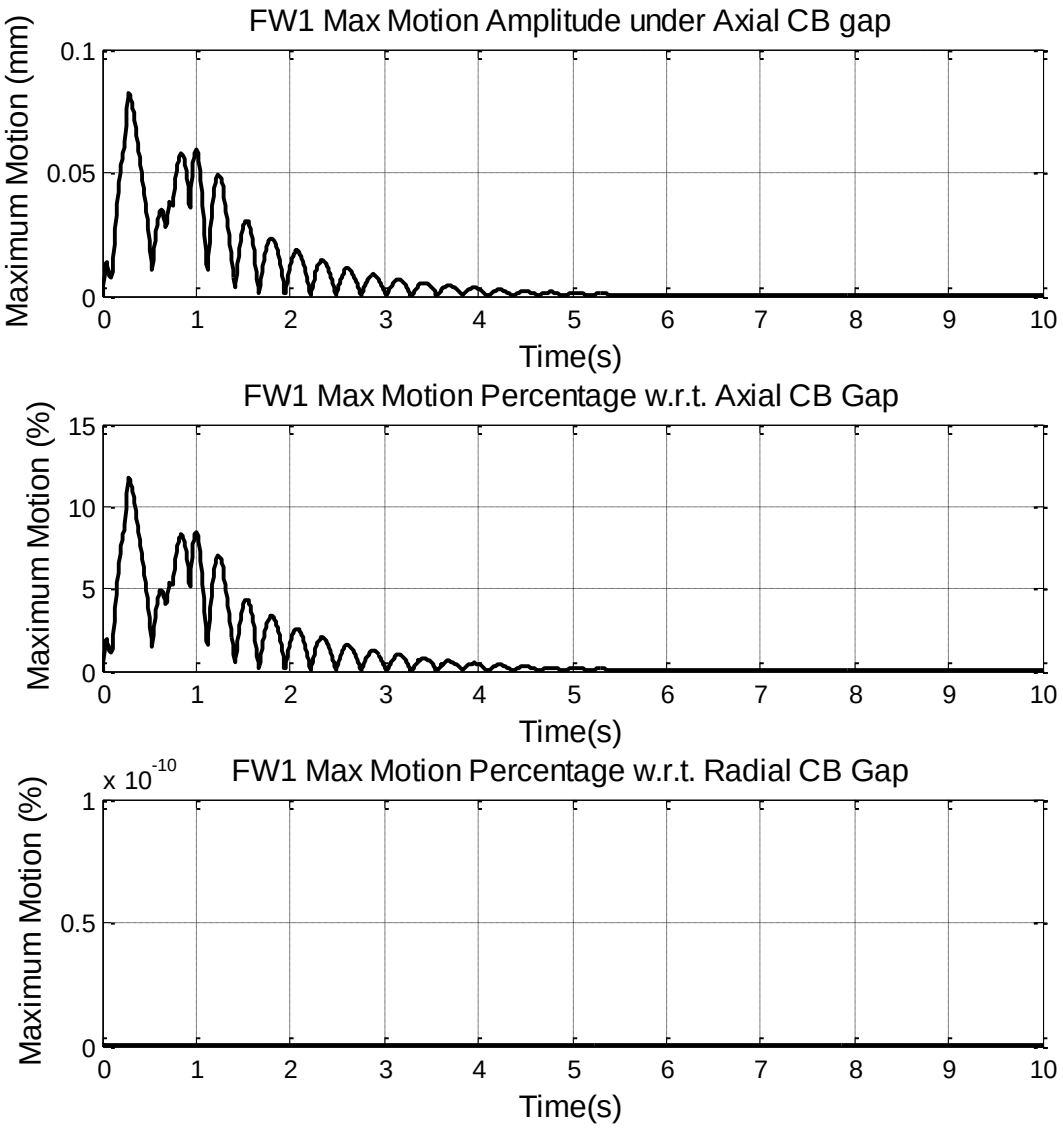

Fig. 6.60 Flywheel 1 Motion under Catcher Bearings due to Average Bridge Bump

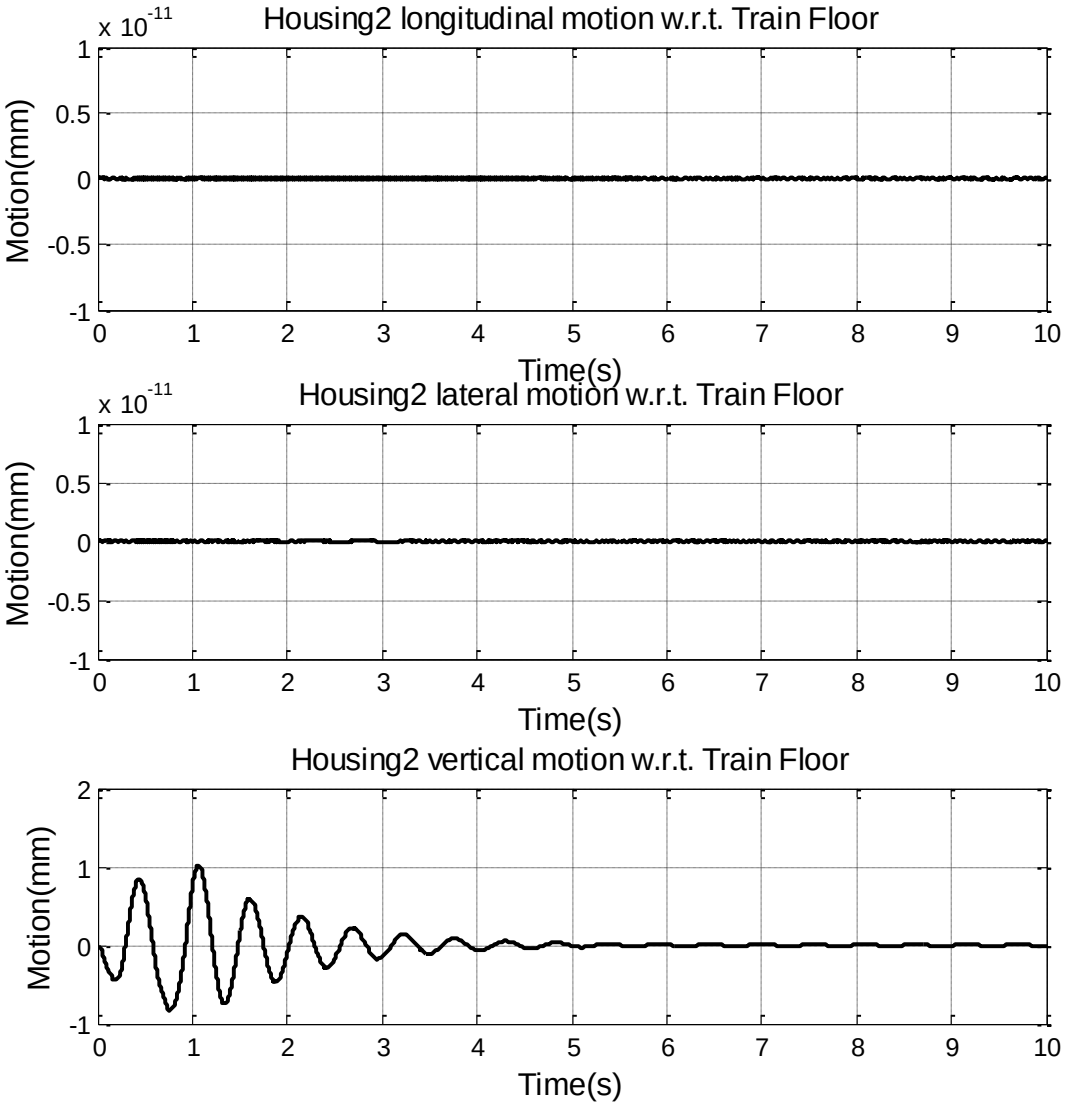

Fig. 6.61 FW2 Housing Transitional Vibration Responses due to Average Bridge Bump

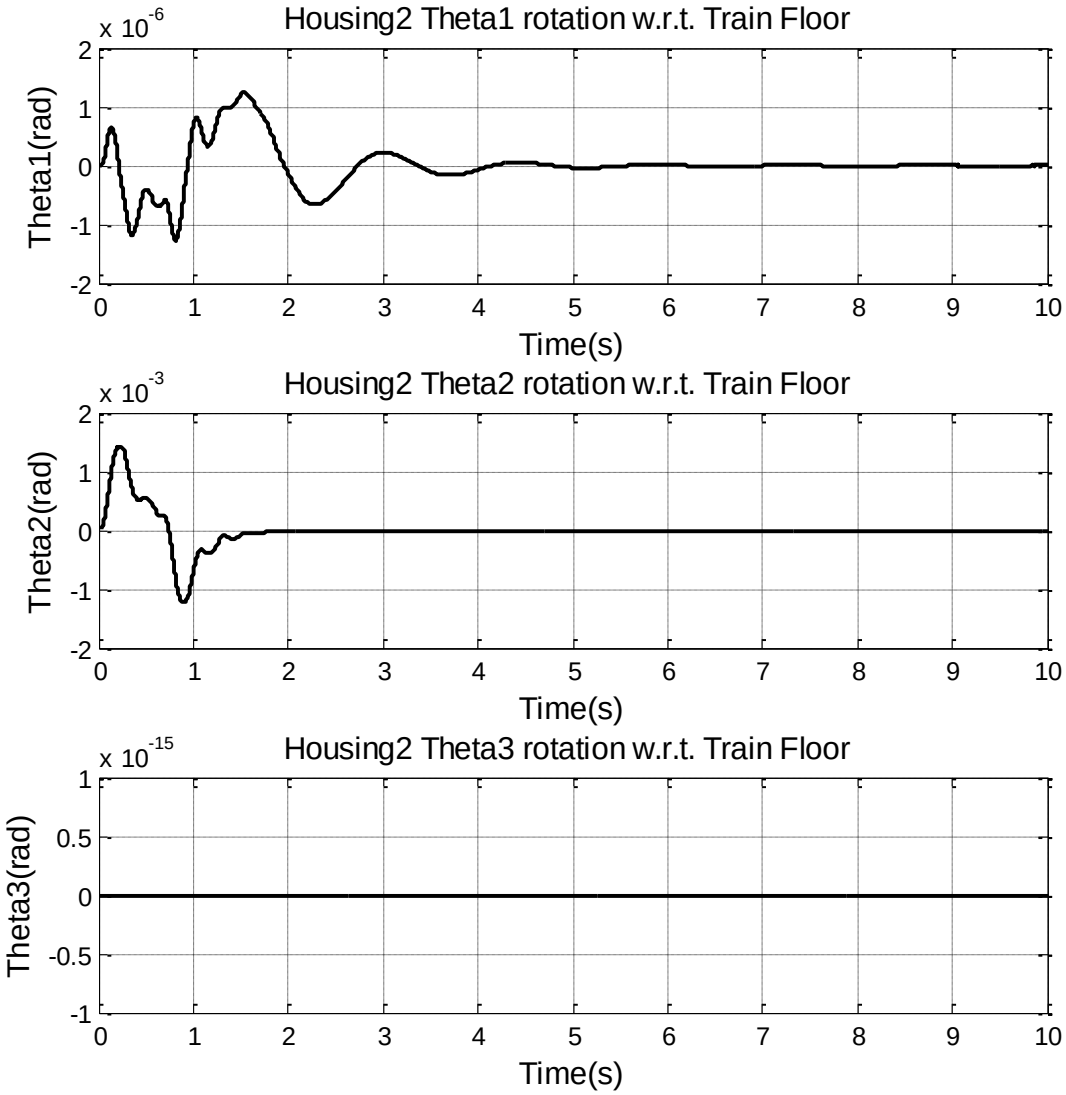

Fig. 6.62 FW2 Housing Rotational Vibration Responses due to Average Bridge Bump

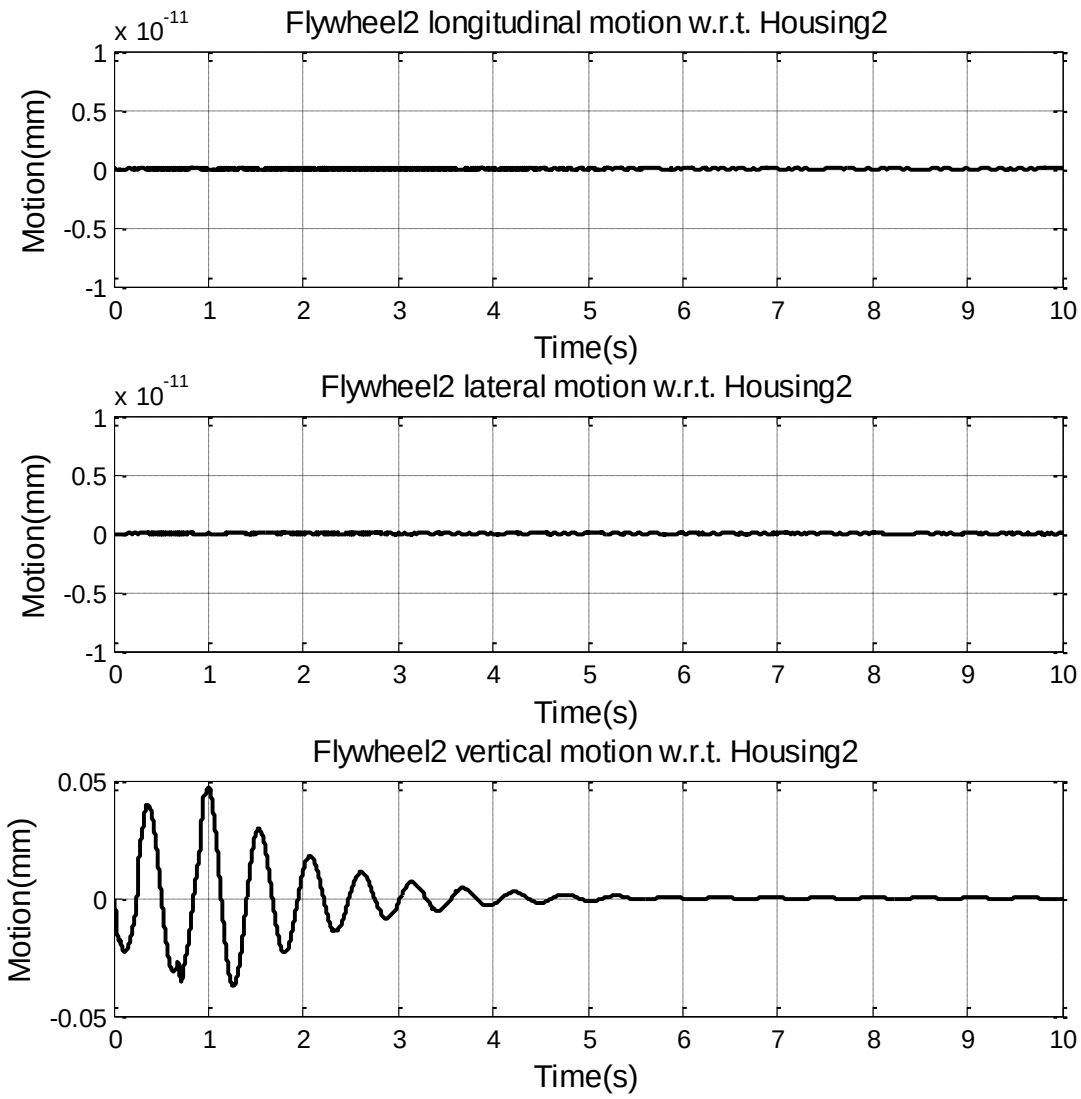

Fig. 6.63 Flywheel 2 Transitional Vibration Responses due to Average Bridge Bump

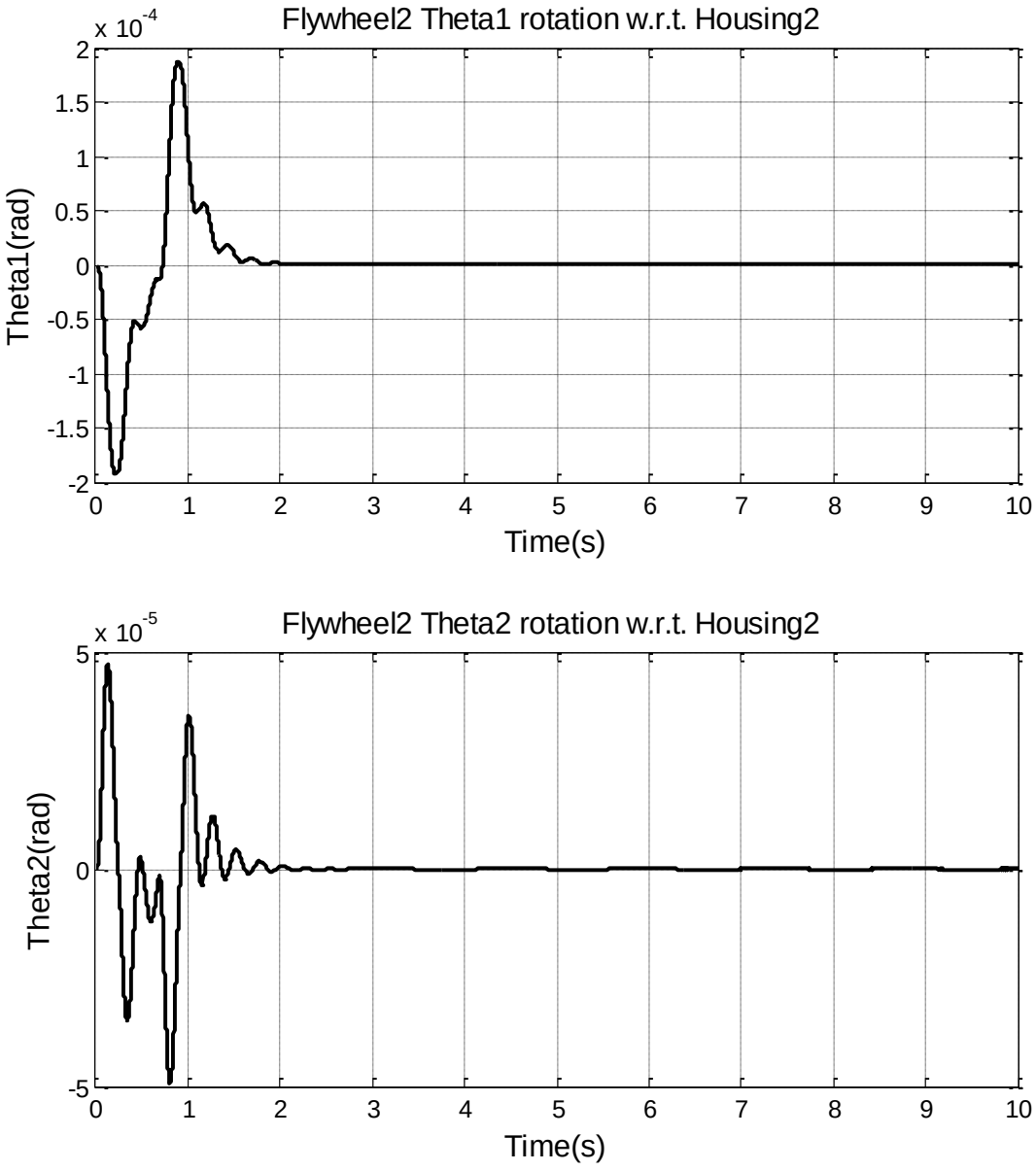

Fig. 6.64 Flywheel 2 Rotational Vibration Responses due to Average Bridge Bump

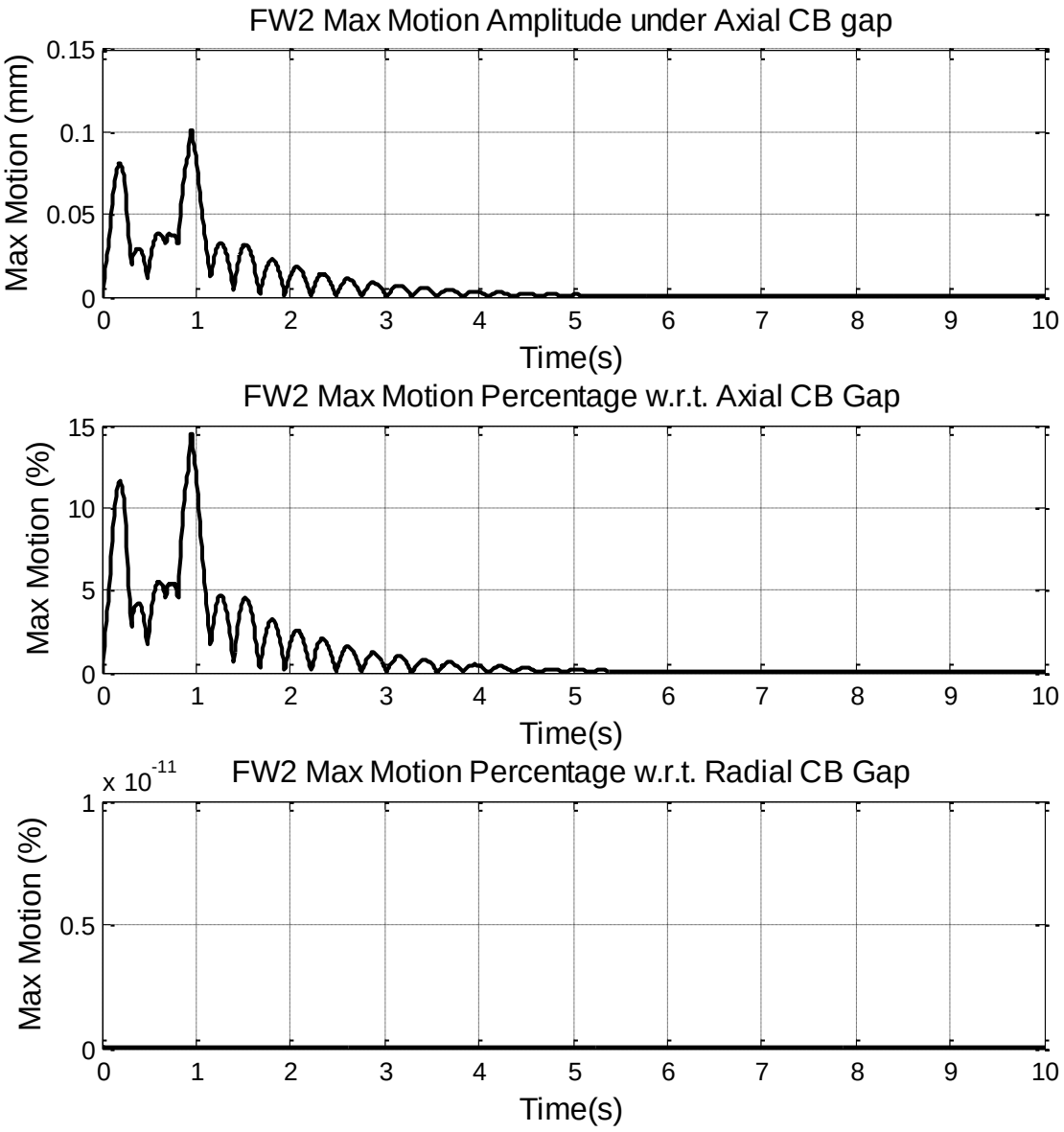

Fig. 6.65 Flywheel 2 Motion under Catcher Bearings due to Average Bridge Bump

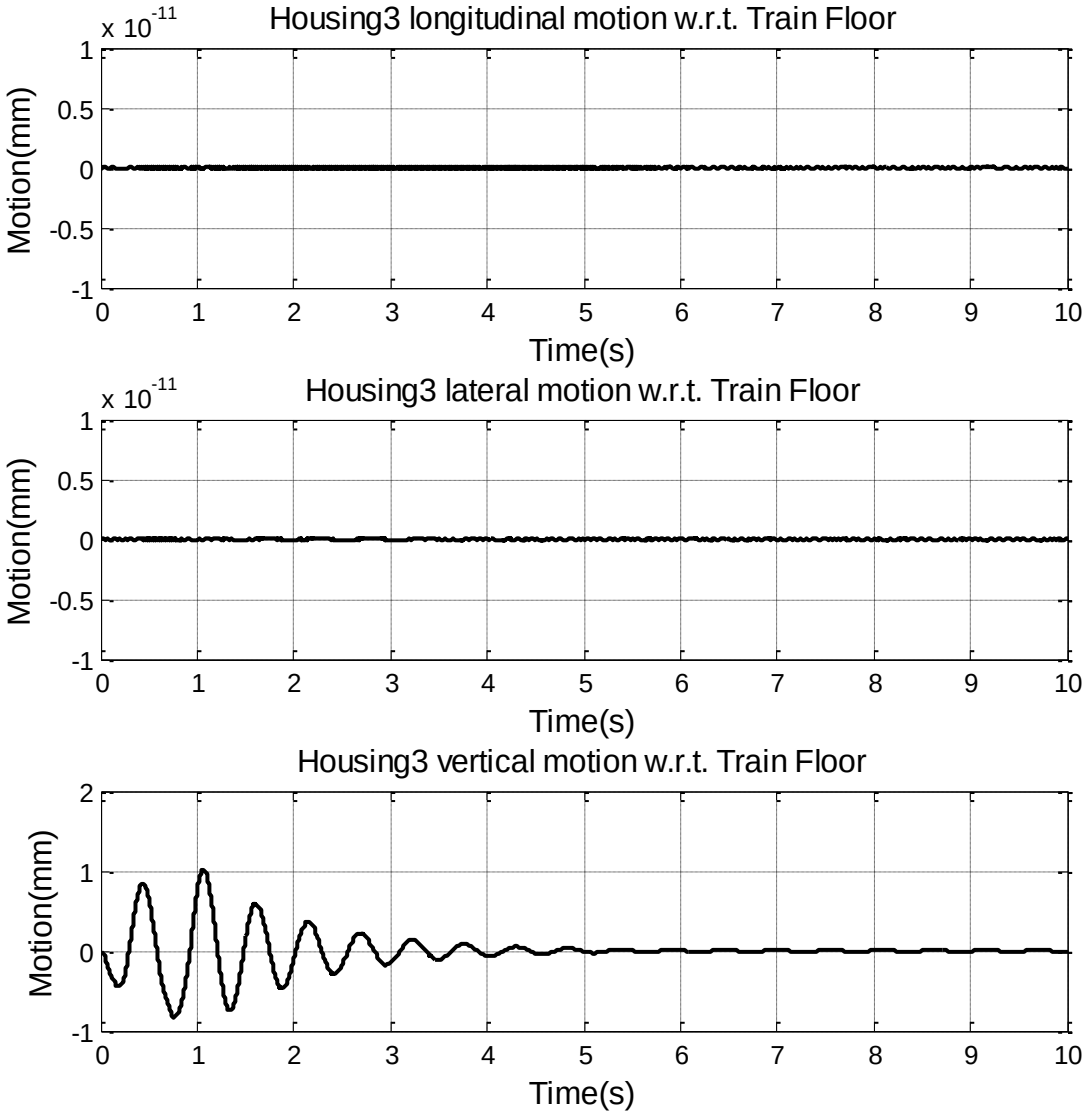

Fig. 6.66 FW3 Housing Transitional Vibration Responses due to Average Bridge Bump

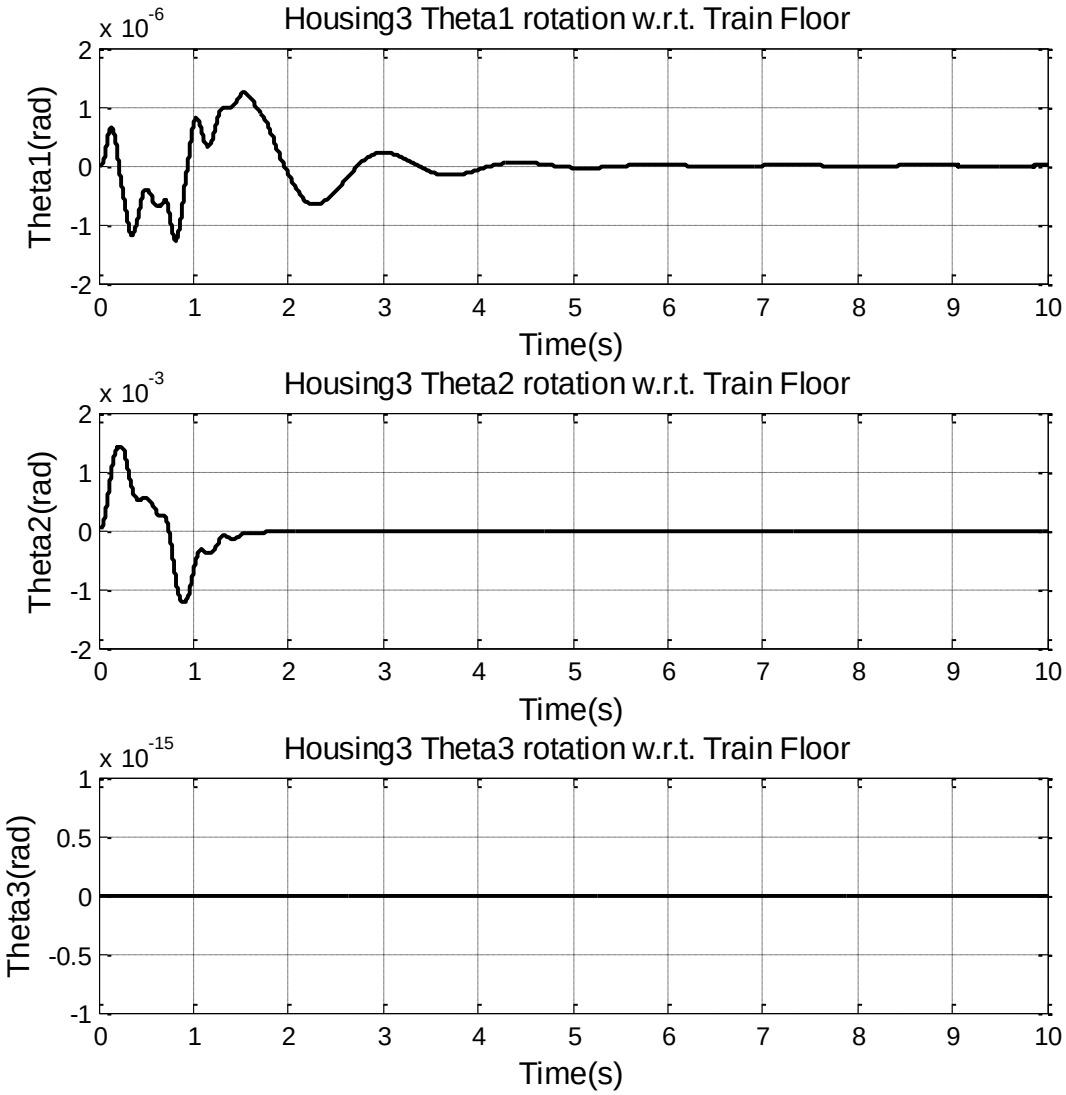

Fig. 6.67 FW3 Housing Rotational Vibration Responses due to Average Bridge Bump

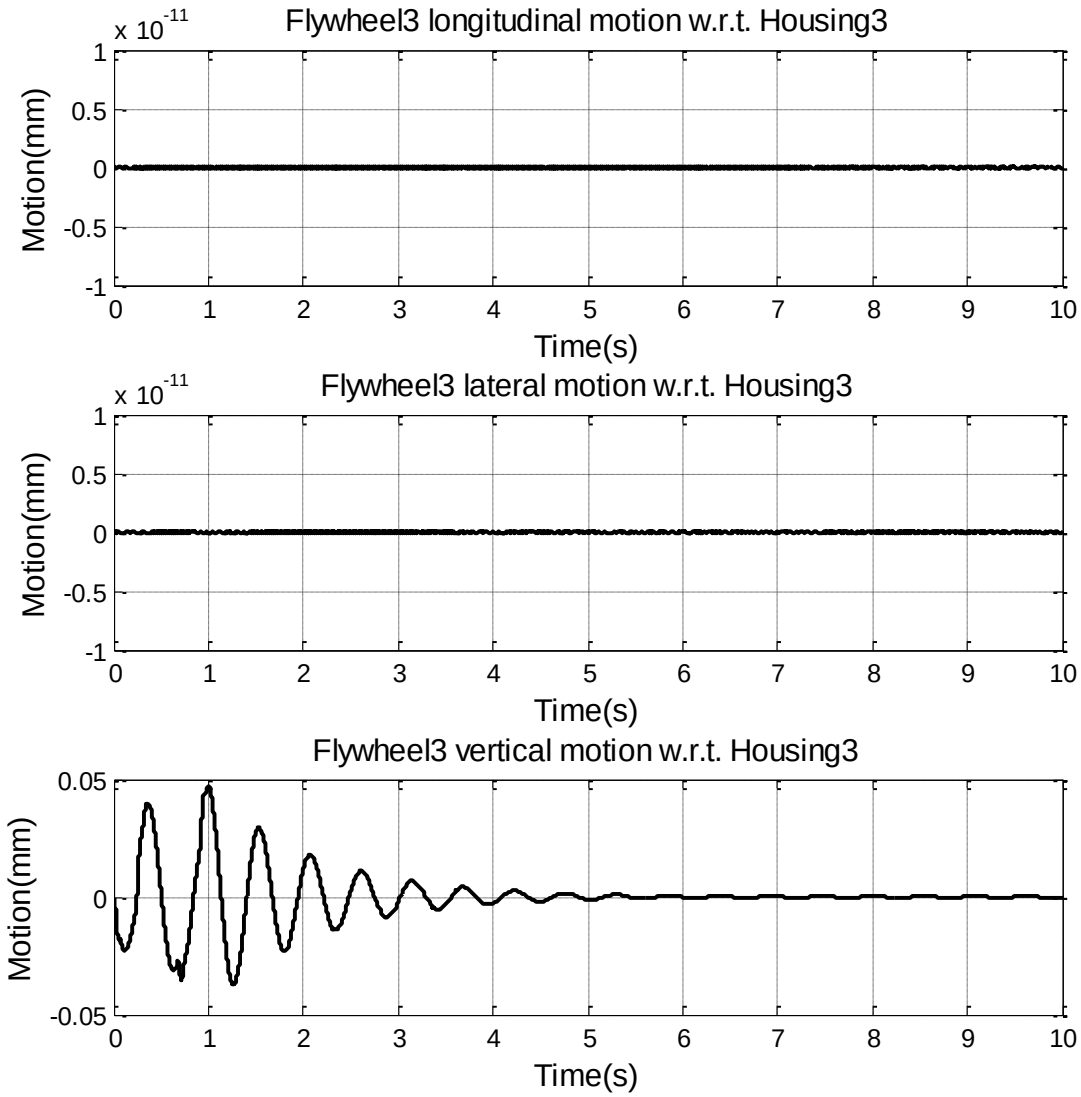

Fig. 6.68 Flywheel 3 Transitional Vibration Responses due to Average Bridge Bump

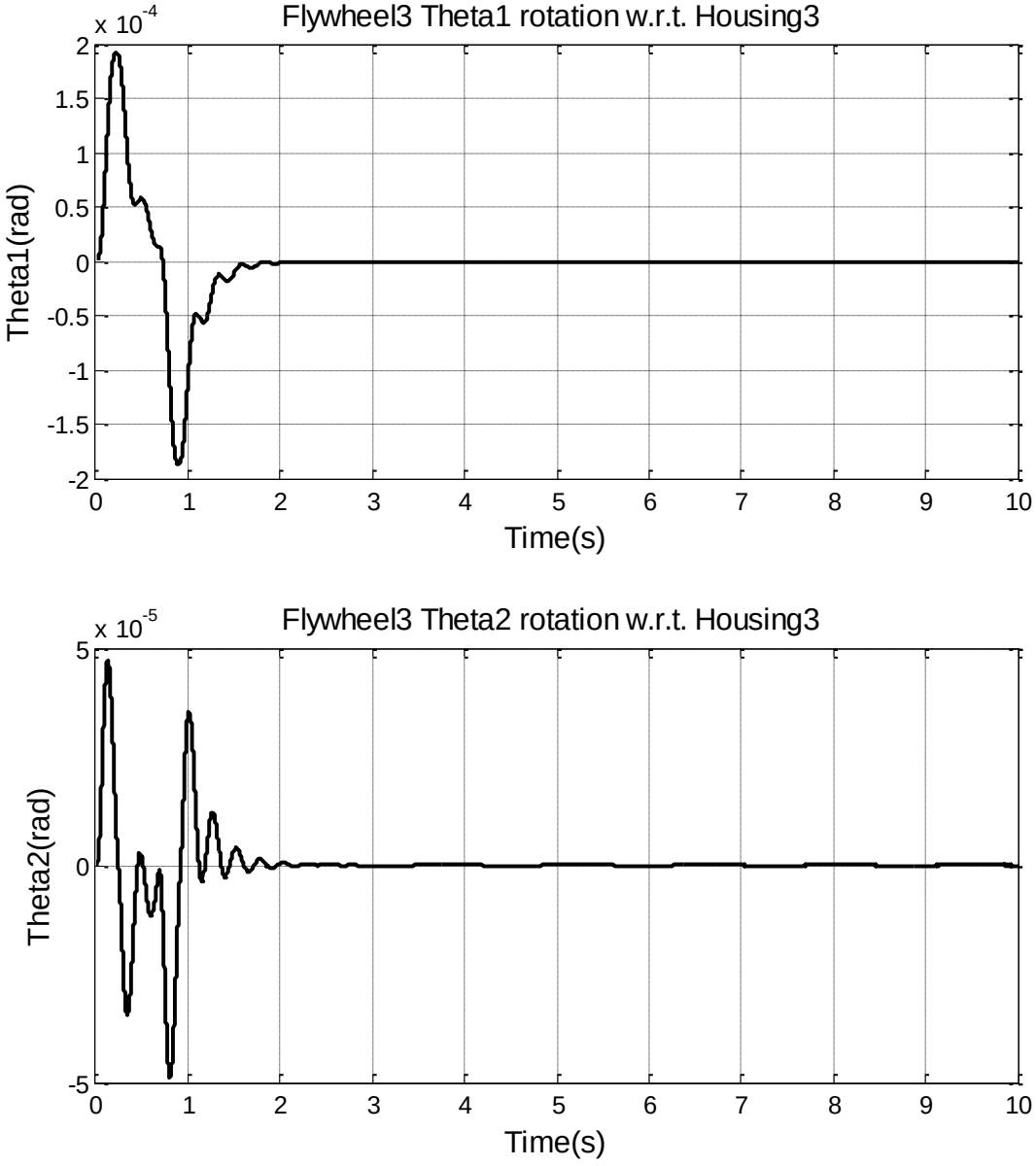

Fig. 6.69 Flywheel 3 Rotational Vibration Responses due to Average Bridge Bump

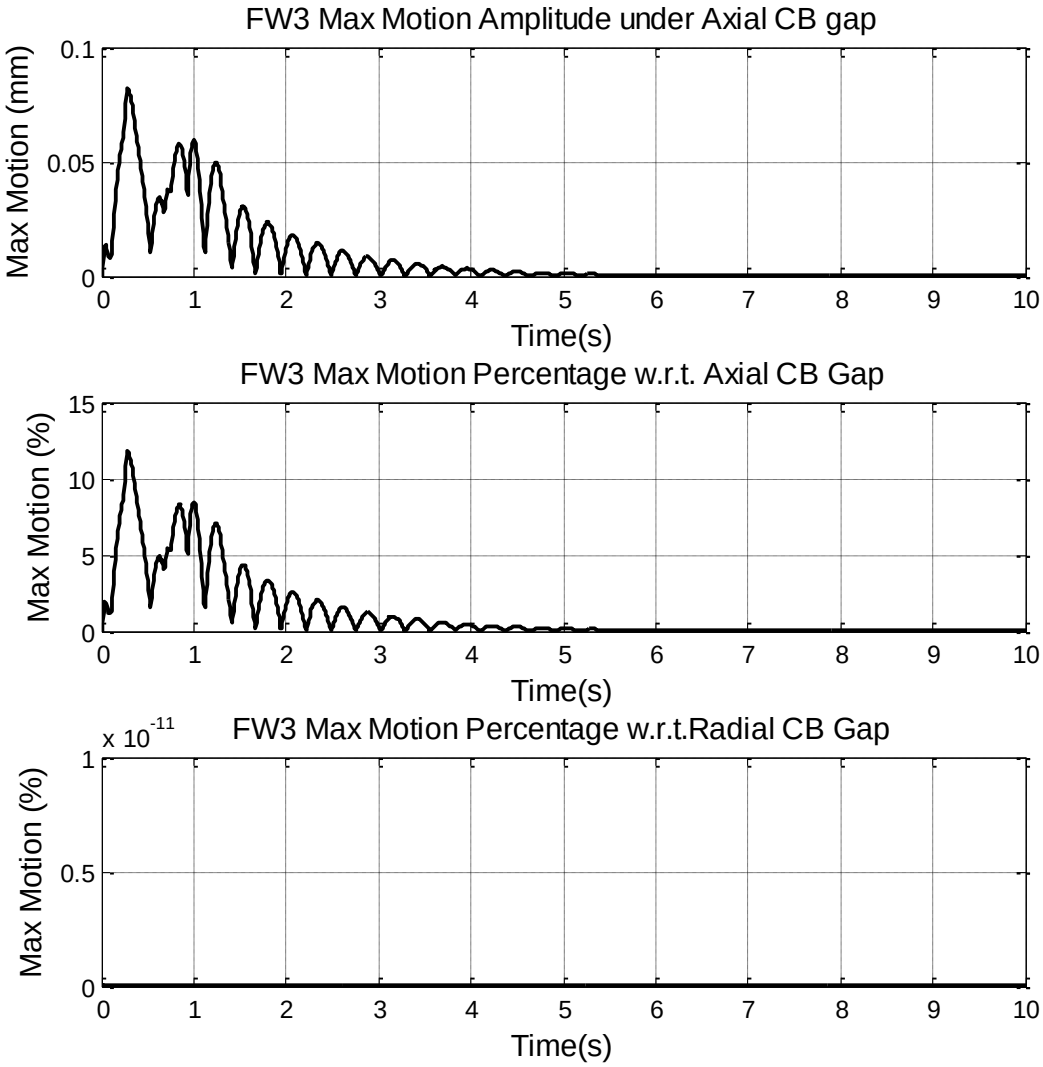

Fig. 6.70 Flywheel 3 Motion under Catcher Bearings due to Average Bridge Bump

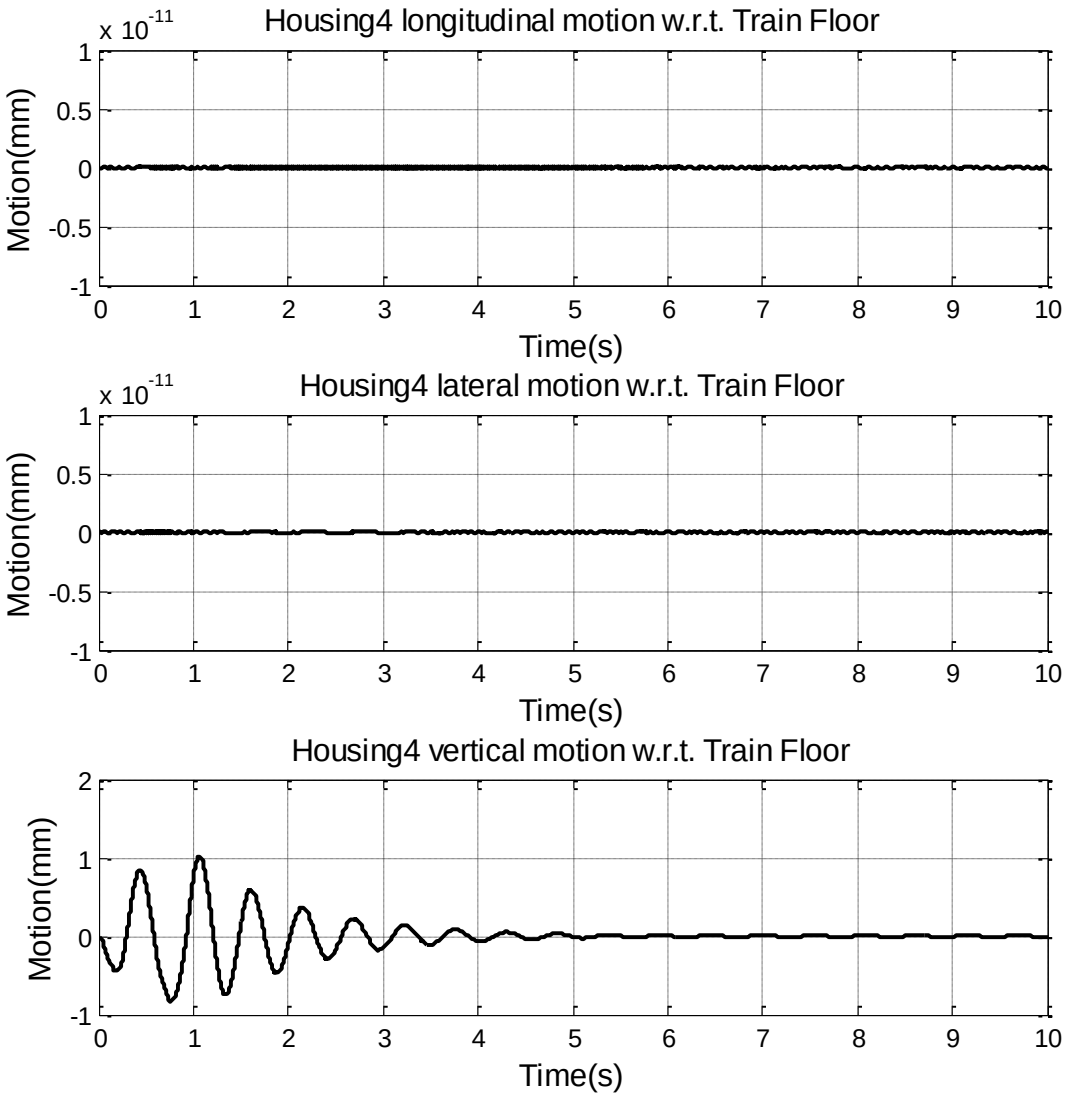

Fig. 6.71 FW4 Housing Transitional Vibration Responses due to Average Bridge Bump

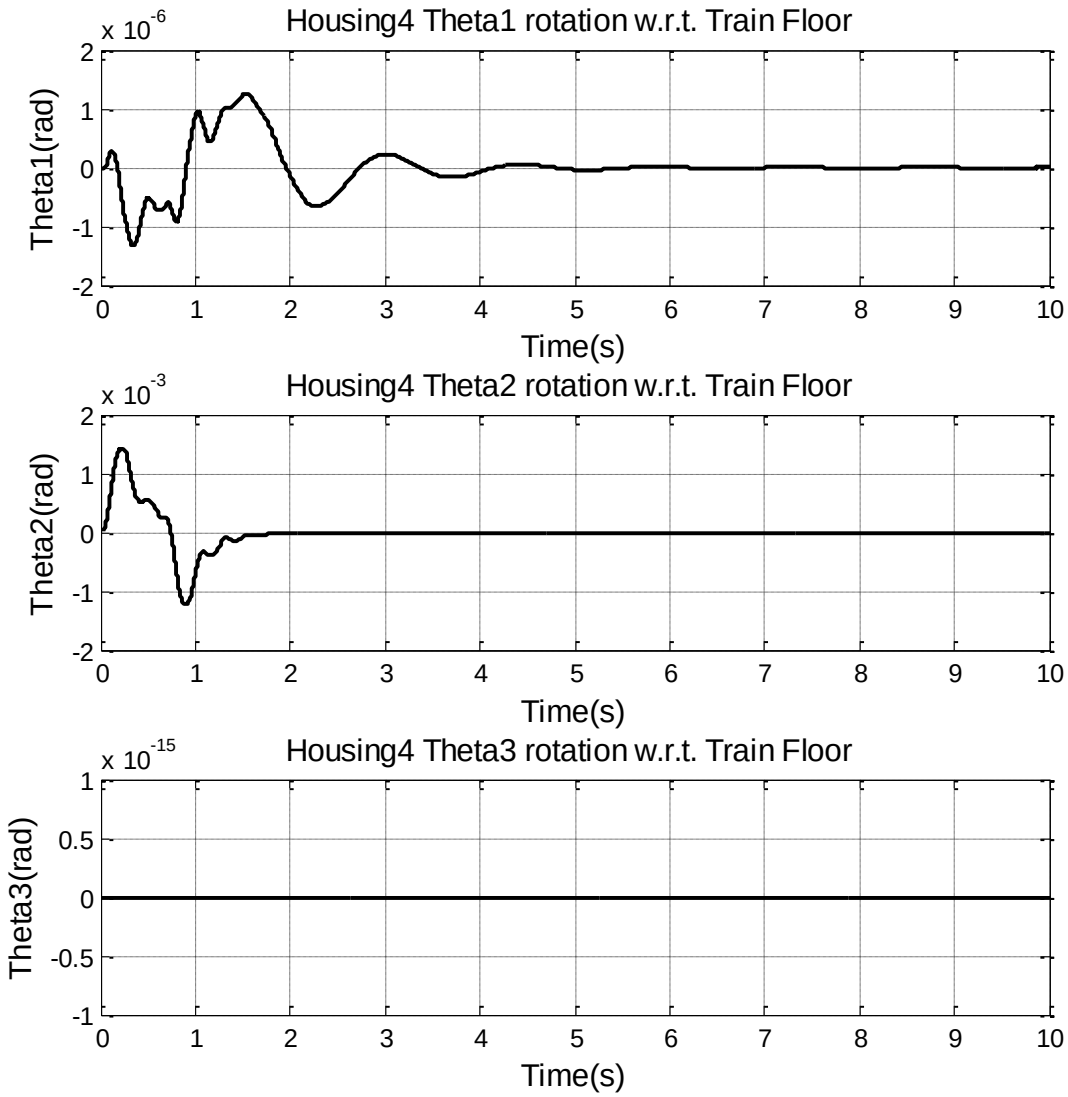

Fig. 6.72 FW4 Housing Rotational Vibration Responses due to Average Bridge Bump

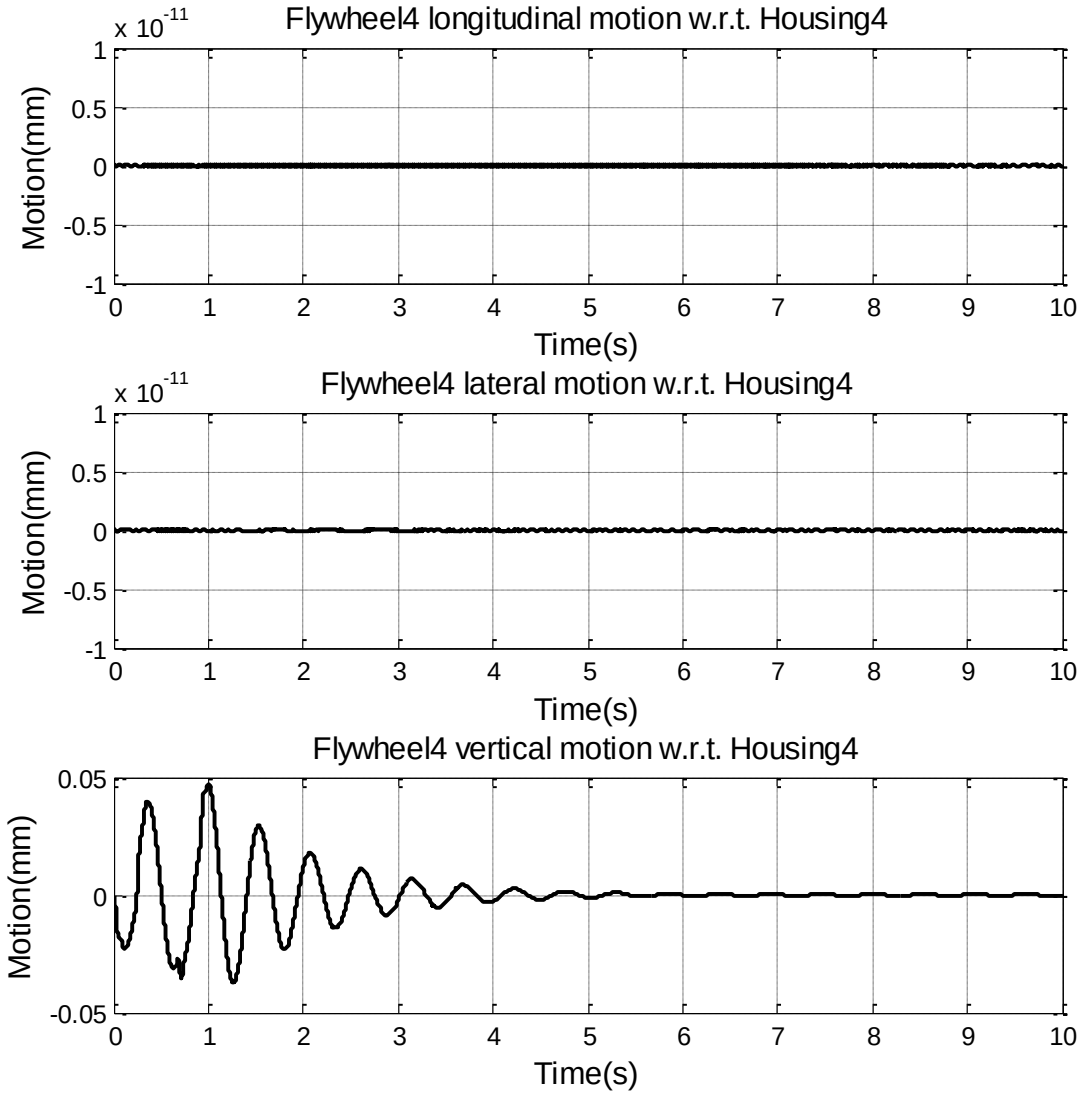

Fig. 6.73 Flywheel 4 Transitional Vibration Responses due to Average Bridge Bump

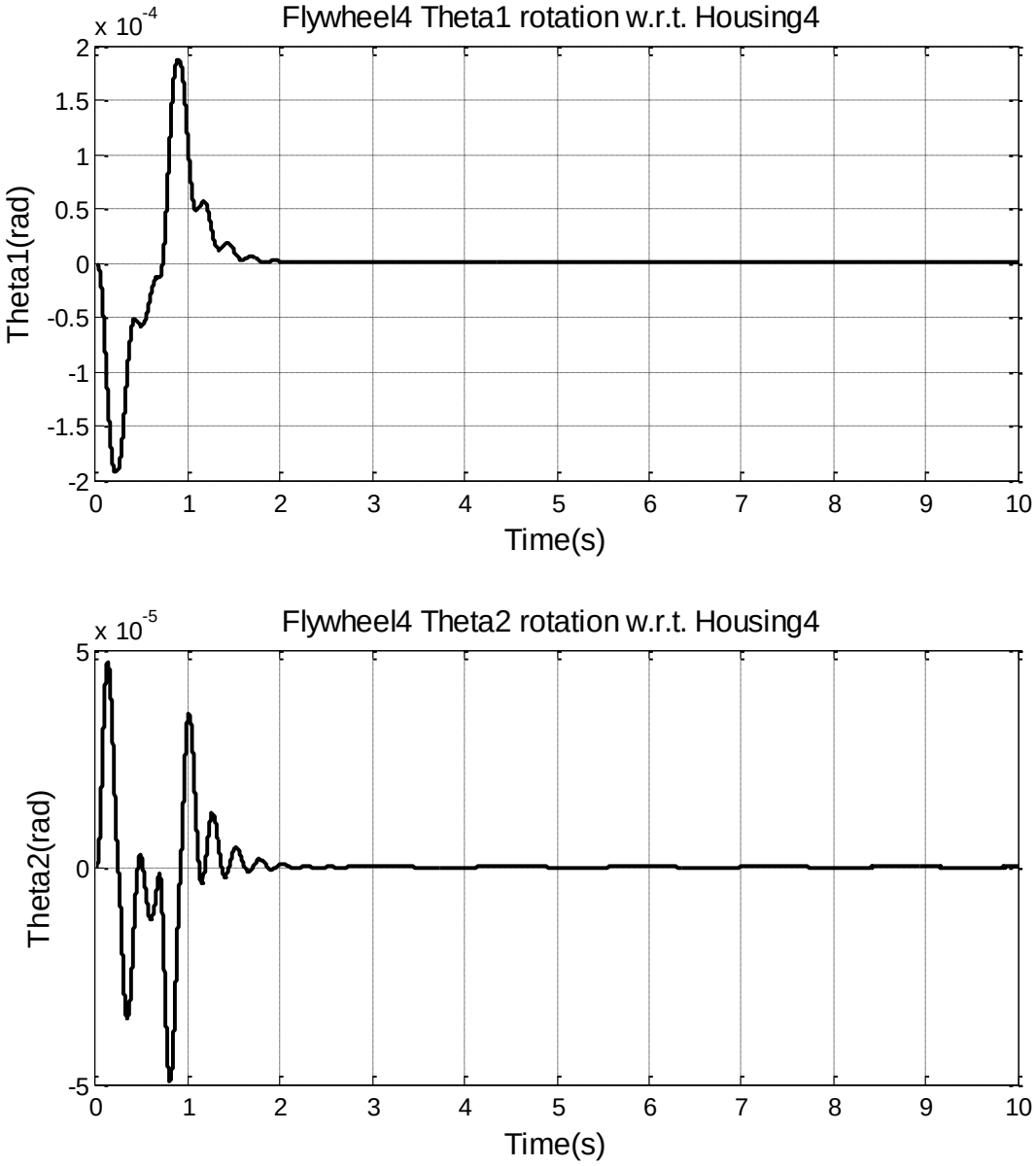

Fig. 6.74 Flywheel 4 Rotational Vibration Responses due to Average Bridge Bump

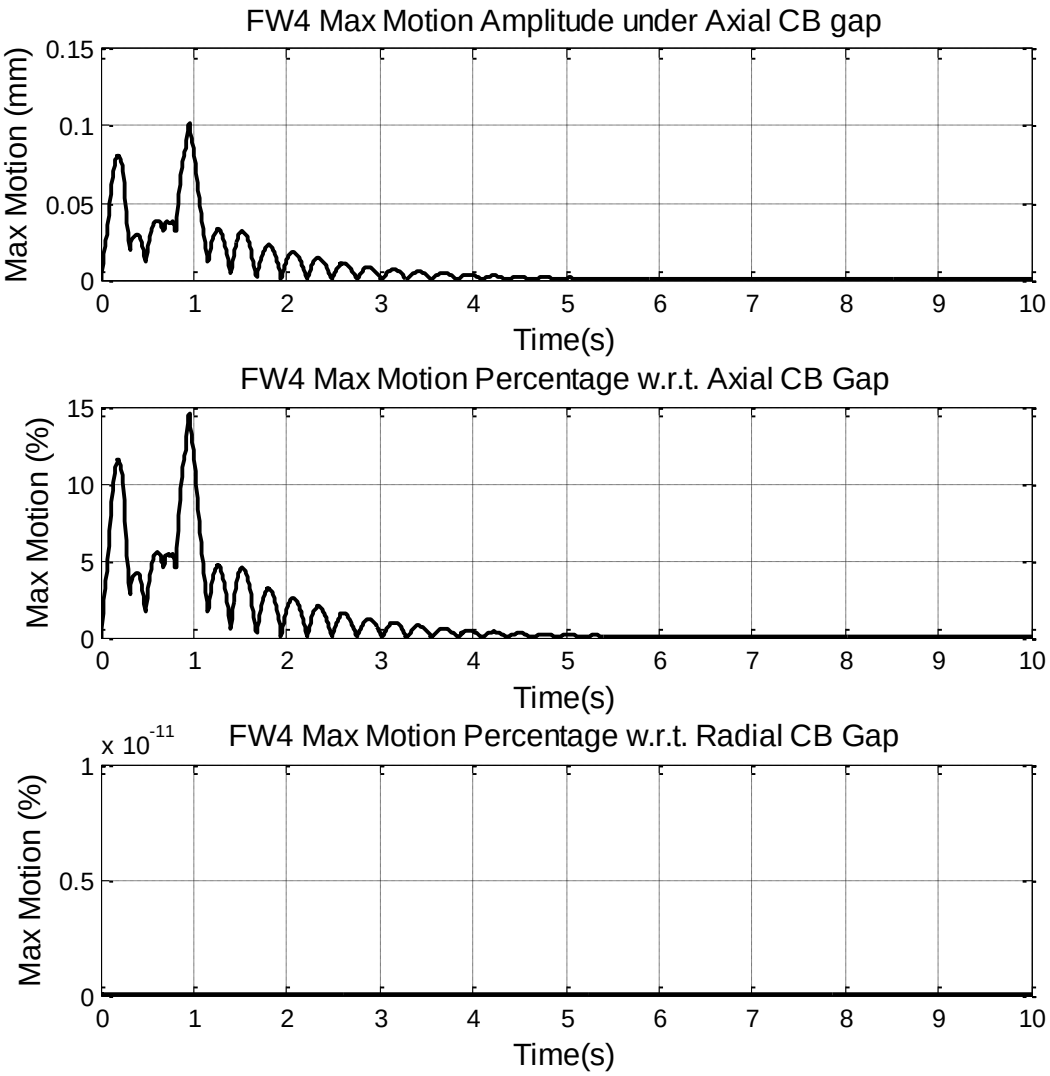

Fig. 6.75 Flywheel 4 Motion under Catcher Bearings due to Average Bridge Bump

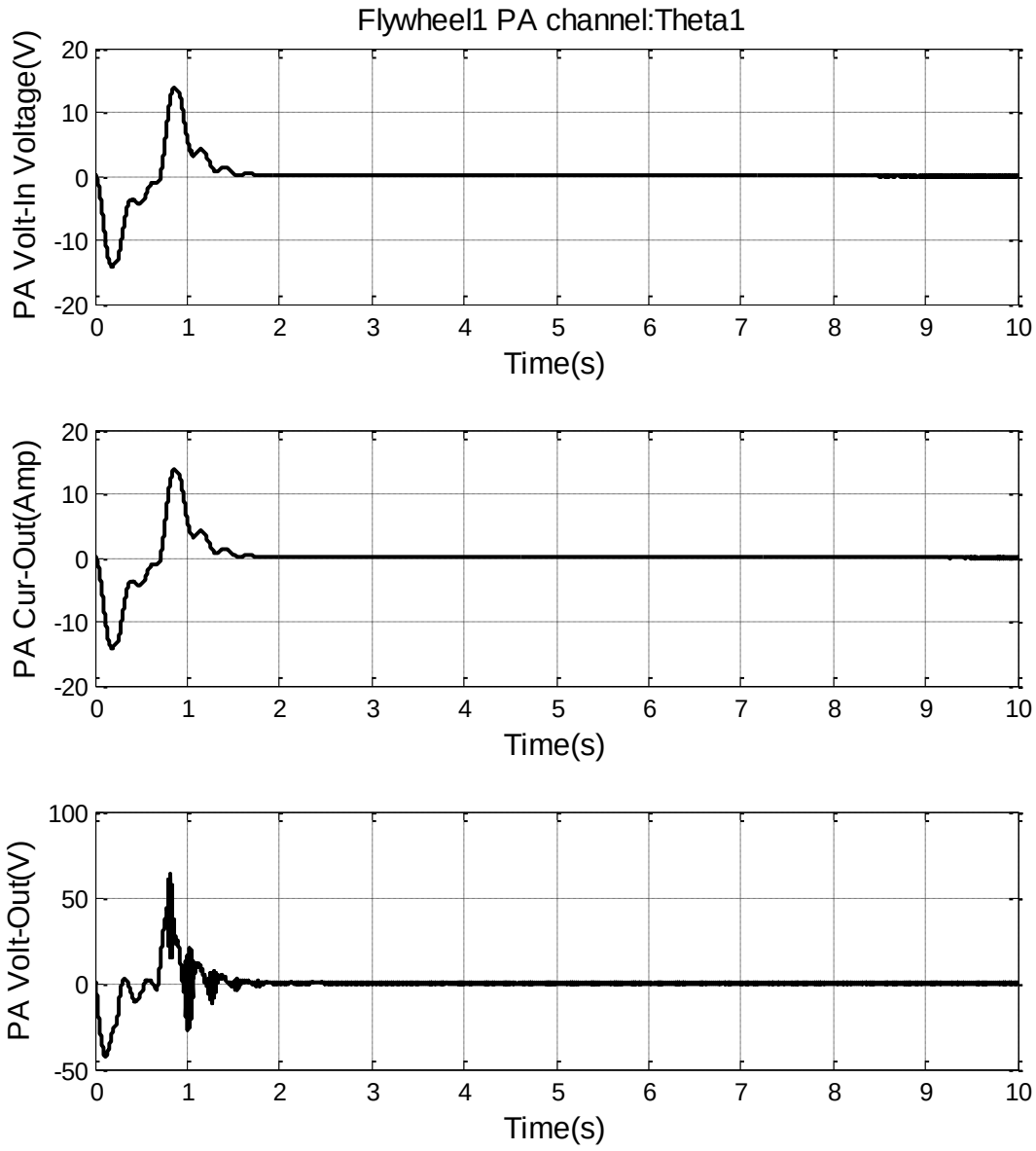

Fig. 6.76 Flywheel 1 Theta 1 Power Amplifier Responses due to Average Bridge Bump

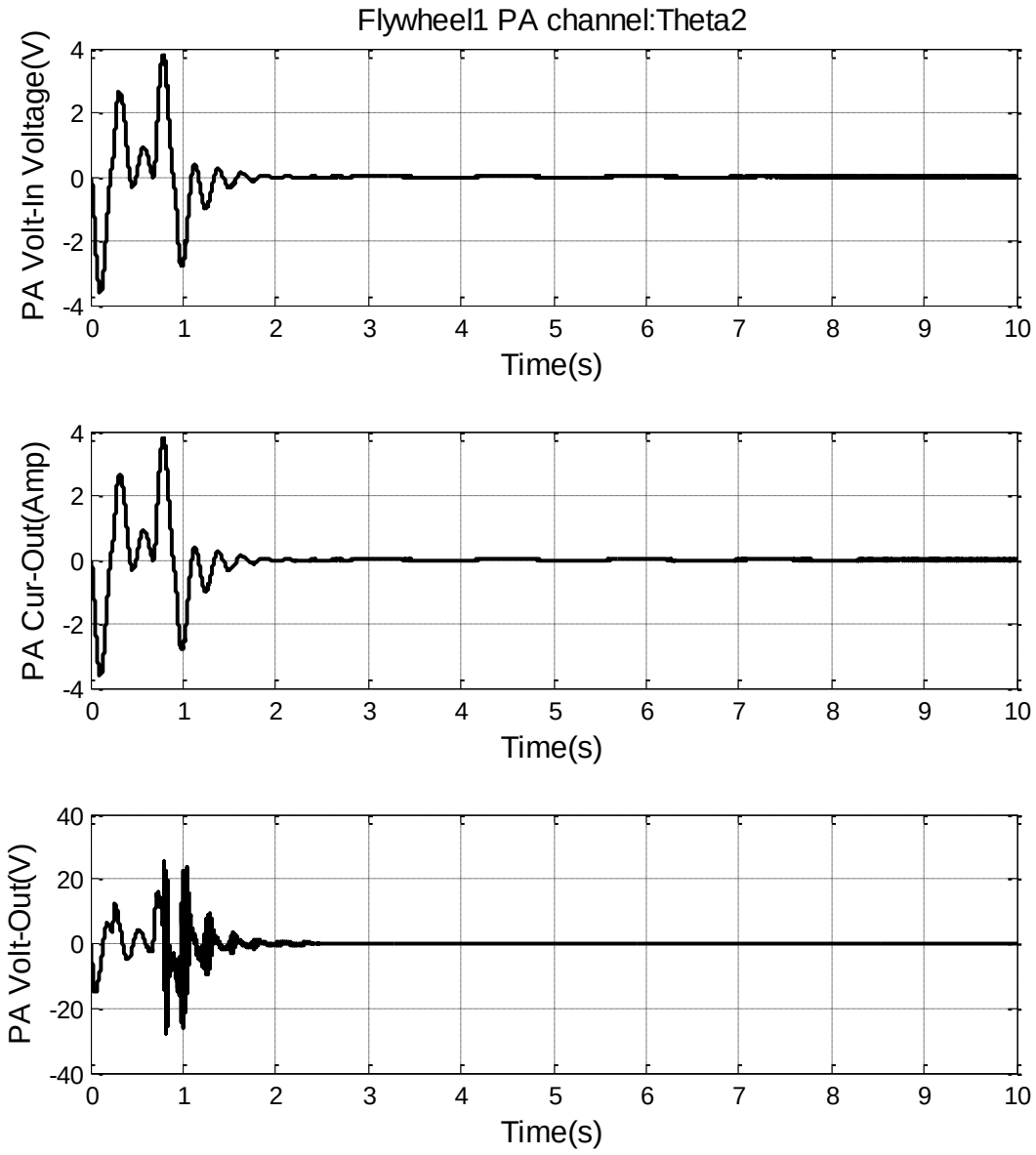

Fig. 6.77 Flywheel 1 Theta 2 Power Amplifier Responses due to Average Bridge Bump

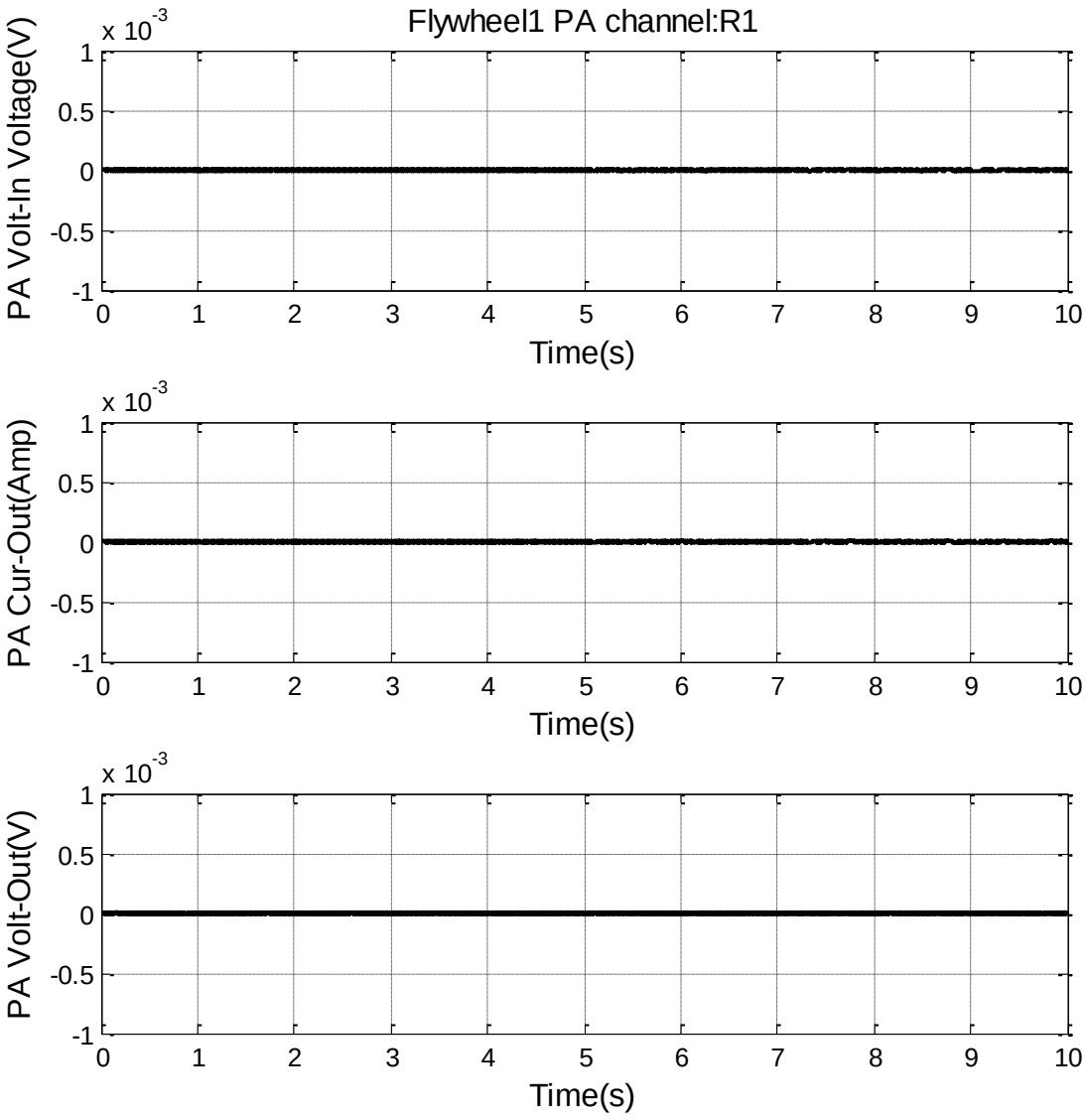

Fig. 6.78 Flywheel 1 Radial 1 Power Amplifier Responses due to Average Bridge Bump

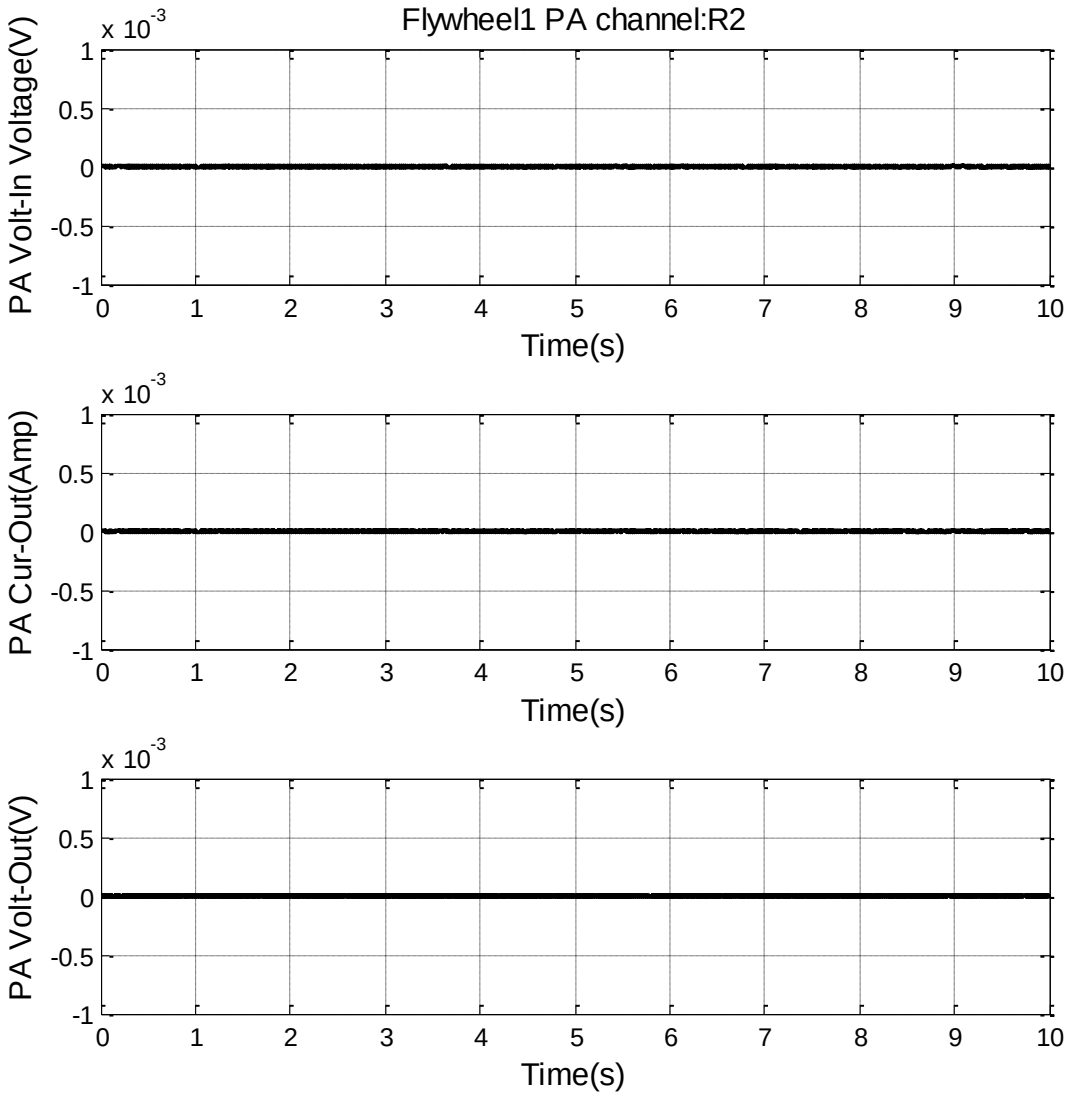

Fig. 6.79 Flywheel 1 Radial 2 Power Amplifier Responses due to Average Bridge Bump

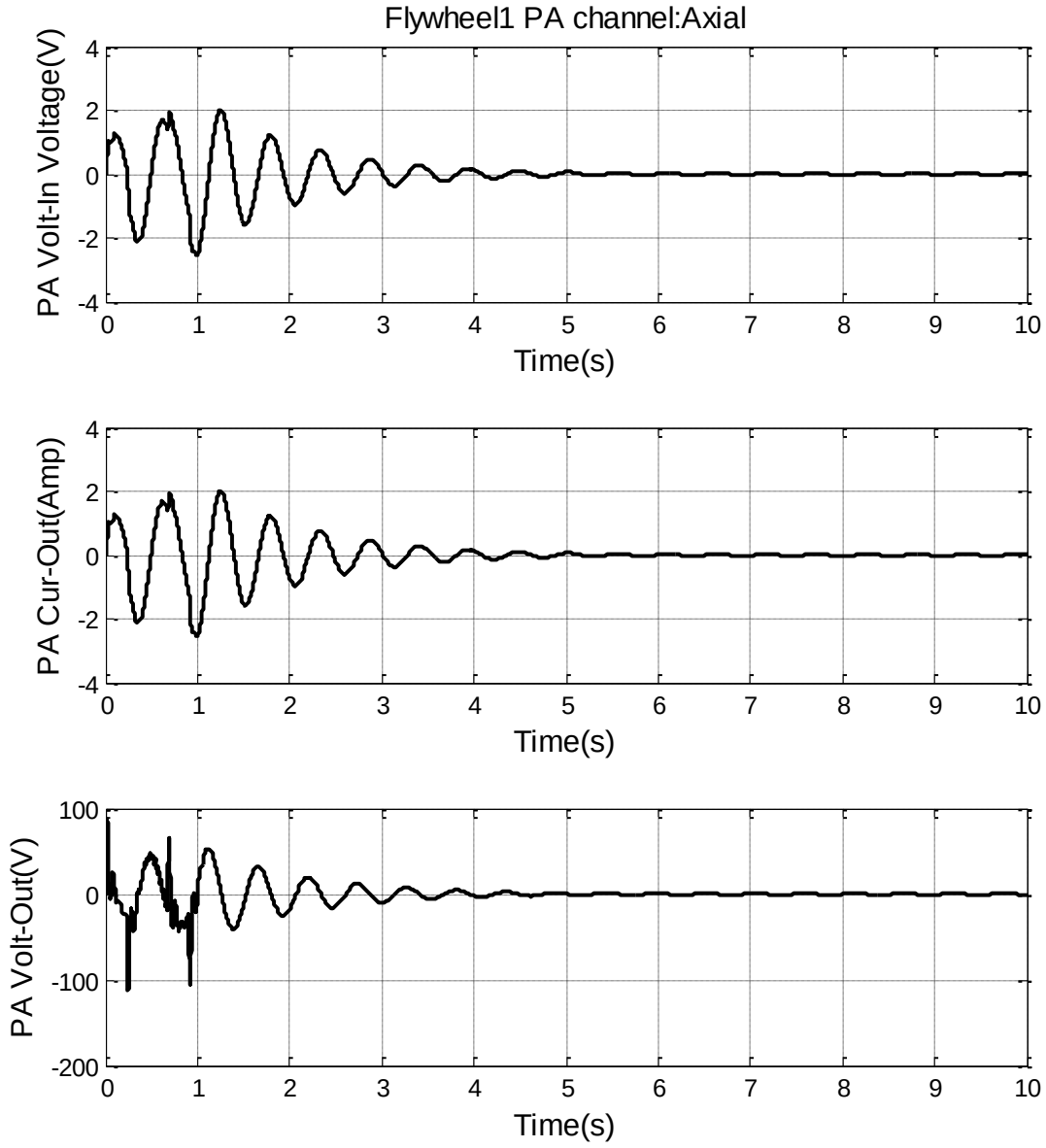

Fig. 6.80 Flywheel 1 Axial Power Amplifier Responses due to Average Bridge Bump

The bump size in Fig. 6.53 is only an average bump value. There is good chance that the bump size will be much bigger. So a simulation was carried out on a bump with 5X bigger slope (165mm rise with in 5.1m length). The maximum motion under catcher

bearings will appear at flywheel 2 and the values are as plotted in Fig. 6.81. The maximum motion under axial catcher bearing is 0.51mm, which is 72.5% of the axial catcher bearing gap. This proves that the flywheel can safely pass the bump size 5 times the average value. However, if the bump gets bigger, the flywheel may hit the catcher bearing and a de-levitation method will be needed as discussed by Zhang [52].

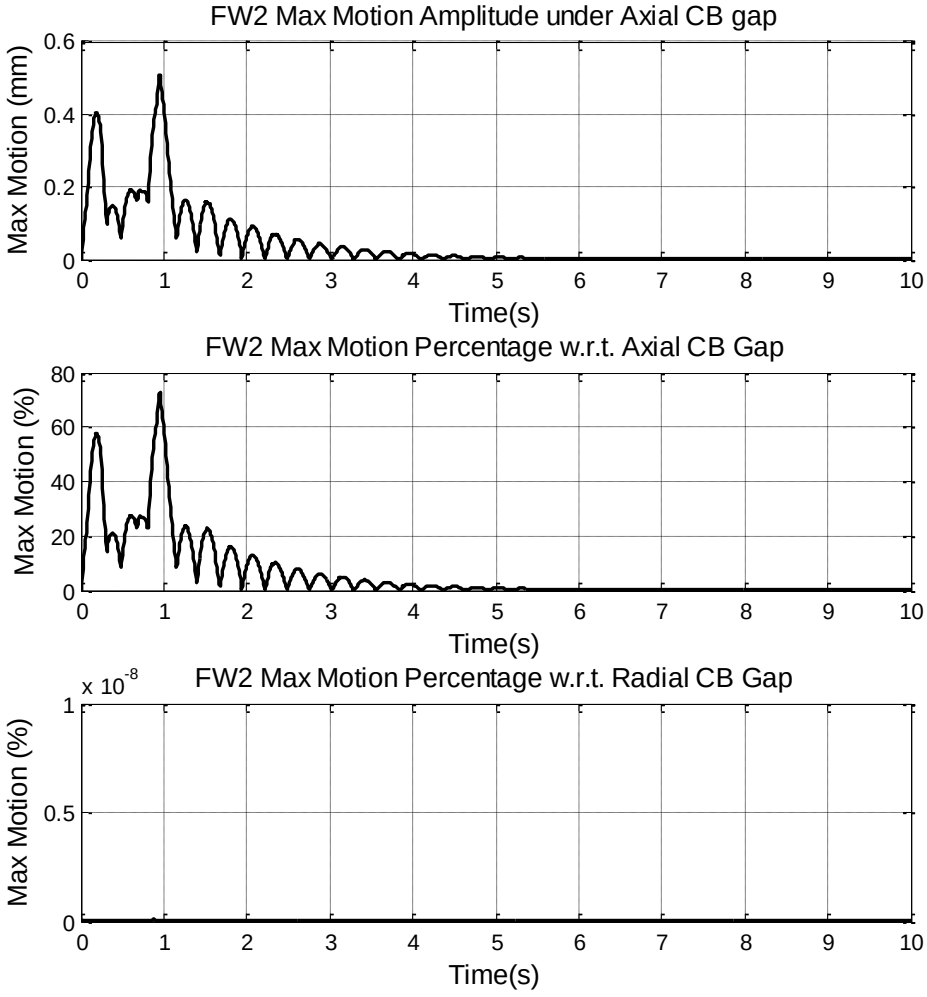

Fig. 6.81 Flywheel 2 Motion under Catcher Bearings due to Bump with 5 times Average Bridge Bump Size

6.5.2 Train Turning Simulation

A transient simulation was carried out to verify the flywheel assembly can endure the centrifugal forces generated while the train is turning its direction. Jankowski provides the minimum railway curve radius for high speed railway network [55]. The maximum speed for a track radius of 6500m is 350 km/h. This leads to a maximum centrifugal acceleration of 1.45m/s^2 (0.148g).

Since our model does not have a super elevated tracks and the trains under investigation have much higher profile, an acceleration of 55% of the 1.45m/s^2 is used during our simulation. Assuming the train speed is 50MPH (22.352 m/s), the corresponding minimum track radius will be 620m (2034ft). The centrifugal acceleration was assumed to reach the maximum value within 3s.The train is moving in x direction and the centrifugal acceleration will be in the y direction.

The linear and angular motion for the train floor are as shown in Fig. 6.82 and Fig. 6.83 The steady state motion of the train floor is 5.80mm in centrifugal force direction. The maximum motion is 5.96mm. There is virtually no motion in longitude (x axis) direction and negligible motion in vertical (z axis) direction. The major rotation happens around the train moving direction and the maximum value is -0.0131 rad, with a steady state value of -0.0123 rad. The angular vibration around lateral axis is negligible, with a maximum value of 1.19e-8 rad.

As explained and shown in the previous section, all flywheels and their housings will have similar behaviors since the housings are bonding with rigid connections. Only results for flywheel 1 and its housing are listed in this dissertation. Fig. 6.84 and

Fig. 6.85 present the motions for flywheel 1's housing. The vertical motion of the housing is nearly negligible. The housing will have a lateral maximum offset of 0.316mm and a steady state offset of 0.307mm. The maximum relative rotation between housing and train floor appears around x axis and the value is 1.149e-3 rad. The maximum relative motion in y axis is 1.30e-6 rad.

Fig. 6.86 and Fig. 6.87 plotted the relative motions between the center of flywheel 1 and its housing. The biggest motion appears in the direction of centrifugal force (y axis) and the value is under 0.053mm. The relative rotation around x axis is between 1.54e-5rad and -1.48e-5rad. The maximum flywheel absolute angular motion is -0.0138rad around x axis. The maximum relative rotation appears around y axis, which is between -2.03e-4 rad and 0.72e-4rad. This large motion is due to large gyroscopic moments generated by the absolute angular velocity around x axis. The power amplifier responses are as plotted in Fig. 6.88 -Fig. 6.92. The maximum current around Theta1 axis is 1.08 Amps. The maximum current around Theta2 is 14.68 Amps, with a maximum voltage of 30.8 Volts. There is virtual no current in x axis since no force is needed on this axis. On y axis, the maximum radial current needed is 4.1 Amps. The excitation on axial bearing is very little and close to zero.

The maximum motion under catcher bearings for flywheel 1 and flywheel 2 are as plotted in Fig. 6.93 and Fig. 6.94. They have almost identical values. The maximum motion under axial catcher bearing will be 0.071mm and 10.2% of the total gap. The maximum motion under radial catcher bearing is 10.5% of the radial catcher bearing gap, with a steady state value of 10.2%. The steady state motion is due to the magnetic

bearing closed-loop radial stiffness trying to counteract the centrifugal forces.

In conclusion, the flywheel will pass through the turning curve without hitting the catcher bearings and letting the power amplifier saturate.

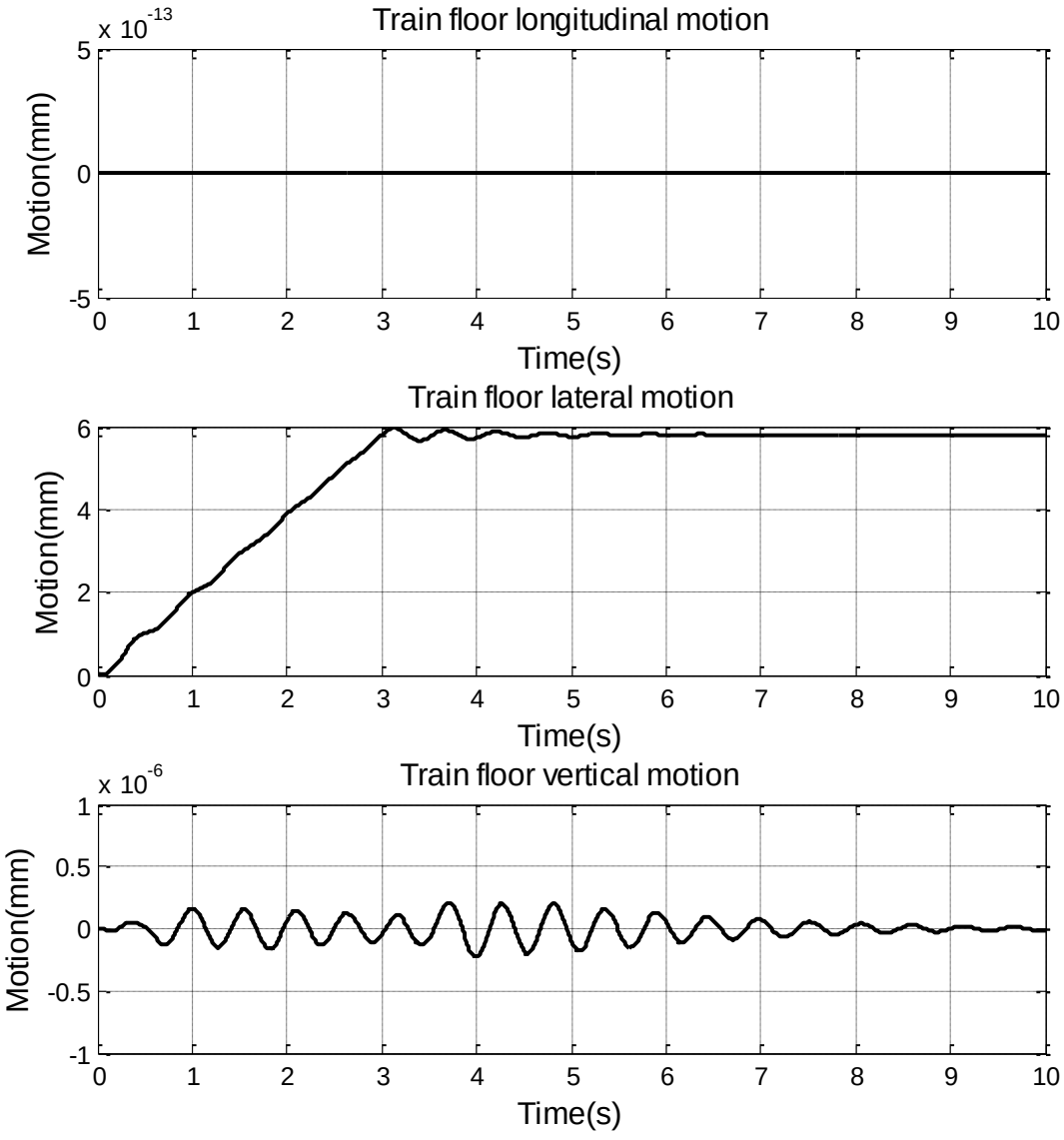

Fig. 6.82 Train Floor Linear Motion Response to Centrifugal Forces

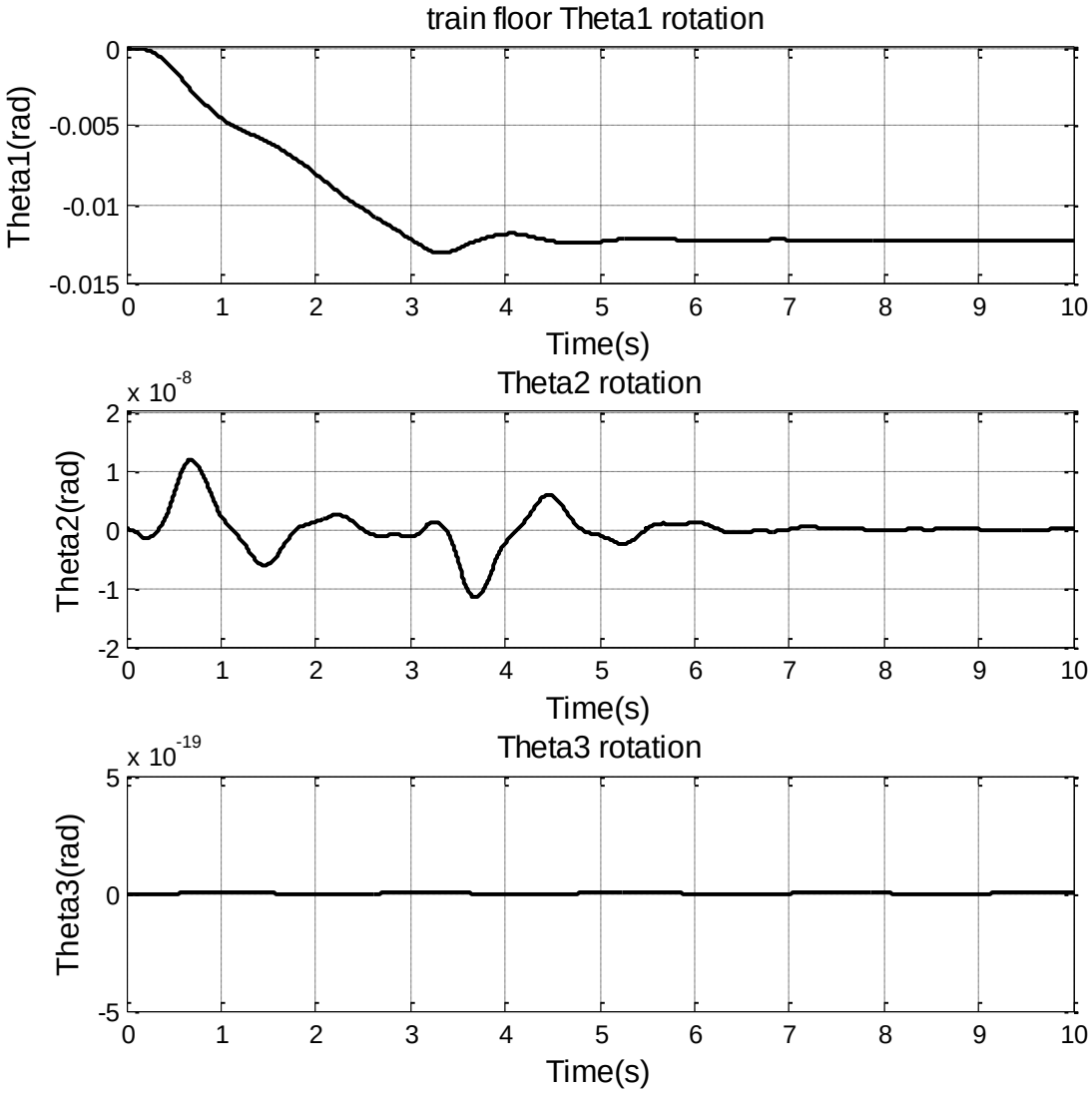

Fig. 6.83 Train Floor Angular Motion Response to Centrifugal Forces

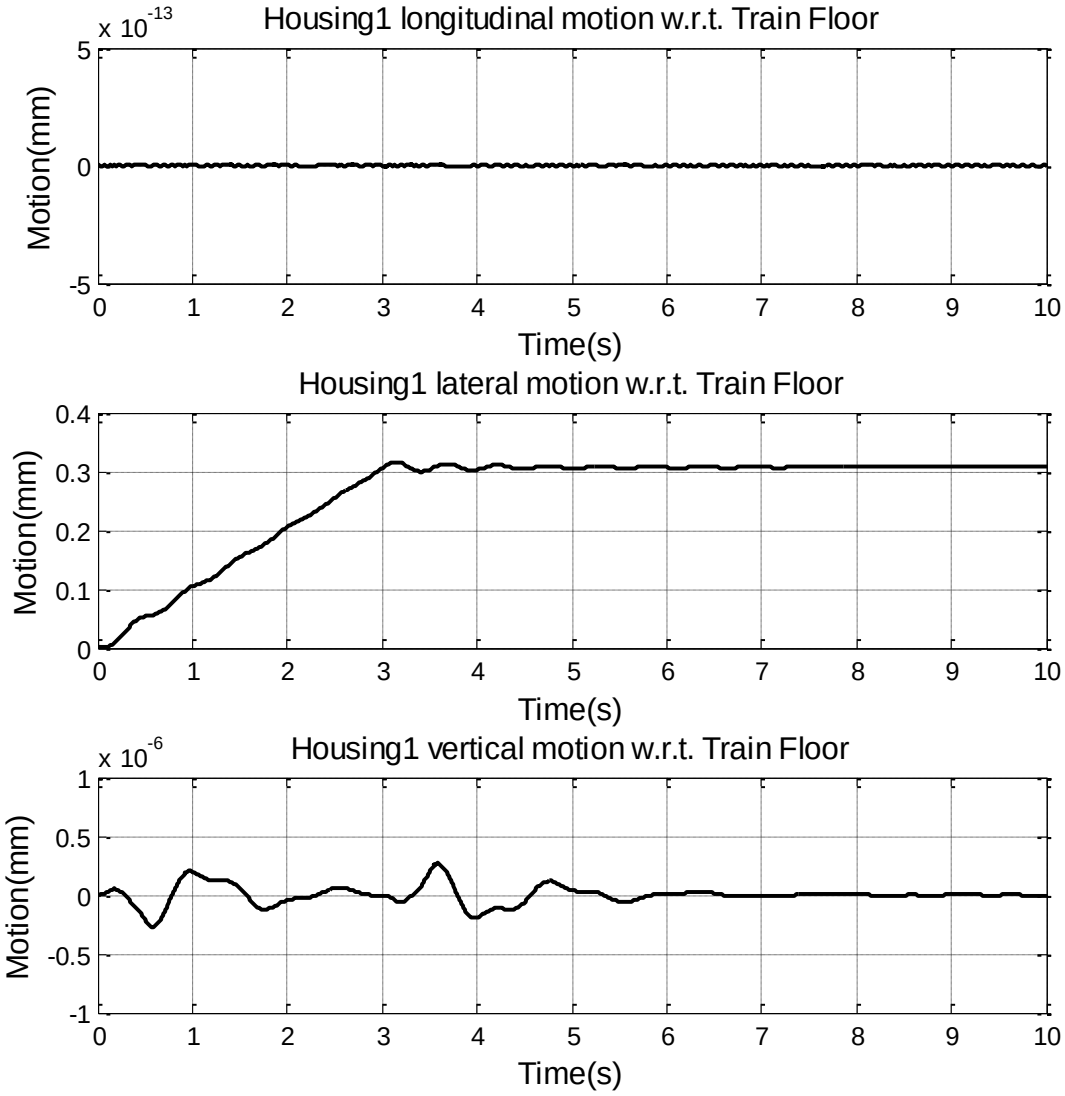

Fig. 6.84 Flywheel Housing 1 Linear Motion Response to Centrifugal Forces

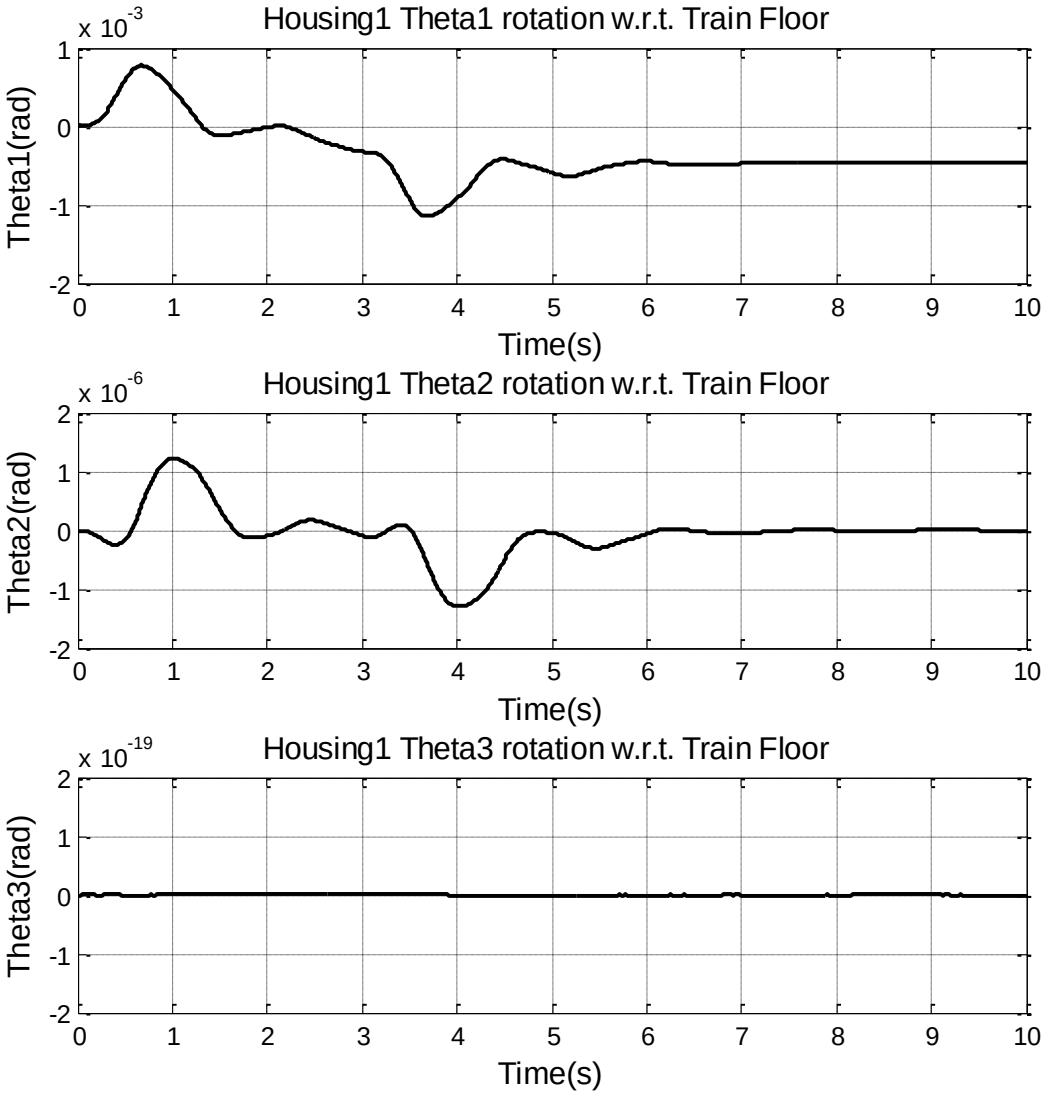

Fig. 6.85 Flywheel Housing 1 Angular Motion Response to Centrifugal Forces

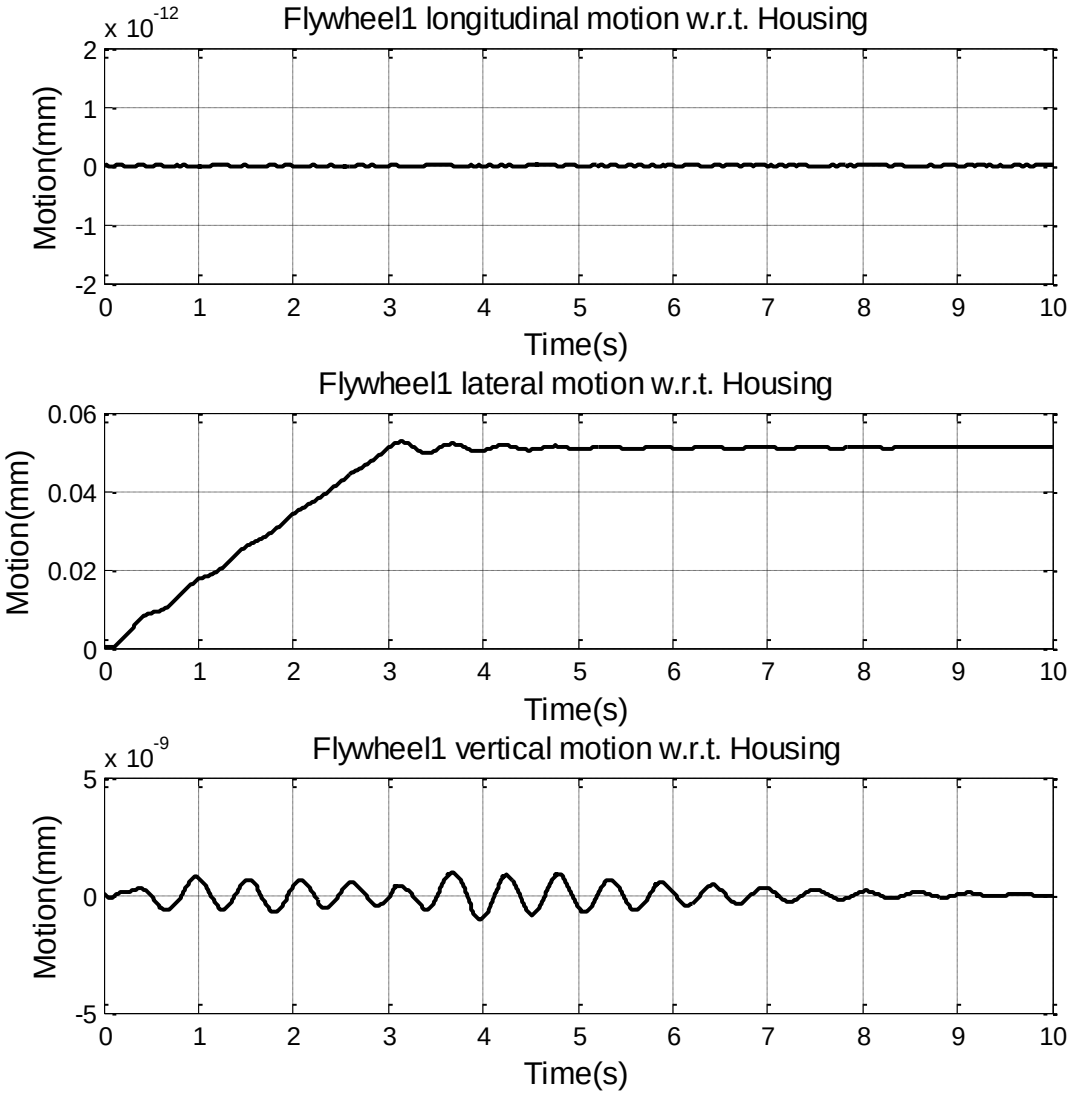

Fig. 6.86 Flywheel 1 Linear Motion Response to Centrifugal Forces

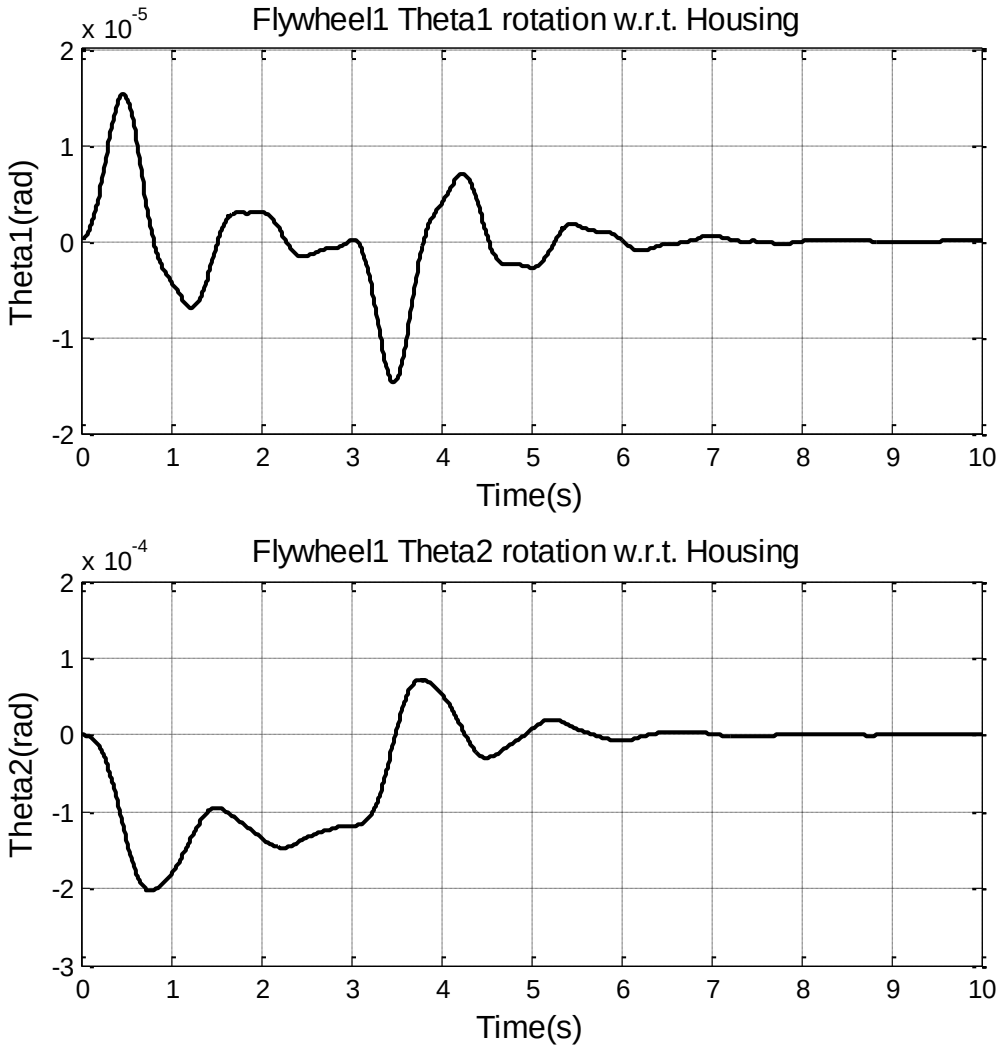

Fig. 6.87 Flywheel 1 Angular Motion Response to Centrifugal Forces

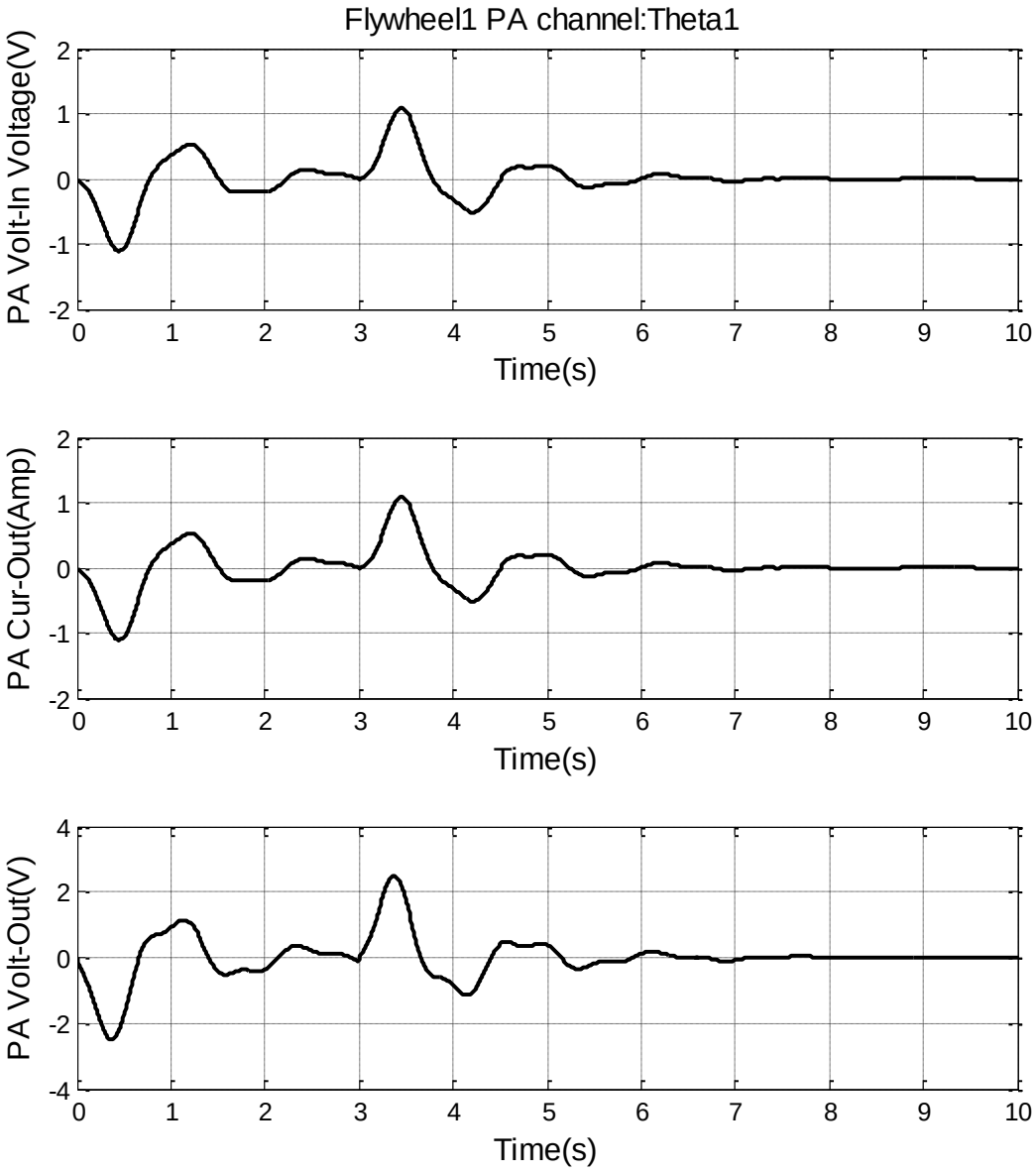

Fig. 6.88 Flywheel 1 Theta1 Power Amplifier Response to Centrifugal Forces

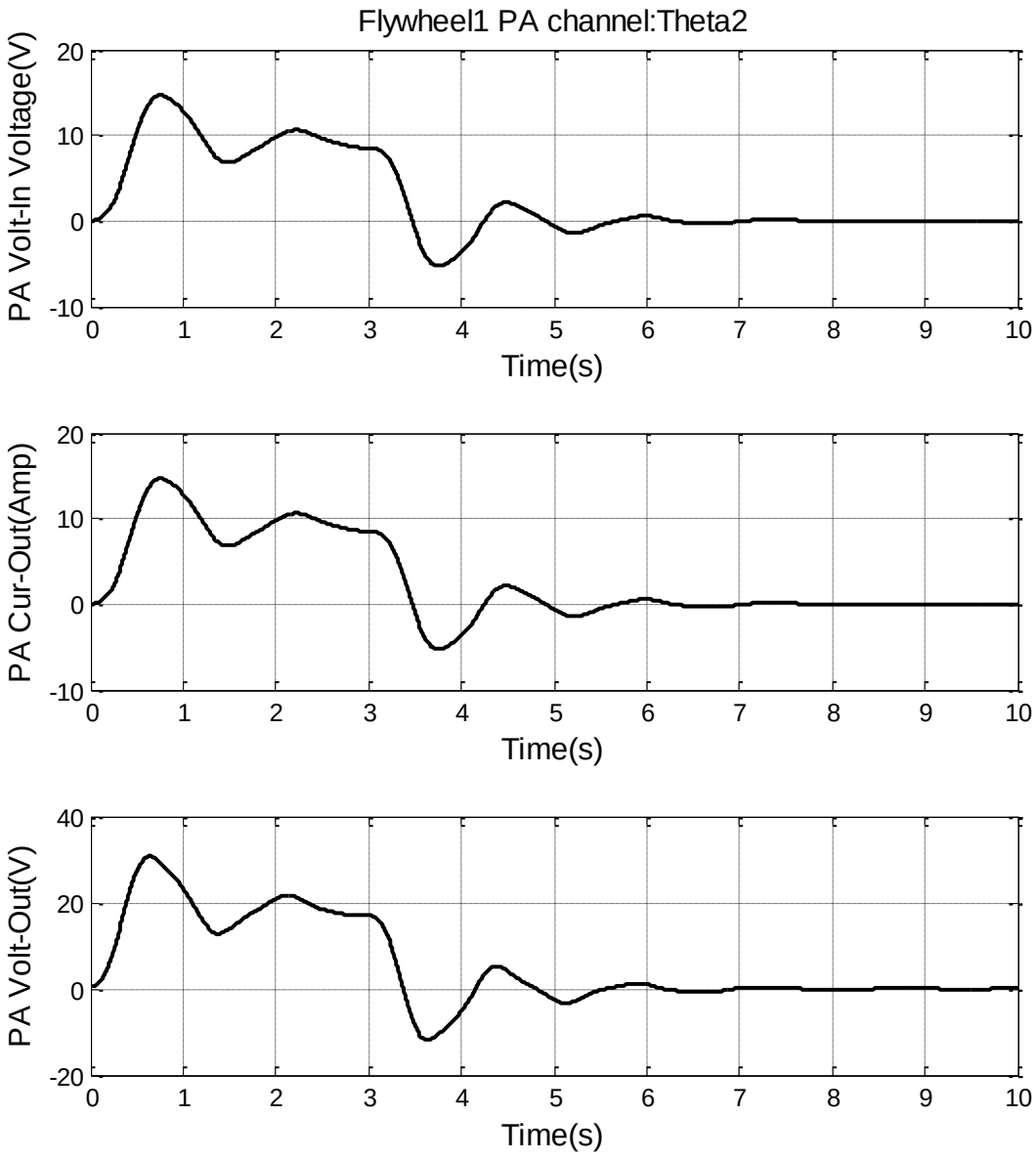

Fig. 6.89 Flywheel 1 Theta2 Power Amplifier Response to Centrifugal Forces

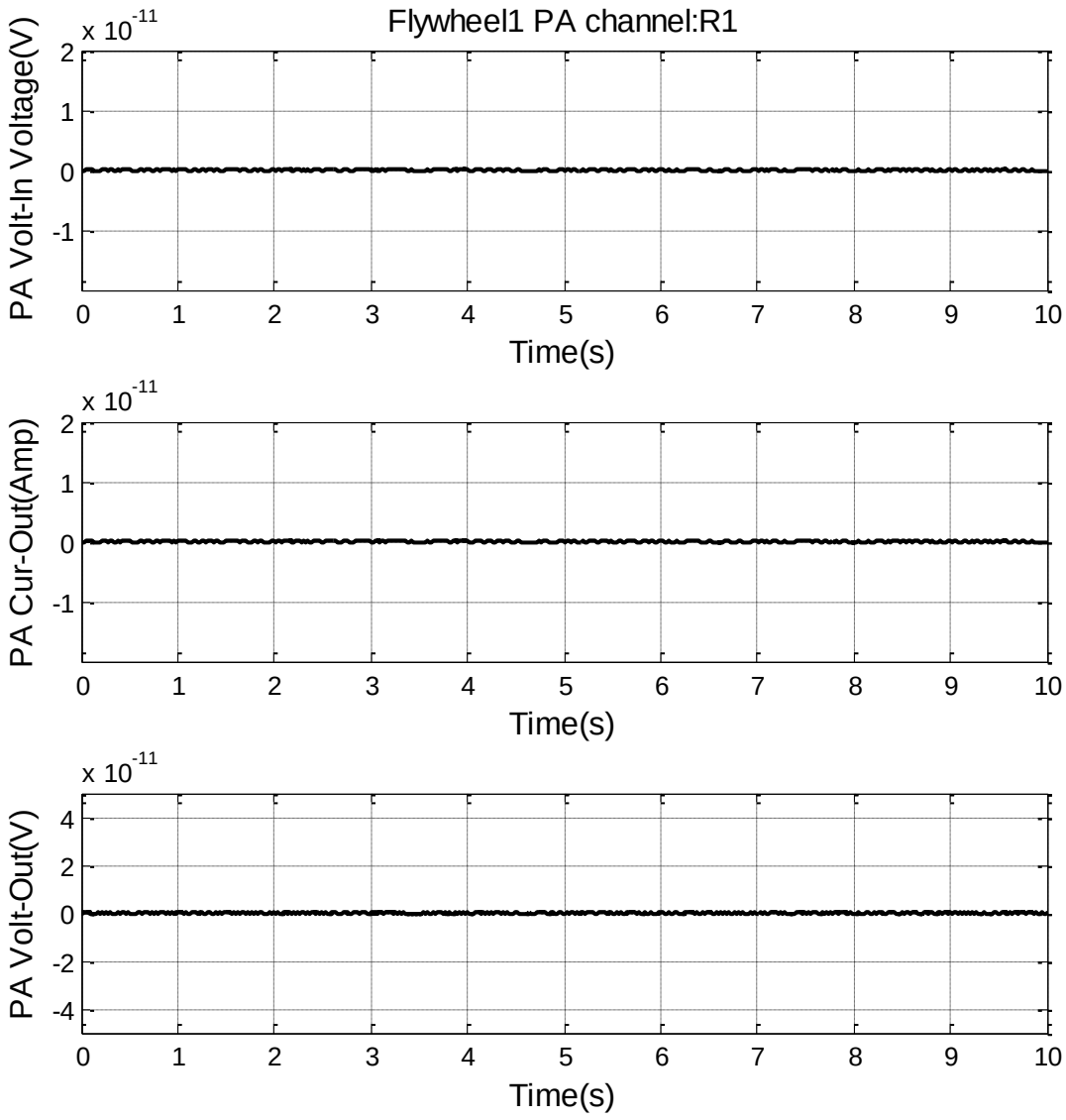

Fig. 6.90 Flywheel 1 Radial 1 Power Amplifier Response to Centrifugal Forces

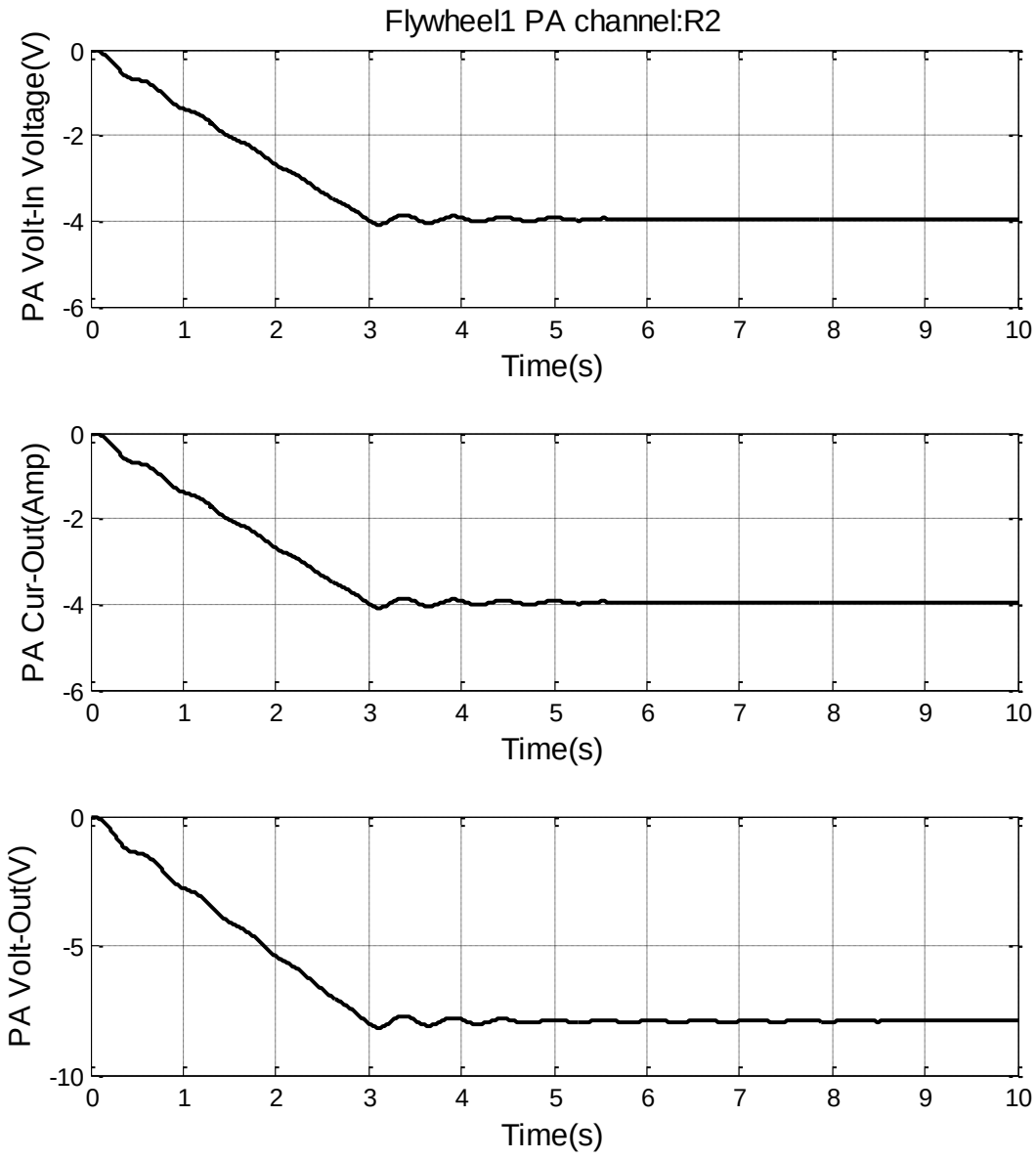

Fig. 6.91 Flywheel 1 Radial 2 Power Amplifier Response to Centrifugal Forces

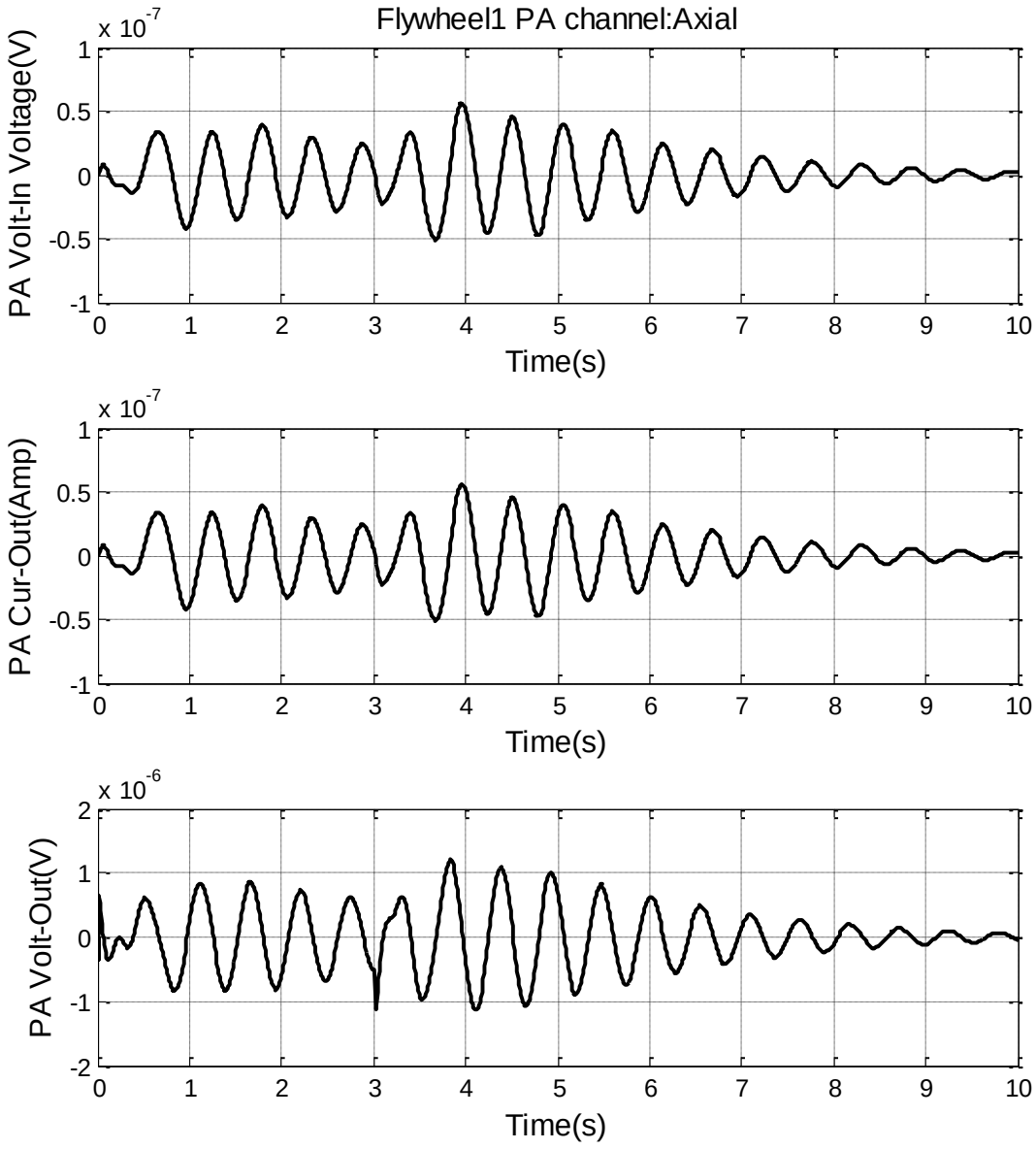

Fig. 6.92 Flywheel 1 Axial Power Amplifier Response to Centrifugal Forces

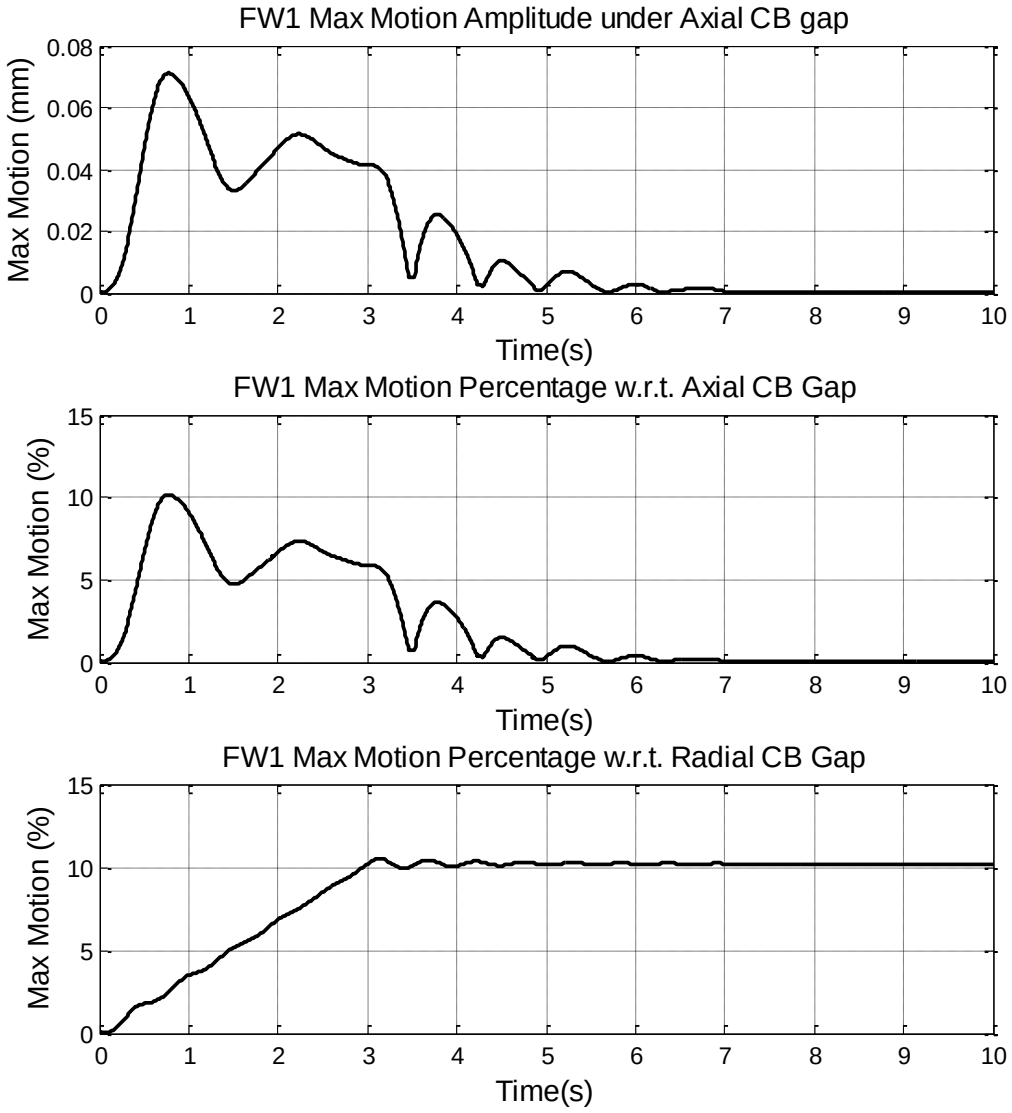

Fig. 6.93 Flywheel 1 Motion under Catcher Bearings due to Centrifugal Forces

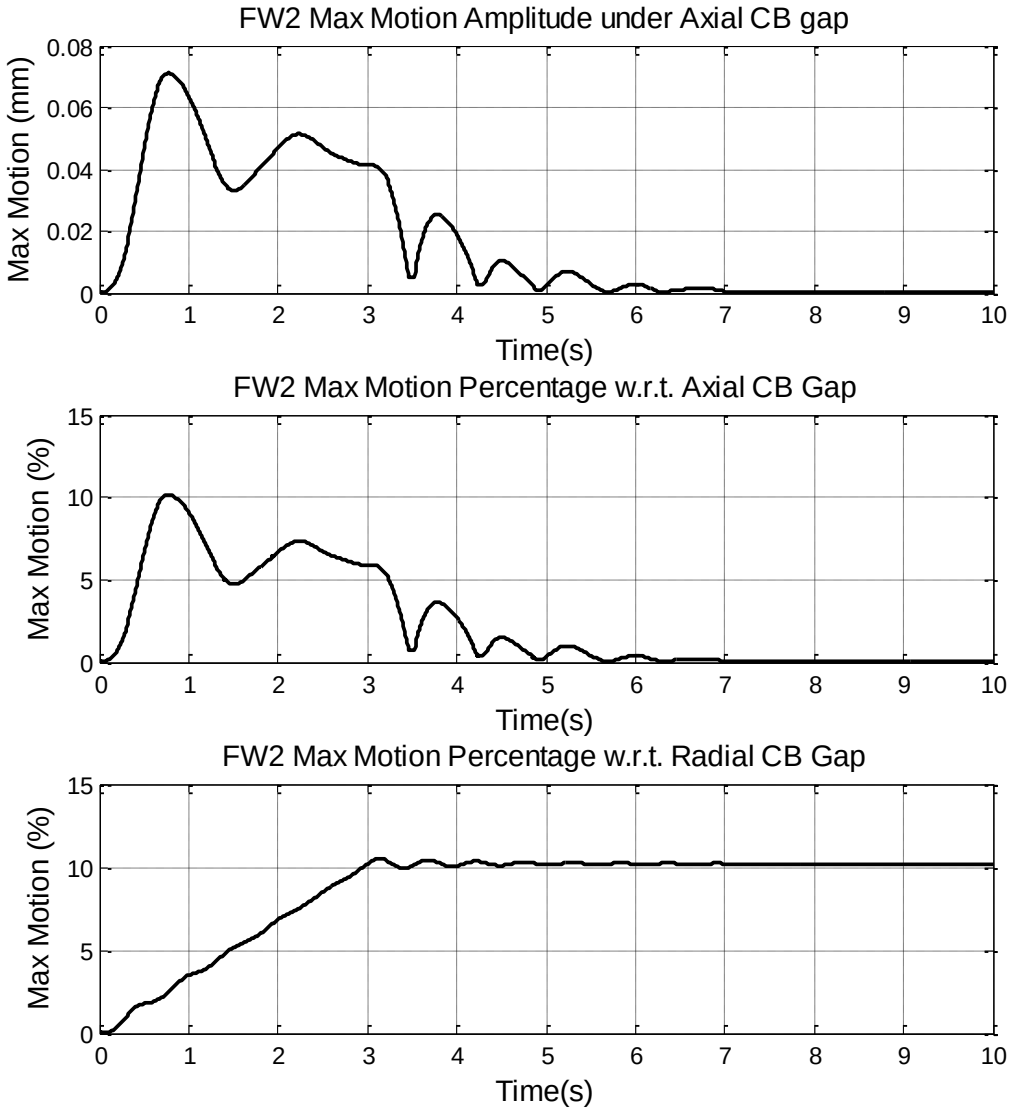

Fig. 6.94 Flywheel 2 Motion under Catcher Bearings due to Centrifugal Forces

6.5.3 Tolerance Simulation

To test the engineering tolerance, several cases were simulated with isolator stiffness/damping parameters changed. Since our major target is to prevent the flywheel from hitting the catcher bearing during train operations, the maximum relative motions under catcher bearings and power amplifier peak values are listed in Table 6.5 and Table 6.6. It must be mentioned again that the nominal gap between flywheel disk surface and axial catcher bearing is 0.7mm and the radial catcher bearing gap is 0.5mm.

Table 6.5 gave out the results for Ramp Passing cases. As can be seen in the table, several combinations of parameters with variations between +/-20% were simulated. The results show around +/-9.8% variation about the maximum motion values under axial catcher bearing with nominal parameters. The maximum possible motion under axial catcher bearing will be 0.112mm and much smaller than the 0.7mm catcher bearing gap. So our ramp passing parameters should pass the engineering tolerance test. Table 6.6 presented the results for Train Turning cases. The same sets of +/-20% parameters changes as used for Table 6.5 were implemented in these simulations. The results show a variation of +/-2.8% for the biggest movement under catcher bearing. The maximum motion under axial catcher bearing is 0.073mm and also much smaller than the gap. The motion under radial catcher bearing remains unaffected (10.5% of gap) by the isolator variations since it is mainly determined by the bearing control effort to counteract the centrifugal force of the flywheel.

As shown in these results, the flywheel energy storage system can safely pass our investigated average ramp and turning cases with +/-20% tolerance on parameters.

Table 6.5 Tolerance Analysis for Ramp Simulation

Case Descriptions	Maximum Relative Rotations (radian)	Maximum Relative Axial Motion between Center of Flywheel and Housing (mm)	Maximum PA Current (Amps)	Maximum PA Voltage (Volts)	Maximum Motion under Axial Catcher Bearing (mm)	Maximum Motion under Radial Catcher Bearing (% gap)
Simulated Bump Case with designed parameters	1.93e-4	0.047	14.1	104	**0.102 (14.5%)**	**0**
All Stiffness reduced to 80%	1.89e-4	0.046	13.9	105	**0.099 (14.2%)**	**0**
All Stiffness increased to 120%	1.95e-4	0.048	14.3	108	**0.104 (14.8%)**	**0**
All Damping reduced to 80%	1.75e-4	0.048	12.8	106	**0.098 (14.0%)**	**0**
All Damping increased to 120%	2.07e-4	0.047	15.2	107	**0.104 (14.9%)**	**0**
All Stiffness and damping reduced to 80%	1.71e-4	0.047	12.5	104	**0.095 (13.6%)**	**0**
All Stiffness and Damping increased to 120%	2.09e-4	0.047	15.4	107	**0.106 (15.1%)**	**0**
Positive Axis Stiffness and Damping increased to 120%, the opposite side reduced to 80%	2.15e-4	0.047	15.8	107	**0.112 (15.9%)**	**0**
Negative Axis Stiffness and Damping increased to 120%, the opposite side reduced to 80%	1.86e-4	0.047	13.7	106	**0.092 (13.1%)**	**0**

Table 6.6 Tolerance Analysis for Train Turning

Case Descriptions	Maximum Relative Rotations (radian)	Maximum Relative Axial Motion between Center of Flywheel and Housing (mm)	Maximum PA Current (Amps)	Maximum PA Voltage (Volts)	Maximum Motion under Axial Catcher Bearing	Maximum Motion under Radial Catcher Bearing (% gap)
Simulated Bump Case with designed parameters	2.03e-4	1.0e-9	14.7	30.8	**0.071 (10.2%)**	**10.5%**
All Stiffness reduced to 80%	2.00e-4	1.1e-9	14.5	30.3	**0.070 (10.0%)**	**10.5%**
All Stiffness increased to 120%	2.06e-4	0.98e-9	14.9	31.1	**0.072 (10.3%)**	**10.5%**
All Damping reduced to 80%	2.00e-4	0.75e-9	14.4	30.2	**0.070 (10.0%)**	**10.5%**
All Damping increased to 120%	2.06e-4	1.34e-9	14.9	31.3	**0.072 (10.3%)**	**10.5%**
All Stiffness and damping reduced to 80%	1.96e-4	0.80e-9	14.2	29.6	**0.069 (9.8%)**	**10.5%**
All Stiffness and Damping increased to 120%	2.08e-4	1.28e-9	15.0	31.5	**0.073 (10.4%)**	**10.5%**
Positive Axis Stiffness and Damping increased to 120%, the opposite side reduced to 80%	2.03e-4	2.83e-5	14.7	30.7	**0.071 (10.1%)**	**10.5%**
Negative Axis Stiffness and Damping increased to 120%, the opposite side reduced to 80%	2.03e-4	2.84e-5	14.7	30.7	**0.071 (10.1%)**	**10.5%**

6.6 Conclusion

This chapter first investigated the optimization algorithm of the train regenerative braking. The ‘maximum energy recovery’ algorithm and the ‘balanced energy recovery & braking effort’ algorithm were proposed and compared. It was found that the maximum energy recovery method will recovery similar amount of energy to the balanced method, when the performance control variable b of the later method was biased toward the maximum energy recovery region.

The ‘balanced energy recovery & braking effort’ algorithm was used during the simulation for the line haul, switcher and high speed rail operations. For the line haul operation, the EPA average schedule was used to evaluate the savings of diesel fuel and NOx emissions by implementing the flywheel energy storage system. Energy consumption during Notch 1-6 of the EPA line haul schedule was supplied by the flywheel energy storage system instead of the diesel engine. By doing this, 33.9% of the total diesel consumption can be reduced. The NOx emission also had a reduction of 29.9% during the 3 hour simulated operation. Nearly 100% of the flywheel energy can be recovered during the regenerative braking phase. Using the rain flow counting algorithm and Miner’s law, the S-N life for non-notched discs are 3e6 cycles (infinite life). Also by using the Paris’s law, it will take 80k simulated cycles for a 0.02in through-the-thickness crack at the weakest location to grow to a critical size. That’s 240k hours of continuous operation.

Due to the easy access to power grids at switcher yard, flywheel stored energy was used as the only form of energy to power the switcher services. The EPA average

switcher schedule was used during the simulation. The system can operate continuously without recharging for 3 hours. 100% of diesel and NOx emission can be saved since the only energy consumed is in the electric form. The S-N lives for non-notched flywheels are 72992 simulated. This equals 218976 hours (25 years) of continuous operation. It will take 15k simulated cycles (45k hours) for a 0.02in through-the-thickness crack at the weakest location to grow to a critical size. The lives of the flywheels can be greatly improved if they get recharged every one or two hours since this will reduce the depth of discharge and stress variation within the flywheels.

High Speed Rail operation was also simulated on an assumed route of 480 miles with 8 stops. To reduce system cost and the weight of the slug car for this passenger train application, the total number of flywheels used is 8 instead of 10 used for line haul and switcher service. Fuel reduction for this simulation is 19.2%, with 16.8% reduction in NOx emission. The predicted S-N lives are 1.25e6 cycles (infinite). It will take 8.3k simulated cycles for a 0.02in through-the-thickness crack at the weakest location to grow to a critical size. This converts to a 4.15k round trips and 11.4 years of operation if one round trip was made each day (14hours/960miles per day). The lives of the flywheels will be greatly improved if 10 flywheels were used.

There are several general points that can be useful to implement the flywheel energy systems into other train applications.

1. Engines notches with higher fuel consumption and NOx emission per unit of power produced should have higher priorities to be replaced by the flywheel power.

2. If permitted, an earlier and smoother braking period will save more fuel and NOx. This is due to two effects. First, an earlier braking effectively shortens the engine running time. Second, the slower braking period within a reasonable will allow more energy to be recovered by the regenerative braking.
3. A higher motor/generator constant for traction motors will generally lead to better energy recovery during regenerative braking.
4. The flywheel discharge limits should be tuned so that the energy discharged during the acceleration phase can be recovered by the regenerative braking. This will also help the cycle life of the flywheel since it will effectively reduce the discharge depth.
5. For flywheel powered switcher services or operations whose regenerative energy cannot recover the energy consumed, the flywheel should be recharged whenever the conditions allow. This will indeed reduce the depth of discharge and increase the flywheel life.
6. Flywheel motor/generator constant (K_{fw}), flywheel voltage & current need to be checked to ensure the simulation won't violate the physical limitation of the system.
7. Adhesion must also be checked during the whole simulation to ensure the locomotive will not have a traction problem.

The average bump size was used to test the effectiveness of the vibration isolators for the flywheel assembly. The maximum motion between flywheel surface and axial

catcher bearing is 0.102mm, which is 14.5% of the axial catcher bearing gap. A 0.082g centrifugal acceleration was gradually imposed on the flywheel within 3s to test the vibration behavior of the flywheel assembly during train turning. The acceleration is 55% of the value that 350Km/h high speed train will face at its minimum turning radius of 6.5km.The results show maximum 0.071mm (10.2% of gap) relative motion under the axial catcher bearing and the flywheel is quite safe from hitting it. However, the current for one of the moment control axis is 14.1Amps which is okay but at high end of the output range for small scale power amplifiers. This makes it necessary for the further investigation on high capacity power amplifiers and possible force saturations of the magnetic bearings.

The engineering tolerance issue was also investigated. The isolator parameters were varied by +/-20% and several combinations were simulated for both ramp passing and train turning cases. Around +/-9.8% and +/-2.8% of variations in maximum relative motions between flywheel and axial catcher bearings were found correspondingly for ramp passing and train turning cases. The maximum motion is 0.112mm for the ramp passing case and 0.073mm for the train turning case. They are both much smaller than the 0.7mm axial catcher bearing gap. The max relative motions under the radial catcher bearing are zero for the ramp passing cases and remains 10.5% of the total radial catcher bearing gap for train turning cases. This proves that the vibration isolation system will still work for the cases simulated with 20% parameter variations.

CHAPTER VII

CONCLUSION AND FUTURE WORK

The major contribution of this dissertation is to develop a reliable and economical flywheel based energy storage system. Advantages of the shaftless flywheel design over traditional energy storage flywheels were discussed from the perspectives of stress, S-N life and fatigue crack growth rate.

A 4340 wheel with 88in diameter and 5in thickness was simulated as an exemplary candidate shaftless design. The 8600lbf flywheel will be rotating at 4906RPM to bear 90kWh of kinetic energy. With a maximum Von-Mises stress of 155.6ksi, the wheel has an energy density of 10.38 Wh/lbs. For a 100% energy discharge, the wheel will have a S-N life of 20k cycles. For 60% discharge cycles, the S-N life will become 1000k. An initial crack of 0.02 in at the weakest location will take 16.1k 50% discharge cycles to reach a critical size. For a 10k life of 50% discharge cycles, the initial crack size needs to be under 0.0335in.

A novel magnetic bearing structure was proposed to hold the shaftless flywheel in place. 3D static magnetic analysis was performed to retrieve the static load capability as well as the position and current stiffness of the magnetic bearing. 3D harmonic analysis retrieved the current stiffness transfer function to take into account the frequency weakening effect caused by eddy currents. Closed-loop controllers were modeled and simulated to verify the controllability of the novel flywheel energy storage system. It was found that the speed following notch filter need to be deactivated at low running

speeds to avoid the stability problem. The notch filter will not affect the stability of the system at normal flywheel rotating speed ranges and will be engaged to suppress runout and unbalance disturbances.

Eddy loss at nominal operating position was simulated. Hysteresis loss was also calculated based on the measurement of the heat treated 4340 sample. The combined eddy/hysteresis loss was estimated to be under 315Watts for our magnetic bearing design. This will be a 0.35% hourly energy loss ratio for the 90kWh flywheel. The actual loss rate will be lower as the flywheel speed become slower during the energy reduction process. The system temperature is simulated in a vacuumed environment with radiation as the only heat exchange method. With 315Watts bearing loss and 2kW motor loss (2% for 200kW motor), the maximum temperature of the system will be 72 Celsius, which is safe for our design.

Another novel concept of motor design was described and preliminary simulations were carried. The major advantage of the proposed architecture is the capability to vary the Motor/Generator constant by physically moving the motor stator in/out. Grid charging simulations were carried out and found that the variable constant capability can ensure the flywheel get fully charged, which is only possible for cases within a limited range of fixed Mot/Gen constant. In addition to this, the variable constant case can help the flywheel energy storage system get fully charged much quicker than any cases with a fixed Mot/Gen constant.

The application of the 90kWh flywheels on train locomotive was then discussed. The optimization method of the regenerative braking was investigated and two methods were

introduced. The first method will give a maximum energy recovery. The second method introduced a *b* parameter that will balance the energy recovery and braking effort. It was proved that the recovered energy ratio is a monotonically increasing function of the performance control parameter *b*. It was also proved that the braking effort is a monotonically decreasing function of *b*. In other words, with a higher *b*, the regenerative braking will harvest more energy with a longer braking time/distance. The results of the two methods were benchmarked and found that the first method will have an energy recovery value very close to the maximum value that the second method can reach with a big *b* value. It was also found that a bigger traction motor torque constant K_{tm} will increase the energy recovery as well as shorten the braking distance given the adhesion of the system is big enough.

Finally, the flywheel assembly with 4 flywheels was modeled on train floor and the vibration isolation was simulated. It turned out that the flywheel system will pass the 1:150 ramps at 50MPH train speed with no risk of hitting the catcher bearings (0.102mm maximum possible motion under axial catcher bearing compared with 0.7mm gap). In the same time, the flywheel can safely pass the test of a 50MPH train turning with a 620m track radius (0.071mm maximum motion under axial catcher bearings (10.2% of axial gap); 10.5% maximum motion under radial catcher bearing gap). The system tolerance was verified with +/-20% variance of isolator stiffness/damping values. The motions under axial catcher bearing vary under +/-9.8% and +/-2.8% respectively for the two cases and the flywheel surfaces are all far away from hitting the catcher bearings.

In conclusion, the shaftless flywheel has big advantages over traditional flywheel

designs with shaft due to its better fatigue life and lower cost. The proposed novel homopolar combo magnetic bearing is feasible in the sense of load capability, control stability, eddy and hysteresis losses, and operating temperature with in vacuum. The magnetic bearing and shaftless flywheel construct a perfect system for low cost energy storage systems.

The balanced energy recovery and braking distance method is a good candidate for optimized regenerative braking due to its ability to increase energy recovery and decrease braking distance. The capability of real-time tuning energy recovery and braking behavior also give it more advantage. The proposed diesel locomotive-slug car architecture makes a general sense in that it can be easily and efficiently applied to various types of traditional locomotives and train operations.

Some future works may be done to extend the research on the shaftless flywheel energy storage system. These may include:

1. Optimization of the solid flywheel shapes to retrieve higher energy storage density.
2. Optimization of the Combo Magnetic Bearing structure to minimize eddy current effect, to minimize the position stiffness, to maximize the current stiffness and to minimize the coil inductance.
3. Nonlinearities analysis of magnetic bearings. Flux saturation and power amplifier saturation need to be considered to analyze the nonlinear behavior of the magnetic bearing suspension.

4. The vibration isolation scheme for the flywheel energy storage system on the train. Cost of gimbal mounts for the flywheel assembly need to be investigated and compared with the vibration isolator method studied in this dissertation. Gimbal mounts will completely eliminate the angular vibrations of the flywheel system. Large angular vibrations will require large moments to be generated by magnetic bearing and may incur much larger eddy loss on the system.
5. Study of the lateral stress incurred by vibrations during operation of the flywheel system. Analysis of the fatigue effects related to lateral stresses.
6. Building of prototypes for the flywheel energy storage system. Prototypes need to be built to verify and correlate with the FEM simulation results on magnetic bearing performances and losses.

REFERENCES

[1] Glaser, J. A., 2007, "US Renewable Energy Consumption," Clean Technologies and Environmental Policy, **9**(4), pp. 249-252.

[2] Eisberg, N., 2007, "US Energy Roadmap - Renewable Energy Could Curb Climate Change in US," Chemistry & Industry, **5**, pp. 7-7.

[3] Heiman, M. K., 2006, "Expectations for Renewable Energy under Market Restructuring: the US Experience," Energy, **31**(6-7), pp. 1052-1066.

[4] Apergis, N., and Payne, J. E., 2011, "The Renewable Energy Consumption-Growth Nexus in Central America," Applied Energy, **88**(1), pp. 343-347.

[5] Zografakis, N., Sifaki, E., Pagalou, M., Nikitaki, G., Psarakis, V., and Tsagarakis, K. P., 2010, "Assessment of Public Acceptance and Willingness to Pay for Renewable Energy Sources in Crete," Renewable & Sustainable Energy Reviews, **14**(3), pp. 1088-1095.

[6] Zhang, X. T., Gao, Y. F., and Shi, G. H., 2010, "Application and Development of Renewable Energy: A Case Study of Solar Energy Utilization in Baoding, China," ES2010: Proceedings of ASME 4th International Conference on Energy Sustainability, Phoenix, Arizona, **2**, pp. 1009-1015, 1117.

[7] Zahedi, A., 2010, "Australian Renewable Energy Progress," Renewable & Sustainable Energy Reviews, **14**(8), pp. 2208-2213.

[8] Strasik, M., Hull, J. R., Mittleider, J. A., Gonder, J. F., Johnson, P. E., McCrary, K. E., and McIver, C. R., 2010, "An Overview of Boeing Flywheel Energy Storage Systems

with High-temperature Superconducting Bearings," Superconductor Science & Technology, **23**(3), Article No.034021, pp. 1-5.

[9] EPA, 2010, "eGRID2010 Year 2007 Plant and Aggregation Files and File Structure Document," U. S. Environmental Protection Agency, http://www.epa.gov/cleanenergy/energy-resources/egrid/index.html, Last Accessed: 2011-08-02.

[10] Sierra_Research_Inc, 2004, "Development of Railroad Emissions Inventory Technologies," Sierra Research Inc. prepared for the Southern States Air Resources Managers Inc., Report No. 2004-06-02. http://www.metro4-sesarm.org/pubs/railroad/FinalMethodologies.pdf, Last Accessed: 2011-08-02.

[11] EIA, 2010, "Annual Energy Review 2009," U. S. Energy Information Admin., http://www.eia.gov/totalenergy/data/annual, Last Accessed: 2011-08-02.

[12] Briginshaw, D., 2004, "Hybrid Traction System Benefits Environment: Japan's New Energy Train Project Uses a Hybrid Diesel-electric Traction System to Achieve Major Reductions in Energy Consumption, Noxious Emissions, and Noise," International Railway Journal, **44**(12), pp. 32-32.

[13] Donnelly, F. W., Cousineau, R. L., and Horsley, R. N. M., 2004, "Hybrid Technology for the Rail Industry," Proceedings of the 2004 ASME/IEEE Joint Rail Conference, Baltimore, Maryland, pp. 113-117,221.

[14] Cousineau, R., 2006, "Development of a Hybrid Switcher Locomotive," IEEE Instrumentation & Measurement Magazine, **9**(1), pp. 25-29.

[15] Flaherty, P. A., 2005, "Multi-stage Hybrid Drives for Traction Applications," Proceedings of the 2005 ASME/IEEE Joint Rail Conference, Pueblo, Colorado, pp. 171-

175, 245.

[16] Akli, C. R., Roboam, X., Sareni, B., and Jeunesse, A., 2007, "Energy Management and Sizing of a Hybrid Locomotive," 12th European Conference on Power Electronics and Applications, Aalborg, Denmark, pp. 5160-5169, 5336.

[17] Jaafar, A., Akli, C. R., Sareni, B., Roboam, X., and Jeunesse, A., 2009, "Sizing and Energy Management of a Hybrid Locomotive Based on Flywheel and Accumulators," IEEE Transactions on Vehicular Technology, **58**(8), pp. 3947-3958.

[18] Thelen, R. F., Herbst, J. D., and Caprio, M. T., 2003, "A 2MW Flywheel for Hybrid Locomotive Power," IEEE 58th Vehicular Technology Conference, Orlando, Florida, pp. 3231-3235, 3551.

[19] Murphy, B. T., Ouroua, H.,Caprio, M. T., Herbst, J. D., 2004, "Permanent Magnet Bias, Homopolar Magnetic Bearings for a 130 kW-hr Composite Flywheel," 9th International Symposium on Magnetic Bearings, PN288, Lexington, Kentucky.

[20] Herbst, J. D., Caprio, M. T., Gattozzi, A. L., and Graf, C., 2005, "Challenges and Solutions for the Use of Flywheel Energy Storage in High Power Applications," International Conference on Electrical Energy Storage Applications and Technology, PN305, San Francisco, California.

[21] Yoo, S. Y., Lee, W. R., Bae, Y. C., and Noh, M., 2010, "Design of Magnetically Levitated Rotors in a Large Flywheel Energy Storage System from a Stability Standpoint," Journal of Mechanical Science and Technology, **24**(1), pp. 231-235.

[22] Kurita, N., Ishikawa, T., and Matsunami, M., 2009, "Basic Design and Dynamic Analysis of the Small-sized Flywheel Energy Storage System - Application of Lorentz

Force Type Magnetic Bearing," International Conference on Electrical Machines and Systems, Tokyo, Japan, pp. 415-420.

[23] Zhu, D. H., Cheng, X., and Zhu, H. Q., 2009, "Structure and Performance Analysis for AC-DC Three Degrees of Freedom Active Magnetic Bearings," IEEE 6th International Power Electronics and Motion Control Conference, Wuhan, China, pp. 2193-2197.

[24] Patrick, T., MacMullen, C. S., 2000, "Combination Radial-Axial Magnetic Bearing," Proceedings of International Symp. on Magnetic Bearing, Zurich, Swizerland, pp. 473-478.

[25] Jiancheng, F., Jinji, S., Yanliang, X., and Xi, W., 2009, "A New Structure for Permanent-Magnet-Biased Axial Hybrid Magnetic Bearings," IEEE Transactions on Magnetics, **45**(12), pp. 5319-5325.

[26] Fang, J. C., Sun, J. J., Liu, H., and Tang, J. Q., 2010, "A Novel 3-DOF Axial Hybrid Magnetic Bearing," IEEE Transactions on Magnetics, **46**(12), pp. 4034-4045.

[27] Bakis, C. E., Weaver, E. J., and Shirey, C. L., 1999, "Quasi-static and Fatigue Behavior of Composite Flywheel Materials in Air and Vacuum Environments," Proceedings of the 8th Japan-U.S. Conference on Composite Materials, Inner Harbor, Baltimore, pp. 831-840.

[28] Tzeng, J. T., and Moy, P., 2009, "Composite Energy Storage Flywheel Design for Fatigue Crack Resistance," IEEE Transactions on Magnetics, **45**(1), pp. 480-484.

[29] Stevens, K., Thornton, R., Clark, T., Beaman, B. G., and Dennehy, N., 2002, "A Shaftless Magnetically Levitated Flywheel for Spacecraft Multifunctional Energy

Storage and Attitude Control Subsystem Applications," Advances in the Astronautical Sciences, Guidance and Control, **111**, pp. 385-403, 522.

[30] BeaconPower, 2010, "High Speed,Low Cost, composite Ring with Bore-Mounted Magnets," Project Poster for DOE (Department of Energy) Recovery Funding For Cutting-Edge Cleantech Research. http://www.beaconpower.com/files/DOE-ESS-Project-Update-Poster-11.10.pdf, Last Accessed: 2011-08-02.

[31] Optimal Energy Systems Inc., 2006, "High Voltage Charging FPoM:60 MJ Energy Storage," Space Power Workshop, Manhattan Beach, California.

[32] Soeder, J., Beach, R., 2010, "NASA Glenn Research Center Power Capabilities," HBCU/MI STEM Collaboration Symposium, Dayton, Ohio.

[33] U.S. Department of Defense, 1998, *Millitary Handbook-MIL-HDBK-5H: Metallic Materials and Elements for Aerospace Vehicle Structures*, U.S. Department of Defense, http://www.knovel.com/web/portal/browse/display?_EXT_KNOVEL_DISPLAY_bookid=754&VerticalID=0, Last Accessed: 2011-08-02.

[34] Boyer, H. E., 1986, *Atlas of Fatigue Curves*, ASM International, Metals Park, Ohio.

[35] Blauel, J. G., Beinert, J., and Wenk, M., 1977, "Fracture-Mechanics Investigations of Cracks in Rotating-Disks," Experimental Mechanics, **17**(3), pp. 106-112.

[36] Bueckner, H. F., and Giaever, I., 1966," Stress Concentration of a Notched Rotor Subjected to Centrifugal Forces," Journal of Applied Mathematics and Mechanics, **46**(5), pp. 265-273.

[37] Owen, D. R. J., and Griffiths, J. R., 1973, "Stress Intensity Factors for Cracks in a Plate Containing a Hole and in a Spinning Disk," International Journal of Fracture, **9**(4),

pp. 471-476.

[38] Williams, J. G., Isherwood, D.P., 1968, "Calculation of the Strain-energy Release Rates of Cracked Plates by an Approximate Method," The Journal of Strain Analysis for Engineering Design, **3**(1), pp. 17-22.

[39] Pilkey, W. D., 1994, *Formulas for Stress, Strain, and Structural Matrices*, John Wiley & Sons, New York.

[40] Liaw, P. K., Leax, T. R., and Donald, J. K., 1987," Fatigue Crack-Growth Behavior of 4340 Steels," Acta Metallurgica, **35**(7), pp. 1415-1432.

[41] Williamson, S., and Chan, E. K. C., 1993, "Three-Dimensional Finite-Element Formulation for Problems Involving Time-Varying Fields, Relative Motion, and Magnetic Saturation," Science, Measurement & Technology, IEE Proceedings A, **140**(2), pp. 121-130.

[42] Kenny, A., 2001, "Nonlinear Electromagnetic Effects on Magnetic Bearing Performance and Power Loss," PhD Dissertation, Texas A&M University, College Station, Texas.

[43] Kim, C., 1995, "Magnetic Bearing Eddy Current Effects on Rotordynamic System Response," PhD Dissertation, Texas A&M University, College Station, Texas.

[44] Vector Fields, 1998, *Opera 3d: Training Course Notes*, Vector Fields Software Inc., Kidlington, UK.

[45] Zienkiewicz, O. C., 1977, *The Finite Element Method*, McGraw-Hill, London, UK.

[46] Havelka, D. L., 1997, "Calculation of Rotational Power Losses in Eight Pole Radial Magnetic Bearings," Master of Science Thesis, Texas A&M University, College Station,

Texas.

[47] Hay, W., 1982, *Railroad Engineering*, John Wiley & Sons, New York.

[48] Deb, K., Pratap, A., Agarwal, S., and Meyarivan, T., 2002, "A Fast and Elitist Multiobjective Genetic Algorithm: NSGA-II," IEEE Transactions on Evolutionary Computation, **6**(2), pp. 182-197.

[49] Deb, K., 2001, *Multi-objective Optimization Using Evolutionary Algorithms*, John Wiley & Sons, New York.

[50] Lawson, L. J., and Cook, L. M., 1979, "Wayside Energy Storage Study. Volume IV. Dual-mode Locomotive: Preliminary Design Study. Final Report June 1978-October 1978," Prepared for U.S. Department of Tranportation and Federal Railroad Admin., Report No.FRA/ORD-78/78.IV, http://www.fra.dot.gov/downloads/Research/ord7878-IV_Wayside_Energy_Storage_Study_Volume_IV.pdf, Last Accessed: 2011-08-02.

[51] Nieslony, A., 2009, "Determination of Fragments of Multiaxial Service Loading Strongly Influencing the Fatigue of Machine Components," Mechanical Systems and Signal Processing, **23**(8), pp. 2712-2721.

[52] Zhang, X. H., 2009, "Vibration Isolation of a Locomotive Mounted Energy Storage Flywheel," Master of Science Thesis, Texas A&M University, College Station, Texas.

[53] Nicks, J., 2008, "The Bump at the End of the Railway Bridge," PhD Dissertation, Texas A&M University, College Station, Texas.

[54] Sun, Y. Q., and Dhanasekar, M., 2002, "A Dynamic Model for the Vertical Interaction of the Rail Track and Wagon System," International Journal of Solids and Structures, **39**(5), pp. 1337-1359.

[55] Jankowski, B., 2011, “High Speed Rail Routing Based on the French/Spanish, German, Japanese, and Chinese Patterns”, European Commission Workshop on Approaching a European High Speed Rail Network, TAIEX Workshop INFRA 43407, Kyiv, Ukraine.

.

VITA

Zhiyang Wang was born in Daqing, China and grew up there. He joined Harbin Institute of Technology in 1998. He received his Bachelor of Science degree in 2002 in Mechatronics and his Master of Science degree in 2004 in Mechatronics and Robotics. After that, he started as an application engineer at Teradyne Inc. In August 2006, he began his study at Texas A&M University for his Ph.D. degree in mechanical engineering. Mr. Wang has worked closely with Dr. Palazzolo in the Vibration Control and Electromechanics lab since Jan 2007. During this time, he focused most of his time on developing a novel shaftless flywheel energy storage system and its magnetic levitations, which can be used in railroad locomotives as well as other areas that need large scale energy storage systems. He also developed a rotordynamic vibration/modal test software suite for turbomachines and a FEM rotordynamic analysis code for rotors levitated with magnetic bearings. His earlier dissertation work was sponsored by the Texas Transportation Institute (TTI) and the Association of American Railroads (AAR). The later work was supported by the Turbomachinery Research Consortium (TRC).

Zhiyang Wang may be contacted at the following address:

Vibration Control and Electromechanics Laboratory

Department of Mechanical Engineering, MS 3123

Texas A&M University

College Station, Texas, 77843-3123

979-845-4580